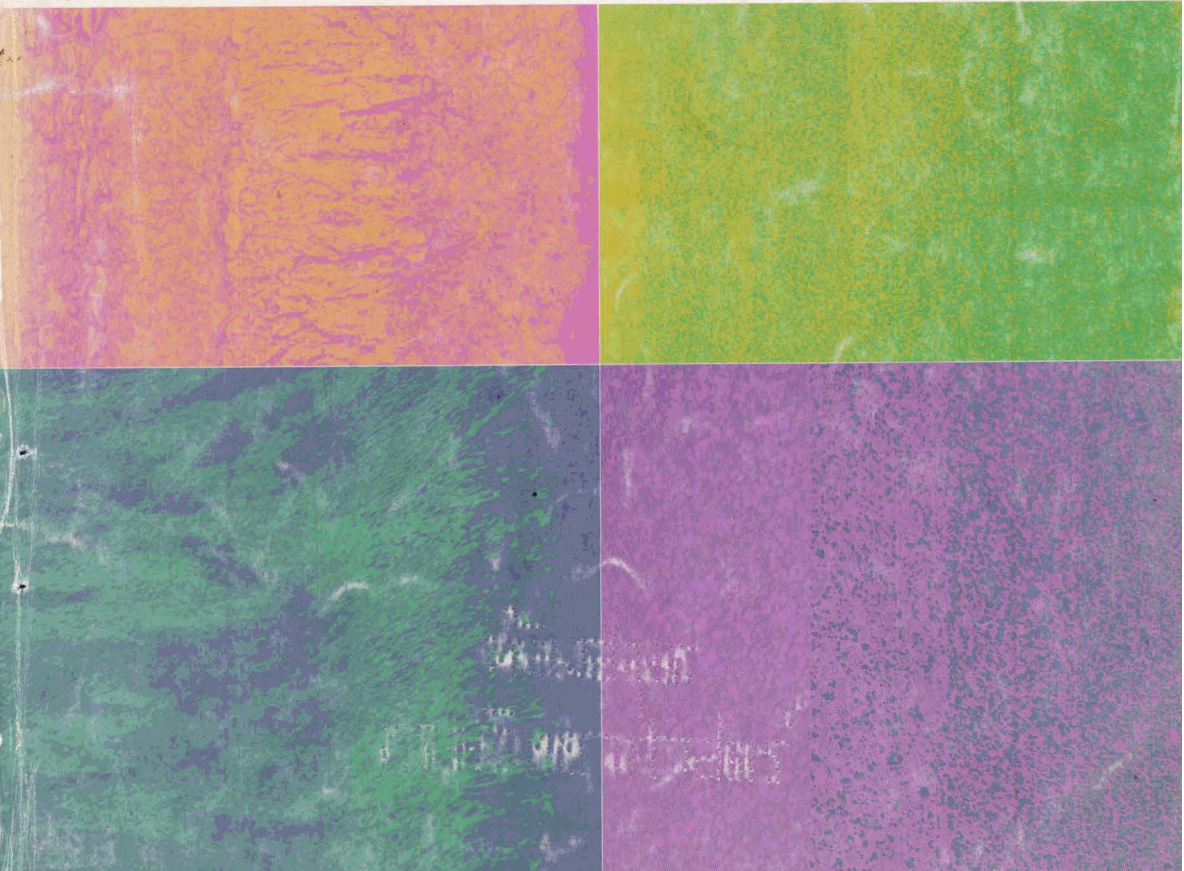


Journal of the CERAMIC SOCIETY of Japan, *International Edition*

Vol.98 Mar.1990

14 Papers from Nippon Seramikkusu Kyokai Gakujutsu Ronbunshi, Vol.98 No. 3 1990

NIPPON SERAMIKKUSU KYOKAI GAKUJUTSU RONBUNSHI Vol. 98 1990



Editorial Board

Dr. Teruo Sakaino
Prof. Emeritus, Tokyo Institute of Technology
Dr. Nobuyasu Mizutani
Prof., Tokyo Institute of Technology
Dr. Rikuo Ota
Prof., Kyoto Institute of Technology
Dr. Yusuke Moriyoishi
Director, Nat. Inst. for Res. in Inorganic Materials
Dr. Kitao Takahara
Prof., Nagoya University
Yukio Endo
Chairman
Koyo-sha Co., Ltd.
Dr. Takashi Hanazawa
Executive Director,
The Ceramic Society of Japan
Seiji Iwata
Executive Director,
Japan Fine Ceramics Association
Keiji Hayashi
Managing Editor

Editors

Managing Editor Keiji Hayashi
Associate Editors Akiko Ogawa
Nigel Madge
Art Director Prof. Yuji Isa
Assistant Artists Chizuru Shibata
Miho Nagahama
Kumiko Koseki
Assistant Youko Matsumoto
Circulation Keiji Hayashi
Publisher

Published Monthly by
FUJI TECHNOLOGY PRESS
LTD.

7F Daini Bunsei Bldg.
11-7, Toranomon 1-chome
Minato-ku, Tokyo 105, Japan
Tel: (03)-508-0051
Fax: (03)592-0648

One year subscription
Air Mail ¥200,000
Copyright - 1990 by
The Ceramic Society of Japan and
Fuji Technology Press Ltd. All
rights reserved.

No part of this publication may be reproduced, stored in a retrieval system, or transmitted, in any form or by any means, electronic, mechanical, photocopying, recording, or otherwise, without the prior written permission of the publishers. The papers, excluding those on information and communications, reviews, etc., were originally received by Nippon Seramikkusu Kyokai Gakujutsu Ronbunshi, and translated for this journal. The responsibility for the translation lies with the Publisher.

Papers:

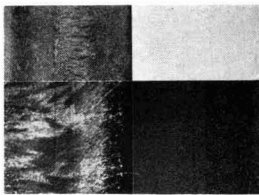
- **Fracture Energy and Tensile-Strength of Silicon Nitride at High Temperatures** 244 (4)
Tatsuki Ohji, Seisuke Sakai, Masaru Ito, Yukihiro Yamauchi, Wataru Kanematsu and Shoji Ito
- **Effect of Tantalum Carbide Addition on the Properties of SiC-B-C Ceramics** 252 (12)
Toshiaki Mizutani and Akihiko Tsuge
- **Dynamic Fatigue Behavior of Ceramics at Elevated Temperatures** 259 (19)
Yukihiro Yamauchi, Seisuke Sakai, Masaru Ito, Tatsuki Ohji, Wataru Kanematsu and Shoji Ito
- **Densification of Calcium-Deficient Hydroxyapatite by Hot Isostatic Pressing** 266 (26)
Soo Ryong Kim, Kazushi Hirota, Fujio P. Okamura, Yasutoshi Hasegawa and Soon Ja Park
- **Synthesis of Tantalum Boride Powder by Solid State Reaction and Its Sintering** 274 (34)
Hideaki Itoh, Yusuke Satoh, Satoshi Kodama and Shigeharu Naka
- **Effect of Alkoxide Grinding Aids and Their Reaction Mechanisms** 279 (39)
Masaki Yasuoka, Tsuyoshi Hayashi, Kiyoshi Okada and Nozomu Otsuka
- **Acoustic Emission Study for Fracture Origin of Sintered Mullite in 4-Point Bending Test** 284 (44)
Yoshiaki Yamade and Teruo Kishi
- **Trial Production of ZrO₂/Al₂O₃ Thin Sheet from Zirconia Powder/Aluminium Hydroxide Sol System** 292 (52)
Kazuro Kawamura, Seiji Yamanaka and Mikiya Ono
- **Preparation of Ytterbium Iron Garnet Powder by Homogeneous Precipitation Method and Its Sintering** 297 (57)
Hajime Haneda, Takagimi Yanagitani, Akio Watanabe and Shin-ichi Shirasaki

Technical Report

- **The Effect of Oxidation for Hot-Pressed β -Sialon-SiC Composites** 305 (65)
Hiroshi Nakamura, Seiki Umebayashi and Kazushi Kishi

Notes

- **Infrared Sensing Properties of a Low Curie Point PTC Thermistor** 310 (70)
Minoru Inaba, Masaru Miyayama and Hiroaki Yanagida
- **Formation of Spherically Aggregated ZrO₂ Particles by Thermal Hydrolysis of ZrCl₄ Concentrated Solution** 314 (74)
Keiji Daimon, Junji Yamada and Etsuro Kato
- **Thermal Diffusivity Measurements of Boron Oxide Melts by Laser Flash Method** 320 (80)
Gaku Ogura, In-Kook Suh, Hiromichi Ohta and Yoshio Waseda
- **Oxidation of TiB₂-Al₂O₃ Composites in Air** 323 (83)
Junichi Matsushita, Shinsuke Hayashi and Hajime Saito



Cover

A concept has been proposed by Japanese scientists to solve the problems of using ceramics as structural materials.

Ceramics are highly heat resistant but have low fracture toughness, while metals have high fracture toughness but less heat resistance. If a new material with the combined advantages of metals and ceramics could be created, it would solve the problems, and thus the concept has been proposed that ceramics and metals should be laminated in layers of atomic order thickness ranging from 100% metal to 100% ceramic. A material with this kind of functional gradient may have the fracture strength of metal combined with the high-temperature resistance of ceramics.

(clockwise from upper left)

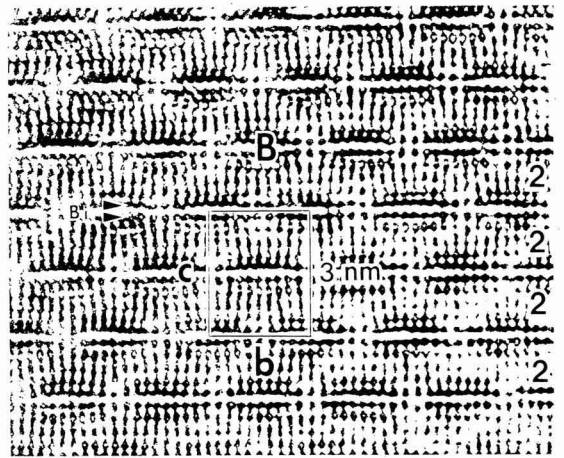
- 1) Cross-sectional surface of SiC-C FGM by SEM
- 2) Cross-sectional surface of SiC-C FGM by EPMA
(1 & 2: Courtesy of Dr. Hirai and Dr. Sasaki, Institute for Materials Research, Tohoku University)
- 3) Example of microscopic observation of ZrO_2 -Ni FGM made by the thin-film lamination method. This sample is a sintered lamination from 100% ceramic to 50% ceramic (Courtesy of Dr. Tamura, NKK)
- 4) Cross-section photo of C-SiC FGM coated on C/C composite. The composition continuously changes from C to SiC (Courtesy of Dr. Igarashi and Mr. Kawai, Sumitomo Electric Industries, Ltd.)

Photos taken for "Research on Basic Technologies for Developing Functionally Gradient Materials for Reducing Thermal Stress" supported by the Science & Technology Agency's 1988 Special Coordination Funds for Promoting Science and Technology

Information & Communications

- News C-39 (87)
- Abstracts of Articles on Ceramics from Selected Journal of the Learned Societies C-43 (91)
- Daily Records C-53 (101)

Papers, Letters and Notes



High resolution electron microscope photograph of the modulation doped structure of $\text{Bi}_2\text{Sr}_2\text{CaCu}_2\text{O}_y$ ($T_c=80\text{K}$) in the [100] direction. Figures at right side indicate number of copper layers, symbol B indicates bismuth rich region.

Fracture Energy and Tensile Strength of Silicon Nitride at High Temperatures

Tatsuki Ohji, Seisuke Sakai, Masaru Ito, Yukihiko Yamauchi, Wataru Kanematsu and Shoji Ito

Government Industrial Research Institute, Nagoya
1-1, Hirate-cho, Kita-ku, Nagoya 462, Japan

The work-of-fracture (WOF) tests were conducted for hot-pressed silicon nitride at high temperatures above 1000°C to investigate displacement rate (D-rate) dependence of effective fracture energy, and then the bridging stress at a crack interface was estimated from the increment of fracture resistance with crack extension (R-curve behavior) to discuss its correspondence to tensile strength. The effective fracture energy and the bridging stress increased with lowering D-rate, and then decreased, probably due to the activated pulling out work of grains and its sensitivity to change in D-rate. The bridging stress was shown to correspond to a great part of tensile strength in the range where a plasticity was seen in the stress-displacement (S-D) curve, implying a large contribution of grain bridging toward bearing an applied tensile stress during slow crack extension.

[Received August 25, 1989; Accepted November 22, 1989]

Key-words: Silicon nitride, High temperature, Chevron notch bend test, Fracture energy, R-curve behavior, Bridging stress, Tensile strength

1. Introduction

Silicon nitride, which is considered one of the most promising structural ceramics, exhibits non-elastic behavior in high-temperature mechanical strength tests above 1000°C due to the softening of glassy phase formed at grain boundaries as a result of processing with sintering additives like alumina, yttria, magnesia, etc.¹⁻³⁾ In accordance with lowering the viscosity of glassy phase at high temperatures, the cavities formed at grain boundaries or their triple points enhance subcritical crack growth, SCG, resulting in non-elastic stress-displacement, S-D, curves.

The toughening of non-transforming ceramics can often be attained by microcracking in the frontal process zone and grain bridging in the following wake region; the former sometimes accompanies the residual compressive stress in the wake region, leading to a rising R-curve behavior, the increase of fracture resistance with crack extension, as well as the latter case.⁴⁾

¹¹⁾ However, the softening of grain boundary glassy phase of silicon nitride at high temperatures is assumed to bring the similar effect of plastic deformation of dislocation, which will make it difficult to produce microcracks.¹²⁾ Hence, the increase in fracture toughness of silicon nitride at high temperatures, which has been reported by several researchers,^{1,13-16)} is attributed to the grain bridging; the softening of glassy phase will give the appropriate bonding force between

grains for the most activated pulling-out works. Particularly the elongated silicon nitride grains are supposed to make a large contribution for it. This toughening mechanism is anticipated to bring about the rising R-curve behavior.

The high temperature fractures of silicon nitride are dependent on viscosity of glassy phase as well as grain morphology, etc. and, therefore, strongly affected by strain rate, or D-rate. Accordingly, the properties concerning fracture energy should also be dependent on D-rate. It was reported that in alumina containing glassy phase the effective fracture energy or the crack propagation resistance heavily depended on D-rate at high temperatures, and the stress intensity factor took the maximum value at a certain D-rate.^{17,18)} It was also known that fracture toughness of silicon nitride at high temperatures showed strong dependence on D-rate.^{19,20)}

In this study, a chevron notch bend, CNB, specimen, which facilitate stable fracture in brittle materials due to its triangular ligament configuration, is used to measure the work-of-fracture, WOF, of hot-pressed silicon nitride at high temperatures at various D-rate from 0.1 to 0.0001mm/min, and the dependences of effective fracture energy and rising R-curve behavior on D-rate were discussed. Then, the bridging stress at the crack interface, which is estimated from the increment of fracture resistance against crack extension, is compared with tensile strength measured at the same temperature in air atmosphere.

2. Experimental Procedures

Commercially available hot-pressed silicon nitride doped with 5wt% yttria and 3wt% alumina containing impurities of 0.007% Mg, 0.008% Cr, 0.032% Fe and 0.026% Ca (wt%) was used in this study. The density was determined to be 3.20Mg/m³ by water immersion. Although some types of hot-pressed silicon nitride showed improvements of high temperature strength due to crystallization of grain boundary glassy phase into mellilite phase, etc.,^{21,22)} powder X-ray analysis of this material revealed little reflection from the mellilite one.

The dimensions and geometry of the CNB test specimen is shown in Fig.1. The width of chevron notch was 100μm, and three point bending tests with lower span of 30mm were carried out. The most important problem in WOF tests is to use a stiff testing machine.²³⁾ As a matter of fact, in high temperature measurements, if loading rods, etc. are connected by a screw, the slack due to thermal expansion brings about degradation in stiffness of loading system. Hence in this experiment, a silicon carbide loading rod consisting

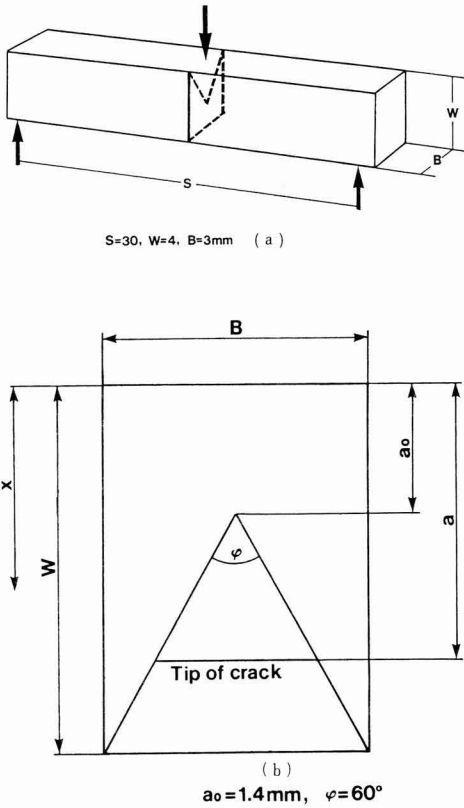


Fig. 1. Geometry and dimensions of CNB test specimen.

of one body, which was linked with water-cooling stainless rod outside the furnace, was used, and the slack at that connection by thermal expansion is eliminated by strictly tightening screws after the furnace was heated up to the test temperature. The other testing equipments inside the furnace were all made of silicon carbide. The “blank” tests without specimens were carried out to know the compliance of testing system for each temperature and D-rate, which corrected the load-deflection curves obtained in WOF tests into the true ones.

The tensile test specimen, whose geometry and dimensions are shown in Fig.2, were fabricated from the same billets of hot-pressed silicon nitride. This type of specimen, where the elongation of gauge length between two arms was measured by optical extensometer (Zimmer OHG, Model 4100) through silica glass windows mounted at both sides of furnace, was often used by several researchers so far,^{24,25)} and the method of elongation measurements here was similar to them. The detailed tensile testing method was previously described.²⁶⁾

Both tests were carried out in air atmosphere. The furnace was heated to the test temperature in about one

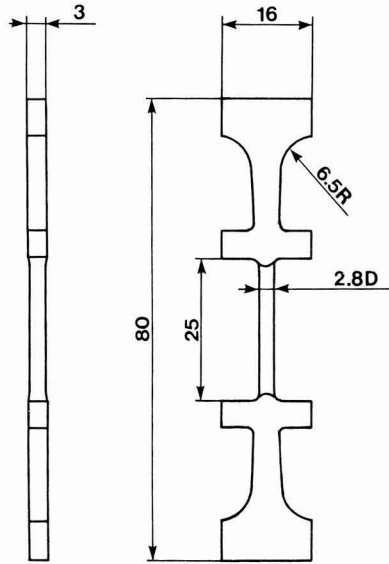


Fig. 2. Geometry and dimensions of tensile test specimen.

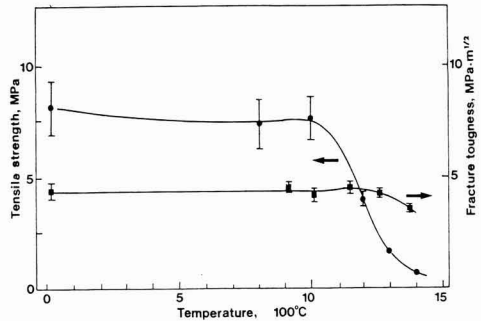


Fig. 3. Temperature dependences of tensile strength and fracture toughness. 5 and 3 specimens were tested respectively. Points are averages, and bars indicate the standard deviation.

hour, and the specimen was held at this temperature for 30min before the tests were started to achieve thermal equilibrium.

3. Results and Discussion

The softening of grain boundary glassy phase of silicon nitride at high temperatures is known to result in the rapid decrease of mechanical strength. The temperature dependences of tensile strength and frac-

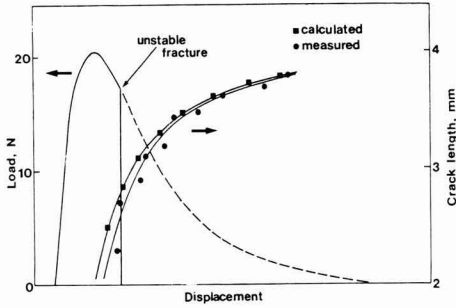


Fig. 4. An example of L-D diagram of CNB test for determining crack length, and a comparison between calculated and measured crack lengths. D-rate is 0.01mm/min and temperature 1260°C.

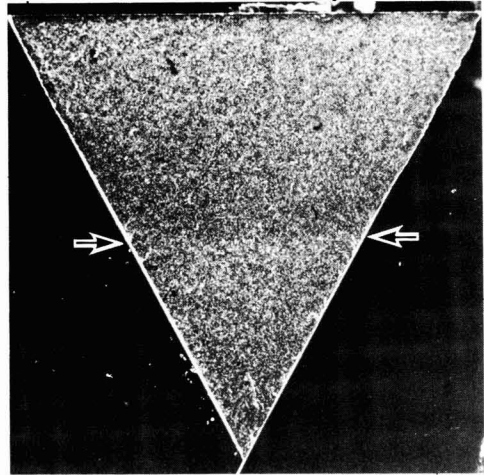


Fig. 5. An example of fracture surface of CNB test for measuring crack length. Arrows indicate a border between stable and unstable fractures caused by a rapid change of D rate.

ture toughness of this material, which were measured at D-rates of 0.1 and 0.01mm/min, respectively, are shown in Fig.3. The fracture toughness was determined from the maximum loads in CNB test as will be shown later. Tensile strength was degraded at a little higher temperature than 1000°C, where internal friction was rapidly raised with a peak, and elasticity began to drop.²⁷⁾

In general cases of ceramics CNB tests with changing D-rate resulted in “stress intensity factor”-“crack growth velocity,” so called K_I - v relationship, because D-rate positively corresponding to crack growth velocity. At 900° and 1020°C, the CNB tests at various D-rate from 0.1 to 0.001mm/min produced the result that a lower D-rate, in other words a lower crack growth velocity, yielded a lower fracture toughness value, leading to a reasonable K_I - v relationship, though the difference was very small.²⁸⁾ However, in the similar tests above this transient temperature, the opposite tendency that a lower displacement lead to a higher WOF was obtained, and therefore the explanation on the standpoint of K_I - v relationship is probably improper. In this study the results in this temperature range were treated as the variation of stress intensity factor against the crack length, or R-curve behaviors.

3-1. Real and Calculated Crack Lengths in CNB Tests

Crack lengths during CNB tests can be calculated from the change in compliance using Bluhm’s slice model.^{29,30)} This calculation requires as a premise that the material is an elastic body, and therefore its application into the material showing some plastic reaction sometimes leads to a gap between actual and estimated crack lengths. Bornhauser et al. succeeded in a direct measurement of crack length during notched beam bend tests at 1000°C using pure alumina and alumina containing glassy phase and found the difference between measured and calculated crack lengths in the latter alumina.³¹⁾ Thus it is necessary to verify the applicability of the calculation methods into fractures of silicon nitride at high temperatures.

For this purpose, following experiments were conducted. At a certain halfway point of a WOF test at 1260°C, D-rate was changed from 0.01 to 10.0mm/min to abruptly bring about an unstable fracture, as indicated by solid line of Fig.4. A microscopic observation for the ligament portion revealed a border between stable crack growth wake at 0.01mm/min and the catastrophic one at 10.0mm/min. Figure 5 shows a fracture surface of the example of Fig.4. These operations were conducted at the various halfway points by use of several specimens, and as a result a real crack length curve against displacement was obtained. In Fig.4, the real crack length curve against displacement measured at 1260°C and 0.01mm/min is compared with the calculated one using Bluhm’s slice model. There is a fairly good agreement between them. This method is applicable only when the load-displacement (L-D) curves of WOF test is completely reproducible, and for this reason, the identical notch introduction works into the specimens are strictly required.

3-2. Work-of-fractures

At 1260°C, WOFs is not physical properties but are heavily dependent on D-rate. Figure 6 shows L-D curves at D-rates of 0.1, 0.01, 0.001 and 0.001mm/min at 1260°C. Figure 7 illustrates the dependences of effective fracture energy, γ_{eff} and fracture toughness, K_{IC} , on D-rate at 1260°C. The γ_{eff} and K_{IC} of Fig.7 are defined as follows:

$$\gamma_{eff} = W_{WOF}/2A \quad \dots \dots (1)$$

and

$$K_{IC} = (2E'\gamma_{eff})^{1/2} \quad \dots \dots (2)$$

where W_{WOF} is the energy under L-D curve, and A is

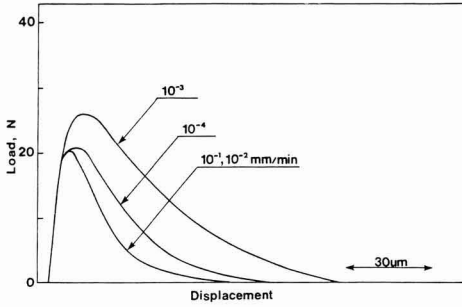


Fig. 6. L-D diagrams of WOF tests at 1260°C. 3 specimens were tested for each diagram.

the area of ligament portion. E' is the elasticity for plane strain condition defined as $E' = E/(1-\nu^2)$, where ν is the Poisson's ratio. In the materials showing changing fracture resistance with crack extension, Eq. (2) yields the average value. Although the value of K_{IC} is correlated with γ_{eff} through E' , K_{IC} dissipated its physical meaning at these temperatures, and was significant only in relative comparison as a substitute for γ_{eff} .

The L-D curves of WOF tests and effective fracture energies were almost identical at 0.1 and 0.01mm/min, but as the rate was lowered below 0.01mm/min, effective fracture energy was increased with inflation of L-D curves. It reached the maximum value around 0.001mm/min, which was almost triple of those above 0.01mm/min. Then, the effective fracture energy began to decrease and resumed to show a less dependence on D-rate around 0.0002mm/min.

As stated above, bridging or pulling out of grains are considered to be the primary factor for increasing fracture resistance of silicon nitride at high temperatures. The strong dependence of effective fracture energy on D-rate suggests the friction produced in pulling out of grains, which is affected by strain rate due to visco-elastic characteristics of glassy phase, makes great contribution into the change of effective fracture energy. The bridging effect of grains, particularly elongated ones, in the wake region following the crack tip is supposed to be a predominant factor for increase of effective fracture energy at 0.001mm/min.

The change of effective fracture energy with D-rate may be explained as follows. In high rate region, or in quick stress application, the fracture occurs in brittle manner as seen from changes in both S-D curves and fractographies of tensile tests for similar silicon nitride at 1260°C,³²⁾ leading to low effective fracture energy. In this region, pulling out of grains is hard to be produced because the interfacial shear stress at the grain boundary is excessively high. As the D-rate is lowered, however, this stress is reduced to such a degree that the grains can be pulled out. In the range where the pulling out is possible, the higher shear stress yields larger fracture resistance, and hence effective fracture energy is decreased with the further decrease of D-rate.

Fracture resistance, K_{R} , at a certain point of the L-D curve in a WOF test can be calculated as follows:

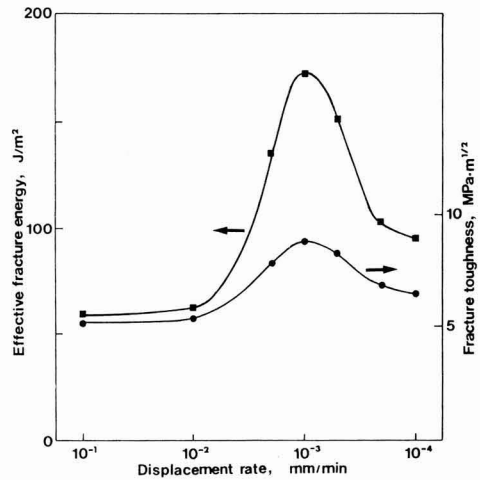


Fig. 7. D-rate dependences of effective fracture energy and fracture toughness at 1260°C.

$$K_R = (E' / 2 dx/dA)^{1/2} P \dots\dots\dots (3)$$

where x is the compliance, A is the crack area, and P is the load. In CNB test fracture toughness is usually calculated from the maximum value of P as $(E' / 2 dx/dA)^{1/2}$ must take the minimum under the condition that K_R is constant irrespective of crack length (flat R-curve behavior). The fracture toughnesses calculated from the maximum loads of 0.01 and 0.001mm/min in Fig.6 are 4.6 and 5.4MPa^{1/2}, respectively. This difference is much smaller than that between "average" values calculated using Eq. (2) as shown in Fig.7, suggesting that increase of resistance with further extension of crack at 0.001mm/min.

3-3. R-curve Behavior and its D-rate Dependence

By use of Eq. (3), the variations of fracture resistance, K_R , against crack growth, namely R-curve behaviors, were obtained. The results in WOF tests at 1260°C are shown in Fig.8. Although WOF tests at 900° and 1020°C resulted in flat R-curve behaviors which were similar to behaviors reported for silicon nitride by some researchers,^{33,34)} rising R-curve behaviors were observed at 1260°C; particularly at 0.001mm/min, K_R grew almost double at 1260°C. Similarly to the variation of effective fracture energy with D-rate, R-curve showed the most intensive rising behavior around 0.001mm/min.

Some toughening mechanisms are present for explaining rising R-curve behaviors for non-transformed ceramics; residual strain effects in process zone wake, grain bridging or grain interlocking effects, etc. Theoretical consideration indicated that R-curve showed steep increase of resistance in the beginning stage of crack extension, followed by "toughness plateau"

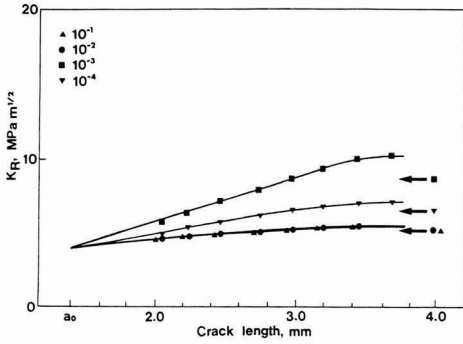


Fig. 8. R-curve behaviors at 1260°C. Arrows indicate fracture toughness calculated from total WOF.

corresponding to the stationary configuration of the advancing crack in a steady state.⁸⁾ However, the experimentally obtained R-curve behavior is seriously affected not only by intrinsic material characteristics like grain size, etc., but also by experimental conditions such as depth of notch, specimen size, etc. and determination method of fracture resistance.^{4,6,7,31)} In addition, crack branching and secondary crack formation make the definition of crack length ambiguous.⁹⁾ The R-curve behaviors shown here involved not only the above uncertainties but also the unsteadiness of CNB test that crack width is varied with crack extension. Nevertheless, they are expedient because the bridging stress at crack interface can be estimated from the increment of fracture resistance, by assuming appropriate stress distribution as shown in the following section.

3-4. Bridging Stress Distribution in Grain Bridging Zone

The bridging stress (or traction) at the crack interface in the grain bridging zone can be estimated from R-curves. The stress value can be simply defined when uniform bridging stress distribution in grain bridging zone is presumed as follows (Fig.9, A):

$$\sigma(X) = \sigma_0 \quad (X \leq X_0) \quad \dots \dots \dots (4a)$$

$$\sigma(X) = 0 \quad (X > X_0) \quad \dots \dots \dots (4b)$$

where σ_0 is the applied uniform stress, X is the distance behind the crack tip, a-x, and X_0 is the bridging zone length. However, the uniform stress distribution is not likely to be produced, because this assumption needs singularities at $X = 0$ and X_0 . The most probable stress distribution is described in Fig.9, B; it increases from $\sigma(0)=0$, reaches the maximum, and decreases tailing off to 0.^{10,35)} In this study a cubic function was assumed to model this distribution as follows.

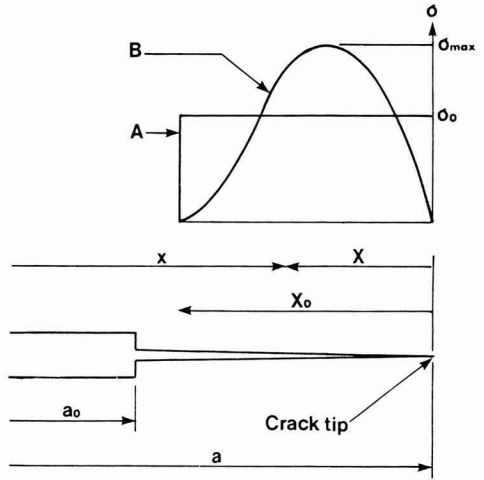


Fig. 9. Schematic of bridging stress distribution at crack interface. a and a₀ are the crack lengths of extended and initial cracks, respectively.

$$\sigma(X) = \sigma_1 X + \sigma_2 X^2 + \sigma_3 X^3 \quad (X \leq X_0) \quad \dots \dots \dots (5a)$$

$$\sigma(X) = 0 \quad (X > X_0) \quad \dots \dots \dots (5b)$$

where $\sigma_1, \sigma_2,$ and σ_3 are coefficients. The continuity of function gives

$$\sigma_1 X_0 + \sigma_2 X_0^2 + \sigma_3 X_0^3 = 0 \quad \dots \dots \dots (6)$$

The increment of resistance value, ΔK_R , for the crack length, a, is expressed by ³⁶⁾

$$\Delta K_R = 2(a/\pi)^{1/2}(1/b(a)) \int_{a_0}^a [\sigma(a-x)b(x)/(a^2-x^2)^{1/2}]dx \quad \dots \dots \dots (7)$$

where $b(x) = B(x-a_0)/(W-a_0)$. By selecting $\sigma_0,$ or $\sigma_1, \sigma_2,$ and σ_3 so that R-curve from Eq. (7) best fits with the experimentally obtained one, bridging stress distribution in bridging zone can be determined.

Figure 10 shows the bridging stress distributions obtained using Eqs. (5) and (6) for the case of 0.001mm/min at 1260°C, and Fig.11 shows R-curves calculated by assuming the stress distributions of Fig.10 in comparison with the real R-curve. It is known that Eq. (6) owns a great superiority to Eq. (5) in expressing a real bridging stress distribution. The estimated bridging stresses, σ_0 and σ_{max} are shown in comparison with tensile strength at 1260°C in the following section, but rather only qualitative discussion should be permitted because the used R-curves themselves include some uncertainties, and σ_{max} in Eq. (6) is largely changed by slight variation in the assumed shape of stress distribution. It

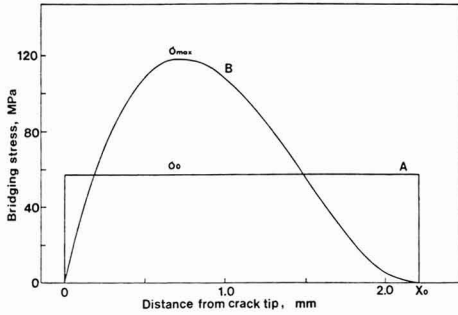


Fig. 10. Bridging stress obtained by assuming uniform, A, and cubic functional, B, distributions for the case of 0.001mm/min at 1260°C.

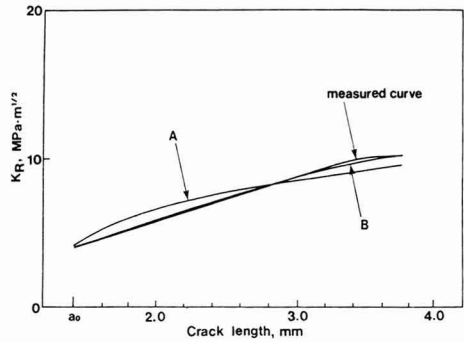


Fig. 11. R-curve measured and calculated by assuming the stress distributions of Fig.10.

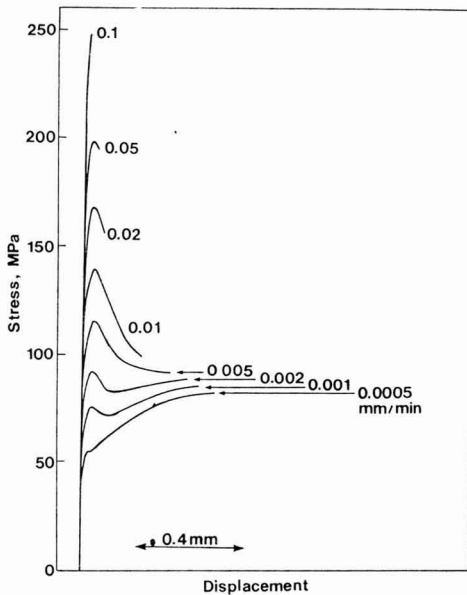


Fig. 12. S-D diagrams as a function of D-rate. Temperature is 1260°C.

seems possible, however, to think that actual bridging stress lies around them.

The crack opening displacement at the end of bridging zone can be determined for the uniform bridging zone as follows.³⁷⁾

$$u = (8\sigma_0 X_0 / \pi E') + (8\sigma_0 K_0 X_0^{1/2} / E' (2\pi)^{1/2}) \dots \dots (8)$$

where u is the total crack opening displacement, and K₀

is the toughness at the crack tip. The calculation for σ_0 of Fig.10 resulted in $u = 4\mu\text{m}$. As the length of elongated grain of hot-pressed silicon nitride is ranging from 5 to 10 μm ,³⁸⁾ this displacement value seems plausible considering a bonding portion length between grain and matrix.

3-5. S-D Diagrams in Tensile Tests

The above described grain bridging toughening mechanisms should have close relationship with the stress-strain curve, because pulling out of grains are caused by softening of glassy phase, which brings a non-elastic stress-strain relationship. The results of tensile tests at 1260°C are shown in Fig.12, where the displacement was a real elongation of gauge section of tensile test specimen measured by electro-optical extensometer. As compared with the results of the similar tests in atmosphere, vacuum the general behavior was almost the same.³²⁾ It is known that in some cases oxidation treatment decreases volume fraction of glassy phase and improves high temperature strength.³⁹⁾ In this study, however, almost no effect of oxidation was observed even for the case of 27 hours exposure at 1260°C.

While the test at 0.1mm/min yielded almost linear S-D curve up to fracture strength (σ_f), those at 0.05mm/min and lower rates produced stress peaks (σ_p) after deviating from linearity, and final strength (σ_f) at the rates from 0.005 to 0.0005mm/min showed the convergence. Fractographic study revealed that fractures at 0.02mm/min and lower rates exhibited "rough wake region," which was recognized as an evidence of "enhanced SCG" by several researchers,^{1,2,40)} while those at 0.1mm/min and higher left no such a region, as shown in Fig.13. This means the appearance of stress drop in S-D diagrams indicates an initiation of SCG.

Figure 14 shows the dependence of tensile strengths (σ_f , σ_p and σ_f) and bridging stresses (σ_0 and σ_{max}) on D-rate. The bridging stress is raised with decreasing D-rate down to 0.001mm/min at which the pulling out works of grains are most activated. The bridging stress

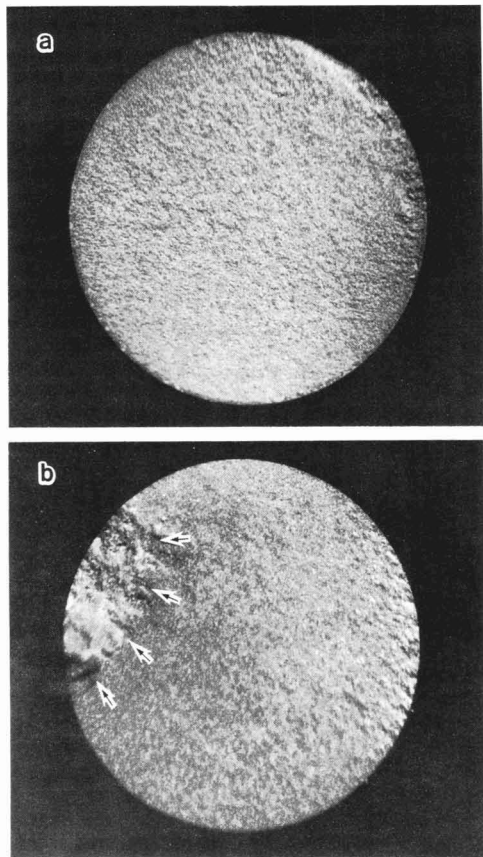


Fig. 13. Optical images of fracture surfaces tested at (a) 0.1 and (b) 0.01mm/min. Arrows indicate "enhanced" SCG wake.

is maximized at 0.001mm/min, like effective fracture energy. It is known that the appearance of SCG wake region in fracture surface of silicon nitride accompanies the steep rise of fracture toughness.^{1,13-15,19} Thus, it can be supposed that the maxima of bridging stress and effective fracture energy at 0.001mm/min are corresponding to tensile strength at 0.05 - 0.01mm/min of Fig.12. In Fig.14, the maxima of bridging stresses were made to coincide with tensile strength at 0.02mm/min. Note the D-rate dependences of bridging stress and tensile strength in the rate range below them; they both similarly decrease with decreasing D-rate, and then enter the region of less dependence on rate.

The plastic behavior (yielding phenomena) observed in tensile tests at some low D-rates as shown in Fig.12 is attributed to slow crack propagation accelerated by spread cavities. This crack growth is accompanied by pulling out works of grains, which should be a primary factor for increasing fracture resistance and make a great contribution for bearing applied stress while crack

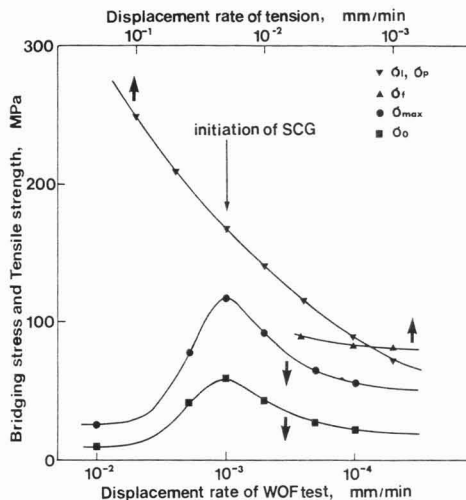


Fig. 14. D-rate dependences of bridging stresses and tensile strengths.

propagates. As the uniform stress is applied in a tensile test, the cracks are produced everywhere throughout a gauge part of specimen. This crack is supposed to be slowly propagated up to the length of about 10 μ m and then be arrested by grains elongated in the stress direction, because 10 μ m is the average interval of elongated grains.³⁸) In the process that this medium-sized crack grows to macrocrack by connecting each other, pulling out of elongated grains should be generated. Thus, the bridging of grains at the interface of this slowly growing crack is assumed to be the same in its mechanism as that in CNB test. As a matter of fact, the comparison in Fig.14 revealed that the bridging stress estimated from R-curve behaviors in WOF tests corresponded to a fairly large part of the tensile strength.

4. Conclusions

Chevron notch bend test of hot-pressed silicon nitride at high temperatures above 1000°C demonstrated that the characteristics concerning fracture resistance were largely dependent on D-rate; at a certain D-rate (0.001mm/min in this study) effective fracture energy took the maximum value and R-curve showed the strongest rising behavior. It was assumed that an increase in fracture resistance and a strong R-curve behavior were attributed to the activated pulling out works of grains, which were heavily affected by a rate-sensitive grain boundary shear stress. The bridging stress at crack interface, which was estimated from the increment of fracture resistance with crack extension, exhibited the D-rate dependence very similar to that of

effective fracture energy. The maximum bridging stress was supposed corresponding to a tensile strength showing stress drop in its S-D curve, from the appearance of the SCG wake region. In D-rate range below the rates giving this correspondence, tensile strength and bridging stress presented the similar D-rate dependence. The bridging stress corresponded to a fairly large part of the tensile strength, and it was implied that, in high temperature tensile test, the bridging of silicon nitride elongated grains should make a great contribution for bearing an applied tensile stress during slow crack growth.

Acknowledgements

The authors thank their colleague S. Sakaguchi for his helpful suggestions to chevron notch bend tests and work-of-fractures.

References:

- 1) F.F. Lange, *J. Am. Ceram. Soc.*, 57, 84-87 (1974).
- 2) R. Kossovsky, D.G. Miller, and E.S. Diaz, *J. Mater. Sci.*, 10, 983-97 (1975).
- 3) T. Ohji, S. Sakai, M. Ito, Y. Yamauchi, W. Kanematsu, and S. Ito, *High Temperature Technology*, 5, 139-44 (1987).
- 4) H. Hubner and W. Jillek, *J. Mater. Sci.*, 12, 117-25 (1977).
- 5) R.F. Pabst, J. Steeb, and N. Claussen, "Fracture Mechanics of Ceramics, Vol.4," Plenum Press (1978) pp.821-33.
- 6) R. Knechans and R. Steinbrech, *J. Mater. Sci., Letter*, 1, 327-29 (1982).
- 7) R. Steinbrech, R. Knechans, and W. Schaarwachter, *J. Mater. Sci.*, 18, 265-70 (1983).
- 8) A.G. Evans and K.T. Faber, *J. Am. Ceram. Soc.*, 67, 255-60 (1984).
- 9) H. Wieninger, K. Kromp, and R.F. Pabst, *J. Mater. Sci.*, 21, 411-18 (1986).
- 10) P.L. Swanson, C.J. Fairbanks, B.R. Lawn, Y-W, Mai, and B.J. Hockey, *J. Am. Ceram. Soc.*, 70, 279-89 (1987); Y-W, Mai and B.R. Lawn, *ibid.*, 70, 289-94 (1987).
- 11) M. Sakai, J. Yoshimura, and M. Inagaki, *J. Am. Ceram. Soc.*, 71, 609-16 (1988).
- 12) R.G. Hoagland and J.D. Embury, *J. Am. Ceram. Soc.*, 63, 404-10 (1980).
- 13) A.G. Evans and S.M. Wiederhorn, *J. Mater. Sci.*, 9, 270-78 (1974).
- 14) R.K. Govila, *J. Am. Ceram. Soc.*, 63, 319-26 (1980).
- 15) D. Munz, G. Himsolt, and J. Eschweiler, *J. Am. Ceram. Soc.*, 63, 341-42 (1980).
- 16) S.H. Knickerbocker, A. Zangvil, and S.D. Brown, *J. Am. Ceram. Soc.*, 68, C99-101 (1985).
- 17) K. Kromp and R.F. Pabst, *Met. Sci.*, 15, 125-29 (1981).
- 18) T. Haug, A.C. Bornhauser, H.G. Schmid, V. Gerold, and R.F. Pabst, "Creep and Fracture of Engineering Materials and Structures, Part 1," Pineridge Press (1984) pp.473-84.
- 19) S.H. Knickerbocker, A. Zangvil, and S.D. Brown, *J. Am. Ceram. Soc.*, 67, 365-68 (1984).
- 20) T. Nose and T. Fujii, *J. Am. Ceram. Soc.*, 71, 328-3 (1988).
- 21) A. Tsuge, K. Nishida, and M. Komatsu, *J. Am. Ceram. Soc.*, 58, 323-26 (1975).
- 22) A. Tsuge and K. Nishida, *Am. Ceram. Soc. Bull.*, 57, 424-31 (1978).
- 23) J. Nakayama, H. Abe, and R.C. Bradt, *J. Am. Ceram. Soc.*, 64, 671-75 (1981).
- 24) F. Wakai, S. Sakaguchi, Y. Matsuno, and H. Okuda, "Proceedings of the First International Symposium on Ceramic Components for Engines," KTK/Reidel (1984) pp.279-85.
- 25) D.F. Carroll and R.E. Tressler, *J. Am. Ceram. Soc.*, 72, 49-53 (1989).
- 26) T. Ohji, "Mechanical Testing of Engineering Ceramics at High Temperatures," Elsevier Applied Science, (1989) pp.119-33.
- 27) S. Sakaguchi, F. Wakai, and Y. Matsuno, "Proceedings of Annual Meeting of Ceramic Society of Japan," (1984) pp.567-68.
- 28) T. Ohji, unpublished work
- 29) J.I. Bluhm, *Eng. Fract. Mech.*, 7, 593-604 (1975).
- 30) T. Nishida, Y. Takei, and T. Nishikawa, *Yogyo-Kyokai-Shi*, 90, 254-61 (1982).
- 31) A. Bornhauser, K. Promp, and R.F. Pabst, *J. Mater. Sci.*, 20, 2586-96 (1985).
- 32) T. Ohji, Y. Yamauchi, W. Kanematsu, and S. Ito, to be published in *J. Mater. Sci.*
- 33) J.A. Salem and J.L. Shannon, Jr., *J. Mater. Sci.*, 22, 321-24 (1987).
- 34) A. Ghosh, M.G. Jenkins, K.W. White, A.S. Kobayashi, and R.C. Bradt, *J. Am. Ceram. Soc.*, 72, 242-47 (1989).
- 35) C-H, Hsueh and P.F. Becher, *J. Am. Ceram. Soc.*, 71, C234-37 (1987).
- 36) M. Sakai and M. Inagaki, "Proceedings of the International Institute for the Science of Sintering Symposium," Elsevier Applied Science, (1988) pp.796-801.
- 37) G.C. Sih, "Handbook of Stress Intensity Factors," Lehigh University Press, (1973).
- 38) T. Ohji, "Proceedings of The 8th Symposium of Basic Science of High-Temperature Materials," (1988) pp.66-70.
- 39) F.F. Lange, B.I. Davis, and M.G. Metcalf, *J. Mater. Sci.*, 18, 1497-505 (1983).
- 40) M. Kawai, H. Fujita, Y. Kanki, H. Abe, and J. Nakayama, "Proceedings of the First International Symposium on Ceramic Components for Engines," KTK/Reidel (1984) pp.269-78.

This article appeared in English in *Nippon Seramikkusu Kyokai Gakujutsu Ronbunshi* (Japanese version), Vol. 98, No.3, 1990.

Effect of Tantalum Carbide Addition on the Properties of SiC-B-C Ceramics

Toshiaki Mizutani and Akihiko Tsuge

Research & Development Center, Toshiba Co.
1, Komukai Toshiba-cho, Saiwai-ku, Kawasaki 210, Japan

The densification of SiC-B-C composites doped with TiC, ZrC, HfC, VC, NbC, TaC or WC were investigated by pressureless sintering. Densities over 90% TD (theoretical density) were achieved by addition of TaC by sintering at a relatively higher temperature. TaC particles suppressed the grain boundary movement. Addition of 10mol% TaC doubled the toughness of composites under the same sintering conditions. Exposed TaC particles were oxidized severely at 1500°C in air, and formed Ta₂O₅ polymorphisms.

[Received September 13, 1989; Accepted November 22, 1989]

Key-words: Silicon carbide, Metallic carbide, Toughness, Densification, Composite, Particle dispersion, Oxidation

1. Introduction

The SiC-B-C ceramic system is interesting in regard to its excellent strength and heat resistivity at high temperature, around 1500°C. However, its low toughness around 3MPa/m has been the largest drawback against structural application to heat engines. Therefore, many toughening methods have been proposed.¹⁾ Many composites with fibers, whiskers or particles have been studied in recent years.²⁻⁶⁾ Initially, the TiC particulate dispersed SiC-Al-C ceramic system was studied by hot-pressing in order to achieve sufficient densification for evaluating worthwhile mechanical properties. Toughening and strengthening were confirmed, and their mechanisms were considered to be the result of crack deflection, originating from the larger thermal expansion coefficient of TiC particles compared with that of the SiC matrix.^{3,4)} However, pressureless sintering is more preferable than hot-pressing for the structural application of these ceramics. It is expected, moreover, that SiC-B-C systems can be toughened without degradation of their excellent high temperature properties.

This study was made to determine some other particulate materials which wouldn't disturb SiC-B-C matrix densification. Seven different heat resistive metallic carbide powders (TiC, ZrC, HfC, VC, NbC, TaC, WC) were selected as candidates for the dispersed particles, based on the following considerations. The stability of the dispersed particles in the SiC-B-C matrix at sintering temperature, around 2000°C, should be important for avoiding unexpected reactions that would disturb SiC-B-C matrix densification. The above metallic carbides have relatively low formation free energies to SiC and very high melting temperatures, around 3000°C.

In this study, densities over 90%TD (theoretical

Table 1. Raw powder properties.

Material	Density g/cc	Molar Vol. cc/mol	Melt. Point °C	F.F.E. KJ/mol	T.E.C. ppm/°C	Young's Modulus GPa	M.P.S. μm	Oxygen Imp. wt%	Mfr.
TiC	4.910	12.5	3,067	-151.4	8.56	470	1.45	0.13	JNM
ZrC	6.633	16.0	3,427	-178.7	7.0	550	1.09	0.81	JNM
HfC	12.657	15.6	3,830	-203.6	7.0	750	3.05	0.01	HCS
VC	5.81	10.8	2,800		6.7	420	1.59	0.40	JNM
NbC	7.801	13.4	3,608	-134.4	7.25	540	1.10	0.39	JNM
TaC	14.497	13.3	3,825	-145.3	6.96	720	2.69	0.13	JNM
WC	15.668	12.6	2,785	-67.0	5.5	700	0.61	0.17	JNM
SiC	3.217	12.5	subl.	-35.4	4.7	386	0.62	1.28	LNZ
B ₄ C	2.52	22.0	2,450	-27.3	5.2	450	0.03		CLY

Referred from "JANAF Thermochemical Tables," D.R. Stull, et al., (1971), and "Особо тугоплавкие элементы и соединения," П. Б. Котельников, et al., Москва, (1969)
 F.F.E. : Formation free Energy at 2300 K
 T.E.C. : Thermal Expansion Coefficient from RT to 2000 K
 M.P.S. : Mean Particle Size
 JNM : Japan New Metal Co. HCS : Herman C. Starck Co.
 LNZ : Lonza Co. CLY : Callery Co.

density) were achieved by addition of TaC. Then, the other properties were evaluated.

2. Experimental

Table 1 shows the material properties of the related metallic carbides and the characteristics of the starting raw powders which were used in this study. B and C aid sources for sintering were amorphous-B powder produced by Herman C. Starck and phenol resin powder furnished by Dainippon Ink & Chemicals Co., respectively.

The amount of B aid addition was fixed to 0.7 atm% for the main composition (SiC-metallic carbide), and the amount of C aid addition was fixed to 2.25 times the oxygen impurity amount in weight in the main composition.⁷⁾ The metallic carbide contents in the main compositions were selected up to 20mol% for the composition dependence of properties.

A slurry was formed for the mixed SiC, boron and metallic carbide powder with an acetone solution of phenol resin and di-ethylene glycol (binder). It was blended in a pot-mill for 3 days. The slurry was dried, granulated and pressed into 33×43×7mm shape. The binder was decreased and the resin was carbonized at 800°C in nitrogen. Sintering was carried out in a carbon heater vacuum furnace for 2 hours at 1950–2200°C. The sintered bodies were cut and polished to 3×4×33mm shapes, the standard size in JIS R1601.

The sintered body densities were obtained either by liquid displacement or size measurement. The standard X-ray diffraction technique using Ni-filtered CuKα

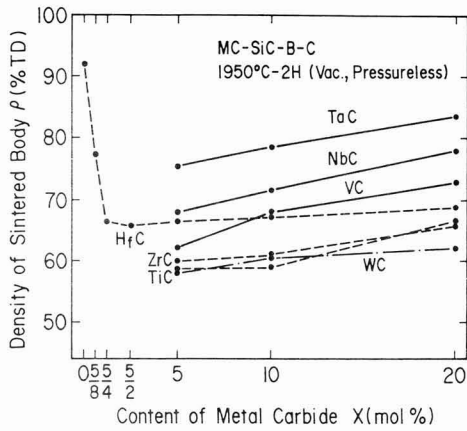


Fig. 1. SiC-metallic carbide composite densifications in vacuum-sintering at 1950°C.

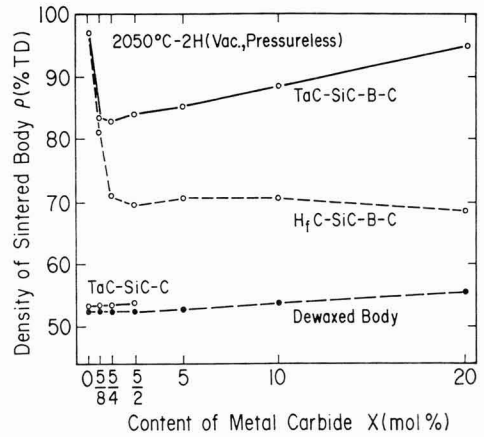


Fig. 2. TaC-SiC-B-C and SiC-HfC-B-C composite densifications in vacuum-sintering at 2050°C.

radiation was used to determine the crystalline phases present in the sintered bodies. Reflected light microscopy (RLM) and scanning electron microscopy (SEM) were used to observe the polished, fractured and heat-treated surfaces. The fracture toughness and strength were measured only for the TaC-SiC-B-C composites, since only they were sufficiently densified over 93% of the theoretical density which was estimated from the composition by using the densities of SiC and individual metallic carbides in Table 1.

Toughness K_{IC} and hardness H_V were evaluated from more than 10 Vickers indent ($P=5\text{kg}$; 15 sec.) measurements. The following equations were used for calculating.⁸⁾

$$K_{IC} = 0.0421a^{0.8}E^{0.4}P^{0.6} / C^{1.5} : C / a > 2.5 \quad \dots \dots (1)$$

$$H_V = 0.01873P / 4a^2 \quad \dots \dots (2)$$

where “a” is the length of the main diagonal of the indent, “C” is the radius of the median crack, and “E” is the Young’s modulus for each sample.

The Young’s modulus depends on the composition and density in general. In this study, however, the Young’s modulus for each dense composite was approximated by a constant ($E=410\text{GPa}$), the usual value that could be obtained in dense single phase SiC ceramics, from the following speculation. The Young’s modulus for a sandwiched layer type composite should be estimated by the geometrical and algebraic means of individual layer values, respectively, for the normal and parallel directions to the layer.⁹⁾ It was considered that the first approximation of the Young’s modulus for a particulate dispersed type composite could be estimated by the mean of the above two estimated values. The highest Young’s modulus in Table 1 is 700 – 750GPa for HfC,

TaC and WC. An estimation example for the 80mol%SiC – 20mol%TaC particulate composite showed an about 15% larger value compared to non-dispersed SiC. This 15% increase in the Young’s modulus deviates the calculated toughness K_{IC} in Eq. 1 only about +6%. This deviation is negligibly small compared with the dispersion of Vickers indentation micro-fracture measurements.

3. Results and Discussion

3-1. Densification Behavior

Figure 1 shows the effect of each added metallic carbide quantity after 1950°C sintering. The density was normalized by the theoretical density. Every metallic carbide more or less disturbed the densification of each mixture. However, 5 – 20mol% TaC or HfC addition respectively provided a higher density than the addition of other carbides with a IVa or a Va element in the periodic table.

Figure 2 shows the results of 2050°C sintering for TaC or HfC dispersed composites, with and without a B aid. The densification degradation became significant around 5/8 mol% addition of each metallic carbide, which corresponds closely to the B aid atomic quantity (0.7 atm%). The density became slightly higher with increasing TaC quantity from 5/4 mol%, in spite of the fact that densification did not occur in the TaC-SiC-C composition without a B aid.

The peaks for each metallic boride were detected in the X-ray diffraction patterns for every sintered body. Table 2 shows the relative peak strengths among SiC, TaC and TaB₂. It seems clear that most of the TaC reacted with the B aid (0.7 atm%) to form TaB₂ at 5/8 mol% TaC addition. The formed TaB₂ quantity increased little with more TaC addition and must be less than 0.35

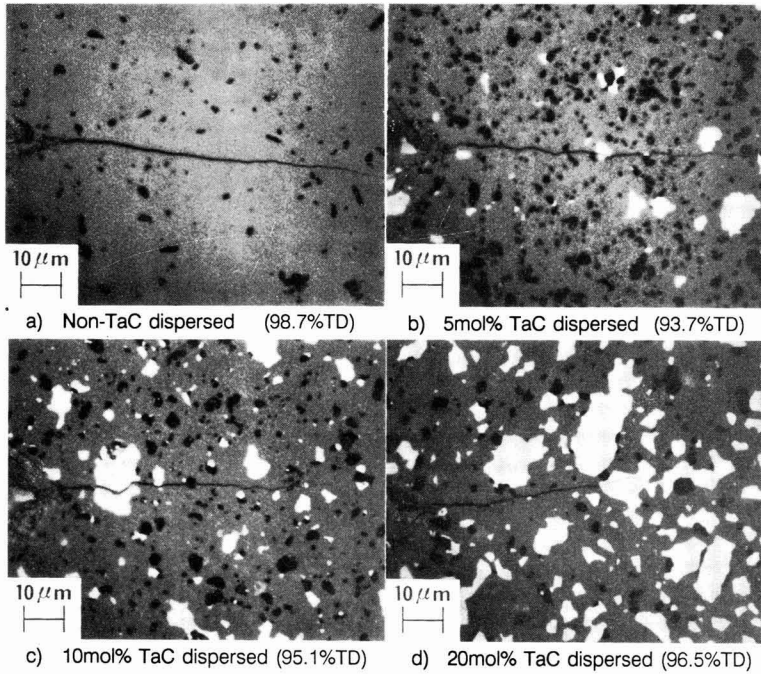


Fig. 3. Polished sintered body surfaces in TaC-SiC-B-C system, sintered at about 2200°C.

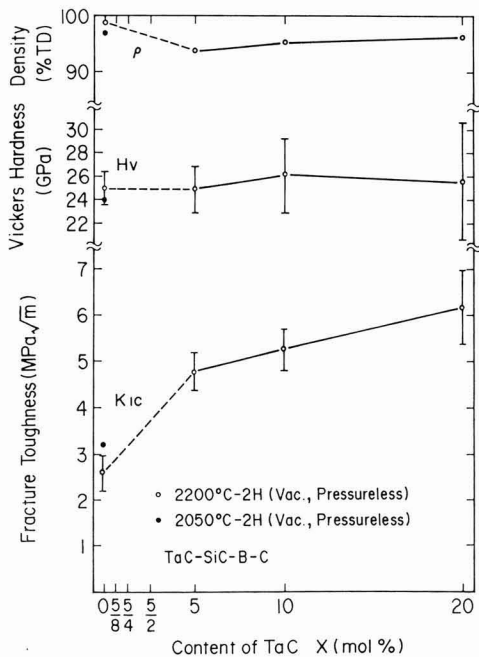


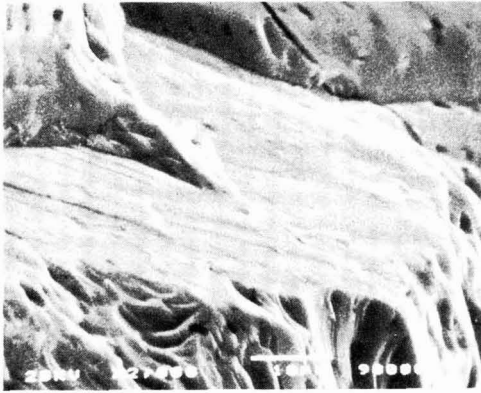
Fig. 4. Variations in density, hardness and toughness with dispersed quantity in TaC-SiC-B-C system, sintered at about 2200°C.

Table 2. Relative diffraction peak heights among SiC, TaC and TaB₂.

TaC Content	(200)TaC (104)6H-SiC	(101)TaB ₂ (104)6H-SiC	(200)TaC (101)TaB ₂
5/8 mol%	0.03	1.0	0.03
5/4 mol%	0.81	1.1	0.71
5/2 mol%	2.6	1.3	1.9
5 mol%	5.8	0.98	5.9
10 mol%	14.	0.93	15.
20 mol%	25.	0.61	41.

mol% with regard to the main composition TaC-SiC. It is considered that the B aid should become stabilized by forming metallic borides and lose its aid effect for the SiC matrix, even in a low carbon pressure (0.015Pa) at around 2300K sintering. Therefore, the densification of a SiC-B-C system with a metallic carbide deteriorated when sintered.

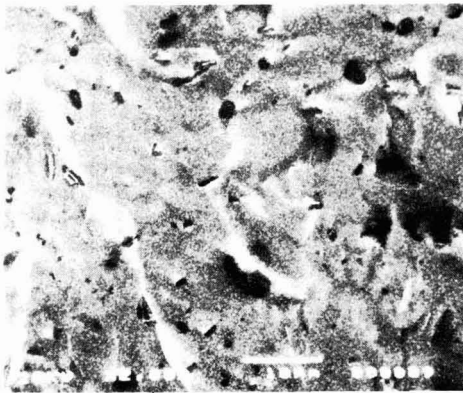
Figure 3 shows micrographs of polished surfaces near the Vickers indent on a sintered TaC-SiC-B-C system. The dispersed bright grains are TaC crystals, and the dispersed dark spots are closed pores, which increased for a relatively low density body. Pores and TaC crystals seem to be distributed independently without any affinity. The TaC crystals have sharp edged shapes, similar to the raw starting powder. This is an



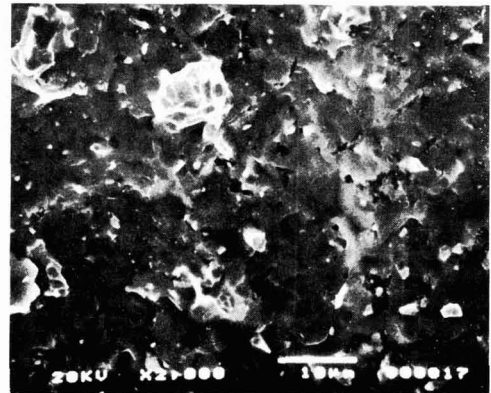
a) Non-TaC dispersed (98.7%TD)



b) 5mol% TaC dispersed (93.7%TD)



c) Non-TaC dispersed (98.7%TD)



d) 5mol% TaC dispersed (93.7%TD)

Fig. 5. SEM photographs of fracture surfaces in TaC-SiC-B-C system, sintered at about 2200°C.

evidence of TaC stability in a SiC matrix. Each median/radial crack is seen to propagate almost straight from the indent edge, and then the crack deflection by the TaC particles is not so clear.

3-2. Mechanical Properties

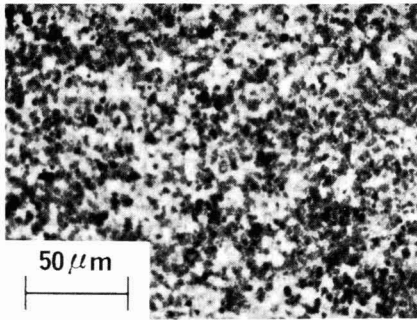
Figure 4 shows the variations in density, toughness and hardness for the TaC-SiC-B-C system, sintered at around 2200°C. The minimum density among these four compositions was 93.7%TD at 5mol%TaC dispersion. The hardness was approximately 25GPa. This seems to be constant in the range between non-dispersed SiC and the 20mol%TaC dispersed composite. On the other hand, the toughness increased with TaC addition, the degree of increase becoming especially large between 0mol% and the 5mol%TaC addition.

Figures 5-a to d show the fracture surfaces for the individual composites. Abnormal exaggerated SiC grain growth appeared and the fracture surface was flat on a micro scale in the case of no TaC addition in Figs. 5-a

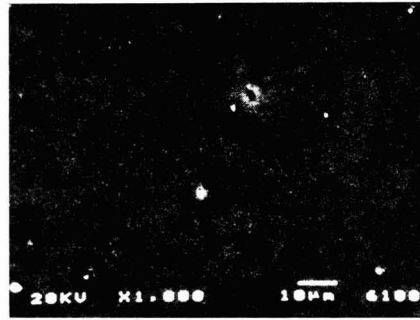
and c. On the contrary, there were no such exaggerated grain growth in bodies where TaC was added, and the fracture surfaces were rough on the micro scale, as shown in Figs. 5-b and d. The dispersed TaC grains could be discriminated from the SiC matrix grains by the brightness and shape differences, as shown in Fig. 5-d. The surface of the fractured TaC grain was similar to a polyhedron and somewhat projected forward.

Dispersed TaC particles should suppress grain growth by pinning grain boundary movement. This microstructure variation is assumed to be the origin for the rapid toughness increase when TaC is added from 0mol% to 5mol%. The slight toughness increase with the TaC amount from 5mol% to 20mol% is considered to be promoted by crack deflection around the dispersed TaC particles by localized stress originating from the difference in the thermal expansion coefficients between the SiC matrix and the dispersed particulate TaC.

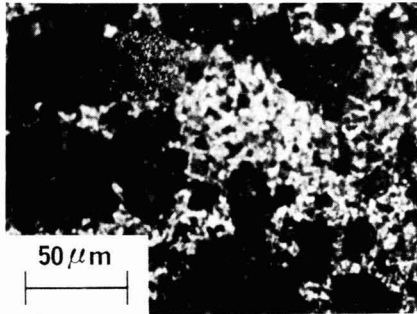
The mechanical strengths of for these composites were about 450MPa, for from 0mol% to 20mol%TaC additions. These values are relatively low and no



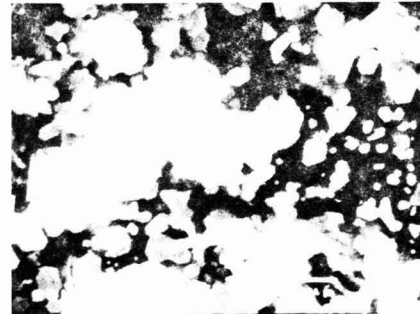
a) Non-TaC dispersed (98.7%TD) RLM



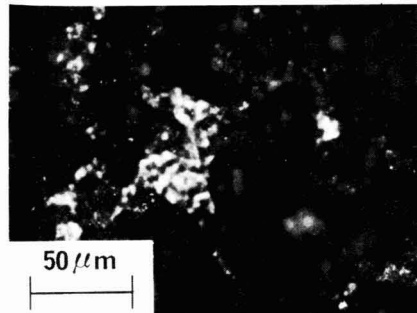
b) Non-TaC dispersed (98.7%TD) SEM



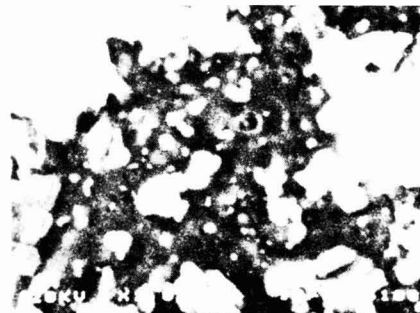
c) 5mol% TaC dispersed (93.7%TD) RLM



d) 5mol% TaC dispersed (93.7%TD) SEM



e) 10mol% TaC dispersed (95.1%TD) RLM



f) 10mol% TaC dispersed (95.1%TD) SEM

Fig. 7. SEM and RLM photographs of oxidized surfaces in TaC-SiC-B-C system.

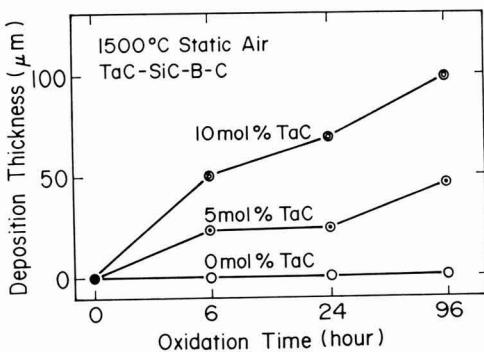


Fig. 6. Thickness variations with oxide deposition on TaC-SiC-B-C system.

promotion with TaC dispersion could be recognized, contrary to the following Griffith's relation.

$$\sigma_f = K_{IC} / (Y\sqrt{C}) \quad \dots\dots(3)$$

where "Y" is the geometrical factor for the maximum defect size "C" within the effective volume of test bar.

It is considered that, because of the large porosity (5-20mol% TaC) or abnormal grain growth (0mol% TaC) in the present experiments, large defects that initiated fracture crack development were not sufficiently suppressed for strengthening with toughening to be observed.

3-3. High Temperature Oxidation Resistance

Color change was negligible in the non-dispersed



a) Non-TaC dispersed (98.7%TD)



b) 5mol% TaC dispersed (93.7%TD)

Fig. 8. SEM photographs of fractured surface edges in oxidized TaC-SiC-B-C system.

sample after the approximately 100 hour heat treatment at 1500°C in static air. However, in TaC dispersed samples, the color changed from black to gray and the size of each sample bar increased a little due to something depositing. Figure 6 shows the deposition thickness increase with time lapse and dispersed TaC quantity.

Figures 7-a to f show the SEM and RLM micrographs of individual oxidized surfaces. There appeared many small and large spots agglomerated or isolated on the TaC dispersed surfaces. They were contrarily bright and dark for SEM and RLM, respectively.

Figures 8-a and b show micrographs for the individual fractured surface edges after oxidation. As usual, there appeared only a thin silica film layer on the oxidized surface (Fig. 8-a), when TaC particles were not dispersed. On the other hand, there were much unknown deposits on the oxidized surface for the dispersed TaC case. The grains of the unknown deposits on the oxidized surface for the dispersed TaC case. The grains of the unknown deposits seem to be a mixture of particles, whiskers, and disks etc., from Fig. 7-d. As shown in Fig. 8-b, an unknown deposit was projecting into the SiC matrix body here and there. As a result, the SiC surface must have been attacked severely during the oxidation and become rough.

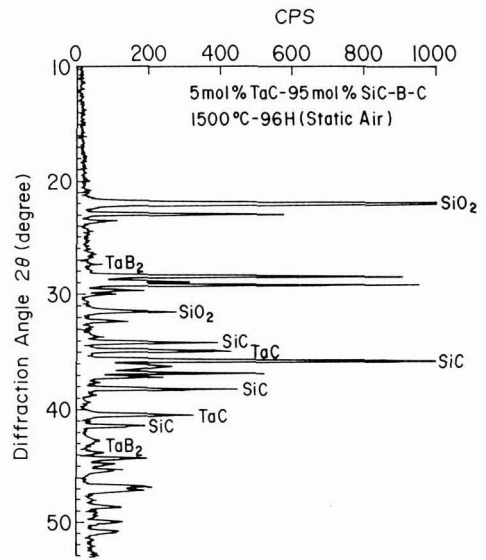


Fig. 9. X-ray diffraction pattern for heat treated TaC-SiC-B-C body at 1500°C - 100H.

Figure 9 shows an X-ray diffraction pattern example for the oxidized body surface with dispersed TaC. There appeared not only the peaks for SiC, TaC, TaB₂ and SiO₂ but also many unknown peaks. The relative height of the above unknown peaks varied with both the dispersed TaC quantity and the 1500°C oxidation time lapse. Most of these peaks corresponded to Ta₂O₅ polymorphism (ASTM 25-922, 27-1447 and etc.).

From the above consideration, the TaC-SiC-B-C bodies seem to be oxidized initially from the point of exposed TaC grains on the surface, and that TaC is transformed to Ta₂O₅ with about 75% volume expansion. Then, these Ta₂O₅ polymorphisms spread like islands on the surface and the roots of the islands seem to penetrate into the SiC matrix body.

Moreover, the 20mol% TaC dispersed sample divided into several pieces by crack formation along the rectangular edges. This phenomenon is considered to be due to the volume expansion of the dispersed particles in the oxidation process.

4. Conclusion

The densification and other properties of seven different metallic carbide added SiC composites with B-C aids were investigated by pressureless sintering. All the metallic compound particles disturbed the densification of the SiC-B-C matrix more or less through the stabilization of the B aid by metallic boride formation.

However, it appeared that densification over 93%TD could be achieved in the SiC-TaC-B-C composite system by a somewhat high sintering temperature. In addition, the dispersed TaC particles suppressed the exaggerated grain growth of the SiC matrix phase. Toughness increased with an increased quantity of dispersed TaC. An about two times greater toughness was achieved with a 90mol%SiC – 10mol%TaC-B-C composition than that for non-dispersed SiC in the same sintering batch. The exposed TaC particles on the body surface were oxidized severely in 1500°C static air to form Ta₂O₅ polymorphisms with volume expansion.

Acknowledgments

The authors are indebted to Mr. Umibe for proofreading and correcting the original English manuscript.

References:

1) K.T. Faber and A.G. Evans, *Acta Metal.*, 31, 565, 577, (1983).

- 2) M. Sakai, *Symp. of Basic Science of Ceram. Jpn.*, 26th, 3, (1988), 27th, 203, (1989).
- 3) G.C. Wei and P.F. Becher, *J. Am. Ceram. Soc.*, 67, 571-74, (1984).
- 4) M.A. Janney, *Am. Ceram. Soc. Bull.*, 65, 357-62, (1986).
- 5) C.H. McMurtry, W.D.G. Boecker, S.G. Seshadri, J.S. Zanghi and J.E. Garnier, *Am. Ceram. Soc. Bull.*, 66, 325-29, (1987).
- 6) H. Endo, M. Ueki and H. Kudo, *Symp. of Basic Science of Ceram. Jpn.*, 26th, 6, (1988).
- 7) T. Mizutani, M. Hayashi and A. Tsuge, *J. Ceram. Soc. Jpn. Inter. Ed.*, 96, 211-16, (1988).
- 8) K. Nihara, R. Morena and D.P.H. Hasselman, *J. Am. Ceram. Soc.*, 65 (7), c. 116, (1982).
- 9) R.W. Davige "Mechanical Behavior of Ceramics," Cambridge Univ. Press, (1979), p. 27.

This article appeared in English in *Nippon Seramikkusu Kyokai Gakujutsu Ronbunshi* (Japanese version), Vol. 98, No.3, 1990.

Dynamic Fatigue Behavior of Ceramics at Elevated Temperatures

Yukihiko Yamauchi, Seisuke Sakai, Masaru Ito, Tatsuki Ohji, Wataru Kanematsu and Shoji Ito

Government Industrial Research Institute, Nagoya
1-1, Hirate-cho, Kita-ku, Nagoya 462, Japan

The dynamic fatigue tests of nine structural ceramics were carried out at temperatures ranging from 800°C to 1500°C in vacuum. The same tests in air were conducted for two ceramics. In ceramics which has a glassy phase in grain boundaries, cracks propagate through grain boundaries due to softening of the glassy phase. A fatigue parameter of ceramics at elevated temperatures is degraded when MgO is used as a sintering additive. In reaction sintered Si₃N₄ and HP-SiC with B and C additives, a subcritical crack growth is not observed but the bending strength of HP-SiC is degraded due to the generation of pores by surface oxidation. It seems that life-time of HP-Si₃N₄ under the static load is predictable from its dynamic fatigue behavior.

[Received August 10, 1989; Accepted November 22, 1989]

Key-words: Silicon nitride ceramics, Silicon carbide ceramics, Dynamic fatigue test, Slow crack growth, Oxidization

1. Introduction

Ceramics have excellent mechanical properties at high temperatures and are attracting interest as high-temperature structural materials. However, many characteristics of their strength properties are still unclear, and the establishment of design criteria for ceramics requires the systematic collection of strength data to clarify the fracture mechanism. In particular, it is essential in order to estimate the life of ceramic parts to be able to elucidate the generation of defects and their growth mechanism. In the previous report,¹⁾ the authors carried out dynamic fatigue tests at room temperature of 10 types of structural ceramics to study the mechanism of crack development at room temperature. This paper reports high-temperature dynamic fatigue tests as adopted in the previous report conducted on nine ceramic materials to investigate their crack propagation mechanisms at elevated temperatures. The study also included the effects of surface oxidation of samples on the results of dynamic fatigue tests. In addition, a comparison was made between the lifetimes of samples under constant load predicted from dynamic fatigue properties and the results of static fatigue tests.

2. Experimental Method

2-1. Preparation of Samples

Ceramics samples were the same as those used in the

previous report¹⁾: five silicon nitride ceramics (N1-N5; common denotation) and four silicon carbide ceramics (C1-C4). N1 and C1 are reaction-sintered bodies, N2 through N4 and C2 and C3 are normal-pressure sintered bodies, and N5 and C4 are hot-pressed materials. Various sintering aids were used: MgO, CeO₂, SrO, ZrO₂ for N2, MgO and Al₂O₃ for N3, Al₂O₃ and Y₂O₃ for N4 and N5, Al₂O₃ for C2 and C3, and B and C for C4. The chemical analyses and densities of the samples are shown in the previous report.¹⁾ Specimens were prepared from a single sintered plate of each material. Silicon nitride was ground with a #400 diamond wheel and silicon carbide with a #600 diamond wheel parallel to the longitudinal direction of the specimens, followed by chamfering with a #800 diamond disc. The final shape was 38mm long, 4mm wide and 3mm thick.

2-2. Tests in a Vacuum

Generally, a dynamic fatigue test is a method to measure the stress corrosion property of glass materials. If the following relationship is established between the crack propagation rate of a material *V* and the stress intensity factor *K_I* at the tip of a crack:

$$V = A \cdot K_I^n \quad (A: \text{constant}) \quad \dots (1)$$

the method can be adopted to evaluate the fatigue parameter *n*. According to earlier work,^{2,3)} the *K_I*-*V* relationship of silicon nitride ceramics at high temperatures is usually described by Eq. (1) with a crack propagation rate of 10⁻⁶m/sec or less, so that the dynamic fatigue test is considered suitable for estimating the high-temperature fatigue parameter of ceramics.

The tests in this program were carried out in a vacuum of 10⁻⁵ Torr at 800° - 1500°C. At least two test temperatures were used for each sample, the temperature where the bending strength started to fall and the temperature 200°C higher. However, in the case of materials whose bending strength does not decrease at elevated temperatures, the maximum temperature was 1500°C. The specimens, together with the whole system including the molybdenum bending fixture, and upper and lower rods, were heated uniformly by a tungsten heater. The inside of the furnace was evacuated to less than 10⁻⁴ Torr, heated to the testing temperature in about 10 minutes, and maintained there for 10 minutes without load to ensure uniform heating.

Dynamic fatigue tests were performed by measuring the 3-point bending strength of the specimens with an outside span of 30mm and at crosshead speeds of 5, 0.5, 0.05, 0.005, and 0.0005mm/min. The three specimens were used for each crosshead speed. The fatigue parameter *n* was determined by first obtaining the stress rate $\dot{\sigma}$ and rupture stress σ_f from the time-load curve, and then

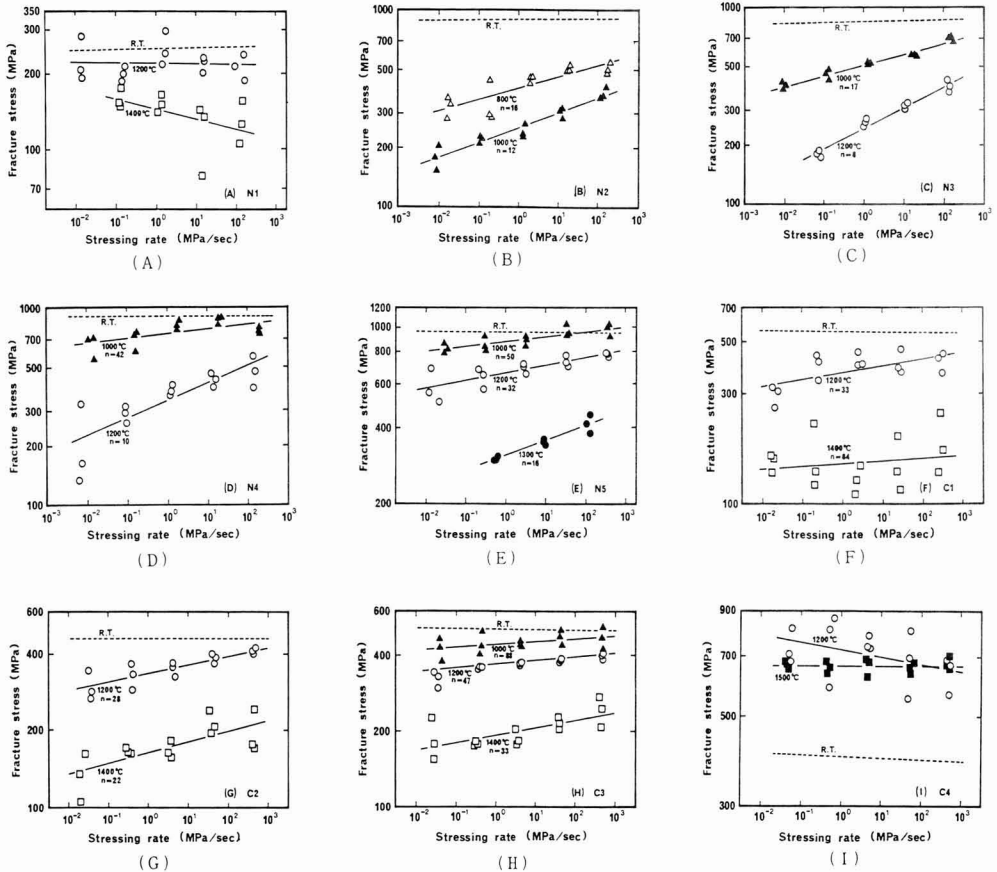


Fig. 1. Results of dynamic fatigue tests in vacuum.

making a linear approximation by the method of least squares on the log-log coordinates, and calculating n by the following equation:

$$\sigma_f = c \cdot \dot{\sigma}^{(1/n+1)} \quad (c; \text{constant}) \quad \dots \dots (2)$$

In this case, the assumptions required to establish equation (2) were that the stress rate is constant over the entire loading period and the crack shape factor does not change with crack growth, so that specimens failing largely out of the elastic deformation range were excluded along with those showing crack growth too great to have a constant shape factor. The standards of judgement were: a specimen did not show deformation visually after testing; and a change in the loading rate in the load-time curve was less than 20% against the linear part. Additionally, the limits of crack growth assumed the defect form was semicircular, the change in the shape factor at the tip of the crack on the surface of a specimen is about 10% or less, and the depth was not greater than about 1mm.

2-3. Tests in Air

Samples N5 and C4 were subjected to dynamic fatigue tests in air in addition to the vacuum tests above. The tests in air used a SiC 3-point bending fixture and upper and lower rods as well as a molybdenum bisilicate heater. The heating rate was 30°C/min., and before testing, specimens were held at the specified temperature for 10 minutes without load to ensure uniform heating.

3. Results and Discussion

3-1. Dynamic Fatigue Properties in a Vacuum

Figure 1(A)-(I) shows the results of dynamic fatigue tests in a vacuum. The fracture stress and fatigue parameters of samples N2 through N5 and C2 and C3 dropped sharply with an increase in testing temperature. These materials contained sintering agent oxides such as

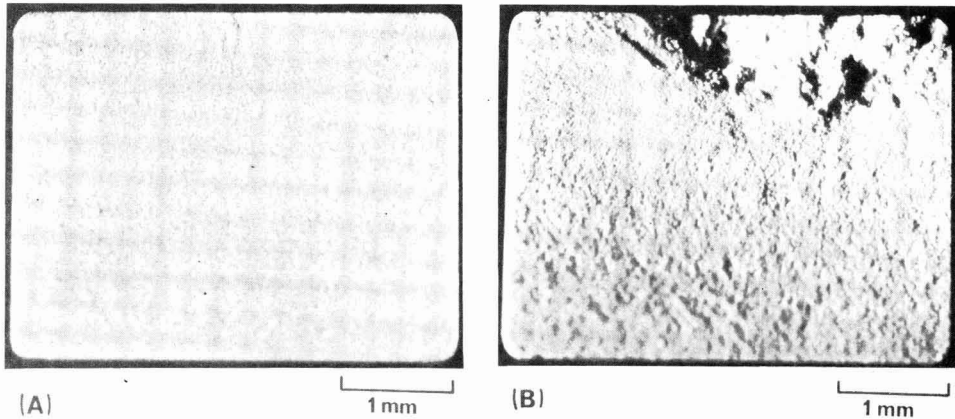


Fig. 2. Fracture surfaces of N2 specimens failed by dynamic fatigue test with crosshead speed (A) 5mm/min and (B) 0.0005mm/min at 1000°C in vacuum.

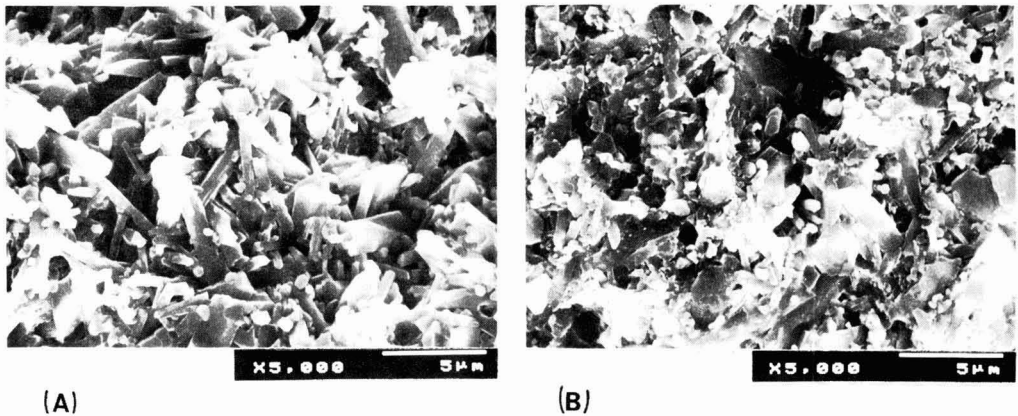


Fig. 3. SEM photographs of (A) slow crack growth region and (B) rapid fracture region on fracture surface of N2 specimen (Fig. 2(B)).

Al_2O_3 and MgO , and the presence of a glassy phase in the grain boundary was confirmed in some samples (N2, N5, C2). Since this glass phase begins to soften at about 1000°C,⁴ the crack growth of these samples at high temperatures is considered to be caused by a decrease in the strength of the intergranular glass phase. Figure 2 is the optical micrographs of an N2 samples showing a substantial decrease in strength and fatigue parameter: (A) the fracture surface of a specimen fractured at 1000°C with a crosshead speed of 5mm/min; (B) the fracture surface of a specimen that fractured at 1000°C with a crosshead speed of 0.005mm/min. Almost no crack growth was observed in specimen (A) fractured at a high stress rate, whereas a trace of substantial crack growth was found in (B) fracturing at a low stress rate. Moreover, Figs. 3(A) and (B) show

SEM photos of the slow crack growth region and fast fracture region of Fig. 2(B) respectively; in the latter some intragranular fracture was detected while in the former intergranular fracture was predominant.

Furthermore, the state of the fractured surfaces of specimens failing at a high crosshead speed was almost the same as that of the fast fracture region (Fig. 3(B)) of specimens failing at a low crosshead speed, and some intragranular fracture was recognized. These observations of the fracture surfaces suggest that the resistance to crack propagation in the grain boundary is affected by the crack propagation rate. That is, in the slow crack growth region the resistance to an intergranular crack is low and it proceeds along the grain boundary, while in the fast fracture region an intergranular crack cannot respond to crack development,

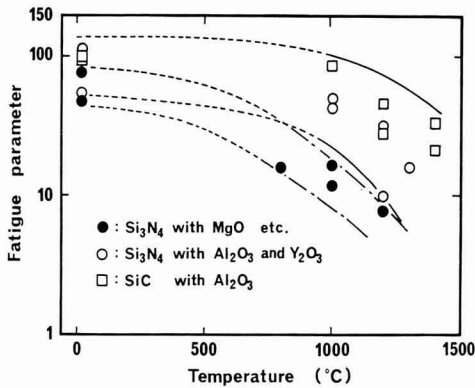


Fig. 4. Temperature dependence of fatigue parameter.

thus increasing the resistance to the crack. As a result, intragranular cracking seems to have occurred in comparatively weak grains. Hence, from the above results, the crack growth at high temperatures of ceramics with glassy phases in the grain boundaries is mainly due to intergranular cracking promoted a decrease in the viscosity of the glassy phases.

As in Fig. 4, the samples employed here can be classified into two groups. The temperature dependence of the fatigue parameters of N4 and N5 containing Al_2O_3 and Y_2O_3 sintering aids was almost the same as that of C2 and C3 with Al_2O_3 , while the fatigue parameters of N2 and N3 with MgO started to decrease at a lower temperature than those of Al_2O_3 -containing ceramics and the absolute values were lower as well. This is probably because the glassy phases of N2 and N3 contained Mg and started to soften at lower temperatures than those of other ceramics without Mg.

In the case of the results of dynamic fatigue tests for reaction-sintered bodies (N1, C1) and ceramics using nonoxides as sintering agents (C4), no decrease in the strength of N1 and C4 occurred even at elevated temperatures and by prolonged loading. The oxygen contents of these samples are relatively low (1 - 2wt%), and no secondary layer such as a glassy phase appears to be present in the grain boundaries, or if present, is an amorphous substance with high-temperature strength.⁵⁾ Moreover, observation of the fracture surfaces of N1 and C4 specimens by an optical microscope did not detect any trace of crack growth as in Fig. 2(B). Consequently, in these samples, crack growth by intergranular cracking did not occur as in the case of ceramics with glass phases in their grain boundaries, thus maintaining the strength even under a low stress rate.

The sample C1, as well as sample N1, is a reaction-sintered body and has a low oxygen content (about 1.6wt%); yet the bending strength decreased with increasing temperature and some crack growth was noticed at 1200°C. This is considered to be because a

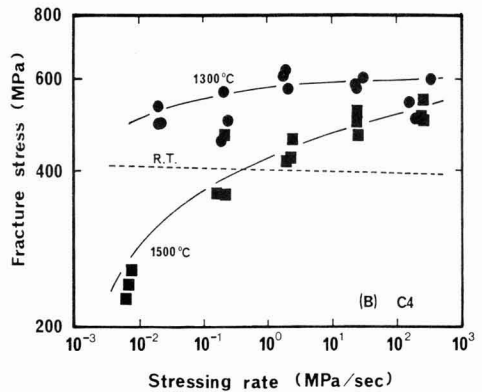
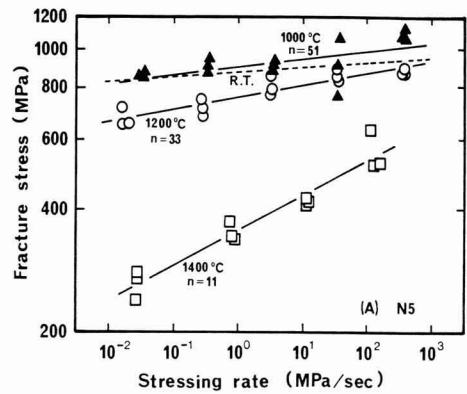


Fig. 5. Results of dynamic fatigue tests in air.

substantial amount of metallic Si remained in this sample (about 10wt%) and acted as the secondary phase in the grain boundary. In fact, Si softens considerably at 1200°C and crack growth by intergranular cracking lowers the strength in the region of low stress rate. However, at 1400°C, Si completely melts and the parts where Si is present act only as defects, so that the strength decreases greatly although no crack growth is detected by prolonged loading.

3-2. Dynamic Fatigue Properties in Air

Figures 5(A) and (B) show the results of dynamic fatigue tests at high temperatures in air with N5 and C4 respectively. When the results of N5 are compared with those in a vacuum (Fig. 1(E)), their values of strength and fatigue parameters are in good agreement up to 1200°C. Consequently, the crack growth in air of this sample is also considered to be basically due to intergranular cracking caused by the decreased viscosity of the glassy phase in the grain boundary. However, there were great variations under different conditions at

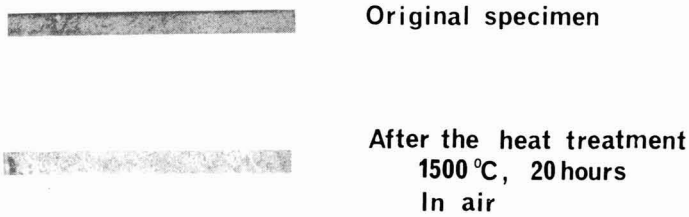


Fig. 6. Change of surface of C4 specimen by heat treatment.

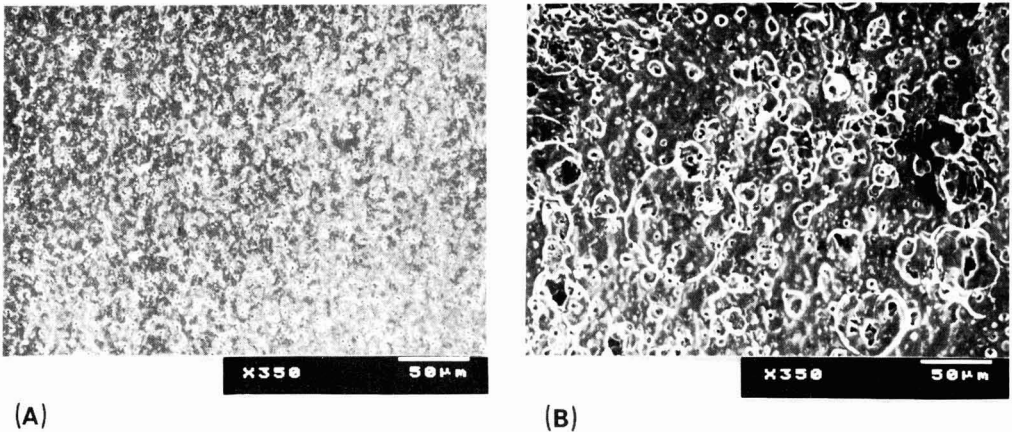


Fig. 7. Surfaces of C4 specimens failed by dynamic fatigue test with cross-head speed (A) 5mm/min and (B) 0.0005mm/min at 1500°C in air.

1300°C or higher. In the experiment at 1300°C in a vacuum, testing with a low stress rate (crosshead speed: less than 0.005mm/min) was hampered by the deformation of specimens and could not be carried out at 1400°C where the specimens started to decompose, while in the test in air they fractured almost in the elastic region even at 1400°C. This is probably because testing in air caused the oxidation of sample surfaces leading to a change in the properties of the intergranular glassy phase. The deformation of N5 at high temperatures is usually considered to be mainly due to intergranular slipping caused by the decreased viscosity of the glassy phase coupled with the formation and growth of cavities at the intergranular triple point.⁶⁾ However, Wakai et al. reported that when the surface of hot-pressed silicon nitride is oxidized, impurity ions such as Mg and Ca inside the glassy phase diffuse to the oxidized layer on the surface, thus increasing the

viscosity of the internal glassy phase and greatly affecting the creep properties.⁷⁾ The sample N5 used here was the same as that used by Wakai et al. so that the differences in dynamic fatigue properties measured under various atmospheres at 1300°C or higher are probably due to surface oxidation and the accompanying change in the intergranular glassy phase.

Subsequently, the results for C4 were compared with those in a vacuum (Fig. 1(1)) finding great differences in the dynamic fatigue properties. Specifically, the strength did not decrease in a vacuum even under a low stress rate, and it was first regarded as a material which did not undergo crack growth even under prolonged loading at high temperatures. However, the strength decreased somewhat at 1300°C and substantially at 1500°C in air in the region of low stress rates. The sample had almost no glassy phase in the grain boundary and is considered not to undergo crack growth by

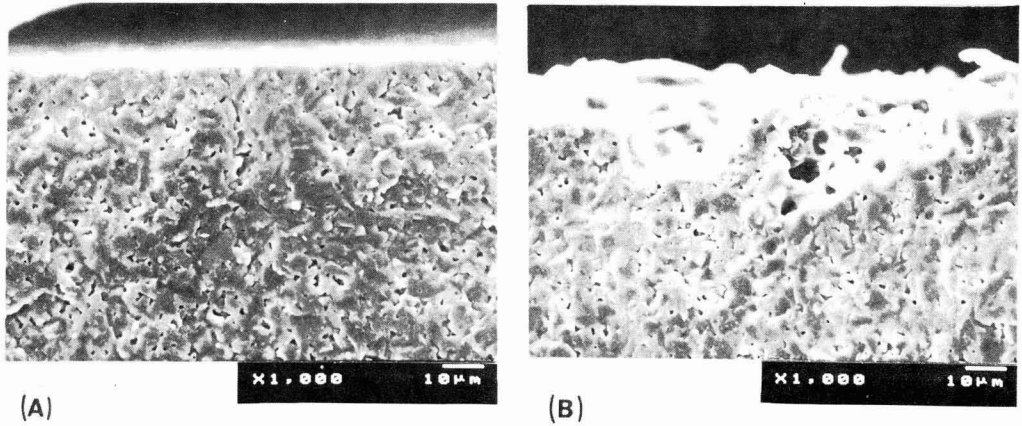


Fig. 8. Fracture surfaces of C4 specimens failed by dynamic fatigue test with crosshead speed (A) 5mm/min and (B) 0.0005mm/min at 1500°C in air.

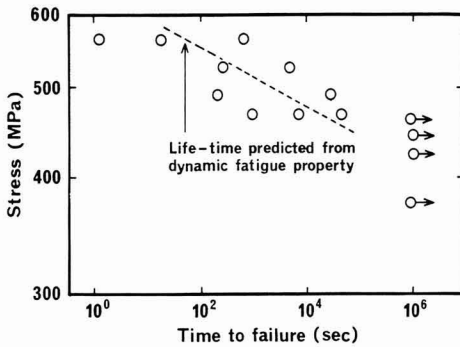


Fig. 9. Static fatigue behavior and predicted life-time from dynamic fatigue behavior of N5 at 1200°C.

intergranular cracking even at elevated temperatures. Hence, a fall in the strength in air after long-period loading would have resulted from crack growth caused by other mechanisms or by causes other than crack growth. Figure 6 shows photos of the change in the appearance of the specimen C4 exposed to air at 1500°C. A number of white substances appeared on the surface of the specimen which had become quite rough after heat treatment. Infrared spectroscopy indicated the white substances were cristobalite including B-O and B-Si bonds. In the test for strength at 1500°C with a crosshead speed of 0.0005mm/min, about 10 hours were required from the start of loading to fracture, during which the same change as in Fig. 6 was observed on the surfaces of the specimens tested in air, while no change in appearance was seen with those tested in a vacuum.

Also, in the test at 1500°C in air with high crosshead speed, the appearance of the specimens remained mostly unchanged. Figure 7 shows SEM photos of the surfaces of specimens tested at 5mm/min (A) and 0.005mm/min (B) crosshead speed. The surface of (A) has no oxidation layer but (B) shows considerable oxidation along with traces of gas evolution from the inside. Figures 8(A) and (B) are SEM photographs showing the fractured surfaces near the surfaces of specimens in Figs. 7(A) and (B) respectively. The fracture origin of the specimen (A) was internal and no change was detected on the surface, while for (B) the origin was a surface defect as in Fig. 8(B). Specimen (B) had such voids in various places. The above results suggest that the decrease in the strength of C4 by prolonged loading is due not to crack growth but to defects caused by surface oxidation. In order to further confirm this, C4 specimens were held at 1500°C in air for 10 hours without load, and then subjected to a 3-point bending test at 1500°C in air with a crosshead speed of 0.5mm/min. As a result, the strength after oxidation without loading also became about 200MPa, which almost agreed with the value at a crosshead speed of 0.005mm/min as in Fig. 5(B).

The formation of defects by surface oxidation as well as the subsequent decrease in strength discussed above was not encountered in the case of N5. The probable reason is that the sample N5 has a glassy phase in the grain boundary, which starts to soften over 1000°C, so that testing at 1500°C causes the specimen to deform considerably hampering the measurement of strength. Consequently, this experiment used 1400°C or lower for the testing temperatures where the surface oxidation of specimens was mild and the defects formed were small. Moreover, crack growth was active due to intergranular cracking promoted by the decreased viscosity of the glassy phase, so that the surface defects to some degree did not affect the strength. In contrast, C4 had little glassy phase in the grain boundary, which allowed almost no crack growth by intergranular cracking and

the influence of surface defects caused by oxidation appeared directly.

3-3. Comparison With Static Fatigue Properties

The life of N5 under a constant load was estimated from the dynamic fatigue properties as in Fig. 1(E), and compared with the measured static fatigue properties. Figure 9 shows the results of static fatigue tests with N5 at 1200°C reported earlier.⁸⁾ Since the conditions of the static fatigue tests (4-point bending; outside span: 50mm; inside span: 30mm; sample cross section: 2mm- \times 4mm) were different from those of the dynamic fatigue tests here, life estimation required adjustment due to the difference in the initial crack length by the effective volume effect. In this case, the Weibull modulus of this material at 1200°C was $m=20$. The broken line in Fig. 9 represents static fatigue life estimated from the dynamic fatigue properties. The measured life values are mostly distributed along this line, and showed relatively good agreement taking the deviation of data into account. The comparison with static fatigue properties is limited to N5 so that hasty conclusions should be avoided, but the above results suggest that the lifetime under a static load can be predicted from the dynamic fatigue properties. This indicates that the dynamic fatigue properties reflect slow crack propagation properties adequately under static stress.

The delayed fracture of ceramics at high temperatures is considered to be caused chiefly by the crack growth of a softened intergranular glassy phase. When the glassy phase softens to some extent, the viscoelasticity is expected to affect the crack propagation properties. For example, in cyclic fatigue with relatively high stress rates as well as in the region with an extremely high crack propagation rate, there is a possibility that the resistance against crack propagation varies. Likewise, dynamic fatigue tests do not assure constant stress values and its influence was predicted beforehand. Nevertheless, this test seems to have prevented the stress rate from influencing the crack propagation properties because the stress rate was low enough for crack growth to respond to stress change, and the crack growth rate effect on the dynamic and static fatigue was low.

4. Conclusions

Dynamic fatigue test with 5 types of silicon nitride and 4 types of silicon carbide ceramics were conducted in a vacuum at 800° - 1000°C. Moreover, some specimens were also subjected to the same tests in air. As a result, the following conclusions were obtained.

1) Crack growth at high temperatures of ceramics with a glassy phase in the grain boundary was mainly due to intergranular cracking caused by the decreased viscosity of the glassy phase both in a vacuum and in air. Addi-

tionally, the high-temperature fatigue parameters are affected by the components of the glassy phase. In the samples used for these experiments, the crack growth of ceramics with MgO sintering aid was active, which is probably because the Mg lowered the viscosity of the glassy phase.

2) Reaction-sintered silicon nitride or hot-pressed silicon carbide with B and C developed almost no crack growth even at elevated temperatures.

3) Reaction-sintered silicon carbide in which metallic Si remained in quantities developed crack growth at 1200°C probably due to intergranular cracking caused by a decrease in Si viscosity, while at 1400°C Si melts completely so that no crack growth was observed, only a substantial reduction in strength.

4) In the case of hot-pressed silicon nitride containing Al_2O_3 or Y_2O_3 , surface oxidation increased the viscosity of the internal glassy phase to improve its plasticity.

5) For hot-pressed silicon carbide with B and C, numerous pores were generated by oxidation on the surfaces of specimens, thus greatly reducing their strength.

Furthermore, a comparison was made between the lifetimes of N5 samples under a constant load estimated from the dynamic fatigue properties and measured static fatigue, which was in relatively good agreement. Hence, the static fatigue lifetimes at elevated temperatures are obtainable from the dynamic fatigue properties.

Acknowledgments

The authors wish to thank Mr. Takashi Kanno, Asahi Glass Co., Ltd., for providing samples. The authors are also grateful to Mr. Norio Ishizuka and Mr. Akira Tsuge, Government Industrial Research Institute, Nagoya, for conducting chemical analyses of samples.

References:

- 1) Y. Yamauchi, Nihon Seramikkusu Kyokai Gakujutsu Ronbunshi, Vol. 96, No.9, 885-889 (1988).
- 2) M. Kawai et al., *Fract. Mech. Ceram.*, Vol.6, 587-601 (1981).
- 3) T. Fett et al., *Int. J. Fract.*, Vol. 36, 3-34 (1988).
- 4) S. Sakaguchi et al., *Yogyo-Kyokai-shi*, Vol.95, No.12, 1219-1222 (1987).
- 5) Y. Ikuhara et al., *Yogyo-Kyokai-shi*, Vol.95, No.6, 638-645 (1987).
- 6) T. Ohji et al., *Yogyo-Kyokai-shi*, Vol.94, No.5, 536-537 (1986).
- 7) F. Wakai et al., *Proc. Int. Symp. Ceram. Compo. Eng.*, 279-285 (1983).
- 8) Y. Yamauchi et al., *Proceedings of the 39th Government Industrial Research Institute, Nagoya Conference (1985)* 79-80.

This article is a full translation of the article which appeared in *Nippon Seramikkusu Kyokai Gakujutsu Ronbunshi (Japanese version)*, Vol.98, No.3, 1990.

Densification of Calcium-Deficient Hydroxyapatite by Hot Isostatic Pressing

Soo Ryong Kim, Kazushi Hirota, Fujio P. Okamura, Yasutoshi Hasegawa and Soon Ja Park*

National Institute for Research in Inorganic Materials

1-1 Namiki, Tsukuba, Ibaraki 305, Japan

* Department of Inorganic Materials Engineering,

College of Engineering, Seoul National University

San 56-1, Shinlim-dong, Kwana-ku, Seoul 151-742, Korea

Stoichiometric and non-stoichiometric hydroxyapatites (Ca/P=1.55, 1.60 and 1.67), prepared by the hydrolysis of brushite or monetite, were densified by the HIP treatment at 100 - 800°C and 320 - 850MPa. The temperature-pressure region for densification depends upon Ca/P ratios. At 600MPa, the lowest temperature of the densification is 300°C for Ca/P=1.55, 400°C for 1.60 and 800°C for 1.67. In the case of calcium-deficient hydroxyapatite the densification temperature decreased with increasing crystal water content. In the case of Ca/P=1.55, the lowest temperature for densification is 500°C at 600MPa for fully dried starting powder, of which n in $\text{Ca}_{10-x}\text{H}_x(\text{PO}_4)_6(\text{OH})_{2-x}\cdot n\text{H}_2\text{O}$ is nearly equal to zero.

[Received August 21, 1989; Accepted November 22, 1989]

Key-words: Calcium-deficient hydroxyapatite, Crystal water, Densification, HIP, Hydroxyapatite, Non-stoichiometric hydroxyapatite, Residual strain

1. Introduction

Bones and teeth contain "impure" calcium phosphate, and the crystalline part is referred to as "biological apatite," which is a type of calcium-deficient hydroxyapatite.¹⁾ It is also known that crystalline apatite can have a variety of functions, when various ions or molecules are introduced into the structure.²⁾

In this study, the authors attempted to densify calcium-deficient hydroxyapatite powder without changing the composition or crystalline structure, in order to develop substitute materials for bones and teeth.

The as-synthesized calcium-deficient hydroxyapatite in an aqueous solution is considered to have a composition in which part of the calcium and hydroxide ions of the stoichiometric composition $\text{Ca}_{10}(\text{PO}_4)_6(\text{OH})_2$ are substituted with hydrogen ions and water molecules.³⁾ It is known that calcium-deficient hydroxyapatite cannot be densified in air, because it is dehydrated when heated for sintering, into a mixture of hydroxyapatite and tricalcium phosphate ($\text{Ca}_3(\text{PO}_4)_2$).⁴⁻¹⁰⁾

Calcium-deficient hydroxyapatite was expected to be densified without decomposition, when heated under a sufficiently high pressure, because water-containing minerals are generally deformed plastically under high pressures. A highly densified product was obtained in preliminary experiments conducted at a pressure up to 150MPa, where powdered apatite packed in a sealed tube was heated under pressure.¹¹⁾ A temperature of at

least 200°C was required at 150MPa to sufficiently densify the powder, which was dried at room temperature under a vacuum. It was also found that calcium-deficient hydroxyapatite powder was not densified, after drying by heating under vacuum.

The observations that the temperature required for densification is very low and the results are very sensitive to drying conditions indicate that water is very important in the densification process.

In this study, calcium-deficient hydroxyapatite was dehydrated under various drying conditions in an attempt to determine the characteristic densification behavior under high pressure, and the densified products were compared with hydroxyapatite of the stoichiometric composition. A new experimental system was developed to carry out the tests under high pressure.

2. Experimental Procedure

2-1. Starting Powders and Their Treatment

The authors specified three types of hydroxyapatite of different Ca/P ratios, to be prepared by the wet process, which were prepared by Central Glass Co., Ltd. The Ca/P=1.55 powder was prepared by the reaction of brushite ($\text{CaHPO}_4\cdot 2\text{H}_2\text{O}$) and ammonia, the powder of Ca/P=1.60 by the reaction of brushite and calcium hydroxide ($\text{Ca}(\text{OH})_2$) suspended in an aqueous solution, and the powder of Ca/P=1.67 by calcining the apatite formed by the reaction of monetite (CaHPO_4), calcium hydroxide and calcium carbide (CaCO_3) suspended in an aqueous solution. Table 1 shows the analyses of these powders, as reported by the manufacturer.

Each starting powder was pressed using a die into a 36mm diameter, 135mm long metallic capsule of lead,

Table 1. Impurity contents and specific surface area of the starting powder.

Ca/P molar ratio	Impurities /ppm								Specific surface area m ² /g
	Cl	SO ₄	Fe	Pb	As	Cd	Na	NH ₃	
1.55	9.0	9.3	2.5	0.2	0.2	<0.07	<100	<120	82
1.60	3.0	8.0	1.8	1.7	<0.2	<0.07	<100	-	60
1.67	5.0	5.0	2.0	1.0	-	<0.5	<120	-	41

silver or gold depending on the treatment temperature. Each capsule, after charging with the starting powder, was sealed off with a welded lid, and heated to drive off the adsorbed gases and moisture from the insulated capsule through a pipe (1.6mm in outer diameter, 0.5mm in inner diameter) provided in the lid. This step was continued until the equilibrium pressure of the vapor phase in the capsule (i.e., pressure within the insulated capsule at the temperature when the exhaust pump was stopped) reached 0.55torr. The extent of drying of the starting powder was essentially determined by the temperature at which the evacuation was carried out. A couple of days were required to evacuate the capsule sufficiently. The chemical species in the exhaust gas were monitored by a quadruple mass spectrometer (Leybold Inficon Inc. QUADREX 100), to confirm that the exhaust gas consisted essentially of water. Furthermore, the capsule under evacuation was separated at times from the evacuation system, to measure the weight and thereby to monitor the water removed. On completion of the evacuation step, the capsule was sealed off by welding the exhaust pipe, and separated from the evacuation system for the test.

2-2. Pressure Vessel

A new type of pressure vessel with pressure durability required for the experiment, was specifically designed and manufactured.¹²⁾ The highest working pressure, inner diameter and effective depth of the vessel were 1000MPa, 90mm and 300mm, respectively. Argon was used as the pressure medium. An electrical furnace (sample chamber inner diameter: 38mm, highest working temperature: 800°C, temperature-level accuracy: $\pm 2^\circ\text{C}$) was placed in the vessel, to keep the sample at the desired temperature).

Table 2. Densification of hydroxyapatite under high pressures and moderate temperatures.

Specimen No.	Ca/P ratio	Number of H ₂ O bonded in molar crystal lattice n	Treatment conditions			Density g/ml	Stability spontaneous breakage
			Temperature °C	Pressure MPa	Duration hrs.		
S-7	1.67	-	200	850	6	2.72	broken
S-5	1.67	-	500	680	4.5	3.00	broken
S-12	1.67	-	500	637	18.5	3.00	stable
S-16	1.67	-	800	600	9	3.15	stable
N1-3	1.60	-	200	800	0.2	-	broken
N1-2	1.60	-	300	670	2	2.00	broken
N1-5	1.60	0.69	400	600	14	3.02	stable
N1-6	1.60	0.69	400	600	9	3.02	stable
N1-1	1.60	0.58	400	580	14	3.08	stable
N2-1a	1.55	1.23	150	600	1	2.77	broken
N2-5a	1.55	-	150	730	15	2.57	broken
N2-3	1.55	0.90	300	600	20	3.05	stable
N2-7	1.55	0.55	300	600	20	3.07	stable
N2-1	1.55	-	300	680	5	-	broken
N2-19	1.55	0.55	400	600	5	3.00	stable
N2-9	1.55	0.31	400	600	7	3.08	stable
N2-2	1.55	0.31	400	600	19	3.09	stable
N2-6	1.55	0.35	400	600	11	3.09	stable
N2-10	1.55	0.33	400	600	20	3.08	stable
N2-4	1.55	0.55	400	320	17	2.65	stable
N2-5	1.55	0.14	500	600	4	3.11	stable
N2-11	1.55	0.10	500	600	11	3.11	stable
N2-12	1.55	0.17	500	600	12	3.11	stable
N2-13	1.55	0.34	500	600	13	3.08	stable

2-3. Infrared Absorption Spectra

Infrared spectra were measured by a spectrometer (Nippon Bio Rad Laboratory FTS 60). It was equipped with absorbance scale, and light passing through the thin specimen was directly measured, to determine the hydrogen content in the sample. The KBr disk method was not used, because of the likely error due to contamination of the KBr tablet with moisture from the air during preparation.

2-4. X-Ray Diffractometry

The starting powders and all of the samples treated under elevated temperature and pressure were analyzed by X-ray diffraction using $\text{CuK}\alpha$ radiation, to investigate the phases present and crystallinity. The densified samples were analyzed directly, after the surfaces of the test pieces were polished. A holder for the densified sample was developed specifically for this task. The diffraction angle was determined by an X-ray powder diffractometer (Philips Model PW1820/00), with a specified repeatability of $\pm 0.001^\circ$ for the 2θ measurement. The step scan procedure was used to measure the lattice constants at the intervals of 0.02° for 10sec.

2-5. Bending Test

A total of ten specimens ($3 \times 4 \times 32\text{mm}$) were prepared from each of the two representative sample types for the 3-point bending tests, conducted with a cross-head speed of 0.5mm/min by a testing machine (Instron Model 1123).

2-6. Analysis of Moisture

About 1g of the densified sample, put in a platinum crucible, was kept at 800°C in air for 20h or longer, until it reached a constant weight. It was confirmed by X-ray powder diffraction that the sample was decomposed into tricalcium phosphate ($\text{Ca}_3(\text{PO}_4)_2$) and hydroxyapatite of the stoichiometric composition ($\text{Ca}_{10}(\text{PO}_4)_6(\text{OH})_2$).

Assuming that the calcium-deficient hydroxyapatite is represented by the formula $\text{Ca}_{10-x}\text{H}_x(\text{PO}_4)_6(\text{OH})_{2-x} \cdot n\text{H}_2\text{O}$, and that the quantity of moisture $(n+1)\text{H}_2\text{O}$ formed by the decomposition reaction $\text{Ca}_{10-x}\text{H}_x(\text{PO}_4)_6(\text{OH})_{2-x} \cdot n\text{H}_2\text{O} + 3x\text{Ca}_3(\text{PO}_4)_2 + (1-x)\text{Ca}_{10}(\text{PO}_4)_6(\text{OH})_2 + (n+x)\text{H}_2\text{O}$ corresponds to the weight loss of the sample heated in air, the n value of the densified sample was calculated.

3. Results

3-1. Pressure and Heat Treatment

The relative density of the starting powder, measured from the volume packed naturally in a container, varied from 5 to 15vol%. The powder was pressed into the capsule under a uniaxial pressure of 20MPa. The compact had a relative density of about 40vol%, measured from the external dimensions and weight. The results of treatment under pressure and heat are given in Table 2.

Ca/P=1.55
HYDROXYAPATITE

HIP'ed at 300°C, 600MPa

Fig. 1. Dense polycrystalline calcium-deficient hydroxyapatite (Ca/P=1.55): specimen No.N2-3 in Table 2, densified at 300°C, 600MPa.

Under pressures up to 850MPa, the sample remained porous, unless heated. The samples treated under pressure at relatively low temperature disintegrated after a time, when they were taken out from the capsules. Disintegration took place sometimes with a noise but without external forces, scattering powdery pieces, when the sample was allowed to stand in air for about 10h. The samples which disintegrated gradually in air were, when put in water at room temperature, totally destroyed explosively in a couple of minutes. The disintegrating samples are denoted as "broken" in Table 2.

The lowest temperature required to densify the sample to a negligible porosity differed greatly, depending on the apatite type used. The sample of Ca/P=1.67 formed a transparent specimen (S-16) when treated at 800°C, while the sample of Ca/P=1.60 formed specimens (N1-1, N1-5 and N1-6) when treated at 400°C.

The sample of Ca/P=1.55 formed transparent specimens (N2-3 and N2-7) which contained no pores, when treated at a low temperature such as 300°C. Figure 1 shows a photograph of the specimen N2-7; it was 5mm thick and as transparent as glass.

Figure 2 illustrates how the temperature required to densify the sample of Ca/P=1.55 varied with the quantity of water n , which was obtained by the method mentioned in Section 2.6.

Figure 3 shows the SEM photos of the sample of Ca/P=1.55 before and after densification, to compare their grain sizes. The lower the treatment temperature, the smaller the grain size. For highly densified samples, the grain size tended to increase by densification when the starting sample contained a relatively large quantity of crystal water.

3.2. Infrared Absorption Spectra

The results shown in Table 2 indicate that densification of the powdered apatite was greatly affected by the Ca/P ratio and quantity of crystal water. Both these factors are related to the components which formed water molecules, when the crystal phase was heated. Figure 4 shows the infrared absorption spectra of the samples treated under conditions believed to be representative. Each specimen was cut from the transparently densified sample, and polished to a 75 μ m thickness.

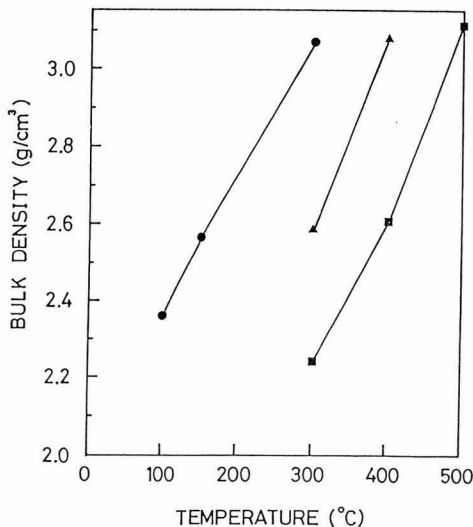


Fig. 2. Densification of calcium-deficient hydroxyapatite (Ca/P=1.55) as a function of temperature under 600MPa. The n values in the formula $\text{Ca}_{10-x}\text{H}_x(\text{PO}_4)_6(\text{OH})_{2-x} \cdot n\text{H}_2\text{O}$ were determined to be \circ ; $n=0.9$, Δ ; $n=0.31$ and \blacksquare ; $n=0.01$, respectively.

The specimen N2-3 shown in Fig. 4 was from the transparent sample densified at 300°C and 600MPa, with crystal water content n of 0.90. It showed an absorption peaks in the wave number range of 3500 to 3000 cm^{-1} , caused by the stretching vibration of the hydrogen-bonded OH group.

The specimen N2-13 was the well-dried sample, densified and transparent by treatment at 500°C and 600MPa with crystal water n of 0.34. Compared to the specimen N2-3, the stretching vibration absorption of the hydrogen-bonded OH group was negligibly small.

3.3. X-Ray Diffraction Analysis

No diffraction peak other than that due to the apatite phase was detected in any of the densified samples shown in Table 2.

The diffraction pattern of the densified specimen N2-3, which was a typical specimen densified at a relatively low temperature of 300°C under 600MPa was compared with that of the starting powder. The crystallinity was increased by densification.

Significant differences were observed in the broadening and angle of the diffraction lines. The crystallinity of the starting powder was higher than that of the samples densified at 150°C under pressure, but was lower than that of the samples densified at higher temperatures. The differences in the diffraction angle 2θ of the samples reached 0.05° in some cases, even in the low angle region.

The lattice constant measured is discussed below, because the procedure used may be debatable.

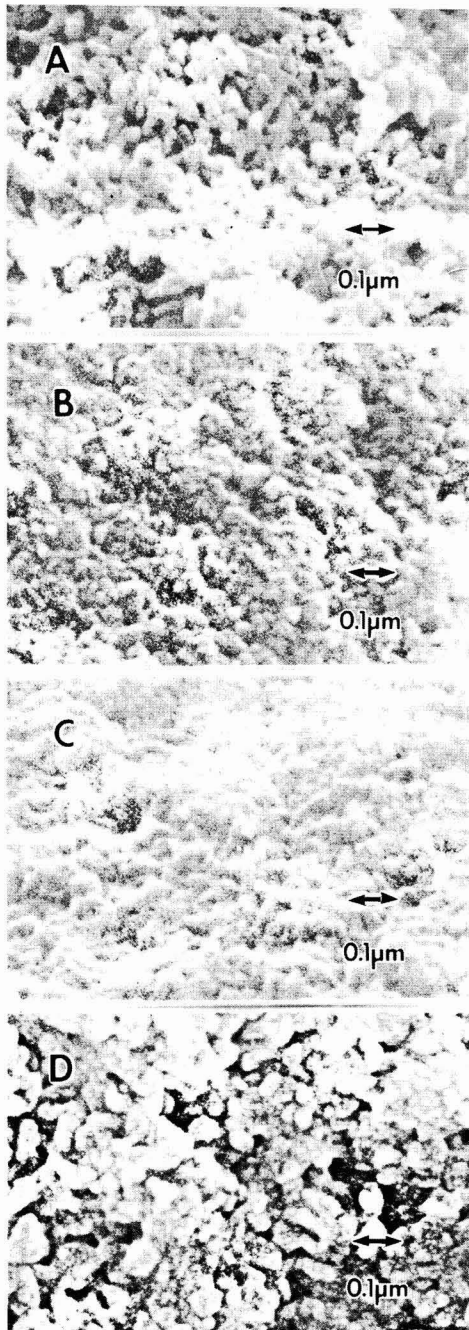


Fig. 3. SEM photographs of starting powder and fracture surfaces of densified calcium-deficient hydroxapatites. A; starting powder, B; evacuated at 150°C, densified at 150°C, 600MPa, specimen No.N2-1p, C; evacuated at 300°C, densified at 500°C, 600MPa, specimen No.2-5, D; evacuated at 28°C, densified at 400°C, 600MPa, specimen No.N2-19.

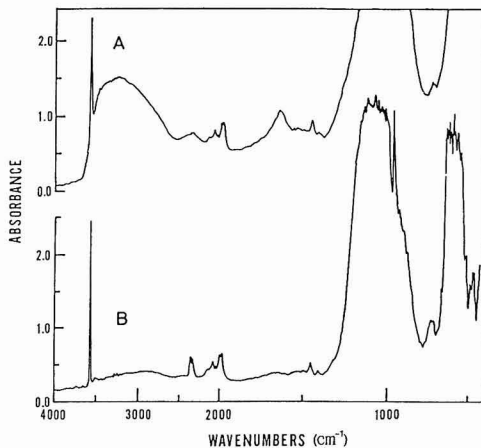


Fig. 4. Infrared absorption spectra of specimens. A; specimen No.N2-3, evacuated at 130°C, B; specimen No.N2-13, evacuated at 500°C.

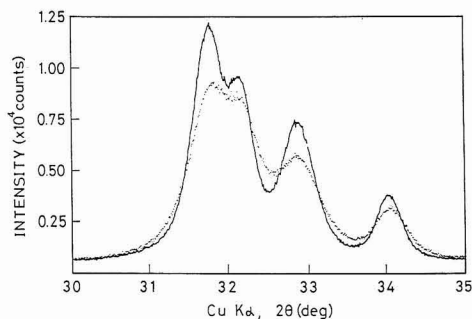


Fig. 5. X-ray diffraction patterns, Dotted line; the starting powder (Ca/P=1.55), solid line; densified at 300°C, 600MPa, specimen No.N2-3.

3-4. Flexural Strength

The flexural strengths of the specimens, N2-7 and N2-11 were compared; the former was characterized by a relatively high crystal water content of 0.55, and the low densification temperature, and the latter by a high dryness (crystal water content: 0.10) and density of 3.11g/cm³ which was the highest among the densified samples, resulting from the high densification temperature. The results are shown in a Weibull plot (Fig. 6). The former had an average strength $\sigma_B = 65.7 \pm 6.4$ MPa and the latter $\sigma_B = 60.1 \pm 7.9$ MPa. These levels are lower than one-third of the reported values for sintered hydroxyapatite of the stoichiometric composition. These samples (Fig. 6) had Weibull coefficients *m* of 8.4 and 7, respectively.

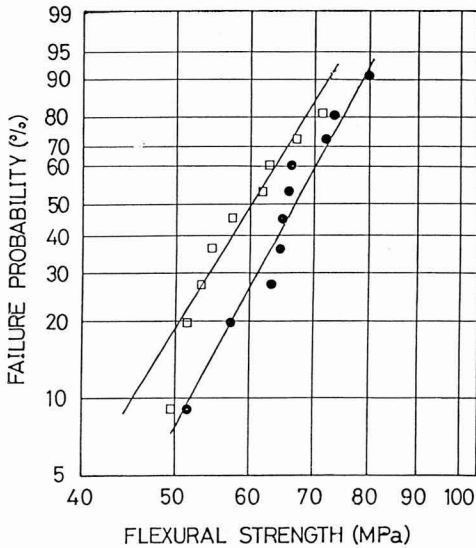


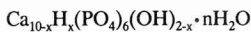
Fig. 6. Weibull plots of the bending test. \square ; specimen No.N2-7, evacuated at 200°C, densified at 300°C, 600MPa, \bullet ; specimen No.N2-11, evacuated at 300°C, densified at 500°C, 600MPa.

It is noted that the specimen N2-11 was weaker than the specimen N2-7, in spite of the higher dryness and density of the former.

4. Discussion

4-1. Measurement and Control of Crystal Water

A number of studies have been made on the structure of calcium-deficient hydroxyapatites, and various models have been proposed for it.³⁾ In this study, crystal water content n was used as an index, based on the generally accepted composition.



The densification process of calcium-deficient hydroxyapatite at a relatively low temperature can be considered in connection with the presence of water, which distinguishes calcium-deficient hydroxyapatite from hydroxyapatite of the stoichiometric composition.

If the densification process is affected by water present in the sample, what will result when it is sufficiently dried to lose crystal water?

In order to discuss the relationship between densification and water content, it is necessary to investigate the quantity of water chemically bonded to the apatite crystal structure, which is then released by heating. However there is no structural analysis re-

ported of single crystals of calcium-deficient hydroxyapatite. Nor by means of the thermal or spectral analyses, there is no established theory regarding water content in the crystalline structures,⁴⁻¹⁰⁾ because the crystal grains are too small to allow easy separation of adsorbed water from crystal water, and because the properties of calcium-deficient hydroxyapatite differ, depending on the method by which it is prepared. Therefore, attempts were made, in this study, to determine the crystal water content for the calcium-deficient hydroxyapatite prepared.

Figure 7 shows the weight loss of the Ca/P=1.55 sample. Dried nitrogen gas flow prepared by evaporating liquid nitrogen was used as the atmosphere. 10g of the hydroxyapatite powder sample was placed in a 25mm-diameter, 125mm-high platinum container, and was hanging from a chemical balance.

The weight of the powder sample was measured at intervals of several hours, while keeping its temperature constant. After keeping the sample at a constant temperature for 20hrs, the weight became constant within an error of 1mg in several hours. The apparently constant weights of the samples at respective temperatures are illustrated in Fig. 7. It should be noted, however, that the weight loss still continued, though very slowly, beyond the apparently constant weight point. This loss was not negligible after a couple of days. It was also found that the water content of the sample powder which was dried by heating it up to 200°C was reabsorbed when the sample was allowed to stand in air at room temperature for about 30 days. This shows that the release and absorption of moisture are reversible, at least up to 200°C.

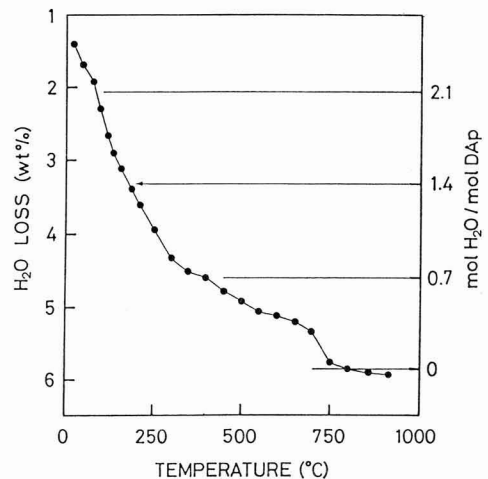


Fig. 7. Weight loss in dry nitrogen gas flow of starting powder (Ca/P = 1.55, $x=0.7$). The powder was kept for about 20hrs until weight become practically constant at every temperature plotted.

When the sample was kept at 800°C, the phase separation into two phases, tricalcium phosphate and stoichiometric hydroxyapatite took place. This phase separation was observed by means of powder X-ray diffraction. This "phase separated" specimen was taken as standard by its weight in the right-side axis of the ordinate in Fig. 7. This axis represents molar water released from the sample. When Ca/P = 1.55, x is equal to 0.7. In Fig. 7, the curve shows changes in its feature at intervals of 0.7 of molar water released.

The sample heated at near 500°C consisted of hydroxyapatite only by powder X-ray diffraction, indicating that the sample lost water but the crystalline structure of hydroxyapatite was intact up to 500°C.

The water content therefore became essentially constant when the powdered apatite sample was kept at a constant temperature under a reduced partial pressure of water in the atmosphere. The results shown in Fig. 7 represent the equilibrium relationship between water content and temperature. This was used to control the water content of the calcium-deficient hydroxyapatite powder in the capsule by keeping it under a vacuum at a temperature in a range from room temperature to 500°C.

4-2. Stoichiometric and Calcium-Deficient Hydroxyapatites

The densification of calcium-deficient hydroxyapatite was greatly affected by the presence of crystal water. Is the difference in densification behaviors between stoichiometric hydroxyapatite and calcium-deficient hydroxyapatite due to the presence of crystal water only?

The specimen N2-11 with $n = 0.10$, which was dried as far as possible under the conditions employed in this study, was densified to a transparent body at 500°C and 600MPa. On the other hand, at least 800°C was required to make stoichiometric hydroxyapatite transparent under the same pressure.

A similar difference was observed in the upper limits of temperature when forming samples that disintegrated. Stoichiometric hydroxyapatite collapsed spontaneously, when treated at 500°C for 4.5h, as shown in Table 2. The Ca/P=1.55 sample densified at 300°C for 5h disintegrated spontaneously, so long as it was sufficiently dried in a well-evacuated system. Thus, there was a difference of about 200° in the upper limit of treatment temperature that caused spontaneous breakage.

Calcium-deficient hydroxyapatite was therefore found to be easier to densify, even when essentially completely dried, than stoichiometric hydroxyapatite. It is considered that a calcium deficiency in the crystalline structures changes the mechanical properties of the crystalline or the system structures, e.g., causing the crystal grains to be more liable to plastic deformation.

4-3. Disintegration of Samples

All of the three types of apatite with different Ca/P ratios disintegrated spontaneously, after having been treated under pressure, as shown in Table 2. Such a phenomenon has not been previously discussed. The authors considered at first that it was caused by compressed gas contained in the sample.

The spontaneous breakage of the samples was repeatable under the same conditions (temperature, pressure and holding time). This phenomenon was also observed with the samples which were not densified to the stage of the formation of closed pore. A high-pressure gas, if contained in the sample, should cause the sample weight to change when it is released from the sample. However, no such weight change was observed in this study.

Next, it was assumed that stress and associated elastic deformation were present in a spontaneously breaking sample, and the stress was released by the breakage. In order to confirm this, additional thermal tests were carried out. A high-pressure gas, if contained in a sample, should reduce the strength of the sample as the temperature is increased, and eventually destroy it by thermal expansion. Elastic deformation caused by a residual stress, on the other hand, will be released at higher temperatures, and the sample will be less liable to breakage.

Samples of the spontaneously breaking specimen N2-1p no longer disintegrated when kept at 150°C in a drier.

The spontaneously broken specimens were obtained when the starting powders were treated at low temperatures, or shorter durations of the treatment under high pressures. It must be pointed out that every specimen broken spontaneously was insufficiently densified. In other words, these specimens retained pores in their texture and withstood an external pressure of 60 to 80kg/mm² during their treatment.

Possibly the crystal grains of the sample were deformed plastically to form defective lattices. These largely remained in the structures, because the temperature and holding time were insufficient to repair them by diffusion, as a result of which the grains were altered.

Spontaneous breakage was not caused by release of external pressure only. Water in the air is related to the spontaneous breakage because the breakage started from the faces in contact with air. Undoubtedly, water accelerates the spontaneous breakage because the sample was rapidly destroyed when put in water. Water can be considered to repair defective lattices in the altered grains, but the role of water molecules in the mechanism of the spontaneous breakage is speculative.

4-4. Density

Dense specimens, which are pore free showed different densities, as shown in Table 2. For example, the density of the apparently transparent N2-2 was 3.05g/cm³, which was lower by 0.06g/cm³ than that of N2-5 (3.11g/cm³), which also seemed to be pore free.

Few researchers have discussed the lattice parameters of calcium-deficient hydroxyapatite. Table 3 shows the lattice parameters of tooth enamel,¹³ and of apatite in equilibrium with monetite or Ca₂P₂O₇ by Skinner.¹⁴ The Ca/P ratio of the tooth enamel differs according to the researchers; 1.62±0.08 by Weatherell and Robinson,¹³ 1.58 by Little and Casciani,¹⁶ and 1.48 to 1.67 by Brudevold and Soremark.¹⁷ Accordingly, tooth enamel is considered to be calcium-deficient hydroxyapatite.

According to the results shown in Table 3, apatite in

Table 3. Unit cell dimensions of hydroxyapatites (in Angstrom).

Specimen Type	Lattice parameters		References	
	a	c		
Tooth enamel	9.441	6.884	Trautz (1955) ^{1,3)}	
	9.440	6.881	Carlstrom(1955) ^{1,3)}	
	9.450	6.879	Glass and Ommel(1960) ^{1,3)}	
	9.442	6.883	Glass(1962) ^{1,3)}	
	9.440	6.872	Holcomb and Young(1980) ^{1,8)}	
Hydroxyapatite synthetic	9.420	6.881	Trautz(1955) ^{1,3)}	
	9.420	6.881	Carlstrom(1955) ^{1,3)}	
	9.420	6.881	Trombe(1970) ^{1,3)}	
	+ portlandite (300°C)	9.421	6.882	Skinner(1973) ^{1,4)}
	+ monetite (300°C)	9.417	6.879	Skinner(1973) ^{1,4)}
	+ monetite (300°C)	9.419	6.881	Skinner(1973) ^{1,4)}
	+ Ca ₂ P ₂ O ₇ (400°C)	9.419	6.881	Skinner(1973) ^{1,4)}
	+ Ca ₂ P ₂ O ₇ (400°C)	9.420	6.880	Skinner(1973) ^{1,4)}
	+ Ca ₂ P ₂ O ₇ (500°C)	9.424	6.887	Skinner(1973) ^{1,4)}
	+ Ca ₂ P ₂ O ₇ (500°C)	9.423	6.882	Skinner(1973) ^{1,4)}
Capsule No. N2-3	9.425	6.880	this work	
Capsule No. N2-11	9.410	6.882	this work	

tooth enamel has an a-axis parameter about 0.2% higher than stoichiometric hydroxyapatite and has almost the same c-axis parameter.

The lattice parameters of the specimens N2-3 and N2-11 prepared in this study were calculated by Applemann's program,¹⁸⁾ assuming that they were hexagonal. The results converged satisfactorily, indicating that the above assumption was valid. The lattice parameters of these systems also changed little.

The density was estimated from the lattice parameters and molecular formula, and was compared with that measured by the Archimedeian method using water.

The estimated densities, from lattice parameters and formulae, of the specimens N2-3 and N2-11 were 3.078 ± 0.013 g/cm³ and 3.043 ± 0.013 g/cm³, respectively.

The bulk density, on the other hand, of the specimens N2-3 and N2-11 were determined to be 3.052 ± 0.002 g/cm³ and 3.109 ± 0.002 g/cm³, respectively.

The differences between these values are larger than the experimental error of the measurement.

The cause of this discrepancy is not well understood at the present stage of investigation. It should be noted that X-ray diffraction gave information about the thin layer extending 100 μ m from the surface. This layer was considered to absorb moisture in air, to have a crystal water number *n* close to the equilibrium level at room temperature and above unity. The density estimated by X-ray diffraction, therefore, may not correlate well with the bulk density for a volume of several cm³. There are many other possible reasons for the discrepancy, e.g., the presence of residual strains.

5. Conclusions

Well-dried, calcium-deficient hydroxyapatite powders

were densified under elevated pressure and temperature, without changing their chemical compositions and crystalline structures, to produce transparent samples.

1) The temperature and pressure conditions to satisfactorily densify the powders varied, depending on their Ca/P ratios. The temperature levels required for the densification were 300°C under 600MPa for the sample of Ca/P=1.55, and 400°C under the same pressure for the sample of Ca/P=1.60.

2) The temperature and pressure conditions for satisfactory densification were also dependent on the dryness of the starting samples. At least 500°C was required under 600MPa for the sample of Ca/P=1.55, which lost more than half of its crystal water.

3) The samples pressed at a temperature too low to densify disintegrated gradually, when allowed to stand in air, even in the absence of an external force.

Acknowledgments

The authors thank Dr. Hideki Monmma for his valuable advice, Dr. Hidehiko Tanaka for his cooperation in the measurement of flexural strength, Dr. Mitsuko Onoda for her cooperation in the measurement and correction of lattice parameters, Mr. Toshiaki Wada for his cooperation in the measurement of lattice parameters, Mr. Masataka Tsutsumi for his cooperation in the taking of SEM photographs, and Messrs. Akira Tanaka and Yasuji Nakaso of Central Glass Co., Ltd. for the production of the apatite powders with such troublesome specifications.

This study was financially supported by the fund for "Research in Biofunctional Ceramics," one of the special research programs of the National Institute for Research in Inorganic Materials.

References:

- 1) R.A. Young, *Clinical Orthopaedics and Related Research*, 113, 249-62 (1975).
- 2) R.A. Young, *Congres des Composes Phosphores*, 98, 980-92 (1980).
- 3) A.S. Posner, *Physiological Reviews*, 49, 760-92 (1969).
- 4) E.E. Berry, *J. Inorg. Nucl. Chem.*, 29, 317-327 (1967).
- 5) C.W. Anderson, R.A. Beebe, J.S. Kittelberger, *J. Phys. Chem.*, 78, 1631-1635 (1974).
- 6) H. Monmma, T. Kanazawa, *Yogyo-Kyokai-shi*, 84, 209-213 (1976).
- 7) S.S. Barton, B.H. Harrison, *J. Colloid Inter. Sci.*, 55, 409-414 (1976).
- 8) H. Monmma, S. Ueno, M. Tsutsumi and T. Kanazawa, *Yogyo-Kyokai-shi*, 86, 590-596 (1978).
- 9) H. Monmma and S. Ueno, *Seikko to Sekkai*, 159, 7-12 (1979).
- 10) H. Monmma, J. Tanaka and S. Ueno, *ibid.*, 165, 16-22 (1980).
- 11) K. Hirota, Report No.43, The Science and Technology Agency's National Institute for Research in Inorganic Materials, 85-7 (1985).
- 12) Y. Iwasaki, M. Akatsu and K. Hirota, *Atsuryoku Gijutsu*, 25, 36-44 (1987).
- 13) G. Montel, *Bull. Soc. Fr. Mineral. Cristallogr.* 94, 300-13 (1971).
- 14) H.C.W. Skinner, *Am. J. Sci.*, 273, 545-60 (1973).
- 15) J.A. Weatherell, and C. Robinson "Biological Mineralization" Ed. I. Zipkin, John Wiley, 43-74 (1973).
- 16) M.F. Little and F.S. Casciani, *Arch. Oral. Biol.*, 11, 565 (1966).

- 17) F. Brudevold and R. Soremark "Structural and Chemical Organization of Teeth" Vol.2, Ed. A.E.W. Miles, Academic Press, N.Y. 247-77 (1967).
- 18) D.W. Holcomb, and R.A. Young, *Calcif. Tissue Int.* 31, 189-201 (1980).
- 19) D.E. Appleman and H.T. Evans Jr., U.S. Geological Survey,

Computer Contributions, 20, Job 9214, NTIS Document PB2-16188 (1973).

This article is a full translation of the article which appeared in *Nippon Seramikkusu Kyokai Gakujutsu Ronbunshi* (Japanese version), Vol.98, No.3, 1990.

Synthesis of Tantalum Boride Powder by Solid State Reaction and Its Sintering

Hideaki Itoh, Yusuke Satoh, Satoshi Kodama and Shigeharu Naka

Faculty of Engineering, Nagoya University
Furo-cho, Chikusa-ku, Nagoya 464-01, Japan

Tantalum boride powders were synthesized by the solid state reaction between tantalum and amorphous boron. Five boride phases (Ta_2B , Ta_3B_2 , TaB , Ta_3B_4 and TaB_2) were formed by heat-treatment of the mixed powders at 1000 - 1800°C for 0 - 120 min. Formation behavior of these borides was dependent on the heat-treatment temperature, in which structurally stable phases formed in order from low to high temperatures. Single phases of TaB_2 , TaB and Ta_3B_4 were obtained by the heat-treatment of the mixed powders with corresponding stoichiometric compositions at 800°, 900° and 1800°C, respectively. Sintered compacts of TaB and TaB_{2+x} were prepared by a high-pressure sintering of synthesized TaB and TaB_{2+x} powders at 4GPa and 1600°C for 15 min. The bulk density of TaB was 13.51g/cm³ (relative density: 95.1%) and the Vickers microhardness was 2550kg/mm². The homogeneous range of the solid solution TaB_{2+x} was $0 < x < 0.55$, the density and the microhardness of which increased with increasing amount of boron in solid solutions.

[Received August 25, 1989; Accepted November 22, 1989]

Key-words: Tantalum boride, Solid state reaction, High pressure sintering, Amorphous boron

1. Introduction

Transition metal borides are expected to have uses as wear- and corrosion-resistant materials or electrode materials because of their high hardness, melting point, and electrical conductivity.¹⁻³⁾ Materials of this kind, however, are difficult to sinter. To overcome this problem, methods have been developed to synthesize high-purity and active boride powders that are suitable for sintering⁴⁻⁸⁾ and to sinter the boride powders containing some sintering aid under high pressure.⁹⁻¹⁵⁾

In the Ta-B system, the presence of five phases, Ta_2B , Ta_3B_2 , TaB , Ta_3B_4 and TaB_2 , has been reported.^{1,16-18)} Of these phases, TaB and TaB_2 have relatively stable structures. The TaB structure is of the rhombic system, having a melting point of 2450°C and a microhardness (Hv) of 3130kg/mm², while the structure of TaB_2 belongs to the hexagonal system, having a relatively wide solid solution range, a melting point of 3070°C (the highest among the five boride phases) and a microhardness of 2500kg/mm², according to the literature.^{1,16)} For the synthesis of tantalum borides by the solid state reaction, the direct reaction between a metal and boron and the thermal reduction of metal oxides have been studied^{9,19-20)}; however, only a few reports have been published on the synthesis by the solid state

reaction at relatively low temperatures below 1500°C. Also, the properties of single-phase sintered compacts containing no secondary phase have not been discussed.

In the present study, various boride powders were synthesized by the solid state reaction between metallic tantalum and amorphous boron, and in particular, single phase powders of TaB , Ta_3B_4 and TaB_2 were prepared by investigating the formation process. The solid solution range of B in TaB_{2+x} was determined. Also, TaB and TaB_{2+x} powders were sintered at high pressure and high temperature to evaluate the sintering properties of the synthesized powders and the density and hardness of the sintered bodies.

2. Experimental

2-1. Synthesis of Tantalum Boride Powders

The starting materials used for this experiment were tantalum powder (particle size: 5-10 μ m, purity: > 99wt%) and amorphous boron powder (particle size: about 0.9 μ m, purity: > 96.6wt%). The powders were independently degassed in a vacuum of 5×10^{-5} torr at 600°C for 60 minutes. Then, the powders were mixed in an agate mortar to achieve the required atomic ratio (B/Ta) of 0 - 3.0. To obtain a mixed powder of a given composition, the composition was determined by using the net amount of boron in the as-received boron powder. The mixed powder was pretreated in a vacuum at 500° - 600°C for 60 minutes, and then re-mixed in a nitrogen gas flow. The pretreated powder was heat-treated in an argon flow at 600° - 1500°C for 0 - 120 minutes. To measure the lattice constants of TaB_{2+x} , the sample was ground and mixed after the treatment at 1500°C for 60 minutes to ensure homogeneity in the synthesized powder, and then heat-treated again at 1500°C for 60 minutes.

2-2. Analysis and Observation of Synthesized Powders

The phases formed in the treated sample were identified by powder X-ray diffraction, and the lattice constant of each phase was measured with silicon as the internal standard. The content and crystallinity of the boride were evaluated by the relative intensity (I/I_S). The diffraction lines used for measurements were 110 for tantalum, 211 for Ta_2B , 201 for Ta_3B_2 , 021 for TaB , 110 for Ta_3B_4 , and 101 for TaB_2 . The diffraction line intensities were corrected by the 200 diffraction line intensity of silicon. ICP emission spectrum analysis was used to check that the mixing ratio was unchanged before and after heat treatment. The particle size and shape of the treated powder were observed with a

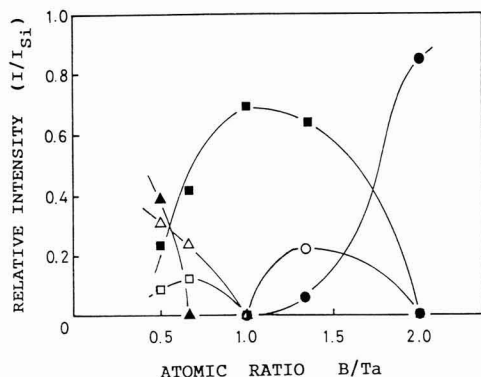


Fig. 1. Relationship between the relative intensity of tantalum boride and the atomic ratio B/Ta. Treatment conditions: $(1400^{\circ}\text{C} \times 60 \text{ min}) \times 2$, Δ : Ta, \blacktriangle : Ta_2B , \square : Ta_3B_2 , \blacksquare : TaB, \circ : Ta_3B_4 , \bullet : TaB_2 .

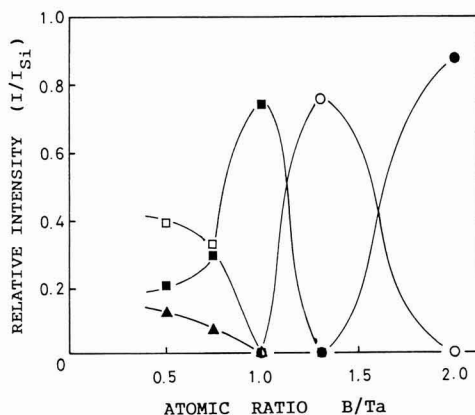


Fig. 2. Relationship between the relative intensity of tantalum boride and the atomic ratio B/Ta. Treatment conditions: $1800^{\circ}\text{C} \times 60 \text{ min}$, \blacktriangle : Ta_2B , \square : Ta_3B_2 , \blacksquare : TaB, \circ : Ta_3B_4 , \bullet : TaB_2 .

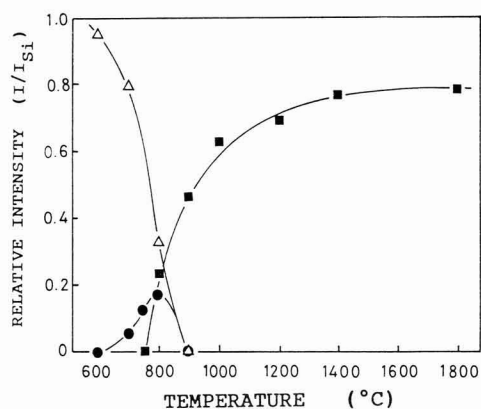


Fig. 3. Variations of relative intensity of formed species as a function of treatment temperature. Starting powder composition: B/Ta=1.0, Treatment time: 60 min, Δ : Ta, \blacksquare : TaB, \bullet : TaB_2 .

scanning electron microscope (SEM).

2-3. Preparation and Evaluation of Sintered Compacts

The synthesized single phase powder was sintered at 4GPa and 1600°C for 15 minutes by using a girdle-type high pressure apparatus.²¹⁾ The microstructure of the sintered compact was observed with a SEM, the density was measured by the Archimedes' method, and the Vickers microhardness was measured under a 200kg load.

3. Results and Discussion

3-1. Formation Behavior of Tantalum Borides

The formation process of tantalum boride was studied at various temperatures by varying the atomic ratio of amorphous boron to tantalum (B/Ta) from 0.5 to 2.0. By heat treatment at 1000°C for 60 minutes, only TaB and TaB_2 , which were structurally stable, formed throughout the composition range, but the other phases did not. Single phase boride powders were obtained from powder mixtures with the corresponding stoichiometric composition.

Figure 1 shows the relationship between the relative intensity and the atomic ratio (B/Ta) for tantalum borides subjected to double heat treatment at 1400°C for 60 minutes. In this way, Ta_2B , Ta_3B_2 , TaB, Ta_3B_4 and TaB_2 were formed. The single phase powders of TaB and TaB_2 with stoichiometric compositions were obtained from the powder mixtures of B/Ta=1.0 and B/Ta=2.0, respectively, but single phases of other borides (Ta_2B , Ta_3B_2 and Ta_3B_4) were not obtained.

Figure 2 shows the relationship between the relative intensity and the atomic ratio (B/Ta) for tantalum borides heat-treated at 1800°C for 60 minutes. The formation behavior is similar to that of borides heat-treated at 1400°C . For Ta_3B_4 , the relative intensity is high, and single phase powder was obtained from the sample with the stoichiometric composition.

The above results indicate that the formation behavior of tantalum borides is dependent on the heat treatment temperature and that structurally stable phases form in order from low to high temperature.

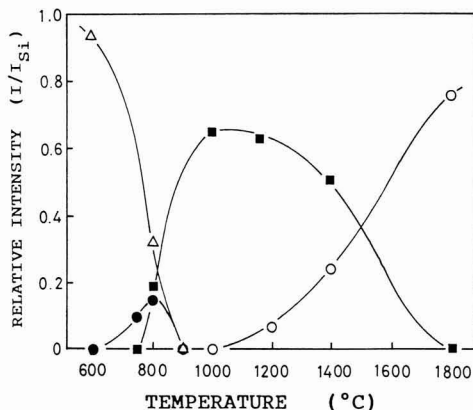


Fig. 4. Variations of relative intensity of formed species as a function of treatment temperature. Starting powder composition: B/Ta=1.3, Treatment time: 60 min, Δ : Ta, \blacksquare : TaB, \circ : Ta₃B₄, \bullet : TaB₂.

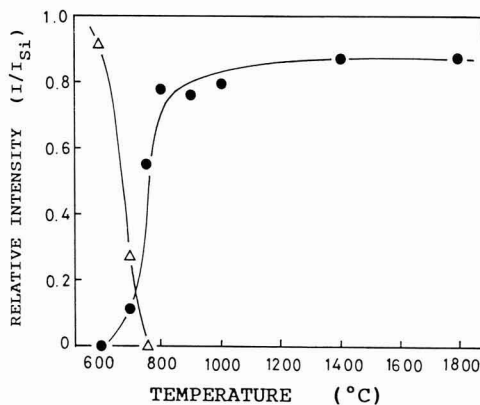


Fig. 5. Variations of relative intensity of formed species as a function of treatment temperature. Starting powder composition: B/Ta=2.0, Treatment time: 60 min, Δ : Ta, \bullet : TaB₂.

This formation behavior is very similar to that of niobium borides⁶⁾ synthesized by the solid state reaction.

3-2. Effect of Heat Treatment Temperature on Formation of Single Phase Powders

The effect of heat treatment temperature on the powder mixtures of B/Ta=1.0, 1.3 and 2.0 with the stoichiometric compositions of TaB, Ta₃B₄ and TaB₂ was investigated. Single phase powders were obtained by heat treatment at 1800°C. The treatment time was set to 60 minutes since there was little effect of heat treatment time on the products formed in the range of 60 to 120 minutes.

Figure 3 shows the relative intensity of the X-ray diffraction line as a function of treatment temperature for tantalum borides formed when the starting powder of B/Ta=1.0 was heat-treated at 600°-1800°C for 60 minutes. At 600°C, only the diffraction line of tantalum was observed. At 700°C, the formation of TaB₂ was observed. With an increase in treatment temperature, the relative intensity of tantalum decreased, while that of TaB₂ increased. Above 800°C, TaB formed, and the relative intensity of TaB₂ decreased. At 900°C, the crystalline phase of TaB only was obtained. At high temperatures above 900°C, the relative intensity of TaB increased gradually, the crystallinity being improved, and leveled off above 1400°C.

Figure 4 shows the relative intensity as a function of treatment temperature for tantalum borides formed from the starting powder of B/Ta=1.3. TaB₂ formed at 750°C, and TaB formed at 800°C. After that, Ta₃B₄ began to form at 1200°C. With an increase in treatment temperature, the relative intensity of TaB decreased, while that of Ta₃B₄ increased. High-temperature treatment at 1800°C was necessary to obtain the crystalline phase of Ta₃B₄ only.

Figure 5 shows relative intensity as a function of treatment temperature for tantalum borides formed from the starting powder of B/Ta=2.0. The starting temperature for the formation of TaB₂ was 700°C. With an increase in treatment temperature, the relative intensity of tantalum decreased, while that of TaB₂ increased; at 750°C, the single phase of TaB₂ had already formed.

As seen from Figs. 3-5, TaB₂ is formed from powders of any composition at low temperatures between 650° and 800°C, but with increasing temperature, a single phase stoichiometric compound corresponding to the powder composition, such as TaB or Ta₃B₄, forms. The formation of TaB₂, a compound with the greatest boron content of the tantalum borides occurs, at relatively low temperatures because of the high stability of diborides, as with the other transition metal borides.^{2,3,10)}

3-3. Homogeneous Range of TaB_{2+x} Solid Solution

It is well known that tantalum diborides have a relatively wide solid solution range for boron. Therefore, the lattice constant was measured by varying the atomic ratio (B/Ta) from 1.9 to 2.9. Figure 6 shows the relationship between the lattice constants on the a- and c-axes of the TaB_{2+x} powder formed by double heat treatment at 1500°C for 60 minutes and the atomic ratio (B/Ta) of the starting powder. The lattice constants vary linearly when B/Ta is above 2.0, which suggests that the homogeneous range of TaB_{2+x} solid solution lies at x=0-0.55. The upper limit agrees nearly with those in the literature.^{16,18-20)} The literature reports the lower limits of 1.5 to 1.8, but in this experiment homogeneity was not observed with excess tantalum. The lattice constants at the lower limit of the uniform region were estimated to be a=3.097 and c=3.232, and those at the upper limit to be a=3.063 and c=3.289. These constants nearly agree with those presented in

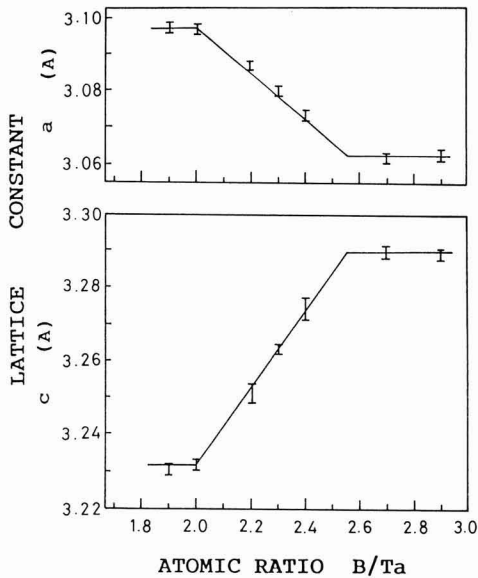


Fig. 6. Lattice constant of the synthesized TaB_{2+x} powder vs. the atomic ratio (B/Ta) of starting powder. Treatment conditions: $(1500^{\circ}C \times 60 \text{ min}) \times 2$.

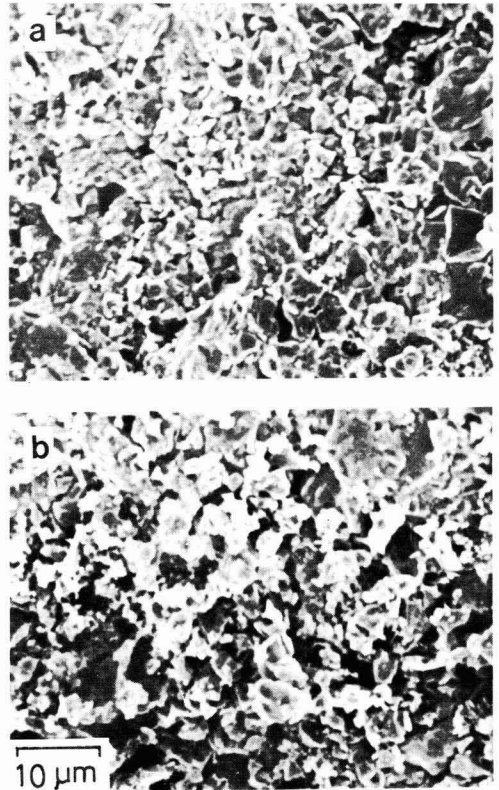


Fig. 7. SEM of the fractured surface of the TaB_{2+x} compacts sintered at 4GPa and $1600^{\circ}C$ for 15 min. (a) B/Ta=2.0, (b) B/Ta=2.3, Synthetic conditions of the TaB_{2+x} powder: $(1500^{\circ}C \times 60 \text{ min}) \times 2$.

the literature.^{19,20,22} The figure indicates that with increasing atomic ratio, the length of the a-axis decreases, while that of the c-axis increases within the solid solution range. This suggests that since stoichiometric TaB_2 belongs to the hexagonal system, excess boron atoms enter the $(0, 0, 1/2)$ position of the crystal lattice, forming a solid solution.^{3,14}

3-4. Sintering Properties of Synthesized TaB and TaB_{2+x} Powders

The particle size and shape of single phase powders of synthesized TaB and TaB_{2+x} were nearly the same as those of the starting tantalum powder; no aggregation or grain growth were observed. Borides may have been formed by the diffusion of boron to metallic tantalum.

Single phase TaB bodies were prepared by sintering the following two powders at 4GPa and $1600^{\circ}C$ for 15 minutes: (a) single-phase synthesized TaB powder and (b) the powder with $(TaB+0.1B)+0.1Ta$ composition, prepared by adding metallic tantalum powder of 10mol% to the powder $(TaB+0.1B)$ synthesized with 10mol% excess boron. The sintered body of sample (b) had lower porosity than sample (a), with a density of $13.51g/cm^3$ (relative density: 95.1%) and a microhardness of $2550kg/mm^2$. The X-ray diffraction of sintered bodies did not detect tantalum, the diffraction line of TaB only being observed. The reaction between free amorphous boron and added tantalum might have caused higher densification.^{5,6}

Figure 7 shows the SEM photographs of the fractured surfaces of TaB_{2+x} compacts obtained by sintering TaB_{2+x} solid solution powders with compositions of B/Ta=2.0 and B/Ta=2.3 at 4GPa and $1600^{\circ}C$ for 15 minutes. No abnormal grain growth was observed in these photographs, with only homogeneous microstructures. The TaB_2 compact with the stoichiometric composition had a density of $10.64g/cm^3$ and a microhardness of $1050kg/mm^2$. As the degree of the solid solution of boron increased, the density and microhardness increased. This is probably because the presence of excess boron atoms strengthens the planar network structure of boron atoms, resulting in increased microhardness.^{18,19} Since the relative density of these single phase bodies is still low, at 85 - 90%, the methods for synthesizing finer boride powders and the

sintering conditions should be improved to increase the sintering density.

4. Conclusions

Tantalum boride powders were synthesized by the solid state reaction between metallic tantalum and amorphous boron, and the single phase powders synthesized were sintered under high pressure. The conclusions from the experiments are as follows:

- 1) Ta_2B , Ta_3B_2 , TaB , Ta_3B_4 and TaB_2 were formed by the solid state reaction at 1000° - 1800°C for 60 minutes. The formation behavior of these borides was greatly dependent on the heat treatment temperature, and structurally stable phases were formed in order from low to high temperature.
- 2) Single phase TaB_2 , TaB and Ta_3B_4 powders were obtained by heat-treating the powder with the corresponding stoichiometric composition at 800°C, 900°C and 1800°C, respectively. The homogeneous range of the solid solution of TaB_{2+x} was $0 < x < 0.55$.
- 3) A single-phase sintered compact of TaB with a density of 13.51g/cm³ (relative density: 95.1%) and a microhardness of 2550kg/mm² was obtained by high-pressure sintering of synthesized TaB powder at 4GPa and 1600°C for 15 minutes. When the TaB_{2+x} solid solution was sintered under the same sintering conditions, the density and microhardness increased with an increased boron content in solid solution.

References:

- 1) G.V. Samsonov and I.M. Minitskii, "Handbook of Refractory Compounds," IFI/Prenum (1980).
- 2) V.I. Matkovich Ed., "Boron and Refractory Boride," Springer-Verlag (1977) pp. 351-376.
- 3) K. Nakamura, *Ceramics*, 24, 500-508 (1988).
- 4) T. Matsudaira, H. Itoh, S. Naka, H. Hamamoto and M. Obayashi, *J. Mater. Sci.*, 23, 288-292 (1988).

- 5) H. Itoh, S. Naka, T. Matsudaira and H. Hamamoto, *J. Mater. Sci.*, 24, 420-424 (1989).
- 6) T. Matsudaira, H. Itoh, S. Naka and H. Hamamoto, *J. Less-Common Metals*, 115, 207-214 (1989).
- 7) H. Itoh, T. Matsudaira, S. Naka, H. Hamamoto and M. Obayashi, *J. Mater. Sci.*, 22, 2811-2815 (1987).
- 8) H. Hamamoto, M. Obayashi, T. Matsudaira, H. Itoh and S. Naka, *Journal of the Japan Society of Powder and Powder Metallurgy*, 35, 128-130 (1988).
- 9) V.I. Matkovich Ed., "Boron and Refractory Boride," Springer-Verlag (1977) pp. 457-493.
- 10) T. Watanabe and Y. Tokunaga, *Bulletin of the Japan Institute of Metals*, 25, 1018-1025 (1986).
- 11) T. Watanabe, *Journal of the Japan Society of Powder and Powder Metallurgy*, 36, 365-370 (1989).
- 12) K. Sakai, *Ceramics*, 24, 526-532 (1989).
- 13) H. Nishikawa, *Ceramics*, 22, 40-45 (1987).
- 14) Y. Miyamoto, E. Kamijo and M. Koizumi, *Journal of the Japan Society of Powder and Powder Metallurgy*, 34, 101-106 (1987).
- 15) O. Odawara, *Ceramics*, 24, 509-514 (1989).
- 16) H. Nowotny, F. Benesovsky and R. Kieffer, *Z. Metallk.*, 50, 417-423 (1959).
- 17) T.V. Massalski, "Binary Alloy Phase Diagram," *Am. Soc. Metals* (1986) p. 386.
- 18) Р. Б. КОТЕЛЬНИКОВ, С. Н. БАШЛЫКОВ, Э. Г. ГАЛИАКБАРОВ и А. И. КАШТАНОВ, "Особые Тугоплавкие Элементы и соединения" Издательство «Металлургия» (1969).
- 19) R. Kiessling, *Acta Chem. Scand.*, 3, 603-615 (1949).
- 20) L. Brewer, D.L. Sawyer, D.H. Templeton and C.H. Dauben, *J. Am. Ceram. Soc.*, 34, 173-179 (1951).
- 21) T. Matsudaira, H. Itoh, S. Naka, H. Hamamoto and M. Obayashi, *Yogyo-Kyokai-shi*, 95, 248-252 (1987).
- 22) S. Okada, T. Atoda and Y. Takahashi, *J. Chem. Soc. Japan*, 1535-1543 (1985).

This article is a full translation of the article which appeared in *Nippon Seramikkusu Kyokai Gakujutsu Ronbunshi* (Japanese version), Vol.98, No.3, 1990.

Effect of Alkoxide Grinding Aids and Their Reaction Mechanisms

Masaki Yasuoka¹, Tsuyoshi Hayashi, Kiyoshi Okada and Nozomu Otsuka

Dept. of Inorganic Materials, Faculty of Engineering, Tokyo Institute of Technology

12-1, O-okayama 2-chome, Meguro-ku, Tokyo 152, Japan

[†] Now with Government Industrial Research Institute, Nagoya

1, Hirate-cho 1-chome, Kita-ku, Nagoya, Aichi 462, Japan

Effect of metal alkoxides as grinding aids in grinding of electrofused alumina powders and the reaction mechanisms were investigated. Dry grinding experiments with and without grinding aids were made using a vibration mill up to 320h. Particle size distribution and specific surface area of powders were measured to estimate the degree of grinding. The degree of dispersion-cohesion of ground powders was evaluated from an angle of repose and particle shape observation by SEM. Surface tension of metal alkoxide liquids and contact angle between metal alkoxide liquids and sintered alumina surface were also measured. Addition of grinding aids caused acceleration of grinding and dispersion for their ground powders. The following two major reasons were considered for these effects. (1) Surface tension of metal alkoxide liquid is smaller than that of water. (2) Hydrolysis of alkoxide excludes water, which tends to cause cohesion of powders, and also forms butyl alcohol which acts as grinding aid itself.

[Received September 20, 1989; Accepted December 11, 1989]

Key-words: Grinding aid, Alkoxide, Dry grinding process, Surface tension, Dispersion, Alumina

1. Introduction

Ceramic powders used as starting materials are mostly sintered and used as densified bodies, and so it is desirable that they consist of fine particles. The fine powders may be produced by the break-down approach, such as the grinding of bulk bodies into fine particles of the required size, and the build-up approach where very fine powders are synthesized by vapor- or liquid-phase processes. The former approach is preferable because of cost in most cases for the volume production of fine ceramic powders. One of the problems involved in the grinding process is lower efficiency with time. Grinding particles produce new surfaces of higher surface activity, and the ground particles adhere firmly to each other, or to the mill walls or grinding media, in order to reduce the surface energy. Thus, the behavior of these activated surfaces is mainly responsible for the lower grinding efficiency. A variety of polar organic materials and fine solid particles are being studied as grinding aids to enhance the grinding efficiency.¹⁻³⁾

In this study, grinding was aided by a metal alkoxide, which was used by Hayashi et al. in the dry-type process for grinding clay,⁴⁾ to investigate the

functions of enhancing grinding efficiency and controlling agglomeration. The mechanisms of action of the metal alkoxide grinding aid were also investigated.

2. Experimental Procedure

The starting powder used in this study was electrofused alumina (WA600, supplied by Showa Denko), the properties of which are presented in Table 1.⁵⁾

Two metal alkoxides, titanium tetra-n-butoxide ($\text{Ti}(\text{OC}_4\text{H}_9)_4$, Alcofine Ti-40, supplied by Kawaken Fine Chemical) and silicon tetra-n-butoxide ($\text{Si}(\text{OC}_4\text{H}_9)_4$, supplied by Tama Kagaku Kogyo), were used as the grinding aids. These compounds are referred to as the Ti- and Si-base aids.

Each sample (0.7kg) was ground at a vibration speed of 1300rpm in a 2l alumina pot with a grinding medium of 2kg of 20mm-diameter alumina balls (SSA-995, supplied by Nippon Kagaku Togyo). The grinding apparatus was a dry type vibration mill (Model MB-1, supplied by Chuo Kakoki). Ten (10g) of the ground sample was collected and treated for up to 320h. Charging the sample into the pot and sample collection were conducted in an atmosphere kept at a RH of 50±5%.

The particle size distribution was measured by a Nikkiso Microtrack analyzer, after the sample was well dispersed ultrasonically in a solution with the pH adjusted with hydrochloric acid. The specific surface area was measured by a Carlo Erba Sorptomatic Series 1800, based on the BET method with nitrogen adsorption. The angle of repose was measured by a Kuramochi Kagaku analyzer, in which 25g of the sample was dropped from a height of 80mm and heaped in a cone in a RH of 50±5%, and the radius of the bottom area and height were measured. Each sample, ground for 320h, was observed with a scanning electron microscope (SEM, MSM-9, Akashi Seisakusho), to determine the grain morphologies.

Table 1. Chemical composition and average particle size of Al_2O_3 powders.

powder	chemical analysis (wt%)					size (μm)
	Al_2O_3	SiO_2	Fe_2O_3	TiO_2	Na_2O	
WA600	99.6	0.02	0.03	tr.	0.2	21.8

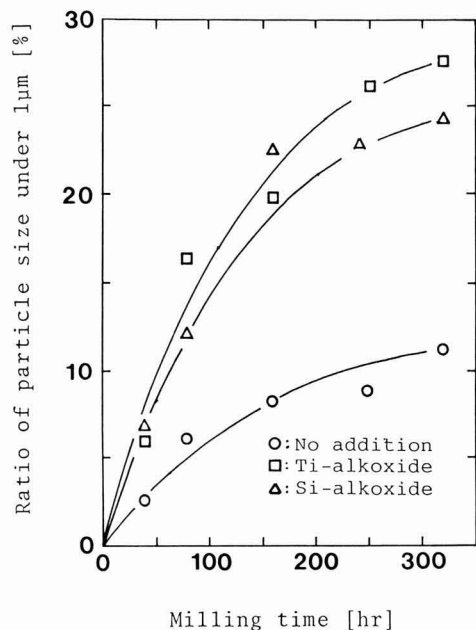


Fig. 1. Effect of grinding aid on ratio of particle size under $1\mu\text{m}$. Ti-alkoxide and Si-alkoxide are $\text{Ti}(\text{OC}_4\text{H}_9)_4$ and $\text{Si}(\text{OC}_4\text{H}_9)_4$, respectively.

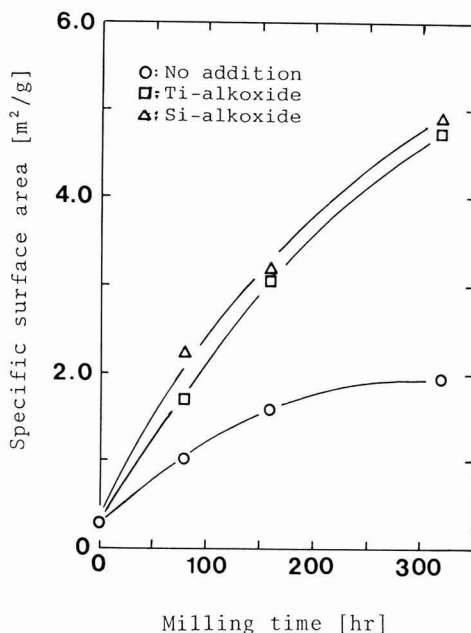


Fig. 2. Effect of grinding aid on specific surface area of Al_2O_3 powder.

The contact angle of each grinding agent with alumina was measured to estimate the wettability, where 0.1mm^3 of the sample was dropped on a cleaned alumina substrate (supplied by Nikko) by a microsyringe was observed with an optical microscope. The surface tension was measured by a CBVP type surface tension meter (Kyowa Kaimen Kagaku A-3).

3. Results and Discussion

3-1. Effects of Grinding Aids

Figure 1 shows the relationship between the content of particles of under $1\mu\text{m}$ size (%) and milling time, indicating the effects of the grinding aids. Each system containing an aid was characterized by a much faster grinding rate than the non-aided system, with a much larger content of fine particles under $1\mu\text{m}$ from the very start of grinding. Furthermore, the difference between the aided and non-aided systems became still larger with time; the contents of the systems with the Si- and Ti-base aids reached 24% and 27%, respectively in 320h, whereas that of the non-aided system was 11%, and a difference as high as 15% was observed between them.

At the same time, the difference between the systems aided by the different agents was much smaller.

Figure 2 shows the effects of milling time on the specific surface area of the ground particles, measured by nitrogen adsorption. The specific surface area also increased much faster in the aided systems, reaching about $5.0\text{m}^2/\text{g}$ in 320h in the aided systems. This compared with about $2.0\text{m}^2/\text{g}$ for the particles of the non-aided system, where the surface area increased little with time beyond 160h. Thus, the aided systems had about 2.5 times higher surface area than the non-aided system. It was further observed that the alumina particles ground in the presence of the aids adhered less to the pot walls than the non-aided particles, and were collected more easily. The latter particles, on the other hand, started to stick in bulk to the walls in 160h. This trend was repeated when they were thoroughly scraped off and then reground. The proportion of the particles adhering to the walls increased with time, to almost 100% in 320h. This corresponded to the virtual ceasing of grinding beyond 160h, as illustrated in Figs. 1 and 2.

Figure 3 shows the angle of repose as a measurement of the agglomeration/dispersion conditions of the ground particles. It was essentially constant at 55° with the non-aided particles, and decreased with the aided par-

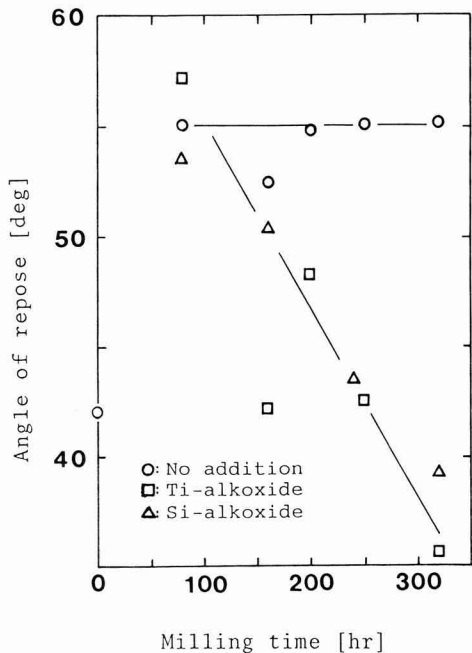


Fig. 3. Effect of grinding aid on angle of repose.

ticles, indicating the enhanced dispersibility of the particles ground in the presence of the aid. Dispersibility during the grinding process is mainly determined by the surface energy of the particles. In other words, it may be considered that the apparent surface energy of the particles rarely decreases while being ground in the absence of an aid, but does decrease significantly in the presence of an aid. A decrease in the angle of repose almost proportional to the milling time might indicate that the proportion of the aid covering the particle surfaces increased with the addition rate. The reason for the low angle of repose of the unground particles is not known. It might result from the surface treatment during the manufacturing process. Figure 4 shows the SEM photographs of each sample ground for 320h. The non-aided sample consisted of a number of fine, ground particles adhering to coarser particles. These finer particles were agglomerated closely, to cover essentially the entire surfaces of the coarser particles. In the aided systems, on the other hand, the coarser particle surfaces were rarely covered by the finer ones and could be observed clearly, indicating enhanced dispersibility.

It is concluded, based on the above results, that the newly formed surfaces of higher energy adhere to each other during grinding in the non-aided system, whereas they adsorbed metal alkoxide in the aided system, reducing the high surface energy.

Thus, the use of metal alkoxide as a grinding aid has been confirmed to greatly enhance the grinding efficiency and dispersibility.

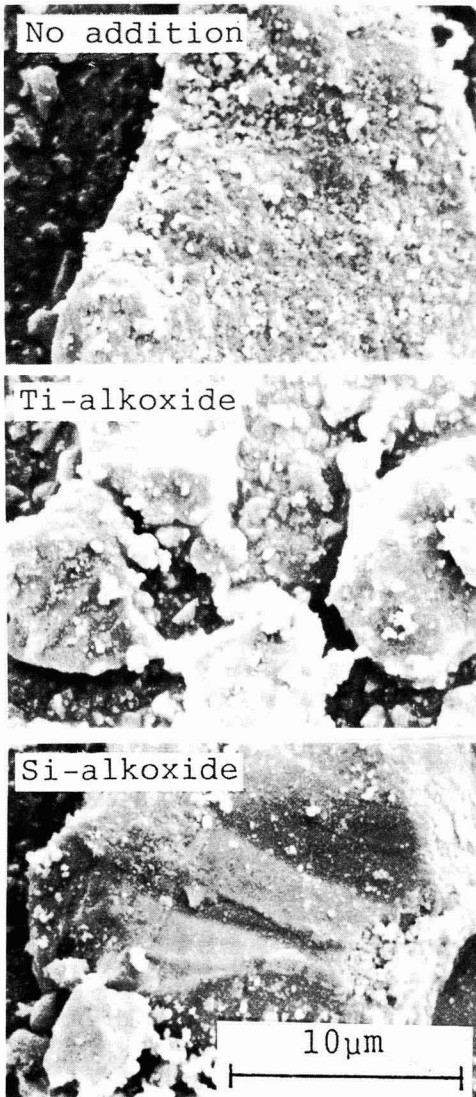


Fig. 4. Scanning electron micrographs of Al_2O_3 powder ground for 320hr with and without grinding aids.

3-2. Characteristics and Mechanisms of Action of Grinding Aids

The results of angle of repose and SEM analysis, discussed in Section 3.1, indicated that the metal alkoxides acted as grinding aids by enhancing the dispersibility of the ground particles. The angle of contact as a measurement of the surface tension and wettability of the liquid on the solid surfaces was determined, in order to understand how the alkoxide acted. Agglomeration of the ground particles is considered to result, as illustrated in Fig. 5, from the adhering of the

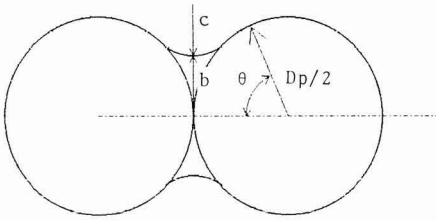


Fig. 5. Schematic model of the bonding force by liquid.⁵⁾

newly formed surfaces to each other via the liquid phase adsorbed on the surfaces, reducing their high surface energy. It is therefore considered that the dispersibility of fine ground particles greatly depends on the difficulty of dividing and separating the adsorbed liquid phases. Moisture present in the grinding atmosphere may be acting as the liquid phase in the non-aided system, instead of the metal alkoxide in the aided system. The force required to divide and separate liquid phase is represented by the following equations as a function of the surface tension T of the liquid phase:

In the sphere-sphere case:

$$F = \pi b \left(\frac{b}{c} + 1 \right) T \quad \dots \dots (1)$$

$$F = \frac{\pi D_p}{1 + \tan(\theta/2)} T \quad \dots \dots (2)$$

In the sphere-plane case:

$$F = \frac{2\pi D_p}{1 + \tan(\theta/2)} T \quad \dots \dots (3)$$

where, b and c are the radii of curvature, D_p is the particle size, and θ is the angle of contact between the particle and the liquid phase at the point of contact. The surface tension of water is $71.96 \times 10^{-3} \text{N/m}$ at 25°C .⁷⁾ The measured surface tensions of the grinding aids were $25.0 \times 10^{-3} \text{N/m}$ and $24.3 \times 10^{-3} \text{N/m}$ for the Ti- and Si-base types. The surface tension of each aid will be lower under actual operating conditions, because the mill temperature is higher than 25°C . The dependence on temperature is not known, and it was assumed that their relative values were unchanged in the temperature range used in this study, i.e., a smaller force was required to separate the agglomerated particles in the aided systems.

Another point which must be taken into consideration is wettability. Poor wettability of the aid on alumina will result in a low grinding efficiency because of an insufficient quantity adsorbed on the solid surfaces. The angle of contact, therefore, was measured to investigate the wettability of the aid. As a result, the Si-base aid was found to spread over the solid surfaces showing expansion wettability, whereas the Ti-base showed adhesion wettability,⁸⁾ with an angle of contact of 17.3° (average of ten particles). The wettability of

both aids on the alumina particles were sufficiently high to allow them to spread over the solid surfaces.

The effects of each grinding aid are discussed below, based on the above results. The angle of contact measured suggests that each aid has sufficient wettability to cover the alumina surfaces in a short time. In addition, the aid is considered to undergo accelerated hydrolysis forming butyl alcohol in the presence of moisture, which is one of the major causes of lowered dispersability of the particles. Hydrolysis will be further accelerated as the alumina surfaces act as the acid catalytic sites. Alcohol is also known to be a grinding aid for cement clinkers,⁹⁾ and thus the alcohol hydrolysis product is expected to also act as a grinding aid. Butyl alcohol has a surface tension of $24.7 \times 10^{-3} \text{N/m}$ at 20°C ,⁷⁾ which is comparable with those of the Ti- and Si-base aids.

The residual quantities of TiO_2 and SiO_2 in the samples ground for 320h were 0.09 and 0.06wt%, as measured from the addition rates. It is necessary to use a metal alkoxide which is the same as the metal component of the powder system to be ground, if the contamination level is a problem.

4. Conclusions

Metal alkoxides were used as aids for grinding alumina in a dry system.

- 1) Use of a metal alkoxide increases the grinding efficiency, and allows the production of fine particles of good dispersibility.
- 2) Each aid is considered to accelerated grinding and enhance the dispersibility of the ground particles by reciprocal effects resulting from the low surface tension of the aid itself and the removal of moisture, which has a high surface tension and acts to agglomerate ground particles, through hydrolysis forming butyl alcohol with a low surface tension.

Acknowledgments:

The authors thank Dr. Seiichiro Hironaka of Tokyo Institute of Technology for his cooperation in the measurement of the angle of contact. They also thank Nippon Surfactant's Nikkoru Technical Center for cooperation in the measurement of surface tension.

References:

- 1) K. Kubo, "Mechanochemistry of Inorganic Materials," Sogo Gijutsu Shuppan, (1987), pp. 157-61.
- 2) F.J. Marulier, ASTM Proc., 61, 1078-93 (1961).
- 3) T. Tanaka and S. Kawai, Kagaku Kogaku, 26, 427-29 (1962).
- 4) T. Hayashi, A. Inoue, M. Ogiwara and N. Otsuka, Yogyo-Kyokai-shi, 87, 622-32 (1979).
- 5) Catalogue of the Showen Denko K.K.
- 6) "Grinding and Properties of Ground Particles," edited by S. Yashima, Baifu-kan (1986), pp. 44-45.
- 7) "Experimental chemistry Series 7, Surface chemistry," edited by the Chemical Society of Japan, Maruzen (1966), pp. 67-68.

- 8) "Chemical Handbook," edited by the Chemical Society of Japan, Maruzen (1966), pp. 529-530. This article is a full translation of the article which appeared in Nippon Seramikkusu Kyokai Gakujutsu Ronbunshi (Japanese version), Vol.98, No.3, 1990.
- 9) N. Ishino, Sekko to Sekkai, 138, 191-97 (1975).

Acoustic Emission Study for Fracture Origin of Sintered Mullite in 4-Point Bending Test

Yoshiaki Yamada and Teruo Kishi*

Sumitomo Metal Industries, Ltd.

16, Sunayama, Hasaki, Kasima-gun, Ibaraki, 314-02, Japan

*Research Center for Advanced Science and Technology, The University of Tokyo

4-6-1, Komaba, Meguro-ku, Tokyo 153, Japan

Acoustic emission signals of sintered mullite were measured in 4-point bending tests. The specimens were prepared from a high-purity mullite powder and sintered at 1650°C for 2h. The 2ch AE signals were detected by the piezoelectric sensors on the both end surfaces of 4-point bending specimens (3mm×4mm×38mm). Detected waves were recorded in a digital wave memory, and then analyzed with a computer to obtain AE location and cumulative AE counts data. In addition, the SEM fractography and the fracture mechanics evaluation were carried out to determine the fracture origins. The experiments revealed the relationship between types of fracture origins and AE signals, and new fracture models were proposed to explain the experimental results.

[Received September 27, 1989; Accepted November 22, 1989]

Key-words: Acoustic emission, Mullite, Fracture origin, 4-point bending, AE location, Fracture model

1. Introduction

1

Mullite ($3\text{Al}_2\text{O}_3 \cdot 2\text{SiO}_2$) is now of considerable interest as a possible replacement for alumina as a high-temperature structural material. The high-temperature properties of mullite were first reported by Pask et al.¹⁾ However, it has a lower fracture toughness than alumina and other ceramics, which has prevented its use in practical applications. To carry out successful studies to develop composite materials with high toughness, an understanding of its fracture mechanism is necessary. The defects that act as the fracture origins in ceramics are classified into surface defects and internal defects. The defects are also classified into crack-type defects and pore-type defects according to their shapes.

The important area in the study of the fracture mechanism of ceramics is the detection and evaluation of microcracks formed during the time when the fracture origin develops into the final fracture. To investigate this problem, several nondestructive testing methods have been used. The acoustic emission (AE) method, one nondestructive test, is expected to be particularly effective because it can trace the fracture process and supply much information that other non-destructive tests cannot. The AE method has previously been used for the study of the relationship between strength and AE signals,^{4,5,6)} the relationship between crack progress and AE signals in DT test,^{7,8,9,10)} the indentation test,^{10,11,12,13)} and the SENB test^{14,15)} for

Al_2O_3 and Si_3N_4 . No use of this method for tests on mullite has been reported.

To understand the fracture mechanism of brittle materials like ceramics, it is necessary to trace the growth process of a crack. For this purpose, the following three evaluation steps are important.

- 1) Initial defect detection by nondestructive testing before destructive testing.
- 2) Nondestructive detection of defect formation and the growth process during loading.
- 3) Defect evaluation by observing the fracture surface.

In the present study, the 2nd step was carried out using the AE method and the 3rd step was carried out by SEM observation. The acoustic emission signals of sintered mullite were measured during 4-point bending tests to investigate the relationship between the fracture origin and the AE properties. By combining the results of the AE study with the information from the fracture surfaces observation, the fracture process of mullite could be more clearly understood.

2. Experimental Procedure

2-1. Specimen

High-purity mullite powder was uniaxially pressed in 4×5×50mm dies, and then the green compacts fired in an electric furnace at 1650°C for 2 hours. The specimen was machined into a JIS 4 point bending test piece measuring 3×4×38mm, with the surface ground by #1200 diamond abrasive. The edges were chamfered by 0.2mm.

2-2. JIS 4-point Bending Test

The 4-point bending test specified by JIS R1601-1981 was performed while acoustic signals were measured simultaneously with the system shown in Fig.1.

The 4-point bending test was performed in air at room temperature by using an autograph testing machine DCS-R-500 (Shimadzu Corporation), with upper span 10mm, lower span 30mm, and crosshead speed 0.04mm/min. A 0.08mm-thick teflon tape was placed between the bending jig and the sample to reduce external mechanical noise to improve the AE measurement.

2-3. Fracture Toughness Test

The SEPB (Single Edge Precracked Beam) method was used to measure the fracture toughness. In this method, a precrack was introduced in a JIS test piece

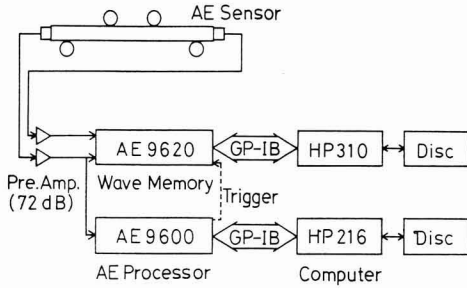


Fig. 1. Block diagram of 2-channel acoustic emission detection and recording system.

of 3×4×38mm by the bridge-indentation (BI) method, and then the 4-point bending test was performed. The fracture toughness value was then calculated from Eq.(1).¹⁷⁾

$$K_{I1} = Y \frac{3P(L_1-L_2)}{2bW^2} \sqrt{a} \quad \dots\dots (1)$$

$$Y = 1.99 - 2.47(a/W) + 12.97(a/W)^2 - 23.17(a/W)^3 + 24.80(a/W)^4$$

- where, P : Breaking load
- L₁ : External span
- L₂ : Internal span
- b : Width of test piece
- W : Height of test piece
- a : Pop-in crack length

2-4. Observation of Fractured Surfaces

The fracture surface of the sample was examined with a scanning electron microscope (Hitachi S-450) to determine the fracture origin.

2-5. AE Measurement

Since the AE signals generated by ceramics are often weak, an AE sensor with high sensitivity and wideband response was needed for the AE measurements. Before the experiment was started, a preliminary test was made by using a commercially available wideband AE sensor (PAC; Picosensor). The preliminary test indicated that few AE signals were measured. Therefore, a newly developed AE sensor¹⁸⁾ was used, the construction of which directly connects an amplifying device to a highly sensitive piezoelectric device (Fuji Ceramics) to reduce the noise, which improved the signal-to-noise ratio by about 13dB compared with conventional AE sensors.

The AE recording was carried out by the system shown in the block diagram in Fig.1.

The highly sensitive AE sensors with built-in pre-amplifier were attached to both longitudinal ends of the test piece. Triggering was done by an AE processor (AE 9600 NF Circuit Block). The waveform detected was stored in a digital wave memory (AE9620), transferred to the computer (HP310, Hewlett-Packard Co.),

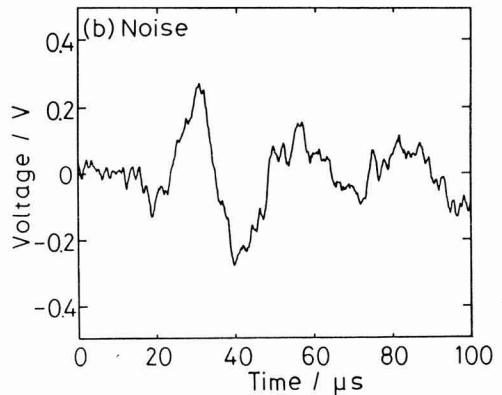
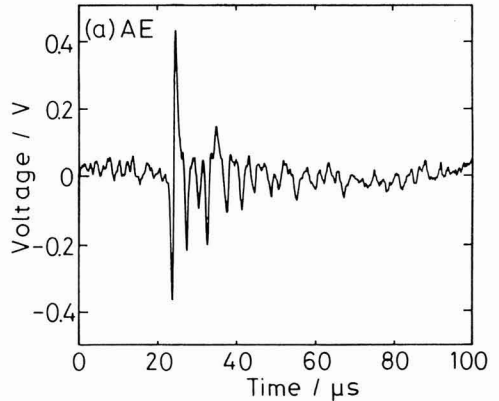


Fig. 2. Typical waveforms; (a) acoustic emission (b) noise.

and recorded on a floppy disk. The wave memory had a sampling time of 50ns, a voltage resolution of 10 bits, a recording length of 2 kwords for 1 event, and a dead time (waiting time for data processing in the wave memory) of 10ms.

2-6. Locating Method and Accuracy

Noise and AE signal were discriminated by directly observing the detected waveform. The discrimination of mechanical noise and AE signal was achieved by striking the surface of a test piece prepared for testing, or by recording pseudo noise waveforms caused by rubbing against the jig and comparing them with the recorded waveform. Figure 2 shows typical AE signal and noise waveforms.

Next, the AE location was determined, by studying the recorded waveforms, and measuring difference in times between the two channels obtained by using the first peaks (first compression wave: longitudinal wave) at each AE event as shown in Fig. 3, and by using the longitudinal wave sound velocity of 7600m/sec obtained separately.

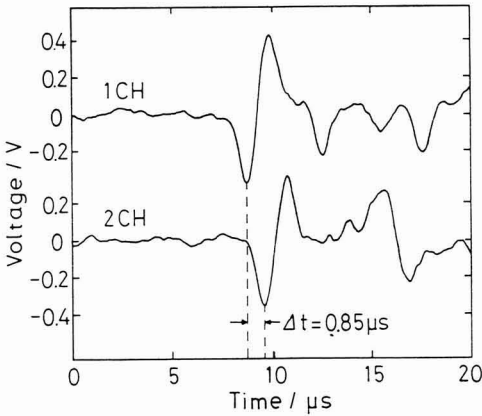


Fig. 3. Arrival time difference of AE signals. Time difference was obtained by using the first peak tops.

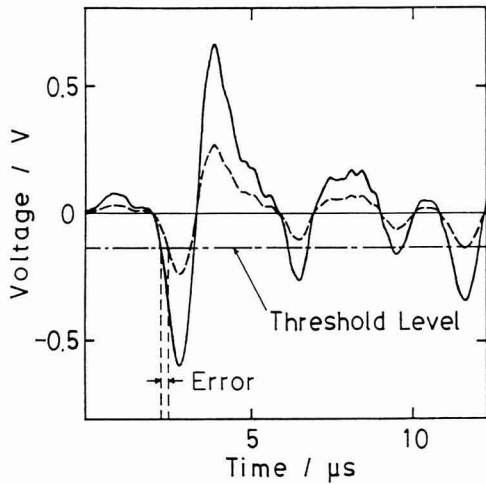


Fig. 4. One example of time error. The time error depends on each signal even with the same threshold level.

This location method is more accurate than the conventional method in which a commercially available measuring device has been used. The method in which the arrival time is when the signal input exceeds the threshold level and the time difference of two channels is determined has the problem of possible shifts in detection time caused by the signal level (Fig.4).

When the signal level is close to the threshold level, the signal that is first detected is not always the

longitudinal waves for both channels, but possibly longitudinal and transverse waves or transverse waves. This sometimes causes a time error amounting to several microseconds, which poses a problem in determining the AE location. The method adopted in the experiment, in which only the longitudinal wave is dealt with, is advantageous for solving this problem.

With this method, the accuracy in the arrival time difference is $0.1\mu\text{s}$ to $0.2\mu\text{s}$, about ± 0.4 to 0.8mm in actual distance when the time resolution is 50ns and the response properties of the sensors are nearly the same.

3. Results and Discussion

3-1. Mechanical Properties and Observation of Fracture Surfaces

3-1-1. Bending Strength and Fracture Toughness

Figure 5 shows the Weibull plot of 4-point bending strength testing of nine test pieces including three test pieces subjected to AE measurement. The mean bending strength was 182MPa , and the shape parameter m was 10.3 . The fracture toughness value K_{IC} obtained by the SEPB method was $1.6\text{MPa}/\text{m}$.

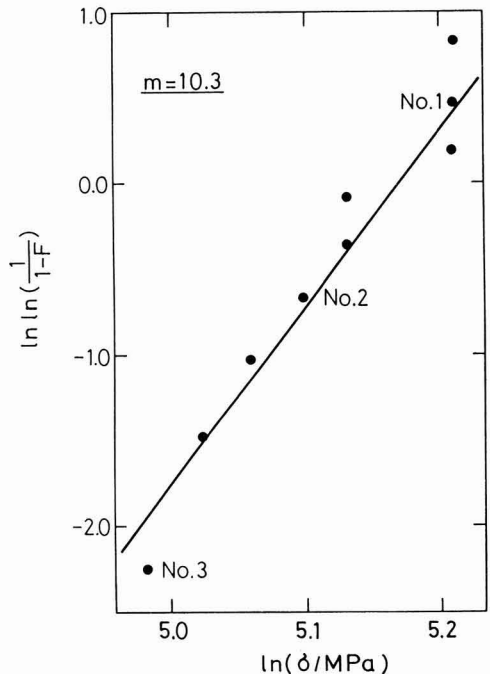


Fig. 5. Weibull plot of 4-point bending strength and fracture probability F (mean-rank method: $F_i = i/(n+1)$).

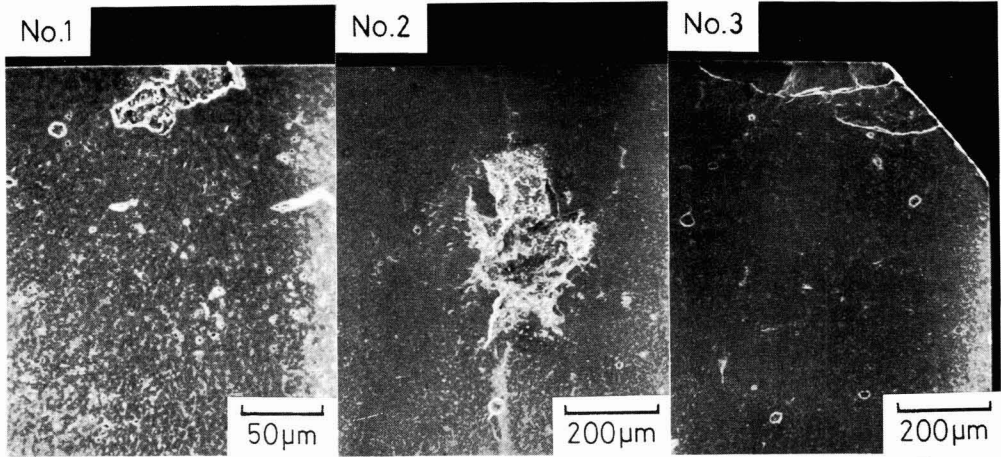


Fig. 6. SEM photographs of fracture origins.
No.1 is a surface pore, No.2 is an inner pore. No.3 is a surface crack.

Sample	Position	Size (µm)
No.1		 a=40
No.2		 min. a=112 c=112 max. a=154 c=210
No.3		 min. a=61 c=112 max. a=72 c=185

Fig. 7. Positions and estimated sizes of each fracture origin on fracture surfaces based on SEM observation.

3-1-2. Determination of Fracture Origin by Observation of Fracture Surface

The fracture surfaces of the three test pieces subjected to AE measurement were observed with a scanning electron microscope. The possible fracture origin was determined on the basis of undulation and ir-

Table 1. Calculation of K_I values for fracture origins.

Sample No.	a _m	c _m	δ_c MPa	δ_{eff} MPa	γ	K_I MPam ^{1/2}
1	40	40	196	196	0.66	1.5
2	112	112	176	130	0.64	1.6
	154	210	176	130	0.73	2.1
3	61	112	157	157	0.86	1.9
	72	185	157	157	0.94	2.3

$$K_{IC} = 1.6 \text{ MPam}^{1/2} \text{ (SEPB)}$$

regularity of the fractured surface, defect size, and other factors.¹⁹⁾ The SEM photographs of the fracture origins are shown in Fig. 6. A crack or pore on the surface or just under the surface was judged to be the fracture origin. Figure 7 shows schematically the sizes, shapes, and positions of the defects which were the probable fracture origins.

The defect in No.1 sample in the figure was a pore, whose shape was estimated to be a semielliptical crack.

The defect in No.2 sample was an internal pore. Since the shape was intricate, the defect was assumed to be an elliptical crack, and the estimated maximum and minimum sizes were measured.

The defect in No.3 sample was a surface crack. The maximum and minimum sizes were measured.

As can be determined from the photographs, it is likely that microcracks were formed near the defect and grew to the critical crack size in all samples.

3-1-3. Evaluation Based on Linear Fracture Mechanics

The stress intensity factor K_I at the crack tip during fracture was calculated from the following equation on the basis of information about the size, shape, and position of the defect obtained in the preceding section by assuming the bending fracture stress to be the critical stress, based on linear fracture mechanics. The results of the calculations are shown in Table 1.

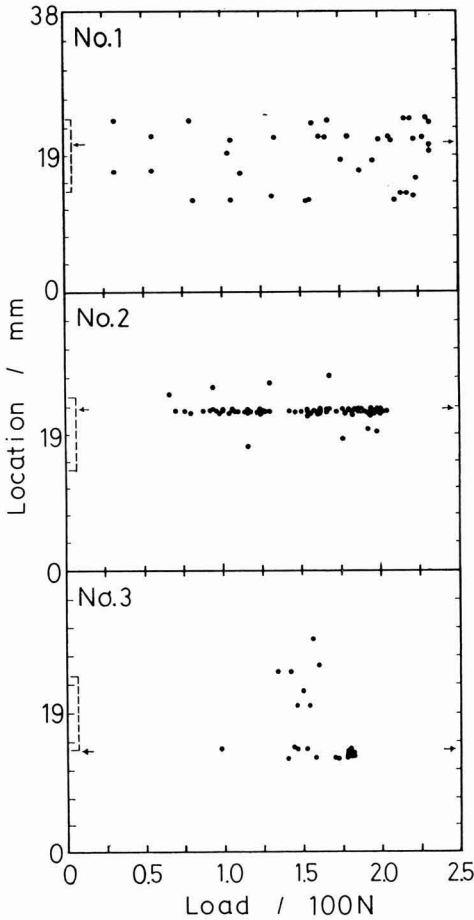


Fig. 8. AE source location as functions of load.
 No.1: wide distribution
 No.2: local
 No.3: wide then local
 ● : one AE event ← : failure site
 } : inner span

$$K_I = Y\sigma_c\sqrt{\pi a_c} \dots\dots\dots (2)$$

where, Y is the shape correction factor.

In this calculation, the defects in No.1 and No.3 samples were assumed to be surface defects, while the defect in No.2 sample was an internal defect. For the defect in No.2 sample, the tensile stress at the pore center during fracture (σ_{eff}) was used for the calculation. The shape correction factor was determined in accordance with the "Stress Intensity Factors Handbook."²⁰⁾

As seen from Table 1 the K_I values are close to the K_{IC} values obtained earlier, though they differ somewhat according to how the size of the initial crack was

estimated. This discussion suggests that the defect found in the SEM observation of fracture surface was the fracture origin, which then caused fracture.

3-2. Evaluation of Fracture Process by the AE Method

The results described in 3-1 were based on information obtained after failure. It is not known what changes occurred in the material in the actual fracture process. It is also not known how the shape of the fracture origin affected the fracture. The solution to these problems was investigated by the AE method.

The cumulative AE counts, AE source location and amplitude were investigated for each defect.

Figure 8 shows the AE source location as a function of the load on each sample. The ordinate represents the AE source location in the longitudinal direction of the test piece. The loading rate was constant because the use of a displacement-restricted testing machine prevented the plastic deformation of the test pieces.

In No.1 sample, AE signals were scattered over the high-stress zone in the middle of the test piece. In No.2 Sample, AE signals occurred at nearly the same position during the time from the start of signal emission to the final failure. In No.3 sample, AE signals occurred in a wide range in the early stage, and just before the failure, AE signals were focussed at the fracture position. This result indicates that the fracture mechanisms differed in No.1, No.2 and No.3 samples.

Figure 9 shows the total AE event count as a function of load. Figure 10 shows the AE amplitude distribution as a function of load. The amplitude was determined from the initial peak voltage used in locating the AE source. One volt was taken as 100dB for the wave memory input. As seen from Fig.9, many AE signals occurred just before the final failure. It is seen from Fig. 8 that these AE signals occurred at the fracture position. Figure 10 indicates that many small-amplitude AE signals occurred just before the final failure on No.2 and No.3 samples (the zones enclosed by the dotted line in the figure). Since the amplitude of the AE signal is considered to be proportional to the size of the microcrack, cracks of relatively small size are likely to be formed. On No.1 sample, these signals were not found.

3-3. Model of Fracture Process

The above results were studied together with observation results of fracture origins, and the modelling of the fracture process in the material was proposed.

1) In No.1 sample, in which a surface pore was the fracture origin, many small defects distributed in the test piece formed microcracks, which resulted in the independent occurrence of AE signals in a wide range. The pore, which was the largest defect, grew slightly when the final failure occurred. Such a round and smooth pore caused fracture without the occurrence of continuous and concentrated AE events because local stress concentration was less prone to occur. A pore which causes fracture is here called an "inactive pore," when a crack grows only slightly.

2) In No.2 sample in which an internal pore was the fracture origin, fracture did not occur immediately in

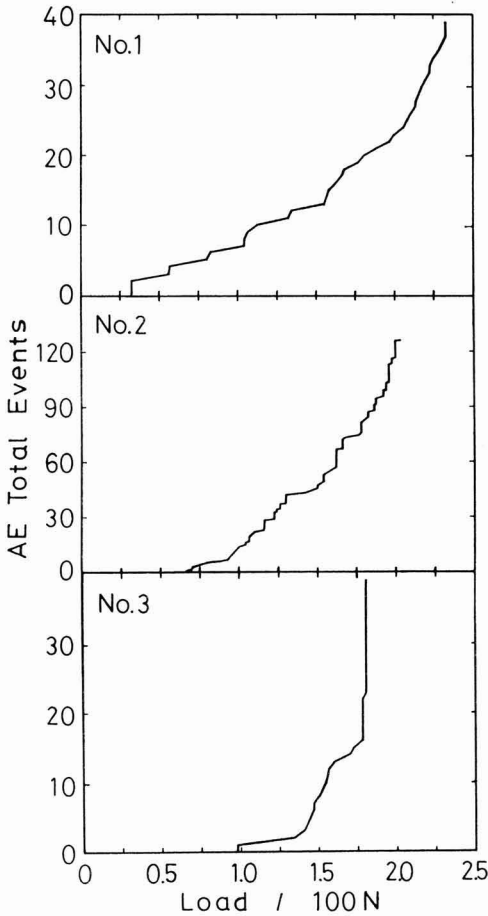


Fig. 9. Total AE event counts as functions of load. No.1 and No. 2 show slow increase. No.3 shows slow increase then rapid increase.

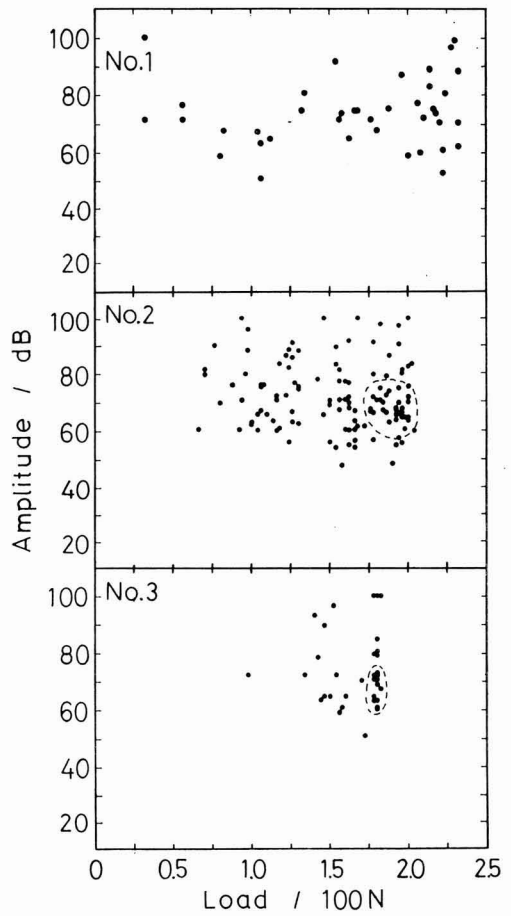


Fig.10. AE amplitude distribution as functions of load. Small-amplitude signals were detected just before failure in specimens No.2 and No.3.

spite of the concentrated occurrence of AE signals at the fracture origin under low loads. This process is greatly different from that in No.1 sample. Although there are several possible reasons for the long-term occurrence of AE signals, one reason based on considering the results of SEM observation is that, as shown in Fig. 11, microfracture first occurred in the high stress concentration zone around the defect, resulting in the development of the crack. The crack, however, grows stably because it has a shape like a chevron notch. Also, since many small pores are distributed around the defect, the crack is temporarily blunted when the crack tip reaches these small pores, and the development of this process causes the defect to gradually grow until the defect grows to the critical size causing unstable fracture.

The difference in cracks in the internal and external zones can be assumed from the observations of the area around the fracture origin (Fig.12), in which the area around the fracture origin is greatly inclined in relation to the main crack surface and is split.

A pore that causes gradual crack growth before the final failure is called an "active pore," while the pore discussed in 1) is called an "inactive pore."

3) In No.3 sample, a surface crack formed the fracture origin. In this sample, AE signals occurred in a wide range under low loads, and concentrated and continuous AE signals occurred at the fracture position just before the final failure. This means that although weak areas in the material are independently fractured in the early stage, one of the weak areas grows at a certain time, causing the unstable growth of the crack until final failure occurs.

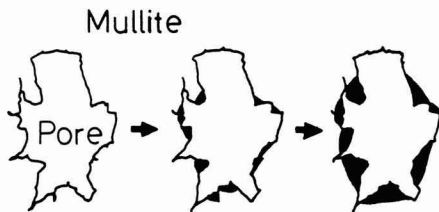


Fig. 11. Schematic model of No.2 fracture origin, showing stable crack growth around initial pore.

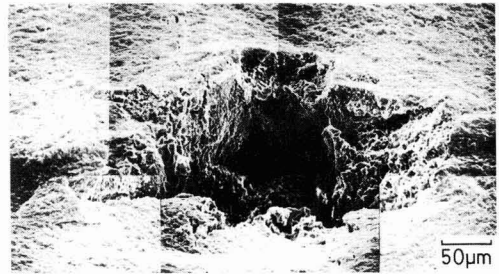


Fig. 12. SEM photograph of No.2 fracture origin.

3-4. Correlation Between AE Signals and Defects

The correlation between the types of fracture origins and AE signal in term of the following AE parameters is studied.

The AE signal properties discussed as a result of the experiment are classified as follows:

- 1) Information about source location
 - a) Wide distribution of AE signals
 - b) Local distribution of AE signals
- 2) Information about total events
 - a) Rapid increase in total events
 - b) Slow increase in total events
- 3) Information about AE signal amplitude
 - a) Concentrated distribution of small-amplitude AE signals
 - b) Random distribution of amplitudes

The relationships between these classifications and the type of defect are listed in Table 2. The combination of parameters leads to the estimation of the properties of fracture origin. This table also indicates that when the source locations were locally distributed and small-amplitude AE signals concentrated before the final failure, some stable cracks (formation and bonding of microcracks) occurred.

The above-mentioned fracture origins are typical ones, and the three examples do not represent all fracture origins.

The AE method can detect microcracks in ceramics and provide useful information about fracture origins, although it is necessary to make AE measurements on many samples and calculate the statistical significance of the results.

4. Conclusions

To investigate the fracture mechanism of mullite in which the surface and internal pores and surface cracks formed the fracture origins, a high-accuracy AE measurement method was developed for 4-point bending tests. The results are as follows:

- 1) A highly sensitive AE sensor with built-in preamplifier was developed. The device enables the detection of AE signals occurring before the failure of one order better accuracy than with the conventional sensor.

Table 2. AE properties of fracture origins.

Types of fracture origins	AE property			Stable crack growth (Microcracking)
	Location	Total event	Amplitude	
In-active pore 196MPa	Wide	Slow increase	Random	Very few
Active pore 176MPa	Local	Slow increase	Concentrated	30% of δ_f - failure
Surface crack 157MPa	Wide ↓ Local	Slow ↓ Rapid increase	Concentrated	95% of δ_f - failure

It also enabled discrimination between the AE signals caused by microcracks and noise and an improvement in source location accuracy by recording and identifying the detected waveforms.

2) The correlation between the AE signal and fracture origin was revealed by analysing the AE signals in terms of source location change in total events, and amplitude (signal intensity). In this experiment, AE signals occurred in a wide range for surface pores, small-amplitude AE signals were concentrated on a local area for internal pores; and small-amplitude AE signals were observed just before the failure for surface cracks.

3) The use of the AE method showed that the fracture process of mullite ceramics depends greatly on the shape of the defect forming the fracture origin, as well as its size.

(Presented at the Annual Meeting of the Ceramic Society of Japan, May, 1989)

References:

- 1) P.C. Dokko and J.A. Pask, J. Am. Ceram. Soc., 60 [3-4] 150-155 (1977).
- 2) N. Claussen and J. Jahn, J. Am. Ceram. Soc., 63 [3-4] 228-229 (1980).
- 3) G.C. Wei and P.F. Becher, Am. Ceram. Soc. Bull., 64 [2] 298-304 (1985).
- 4) G.A. Gogotsi, A.V. Drozov and A.N. Negovskii, Proc. Ultrason. Int., 83, 67-73 (1983).
- 5) A. Katamine, T. Nishiyama, T. Fukuhara and Y. Nozue, The 4th National Conference on Acoustic Emission Proceedings, 110-113 (1983).

- 6) S. Wakayama, T. Koji and H. Nishimura, "Nondestructive Evaluation of New Materials and Their Products" Seminar Proceedings, 181-186 (1988).
- 7) A.G. Evans and M. Linzer, *J. Am. Ceram. Soc.*, 56, [11] 575-581 (1973).
- 8) T. Kishi, T. Ohira, Y. Shinozaki, E. Nakata and Y. Kagawa, The 4th National Conference on Acoustic Emission Proceedings, 104-109 (1983).
- 9) K. Ohta, H. Hashimoto and H. Iwasaki, The 4th National Conference on Acoustic Emission Proceedings, 98-103 (1983).
- 10) K. Honma and T. Torikoshi, *Transactions of the Japan Society of Mechanical Engineers (Vol.A)*, 51 [462], 499-503 (1985).
- 11) Y. Matsuo and A. Nozue, *Transactions of the Japan Society of Mechanical Engineers (Vol.A)* 51 [462], 499-503 (1984).
- 12) N. Ikawa and S. Shimada, *Precision Machines*, 48 [20], 177-183 (1982).
- 13) E. Yasuda, Y. Tanabe, K. Miyahara, T. Fukai, S. Kimura and N. Hada, *Yogyo-Kyokai-Shi*, 95 [5], 503-508 (1987).
- 14) T. Tanaka, H. Niizuma, N. Nakahachi and R. Sato, The 3rd National Conference on Acoustic Emission Proceedings, 142-147 (1981).
- 15) K. Katsuyama and Y. Sato, The 5th National Conference on Acoustic Emission Proceedings, 70-75 (1985).
- 16) T. Nose and T. Fujii, *J. Am. Ceram. Soc.*, 71 [5] 328-333 (1988).
- 17) W.F. Brown, Jr and J.E. Srawley, *ASTM STP 410*, ASTM, Philadelphia (1966).
- 18) M. Shiwa, H. Inaba and T. Kishi, *Nondestructive Evaluation*, Not yet published.
- 19) H. Abe, "Engineering Ceramics," Gihodo Shuppan Co., 1984, 194-202.
- 20) "Stress Intensity Factors Handbook," 1st Ed., Pergamon Press, Oxford, 1987, Vol.2.

This article is a full translation of the article which appeared in *Nippon Seramikkusu Kyokai Gakujutsu Ronbunshi* (Japanese version), Vol.98, No.3, 1990.

Trial Production of ZrO_2/Al_2O_3 Thin Sheet from Zirconia Powder/Aluminum Hydroxide Sol System

Kazuro Kawamura, Seiji Yamanaka* and Mikiya Ono*

Dept. of Materials Science and Engineering, The National Defense Academy

1-10-20, Hashirimizu, Yokosuka 239, Japan

*Mitsubishi Mining and Cement Co., Ltd.

Yokoze-cho, Chichibu-gun, Saitama 368, Japan

A slurry was made from zirconia powder (yttria-stabilized zirconia powder), aluminum hydroxide sol (boehmite sol), binder and plasticizer, and was formed to green sheet by the doctor blade method. The green sheet was sintered in the temperature range of 1300 and 1500°C in air. The optimum alumina constant to obtain a good ZrO_2/Al_2O_3 thin sheet was 10 - 15wt%. Thin sheet sintered at 1400°C was characterized by the thickness of 100 μ m, density of 4.9g/cm³, bending strength of 486MPa, modulus of elasticity of 167GPa, and resistivity of $2 \cdot 4 \times 10^{12}\Omega \cdot \text{cm}$.

[Received October 3, 1989, Accepted November 22, 1989]

Key-words: Boehmite sol, Alumina, Yttria-stabilized zirconia

1. Introduction

Recently, zirconia-based ceramics, in particular those partially stabilized with yttria, have been attracting much attention because of their high strength and toughness. Research has been carried out on the mechanisms involved in the high toughness, as well as the development of tougher, chemically stabler composite materials containing zirconia. Zirconia/alumina composites are systems in which the advantages of both components are utilized, and their structures and mechanical properties have been discussed by a number of researchers and are expected to have wide uses in industry as engineering ceramics.¹⁻⁸⁾

It is essential to achieve a homogeneous mixture of starting powders to produce high-quality zirconia/alumina composites, as is the case with all other ceramic types. The starting powders are preferably very fine, for optimum sintering. Ball milling, one of the most common processes, has a limited mixing/crushing capacity, and neutral coprecipitation, hydrolysis and thermal decomposition are extensively being used to produce fine, uniform composite powders, to investigate the sintering and mechanical characteristics of the products.⁹⁻¹¹⁾ The sinters from mixed powders are formed by a die or in the presence of an adequate binder into thin sheets. The mechanical properties of the thin sheets produced by these methods, however, are normally not very high, because of the presence of residual voids between the particles.

In this study, attempts were made to prepare high-strength, very thin zirconia/alumina composite sheets by replacing powdered alumina with an alumina hydrate. Very thin zirconia/alumina composite sheets, containing

zirconia as the major components, were prepared from a mixture of finely powdered zirconia partially stabilized with yttria and boehmite sol (alumina hydrate), to investigate the structures and strength. Partially stabilized zirconia is well known for its good sinterability.

2. Experimental Procedure

2-1. Preparation and Sintering of Green Sheets

The alumina hydrate (boehmite sol, Mitsubishi Mining and Cement), prepared by hydrolysis of aluminum alkoxide, (7wt% as Al_2O_3) was mixed with easy-to-sinter zirconia powder (partially stabilized with yttria, yttria content 5.46wt%, BET surface area: 28m²/g, average particle size: 210Å, Osaka Cement) in the presence of an adequate quantity of distilled water. The mixture was irradiated with ultrasonic waves, to uniformly disperse the zirconia in the mixture. The dispersed solution was stirred and heated, then methyl cellulose binder was added when the temperature reached 70° to 80°C. A polyethylene-base plasticizer was further added, and the mixture was allowed to cool to room temperature, after having been thoroughly stirred. The slurry thus prepared was defoamed and the viscosity adjusted under a vacuum so that it flowed slowly out of the container. It was then formed into sheets by the doctor blade method. The space between the blade and sheet was adjusted to give a sheet thickness of 0.1 to 0.3mm. The sheets were allowed to stand at room temperature to dry. It was found, after many trials, that the optimum mixture to provide good green sheets consisted 100 parts of alumina which corresponded to boehmite sol and 80 parts of the binder and plasticizer. The green sheet, after having been cut into a suitable size, was sintered at 1300°, 1400° or 1500°C in air, supported by an alumina setter. It was heated at 2°C/min and kept at a given temperature for 1h.

2-2. Analytical Procedures

The density was determined by cutting the sintered sheet into small pieces to measure the density with a Gay-Lussac pycnometer using n-butyl alcohol at 20°C.

The fracture surface, coated with gold, was observed with a SEM image analyzer accessory unit of an electron microscope (JOEL-JEM-1200EX).

X-ray measurement was made using CuK α radiation in a diffractometer (Rigaku Denki) equipped with a monochromator (Rigaku Denki R4-200).

The bending strength was measured by the 3-point

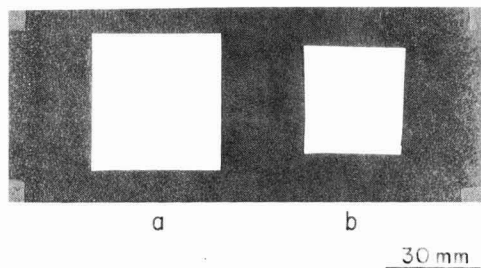


Fig. 1. Appearance of (a) green sheet prepared from yttria-stabilized zirconia powder/boehmite sol system and (b) thin sheet sintered at 1400°C.

bending test using an autograph (Shimadzu AGS-50A), with 20mm span and 0.5mm/min crosshead speed. The as-sintered body, cut out of the green sheet, was used as the specimen. It was 6 to 7mm wide, 32 to 33mm long, and 0.1 to 0.2mm thick. Bending strength (σ) and modulus of elasticity (E) were calculated by the following equations (JIS R1601 and R1602):

$$\sigma = 3PL/2wt^2$$

$$E = L^3P/4wt^3y$$

where P is the maximum load under which the specimen is broken, L is the distance between the fulcrums, w is specimen width, t is specimen thickness, and y is displacement.

A In-Ga alloy electrode layer was spread on the specimen and the resistivity (ρ) was measured by the 2-terminal dc method using a digital multimeter (Takeda Riken Kogyo) as the following equation:

$$\rho = RA/l$$

where R is resistance, A is area and l is thickness of the specimen.

3. Results

3-1. Sintering of Green Sheets

The high strength of the zirconia/alumina composite sheet was reached as expected at a high concentration of zirconia. The green sheets were prepared containing varying quantities of zirconia in a range from 50 to 100wt%. It is essential to prepare a suitable slurry when a good green sheet is to be produced by the doctor blade method. A mixture of powdered zirconia and boehmite sol cannot be made into a good green sheet without binder. There are variety of water-base binders for the doctor blade method,¹²⁾ but methyl cellulose was selected because of its compatibility with both boehmite

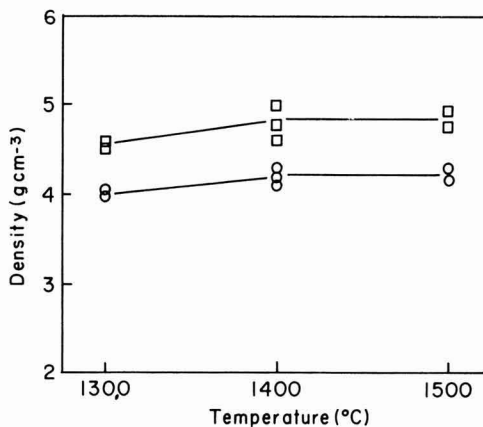


Fig. 2. Bulk density of ZrO₂/Al₂O₃ thin sheet.

- : ZrO₂/Al₂O₃ = 90/10
- : ZrO₂/Al₂O₃ = 85/15

sol and zirconia. In addition, a polyethylene-base plasticizer was used, to improve the rheological properties of the slurry and to provide flexibility to the green sheet. It was necessary to add fairly large quantities of the binder and plasticizer to the zirconia/boehmite system containing a high concentration of zirconia in order to produce good green sheets which did not crack when dried. They were sintered at 1300° to 1500°C; a temperature range in which boehmite is transformed into α -alumina.¹³⁾

The mixtures containing 85wt% and 90wt% of zirconia were sintered into good green sheets. Figure 1 shows the outer appearance of the sheet before and after sintering. The sintered sheet was white in color; the upper face, which was in contact with air while the green sheet was prepared, had a luster and the lower face, which was in contact with the film while the green sheet was prepared, had no luster. Area shrinkage by sintering ($S_1 - S_2/S_1 \times 100$) was 38 to 41%. Figure 2 shows the effects of sintering temperature in a range from 1300° to 1500°C on green sheet density. The green sheets containing 85 and 90wt% of zirconia had densities of 4.25 and 4.9g/cm³, respectively, when sintered at 1400° and 1500°C. The density of those sintered at 1300°C tended to be lower. These results suggested that the sinter was adequately densified at 1400°C. As the densities of zirconia and alumina are 5.49 and 3.98g/cm³, the above densities correspond to 81% and 92% of the theoretical, indicating that the sinter containing 90wt% of zirconia was more densified.

3-2. X-Ray Diffractometry

Figure 3 shows the X-ray diffraction patterns of the sinters prepared at 1400°C. Those of the green sheet consisting of zirconia only and the green sheet in which boehmite sol was sintered as a dry gel are also shown

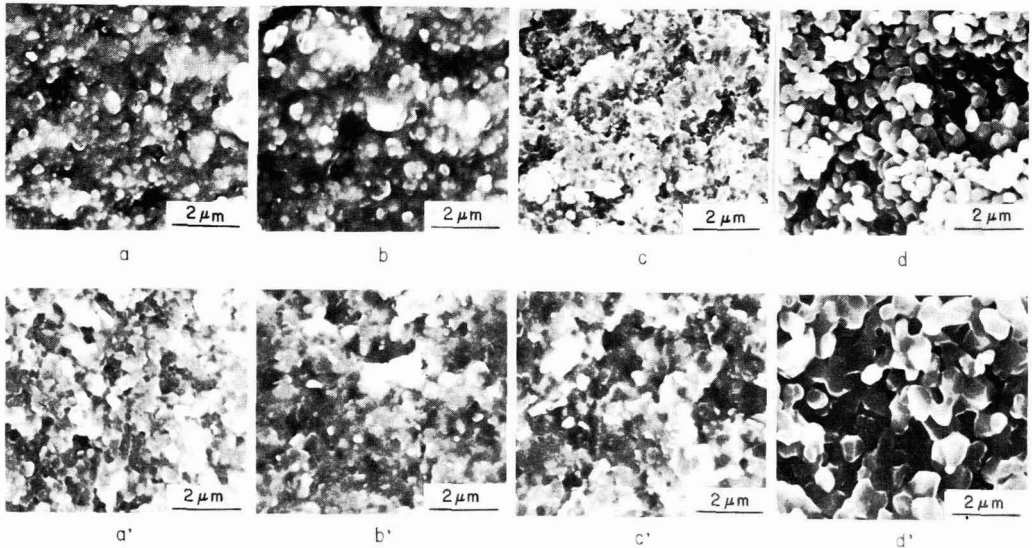


Fig. 4. SEM photographs of fracture surfaces of ZrO_2/Al_2O_3 thin sheets prepared by mixing in various ratios and sintered at 1400°C (a,b,c,d) and at 1500°C (a', b', c', d').

a,a': $ZrO_2/Al_2O_3=100/0$, b,b': $ZrO_2/Al_2O_3=90/10$,
c,c': $ZrO_2/Al_2O_3=85/15$, d,d': $ZrO_2/Al_2O_3=0/100$

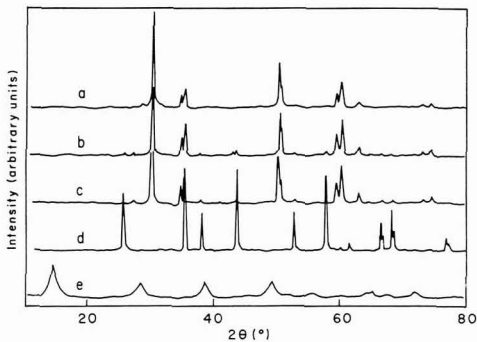


Fig. 3. X-ray powder diffraction patterns of ZrO_2/Al_2O_3 thin sheets prepared by mixing in various ratios and sintered at 1400°C.

a: $ZrO_2/Al_2O_3=100/0$
b: $ZrO_2/Al_2O_3=90/10$
c: $ZrO_2/Al_2O_3=85/15$
d: $\alpha-Al_2O_3$ from boehmite gel
e: Boehmite gel

for comparison. The diffraction peaks of zirconia, shown in Fig. 3a, were the same as those of tetragonal zirconia. The diffraction lines of boehmite gel, shown in Fig. 3e, changed significantly by sintering at 1400°C, as shown in Fig. 3d, indicating that it was transformed into α -alumina. The diffraction patterns of the sinters

containing 90 and 85wt% of zirconia (Figs. 3b and 3c) had the peaks of tetragonal zirconia and α -alumina overlapped with each other. The peaks due to α -alumina were very weak, as anticipated from the presence of high concentrations of zirconia.

3-3. Observation of Structure

Figure 4 shows the fracture surface structures of the composite sheets sintered at 1400 and 1500°C. The structures of the sinters consisting of zirconia only and the sinters in which boehmite sol was sintered as the dry gel are also shown (Figs. 4a, a', d and d'). The zirconia sinter prepared at 1400°C (Fig. 4a) consisted essentially of particles of 0.3 to 0.4 μm . Crystallization was accelerated when the temperature was increased to 1500°C, making the grains angular (Fig. 4a'). α -alumina from the boehmite gel, on the other hand, was porous when sintered at 1400°C, and the grains were partially connected to each other. The grains grew when sintered at 1500°C, but the structures contained a considerable quantity of voids and was not sufficiently monolithic. These observation results indicated that, in the preparation of the zirconia/alumina composite ceramic from the mixture of powdered zirconia and boehmite sol, increasing the zirconia content lowered the temperature at which the composite system could be sintered.

The structures of the sinter containing 90wt% of zirconia (Figs. 4b and b') resembled those of the system consisting of zirconia alone (Figs. 4a and a') in that they consisted of granular particles of relatively uniform size. The grains of the former system, however, did not become angular with crystallization as did those of the latter, and remained granular, even when sintered at

Table 1. Three-point bending strength and elastic modulus of ZrO_2/Al_2O_3 thin sheet.

Composition (wt%)	Sintering tem. (°C)	Bending strength (MPa)	Elastic modulus (GPa)
$ZrO_2/Al_2O_3=90/10$	1300	310	139
	1400	486	167
	1500	433	139
$ZrO_2/Al_2O_3=85/15$	1300	227	158
	1400	387	145
	1500	369	139
$ZrO_2/Al_2O_3=0/100$		470	284

These values are the average of three measurements.

1500°C. No further grain growth was observed. The structures of the sinters containing 85wt% of zirconia (Figs. 4c and c') were not so clearly granular as those of the systems containing 90wt% of zirconia, but on the whole angular.

3-4. Strength Tests

Table 1 gives the 3-point bending strength and modulus of elasticity of the alumina/zirconia composite sheets. Also shown are the properties of a 99.9wt% pure, 100 μ m thick alumina sheet (produced by Mitsubishi Mining and Cement). The results of sintering temperature show that sintering at 1400°C gave the highest bending strength and a high modulus of elasticity. At 1500°C, on the other hand, the bending strength was lower, though changes in modulus of elasticity were not clear. As for the effects of zirconia content, bending strength was higher at 90wt% of zirconia than at 85wt%. However, no difference was observed in modulus of elasticity between these samples.

As shown in Table 1, the sheet with the highest strength was prepared at a zirconia content of 90wt% and a sintering temperature of 1400°C. Its bending strength and modulus of elasticity were 486MPa and 167GPa. It compared favorably in bending strength and had about half the modulus of elasticity of the alumina sheet prepared by the sol-gel process.

3-5. Resistivity

The composite sheets containing 85 and 90wt% of zirconia had resistivities of 4 to 6 $\times 10^{12}$ and 2 to 4 $\times 10^{12}\Omega\cdot$ cm, respectively. Their resistivity was essentially constant, irrespective of the sintering temperature in a range from 1300° to 1500°C.

4. Discussion

Partially stabilized zirconia in which several mol% of yttria is dissolved in zirconia to form a solid solution is tetragonal (metastable phase) up to room temperature. The tetragonal phase is transformed into the monoclinic

in the presence of an external force, to relax the stress,¹⁴⁾ a characteristic which makes partially stabilized zirconia a strong and tough material. However, it loses strength at high temperatures, and also at 200° to 300°C because of the phase transformation. These phenomena greatly hinder extensive industrial applications of the material.^{15,16)} Alumina, on the other hand, is chemically stable, and loses little strength at high temperature. Therefore a high-strength, high-toughness ceramic material is expected to be developed by combining partially stabilized zirconia and alumina, and a number of researchers are studying the possibilities of the composite materials from various angles, including synthesis of the mixed powders and development of improved sintering processes.

In this study, a slurry mixture of partially stabilized zirconia, alumina hydrate, binder and plasticizer was prepared and formed into a green sheet by the doctor blade method, and sintered to produce a zirconia/alumina composite sheet. A very thin sheet which did not crack when dried was prepared by increasing the zirconia content to 85 to 90wt%. It had a bending strength of 370 to 486MPa and a modulus of elasticity of 140 to 167GPa. It is reported that a zirconia/alumina composite prepared by pressing the starting powder mixture and sintering it at 1500 to 1600°C under atmospheric pressure has a bending strength of 600 to 700MPa and a modulus of elasticity of 250GPa at a zirconia content of 90wt%.¹⁷⁾ The lower mechanical properties of the composite sheet prepared by the doctor blade method in this study may not result from the problems associated with zirconia-alumina joining, based on the structure observations (Figs. 4b and b'), but mainly from insufficient densification. A binder or plasticizer will leave behind voids or pores in the composite system, when vaporized during the sintering process, and densification is prevented as their content increases.

It is accepted that, in general, a zirconia/alumina composite has increased bending strength but decreased modulus of elasticity, as the zirconia content increases.^{17,18)} Some researchers have suggested that fracture toughness K_{IC} decreases slightly with zirconia content, and the Vickers strength is particularly high at a zirconia content of 85 to 98%.^{18,19)} It has also been reported that the addition of alumina contributes to the stabilization of the tetragonal phase of partially stabilized zirconia.²⁰⁾ Therefore, the composite sheets containing 85 to 90wt% of zirconia, prepared in this study, are expected to be strong and hard, to have low modulus of elasticity and be chemically stable. These properties are of vital importance for very thin sheets.

4. Conclusions

80 to 300 μ m thick zirconia/alumina composite sheets, containing 85 to 90wt% of zirconia, were prepared from a mixture of partially stabilized zirconia powder, boehmite sol, binder and plasticizer. The composite sheet sintered at 1400°C, which contained 90wt% of zirconia, had a density of 4.9g/cm³, bending strength of 486MPa, modulus of elasticity of 167GPa, and resistivity of 4 $\times 10^{12}\Omega\cdot$ cm.

Acknowledgments

The authors thank Mr. Ichiro Kakci of Osaka Cement for providing zirconia samples, and Messrs. Takeshi Sato, Joji Sato and Tomio Iwata of the Mitsubishi Mining and Cement Institute of Ceramic Materials for their cooperation in the preparation of the composite sheets and in the measurement of properties.

References:

- 1) N. Claussen, *J. Am. Ceram. Soc.*, 59, 49-51 (1976).
- 2) F.F. Lange and M.M. Hirlinger, *ibid.*, 67, 164-68 (1984).
- 3) A.G. Evans and A.H. Heur, *ibid.*, 63, 241 (1984).
- 4) Y. Murase, E. Kato and K. Daimon, *ibid.*, 69, 83-87 (1986).
- 5) L. Mazerolles, D. Michel and R. Portier, *ibid.*, 69, 252-55 (1986).
- 6) T. Arabori, S. Iwamoto and N. Umesaku, *Yogyo-Kyokai-shi*, 94, 742-47 (1989).
- 7) F. Wakai, H. Kato, S. Sakaguchi and N. Murayama, *ibid.*, 94, 1017-20 (1986).
- 8) F.F. Lange and D.J. Green, "Advances in Ceramics, Vol.3," The American Ceramic Society (1981), pp.217-25.
- 9) M. Kihara, T. Ogata, K. Nakamura and K. Kobayashi, *Seramikku Gakujutsu Ronbunshi* 96, 646-53 (1988).
- 10) S. Hori, M. Yoshimura, R. Kurita, S. Kaji and S. Somiya, *Yogyo-Kyokai-shi*, 92, 296-97 (1984).
- 11) K. Daimon, H. Murakami and E. Kato, *The Ceramic Society of Japan 1987 Annual Proceedings*, pp.729-30 (1987).
- 12) K. Saito, *Seramikkusu*, 18, 93-102 (1983).
- 13) K. Sakamoto, *Yogyo-Kyokai-shi*, 67, 114-25 (1959).
- 14) R.C. Garvie, R.H. Hannink and R.T. Pascoe, *Nature*, 258, 703-04 (1975).
- 15) Y. Kubota, *Kino Zairyo*, 1989, pp. 14-25.
- 16) K. Ueda, T. Tsukuma and T. Tsukidate, *The Ceramic Society of Japan 1983 Annual Proceedings*, (1983), pp.125-26.
- 17) S. Kondo, Y. Kuroshima, A. Tsukuda and S. Okada, *The Ceramic Society of Japan 1985 Annual Proceedings*, (1985), pp.655-56.
- 18) M. Rühle and N. Claussen, *J. Am. Ceram. Soc.*, 69, 195-97 (1986).
- 19) T. Ohono, M. Naka and T. Minakami, *The Ceramic Society of Japan 1985 Annual Proceedings*, (1985), pp.203-4.
- 20) Tugio Sato and Masahiko Simada, *J. Am. Ceram. Soc.*, 67, 212-213 (1984).

This article is a full translation of the article which appeared in *Nippon Seramikkusu Kyokai Gakujutsu Ronbunshi* (Japanese version), Vol.98, No.3, 1990.

Preparation of Ytterbium Iron Garnet Powder by Homogeneous Precipitation Method and Its Sintering

Hajime Haneda, Takagimi Yanagitani*, Akio Watanabe and Shin-ichi Shirasaki

National Institute for Research in Inorganic Materials

1-1, Namiki, Tsukuba, Ibaraki 305, Japan

*Konoshima Chemical Co., Ltd.

Takuma-cho, Mitoya-gun, Kagawa 769-11, Japan

$\text{Yb}_2\text{O}_3\text{-Fe}_2\text{O}_3$ powders were prepared from ytterbium and iron chloride solutions by a homogeneous precipitation method where urea was used as precipitant. The precipitation process was carried out stepwise. At first the iron hydroxide was precipitated and then the ytterbium hydroxide was formed. In the firing process of precipitated powder the ytterbium orthoferrite was formed initially from the iron oxide and ytterbium oxide, and monophasic ytterbium iron garnet was obtained above 1200°C. The reactivity and sinterability of the powder obtained by the homogeneous precipitation method were better than that of oxide mixture. The ytterbium iron garnet contained up to 0.1 to 0.2mol% iron oxide in excess of the stoichiometric composition.

[Received October 16, 1989; Accepted November 22, 1989]

Key-words: Synthesis, Homogeneous precipitation method, Sintering, Urea, Yb_2O_3 , Fe_2O_3 , Garnet

1. Introduction

Iron garnet containing rare earth elements such as yttrium has been widely studied to investigate the crystal growth and magnetic properties because of its potential use as a photomagnetic material or magnetic bubble storage.¹⁾ Yttrium iron garnet is the principal compound, for which a number of properties such as electric conductivity and defect structure have been investigated in addition to the magnetic properties.^{2,3)} Also, numerous attempts have been made to replace yttrium by another rare earth element (a typical example is $(\text{Tb}, \text{Yb})_3\text{Fe}_5\text{O}_{12}$) to improve the magnetic properties.⁴⁾ To understand this mechanism, it is necessary to obtain fundamental data on defect structures and other properties; however, there is not enough such data for iron garnet containing rare earth elements other than yttrium.

It is known that a solid solution region of about 0.5mol% lies on the Fe_2O_3 side for yttrium iron garnet.⁵⁾ However, detailed studies on the solid solution of iron garnet containing elements other than yttrium have rarely been carried out. The authors investigated the defect structure of garnet with such a narrow solid solution region by taking $\text{Yb}_2\text{O}_3\text{-Fe}_2\text{O}_3$ as an example. For this material, an adequate homogeneity of the sample must be maintained. The homogeneous precipitation method was used where urea was a precipitant to ensure the uniformity of the composition in this experiment, although the decomposition of nitrate mixtures or coprecipitation has been used for this purpose for

$\text{Y}_2\text{O}_3\text{-Fe}_2\text{O}_3$.^{5,6)}

In the homogeneous precipitation method using urea, the precipitant is formed by the hydrolysis of urea in solution by heat. With this method, the particle size and shape can be precisely controlled by controlling the hydrolysis rate of urea. Fujita et al. obtained Zn_2SnO_4 powders by this method.⁷⁾ This precipitation method can also be used for synthesizing multi-oxide powders other than single-oxide powders.

This report discusses the effect of the conditions under which Yb-Fe hydrates are prepared from Yb and iron chloride solutions using urea on the size and composition of the precipitated powder, as well as the phase relationships and sinterability of powders obtained by firing the precipitated powder.

2. Experimental

2-1. Precipitation

The required quantities of high-purity iron oxide (99.999%) supplied by Fuji Chemicals and ytterbium oxide (99.99%) supplied by Nippon Ytterbium (the impurities contained in these materials are listed in Table I) were weighed and dissolved in high-purity concentrated hydrochloric acid for analysis (supplied by Wako Pure Chemical Industries, Ltd.) of 1.4 times the theoretical quantity. This solution was used as the starting solution.

The starting solution was diluted with water in a 1l quartz beaker to achieve a metal chloride concentration of 0.034 to 0.16M and a total quantity of 300ml. The reason for using a quartz beaker was that it has higher alkali resistance than the conventional borosilicate glass

Table 1. Chemical impurity in raw materials (wt. ppm).

Fe_2O_3					
Zn 0.67	Cu 0.13	Pb 0.84	Ag 0.48	Co 0.74	
Ca 1.44	Ni 0.92	Al 0.86	Hg 1.36	Si 4.35	
Yb_2O_3					
Ce <10	Tb <10	Dy <10	Tm <20	Lu <50	
Ca <10	Fe <5				

type and is attacked less by solutes in hot water. To this diluted solution 38 to 75g urea (superhigh-purity urea from Schwartz/Mann, 2.1M/l to 4.16M/l) was added. This solution was heated from room temperature to 95 to 100°C with stirring by a magnetic stirrer. After being kept at that temperature for a prescribed time, it was poured into 1l cold water. After water was added to 2l, the solution was allowed to stand for 15 minutes, and then suction filtered. The precipitate was washed with deionized water, dried at 140°C for 48 hours, and ground in a high-purity alumina mortar to prepare the powder.

The prepared powder was calcined in air for 4 hours at various temperatures, and further ground and mixed to prepare powders for sintering.

2-2. Sintering

The oxide powders were compacted into pellets under an isostatic pressure of 200MPa, and were sintered in oxygen at the required rate and temperature for the prescribed time. Some samples were obtained by rapid cooling from the holding temperature.

For comparison, the same oxide powders were mixed in ethanol for 48 hours with a resin ball pot mill, and then sintered in the same way as the powder prepared by using urea.

2-3. Characterization of Samples

The hydrate precipitate was observed by a scanning electron microscope (SEM, Akashi Ionics, ISI-DS130) and a transmission electron microscope (TEM, JEOL JEM-4000FX). The particle size of the precipitate was measured by the light scattering method using laser light (Brookhaven Instruments Corporation, Particle Sizer BI-96). The filtrate was analyzed by ICP (Kyoto Koken UOP-2S). The phases of the sample at each stage were identified by powder X-ray diffraction (Rigaku Corporation, Geiger Flex).

Some sintered samples were thermally decomposed under pressure with sulfuric acid and hydrochloric acid to separate iron and ytterbium, so that the ratio of iron to ytterbium was determined by EDTA-Zn back titration. The composition of the other sintered samples was determined by fluorescent X-ray analysis by using the samples subjected to wet analysis as standards. For this analysis, all the samples were mirror polished to minimize the error caused by irregularities in surface conditions.

3. Results and Discussion

3-1. Preparation of Ytterbium Iron Hydrate Using Urea and Change Caused by Heating

Urea in aqueous solution is hydrolyzed by heat to form ammonia and carbon dioxide. The carbon dioxide is evolved from the system as a gas, while most of the ammonia dissolves in the water solution, increasing the pH of the solution. Figure 1(a) shows the change in pH with increasing temperature for a ytterbium iron and urea solution (Yb/Fe=3/5) that was initially acidified

with hydrochloric acid. As Kim et al. pointed out,⁸⁾ the pH value decreases temporarily with increasing temperature, but the hydrolysis of urea accelerates at about 50°C, when the pH value begins to increase. Under the conditions used for this figure, the pH value is temporarily stabilized at about 1.6 by the deposition of iron, and then rapidly increases again. The change in pH slows down at about 5 because of the deposition of ytterbium. At about 5.6, the pH value levels off and the reaction ends. When the sample is allowed to stand with heating for a long period of time, the pH value is slightly decreased by the evolution of ammonia.

The yield of each element was determined as the precipitate in the above-mentioned process by pouring the reaction solution into cold water to stop the reaction and by analyzing the filtrate. As indicated in Fig.1(b), the precipitate is not formed by coprecipitation, but hydrates are deposited in multiple steps. It is therefore concluded that the primary particles consist of separate elements. When the sample is heated for a long period of time, some ammonia is evolved from the system, decreasing the pH value and causing the redissolution of some ytterbium under the conditions of Fig.1, decreasing the yield. It can be seen from the above discussion that a precipitate having the same composition as that of the starting solution is formed by stopping the reaction about 2 hours after heating.

Figure 1(a) includes the pH value of samples rapidly cooled to room temperature. Ytterbium hydroxide precipitates at a pH value above 7 to 8 at room temperature. To achieve the precipitation of the stoichiometric composition, the final pH adjustment at room temperature is important. Even if the starting solution is diluted ($\Delta[\text{Yb}]/[\text{Yb}] < 0.001$) can be attained at a pH value of about 7.5 to 8. In this case, the pH value can be adjusted by changing the concentration of urea with respect to the metallic ions. This is shown in Fig.1(c). With an increasing concentration of urea, the final pH value increases and the reaction time is shortened. When the ratio of metallic ion to urea was kept constant, the change in pH was similar within the experimental error independent of concentration in this experiment.

Figure 2 shows the TEM and SEM photographs of the precipitated powder. As seen from these photographs, the primary particles of about 200 to 400Å aggregate to form secondary particles. The change in secondary particle size with pH was determined by the light scattering method. The result is shown in Fig.1(d). This figure indicates that the particles formed initially have a size of about 300Å. These particles are estimated to be primary particles from the SEM and TEM photographs. While iron hydroxide precipitates, the secondary particles grow slowly, but they grow rapidly with the formation of ytterbium hydroxide. The process of precipitate growth is schematically shown in Fig.3. Considering that the size of primary particles shown in SEM or TEM photographs does not change greatly, and that the secondary particles grow significantly at high pH values as compared with the volume ratio of ytterbium hydroxide (Yb(OH)₃/Fe(OH)₃=3/5), the process of precipitate growth is considered to be as follows. Ytterbium does not form a coating film on the surface of iron hydroxide, but forms

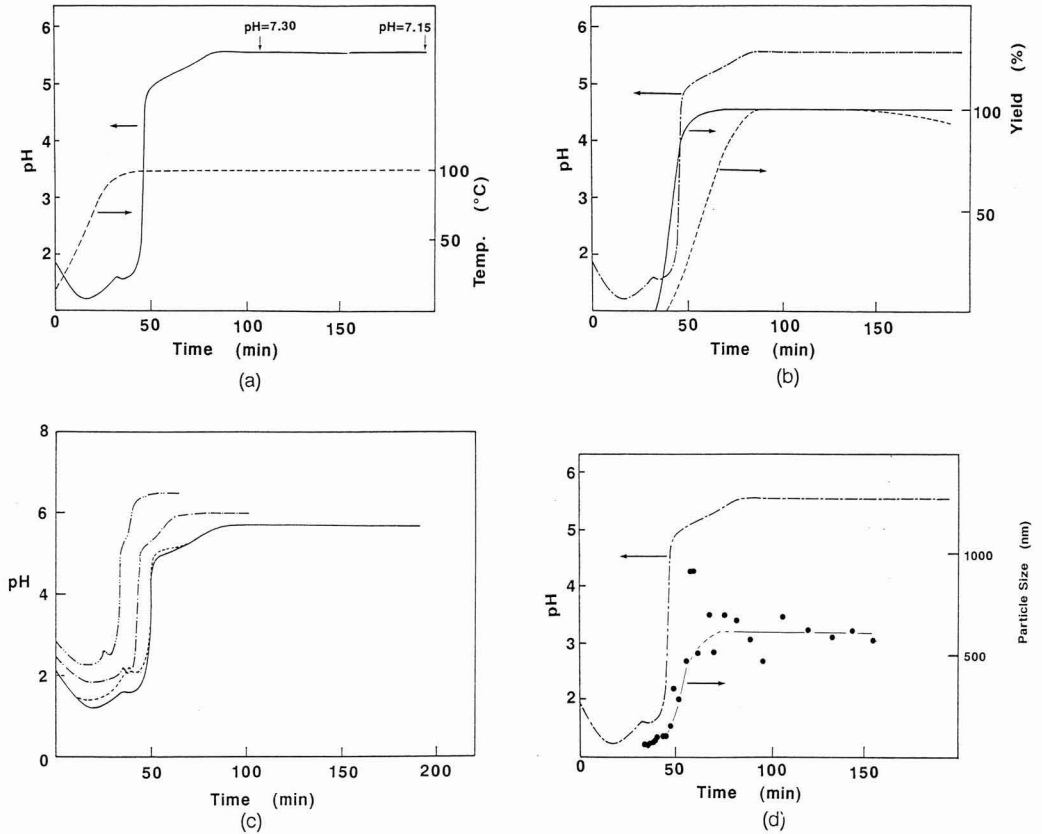


Fig. 1. Changes of pH, temperature, precipitate yields and particle size with reaction time.

(a) Temperature and pH changes (metal chloride; 0.16M/l, and urea; 2.1M/l).

(b) Yields of Fe-hydroxide (—) and Yb-hydroxide (- - - -).

(c) pH changes in the solutions with various concentration.

— ; 0.16M/l metal chloride, 2.1M/l urea.

- - - - ; 0.08M/l metal chloride, 1.0M/l urea.

- · - · - · ; 0.08M/l metal chloride, 2.1M/l urea.

- · · · - · ; 0.034M/l metal chloride, 2.1M/l urea.

(d) Change of particle size of precipitated powder (metal chloride; 0.16M/l, and urea; 2.1M/l).

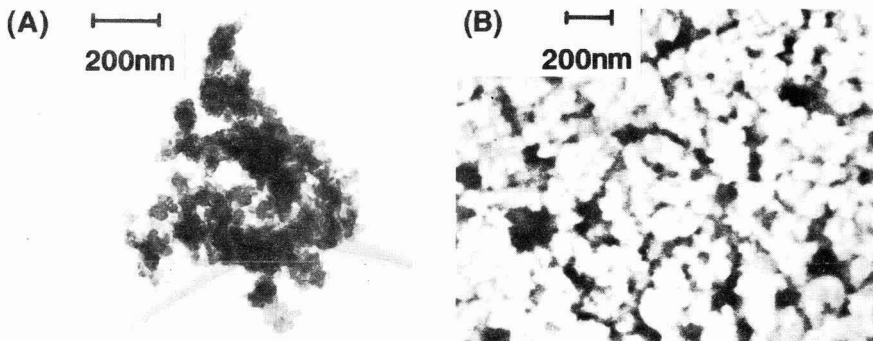


Fig. 2. TEM, (A) and SEM, (B) Photographs of the precipitated powder (metal chloride; 0.16M/l, and urea; 2.1M/l).

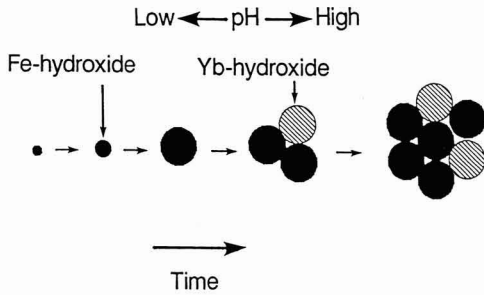


Fig. 3. Schematic drawing of precipitation growth.

primary particles independent of iron hydroxide, and the primary particles of ytterbium hydroxide grow to larger secondary particles while being incorporated by the secondary particles of iron hydroxide that have been formed. Therefore, the reaction accompanying the heating of dried sample is the reaction between the primary particles with different compositions. The final size of the secondary particle depends on the concentration of urea, and the particle size decreases with an increase in urea content with regard to metallic ion.

Figure 4 shows the thermogravimetric curve of precipitated powder. The thermal decomposition temperature is unclear; water is gradually liberated, and the decomposition ends at about 700°C. The change in weight was nearly the same as that obtained by assuming that the precipitate was hydroxide.

The results of powder X-ray diffraction revealed that the precipitated powder had nearly an amorphous pattern, but a very weak peak seemed to be caused by β -FeOOH was observed (Fig.5). Corresponding to this, the electron diffraction analysis pattern had an amorphous spot, though very weak, in the amorphous halo. It is however inferred from the thermogravimetry that the quantity is very small. No clear peak appeared in DTA since the thermal decomposition took place slowly and the reaction proceeded slowly.

At the time when the thermal decomposition had almost ended, a peak consisting of orthoferrite and α -Fe₂O₃ appeared, and the garnet phase did not exist. When the reaction had proceeded sufficiently at 1200°C (12h in air), a single phase of ytterbium was obtained. Compared with the solid state reaction between oxides, the reaction between solid-state oxides, in which unreacted ytterbium oxide and α -Fe₂O₃ orthoferrite phases remain even at 1200°C, is inferior in reactivity to the reaction of powder prepared by using urea. The above discussion suggests that the reaction process of starting powder prepared by using urea is as shown in Fig.6. The respective primary particles independently undergo thermal decomposition, while ytterbium oxide reacts with iron oxide to form orthoferrite. The remaining iron is present as iron oxide. As the reaction proceeds further, orthoferrite reacts with the remaining iron to form garnet.

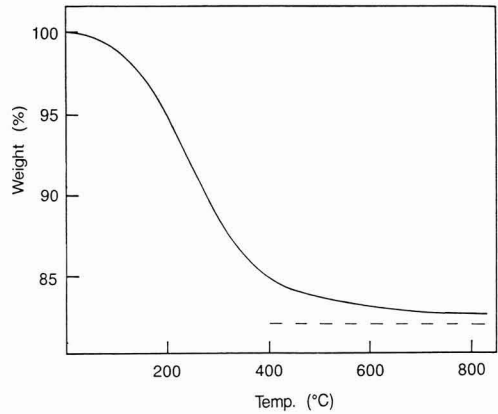


Fig. 4. TG curve of precipitated powder. Dashed line, theoretical value, assuming the precipitate to be hydroxide.

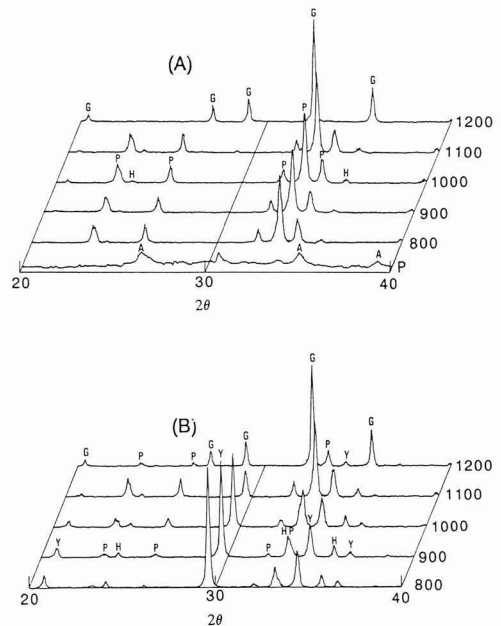


Fig. 5. X-ray patterns of fired precipitated powders and oxide mixture. (A) Precipitated powder, P and numbers at right side denoting precipitate and firing temperature (in °C), respectively. G, garnet, H, hematite, Y, ytterbium oxide, P, ytterbium orthoferrite, and A, α -FeOOH peaks, respectively. (B) Mixture of iron oxide and ytterbium oxide being the same as the starting materials for homogeneous precipitation.

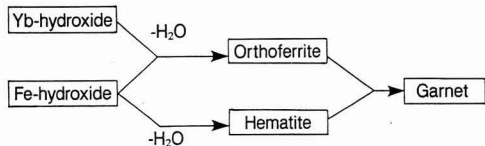


Fig. 6. Reaction process at firing of precipitated powder.

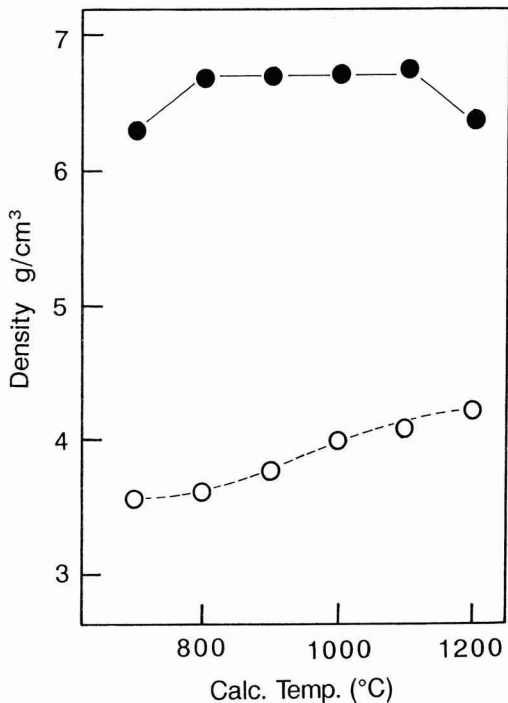


Fig. 7. Sintered and green densities as a function of calcination temperature. ---○---; green density, ●—; sintered density.

3-2. Sintering of Powders Prepared by Using Urea

An attempt was made to sinter the powders calcined at various temperatures. Figure 7 shows the density as a function of calcination temperature for powders fired for 4 hours and sintered in oxygen at a rate of 4°C/min at 1400°C for 12 hours. There is a temperature range where the sintered density is optimum, as with the conventional case, though the range is not so clear, high-density sintered bodies were obtained at temperatures between 800° and 1100°C. For the samples fired at 1200°C, the reaction produces monophasic garnet, but the activity has already been lost, no adequate density

being attained. If the activity is maintained even though some unreacted substances exist during calcination, sintering is not hindered. Figure 8 shows the relationship between sintered density and temperature for the precipitated powder and oxide mixture powder calcined at 800°C. Both the powders consist of monophasic garnet at 1400°C as far as the powder X-ray diffraction pattern shows. When the powder calcined at a temperature below 1200°C was used as described in the preceding section, however, a single phase was not formed in the course of sintering. The major phases are iron oxide and ytterbium oxide for oxide mixture powder, while they are orthoferrite and iron oxide for precipitated powder. For oxide mixture powder, contraction hardly occurred until 1350°C, and expansion at 1350°C. For precipitated powder, the density increased suddenly at about 1100°C and reached the theoretical value at 1400°C. Figure 9 shows an optical micrograph of a thermally etched surface mirror polished for a sintered body from precipitated powder. In this micrograph, no appreciable voids are observed. For the oxide mixture, many pores are found, which means poor sinterability. In addition, Fe₂O₃ phase, which was not found in X-ray diffraction, was observed, which means poor reactivity.

To investigate the effect of composition on sinterability, sintered bodies with various compositions were

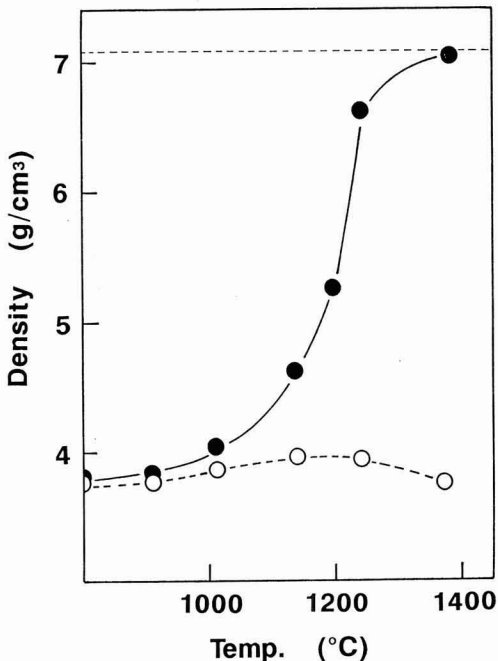


Fig. 8. Comparison of sintered densities of the powders for precipitate and oxide mixture calcined at 800°C. ●—; precipitate, ---○---; oxide mixture. Dashed line, theoretical value from the lattice constant.

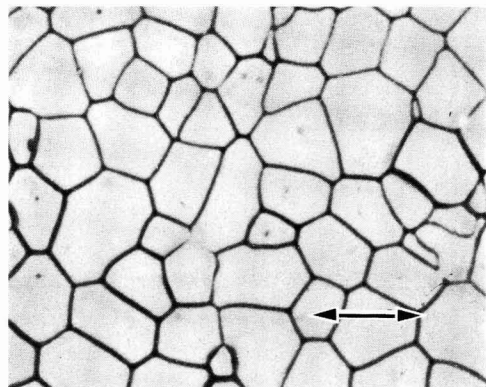


Fig. 9. Optical micrograph of thermal etched $\text{Yb}_3\text{Fe}_3\text{O}_{12}$ surface sintered at 1400°C for the homogeneous precipitated powder. (bar = 20 μm)

prepared. The composition was determined mainly by fluorescent X-ray analysis, by which the composition percentage can be obtained with an accuracy of about 0.1%. Figure 10 shows the sintered density and grain size as a function of composition. Sintering was carried out in oxygen at 1400°C for 12 hours by using powders calcined at 800°C . The sintered density was determined by the pore area on a sample surface that was mirror polished. As seen from the figure, the sintered density decreased with the change in composition by several percent, though it was unchanged at the stoichiometric composition. This is because the different phase deposited hinders high densification above 99%. This tendency has been found in sintered yttrium aluminum garnet.⁹⁾ The grain size increased significantly at a composition of about 0.1mol% iron in excess of the stoichiometric composition. This tendency agrees well with that of yttrium iron garnet.⁵⁾

3-3. Solid Solution of Iron Oxide in Ytterbium Iron Garnet

It is known that yttrium iron garnet contains some iron oxide in the solid state at high temperatures.⁹⁾ For other iron garnet systems, such a solid solution of iron oxide has not been confirmed. For precipitated powders that have good sinterability and reactivity, this solid solution of small amount can be investigated. This report deals with the solid solution in $\text{Yb}_2\text{O}_3\text{-Fe}_2\text{O}_3$ system in oxygen at 1400°C . The sample was sintered in oxygen at 1400°C for 12 hours, and then cooled rapidly. Rapid cooling was achieved by dropping the sample onto an adequately cooled copper plate to eliminate the effect of water. The phase was determined by the integrated intensity ratio of X-ray diffraction peaks from the (420) plane of $\text{Yb}_3\text{Fe}_3\text{O}_{12}$ and the (112) plane of YbFeO_3 on the orthoferrite side. The diffraction intensity of YbFeO_3 was so strong that a phase of about 0.5% (intensity ratio of 0.6%) could be detected. Iron oxide does not appear in a powder X-ray diffrac-

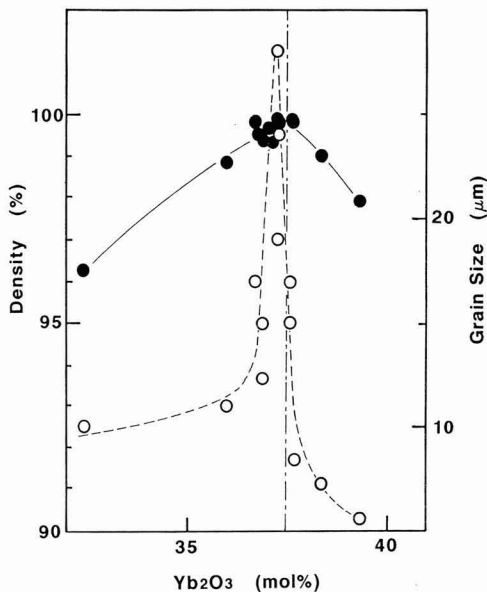


Fig. 10. Sintering and grain growth of ytterbium iron garnet powder from precipitation as a function of composition. —●—; sintered density, ---○---; grain size, dashed line, stoichiometric composition.

tion pattern even if about 1% is present. Therefore, the amount of phase was determined by observing mirror polished surfaces by optical microscopy (the limit is about 0.1%). The precise lattice constant was determined by X-ray diffraction with silicon standard, by using the common method for determining solid solution limits.

Figure 11 shows the amount of phases as a function of composition. The calculated amount of deposited iron oxide in the case where there is no solid solution of iron oxide is shown in the figure. The curve of observed values is on the iron oxide side as compared with the calculated value, which means that there is a solid solution of iron oxide in the ytterbium system like the yttrium system. On the orthoferrite side, the curve converges at the stoichiometric composition, which means that a solid solution is not observed on the Yb_2O_3 side. Figure 11 suggests that the solid solution limit of iron oxide is about 0.2mol%.

Figure 12 shows the lattice constants of samples. The lattice constant was small on the iron oxide side as in the YIG system.⁶⁾ On the Yb_2O_3 side, the lattice constant was already constant near the stoichiometric composition. This means that there is no significant solid solution on this side as concluded by the observation of phases. In the YIG system, the lattice constant and the solid solution amount of iron oxide changed linearly. Therefore, the lattice constant changes with

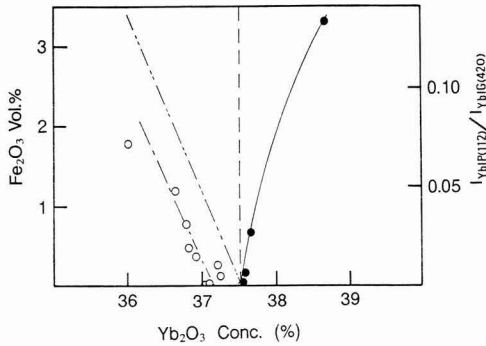


Fig. 11. Amount of second phases as a function of composition. ---○---; amounts of hematite by means of optical microscopy, —●—; ratio of ytterbium orthoferrite (112) plane of X-ray intensity to ytterbium iron garnet (420).

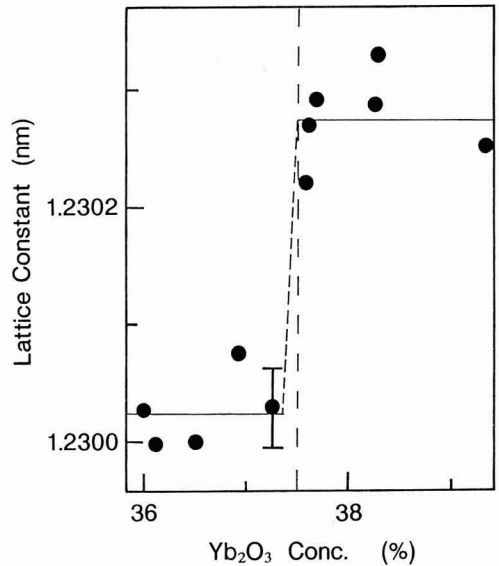


Fig. 12. Lattice constants of ytterbium iron garnet in system $\text{Yb}_2\text{O}_3\text{-Fe}_2\text{O}_3$.

the solid solution amount of iron oxide by the following equation:

$$a = a_0(1-kx) \quad \dots\dots(1)$$

where, a_0 is the lattice constant at the stoichiometric composition, x is the solid solution amount of iron oxide, a is lattice constant, and k is the proportional constant. By normalizing the change of lattice constant by stoichiometric composition, the above equation is converted into Eq.(2).

$$\Delta a/a_0 = (a-a_0)/a_0 = kx \quad \dots\dots(2)$$

According to Paladino et al., in the YIG system, $x=0.25\%$, $a=12.3761$, and $a_0=12.3810$ at 1400°C . Therefore, the proportional constant k becomes 1.58×10^{-3} . In the $\text{Yb}_2\text{O}_3\text{-Fe}_2\text{O}_3$ system as well, Vegard's Law holds. Assuming that the constant k is not dependent on the type of rare earth element, the solid solution amount of iron oxide at 1400°C is 0.13% because $\Delta a/a_0$ in this report is calculated to be 2.0×10^{-4} from Fig.12. This value may be reasonable, considering the observation limit of phases of 0.1% in optical microscopy as described earlier.

4. Conclusions

Ytterbium-iron hydrate was synthesized by the homogeneous precipitation method where urea was used as a precipitant. By using this as the starting material, the sintering of ytterbium iron garnet and the solid solution of iron oxide was investigated. The conclusions are as follows:

- 1) The precipitation process was in two steps. At first iron hydroxide was precipitated. At the later stage where the pH value was higher, amorphous precipitate of ytterbium hydroxide was formed. Therefore, the precipitate was present as a mixture of particles of hydroxides. The particle size of precipitate was 20 to 50nm at the earlier stage, and 100 to 600nm when the reaction ended.
- 2) Monophase ytterbium iron garnet was obtained when the precipitated powder was calcined at 1200°C . Sufficiently high reactivity was proved as compared with the oxide mixture.
- 3) It was found that ytterbium iron garnet contained 0.13 to 0.2% iron oxide in excess of the stoichiometric composition at 1400°C .
- 4) The sinterability of the powder obtained by the homogeneous precipitation method was better than that of the oxide mixture. The presence of small amounts of different phases had little effect on the sinterability.

In summary, a sintered body with uniform and almost theoretical density was obtained in the $\text{Yb}_2\text{O}_3\text{-Fe}_2\text{O}_3$ system prepared by the homogeneous precipitation method using urea.

Acknowledgments:

The authors wish to thank M. Kobayashi and S. Takenouchi at the National Institute for Research in Inorganic Materials for their cooperation in wet analyzing samples, M. Tsutsumi at the National Institute for Research in Inorganic Materials for his cooperation in taking SEM photographs, and M. Yokoyama at the National Institute for Research in Inorganic Materials for his cooperation in taking TEM photographs.

References:

- 1) For example, "Physics of Magnetic Garnet", ed. by A. Paoletti, North-Holland Publishing Co., Amsterdam, 1978.
- 2) A.E. Paladino, E.A. Maguire and L.D. Rubin, *J. Amer. Ceram. Soc.*, **47**, 280 (1964).
- 3) R. Metselaar and M.A.H. Huyberts, *J. Sol. State Chem.*, **22**, 309 (1977).
- 4) K. Machida, Y. Asahara, H. Ishikawa, K. Nakajima and Y. Fujii, *J. Appl. Phys.*, **61**, 3256-58 (1987).
- 5) A.E. Paladino and E.A. Maguire, *J. Amer. Ceram. Soc.*, **53**, 98-102 (1970).
- 6) H.J. Van Hook, *J. Amer. Ceram. Soc.*, **44**, 208-214 (1961).
- 7) K. Fujita, K. Kato and M. Mitsuzawa, *Yogyo-Kyokai-Shi*, **96**, 6-8 (1987).
- 8) Kim, I. Yasui, *Yogyo-Kyokai-Shi*, **95**, 442-449 (1987).
- 9) H. Haneda, A. Watanabe, S. Matsuda, T. Sakai and S. Shirasaki, "Sintering '87", ed. by S. Somiya, M. Shimada, M. Yoshimura and R. Watanabe, Elsevier Science Publishers (1988) pp.381-386.

This article is a full translation of the article which appeared in *Nippon Seramikkusu Kyokai Gakujutsu Ronbunshi* (Japanese version), Vol.98, No.3, 1990.

Effect of Oxidation for Hot-Pressed β -Sialon-SiC Composites

Hiroshi Nakamura, Seiki Umabayashi* and Kazushi Kishi*

Research & Development Centre, Mitsui Mining Co., Ltd.

1, Kou-machi, Tochigi-shi 328, Japan

* Government Industrial Research Institute, Kyushu

Shuku-machi, Tosu-shi 841, Japan

β -sialon with $z=1(+4)$, $z=2(+4)$ and $z=3(+4)$ ($\text{Si}_{6-z}\text{Al}_z\text{O}_{8-z}\text{N}_{8-z}$; $z=0-4.2$, +4: 4eq% excess oxygen over the each z number) from a powder mixture of $\alpha\text{-Si}_3\text{N}_4$, $\alpha\text{-Al}_2\text{O}_3$, AlN and SiC was hot pressed to produce β -sialon-SiC composites. The hot-pressed β -sialon-SiC composites were oxidized in an electric furnace at 1300°C for 100 hours. Bending strength, weight gain, surface roughness and optical microscopic observation of sintered materials were carried out after oxidation. The results are obtained as follows.

- (1) The weight gain of the composite decreased slightly by the addition of SiC.
- (2) The bending strength of the composites was slightly improved after oxidation.
- (3) Weight gain of the composites was little increased as the z number increased, but pitting was observed on the surface of $z=2(+4)$ and $z=3(+4)$ β -sialon-50wt%SiC composites.

[Received October 16, 1989; Accepted December 11, 1989]

Key-words; β -Sialon, SiC, Composite, Hot-press, Oxidation, Bending strength

1. Introduction

β -sialon has high oxidation resistance and high erosion resistance at high temperature, and also has an excellent corrosion resistance against molten metal. Silicon carbide has a high mechanical strength at high temperature, and is therefore expected to be a useful structural material for high temperature use. Sintered bodies of both materials are being used in advanced applications such as gas turbine parts and diesel engine parts, and so the oxidation behavior of these materials in high temperature environments have been investigated by various methods. For instance, Hasegawa et al.^{1,2)} and Kishi et al.³⁾ reported on the oxidation behavior of sintered β -sialon. Sata et al.⁴⁾ reported on the oxidation of powder sialon. Dongliang⁵⁾ reported on the effect of additives on the oxidation behavior of sintered SiC. According to these various reports, cristobalite and mullite are formed on the surface of sintered sialon with the progress of oxidation. For sintered composites of sialon with silicon carbide added, however, there has been little research published on its oxidation behavior, except for the report by Kishi et al.,⁶⁾ which is the only one known to the authors.

Sintered materials of β -sialon-SiC composite were prepared by the following process. First, a powder

mixture of $\alpha\text{-Si}_3\text{N}_4$, $\alpha\text{-Al}_2\text{O}_3$ and AlN was prepared by blending these three materials in various ratios to form the compositions of β -sialon ($\text{Si}_{6-z}\text{Al}_z\text{O}_{8-z}\text{N}_{8-z}$) with z numbers 1, 2 and 3, containing excess oxygen by 4 equivalent % over the content required by the z number (this is expressed here as $z=1(+4)$, $2(+4)$ and $3(+4)$). Then SiC powder was added to this powder, and the mixture was hot-pressed to form sintered β -sialon-SiC composites.

The effect of SiC addition on the oxidation behavior of the sintered composite was investigated.

2. Experimental Procedure

2-1. Samples

Table 1 shows the average particle sizes of the starting powders of $\alpha\text{-Si}_3\text{N}_4$, $\alpha\text{-Al}_2\text{O}_3$, AlN and SiC used in our experiments. A 500g of powder mixture was prepared by weighing of $\alpha\text{-Si}_3\text{N}_4$, $\alpha\text{-Al}_2\text{O}_3$ and AlN in the required ratio to make β -sialon with $z=1(+4)$, and this mixture was put into a 1l teflon vessel, A 400g of ethanol and 30 balls of Si_3N_4 of 15mm in diameter added, and wet-mixed at 100rpm for 48h. The wet-mixed powder was dried completely. SiC powder of average particle size 0.7 μm was added 5, 10, 15, 30 and 50wt% to make the total weight 50g. The SiC-containing powder was placed into a 250ml polyethylene vessel, 40g of ethanol with Si_3N_4 balls of 10mm diameter, and wet-mixed at 130rpm for 24h. Moreover, powder mixtures of $\alpha\text{-Si}_3\text{N}_4$, $\alpha\text{-Al}_2\text{O}_3$ and AlN of $z=2(+4)$ and $z=3(+4)$ containing SiC powder at 50wt% were also prepared in the same way. The powder mixture obtained was dried under a reduced pressure and used as the starting material for sintering.

Table 1. Starting powders.

Powder	supplier	Av. Particle Size (μm)
$\alpha\text{-Si}_3\text{N}_4$	Toyo Soda	0.6
$\alpha\text{-Al}_2\text{O}_3$	Iwatani kagaku	0.8
AlN	Toshiba Ceramics	3.0
$\alpha\text{-SiC}$	H.C. Starck	0.7

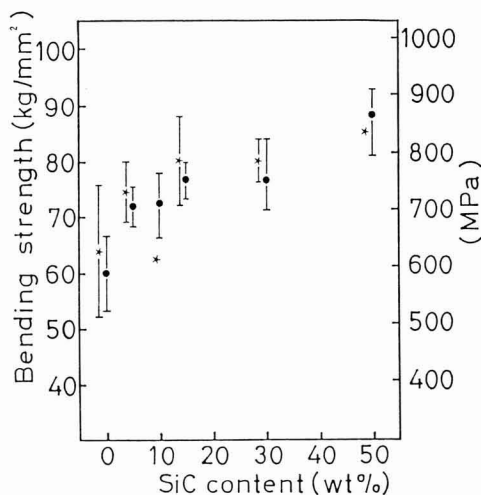


Fig. 1. Bending strength of sintered materials before oxidation (●) and after oxidation (★).

2-2. Oxidation Test of Sintered Composites

Each 20g of the starting material was hot-pressed in a 30×30mm rectangular carbon mold at 1850°C for 60 min under a pressure of 300kg/cm². After grinding the surface of the hot-pressed material using a #270 diamond grinding wheel, test pieces 30mm length and 3×3mm in a cross section were cut out from the sintered material. The test pieces were finished by lapping three faces of each test piece by using a 6μm diamond disk.

For the oxidation test, a test piece was washed by a supersonic cleaning technique in acetone, and then placed with the ends on sintered SiC blocks in the testing apparatus so that the whole test piece was oxidized uniformly. A Kanthal super furnace (with inside dimensions of 200×200×200mm) was used for the oxidation test at 1300°C in air for 100h. For comparison, the same oxidation test was carried out with SC-850, a type of sintered SiC made by Ibiden Co. After the oxidation test, the weight gain, surface roughness and three-point bending strength of the test pieces was measured, and the surface crystalline phases analyzed by X-ray diffraction method. Crystalline phases formed on the surface were identified by X-ray diffraction analysis by setting a test piece on a jig made of aluminum. The conditions used for X-ray diffraction method were applied voltage 40kV, current 30mA, scanning velocity 1°/min, slit widths 0.1 - 1-0.6mm, and a carbon monochromator used. The surface of the test piece was observed with an optical microscope, and the surface roughness measured by using a needle tracer method. The bending strength of the sintered materials both before and after oxidation was measured by the three-point bending strength measurement, testing 4 samples for each hot-pressed sinters, and the testing conditions were span distance 19mm and

crosshead speed 0.5mm/min.

3. Results and Discussion

3-1. Bending Strength of Sintered Materials

Figure 1 shows the bending strength at room temperature of sintered β -sialon and sintered β -sialon-SiC composites before and after oxidation. The bending strength of the sintered materials tended to show a slight increase after oxidation, and this trend of strength increase was remarkable when the sintered composite contained SiC of less than 30wt%. Presumably the bending strength of these sintered materials increased after oxidation because SiO₂ phase or glassy phase was formed in the oxidation process of the sintered materials, which made the defects on the surface of sintered materials less sensitive to fracture. The results obtained of an increase in bending strength of these sintered materials after oxidation agreed with those reported by Hasegawa et al.^{1,2)} The authors had also previously confirmed the increased bending strength of sintered Si₃N₄-50wt%SiC composite after oxidation.⁷⁾

3-2. Weight Gain and Crystalline Phases of Sintered Materials after Oxidation

Table 2 shows the weight gain due to oxidation of β -sialon sintered materials with $z=1(+4)$, β -sialon-SiC composite and commercially available SiC, as well as the crystalline phases identified in the surface layers of the materials after oxidation. In the case of sintered β -sialon, the weight gain after oxidation was 0.24mg/cm², but in the case of sintered β -sialon-SiC composite, it gradually decreased to 0.14mg/cm² with an increase in SiC content. In the case of sintered SiC, the weight gain after oxidation was 0.00mg/cm², which was measured for comparison. This result indicates that weight gain due to oxidation is lower in the case of sintered SiC than that of sintered β -sialon and sintered β -sialon-SiC composite.

Crystalline phases at the surface of the sintered materials after oxidation were identified as α -SiO₂ (cristobalite) in sintered β -sialon and sintered β -sialon-SiC composites. In the case of sintered SiC, the crystalline phase at the surface was also α -SiO₂.

Table 2. Weight gain and crystal phases of sintered materials after oxidation.

Material	Weight Gain (mg/cm ²)	Crystal Phase after Oxidation
β -Sialon Z=1(+4)	0.24	α -SiO ₂
5wt% SiC	0.17	α -SiO ₂
10wt% SiC	0.19	α -SiO ₂
15wt% SiC	0.13	α -SiO ₂
30wt% SiC	0.10	α -SiO ₂
50wt% SiC	0.14	α -SiO ₂
SiC(SC-850)	0.00	α -SiO ₂

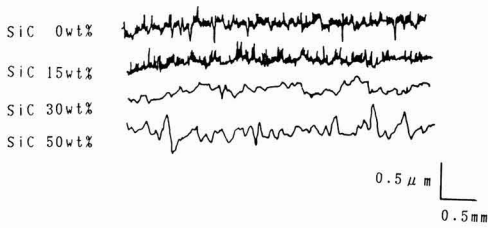


Fig. 2. Surface roughness of sintered materials after oxidation.

3-3. Relationship between SiC Content and Surface Roughness of Sintered Materials after Oxidation

Both sintered β -sialon with $z=1(+4)$ and sintered composites of β -sialon with $z=1(+4)$ and various SiC contents had little difference in surface roughness before and after oxidation, and the surface roughness was commonly measured as $0.03\mu\text{m} R_{\text{av}}$. However, as shown in Fig. 2, with the increase in SiC content of β -sialon, the surface condition of the sintered β -sialon-SiC composite after the oxidation test gradually changed, with the fine roughness on the surface tending to decrease, making the surface smooth. As a result, an increased SiC content in the sintered β -sialon-SiC composite brought an increased gloss on the surface of the sintered composite, making the surface shiny. In contrast, when sintered Si_3N_4 -50wt%SiC composite was oxidized under the same conditions, no similar shiny surface was resulted, but instead the surface was roughened and lost its gloss. We have not clarified why the surface condition of this composite after oxidation changed with the increase in SiC content, but we suppose that SiO_2 formed by oxidation of SiC on the surface reacted with the aluminum silicate formed by oxidation of sialon, forming amorphous films on the surface of the sintered composite, and these films covered the surface of sintered composite uniformly, so, this surface became glossy.

3-4. Relationship between z Number in β -sialon and Surface Roughness of Sintered Materials

Table 3 shows the surface roughness of the sintered β -sialon-SiC composite after oxidation, in which the z number of β -sialon was $z=1(+4)$, $2(+4)$ and $3(+4)$ and the content of SiC was 50wt% respectively. Figure 3 shows microscope observation of the surface of the sintered β -sialon-50wt%SiC composite after oxidation, in which the z number of β -sialon was $2(+4)$ and $3(+4)$. The surface roughness of the sintered β -sialon-SiC composite increased with an increase of z number of β -sialon. This increase in surface roughness was caused by pitting on the surface of the sintered β -sialon-SiC composites after oxidation, as shown in Fig. 3. Figure 4 shows a microscope observation of the surface of sintered SiC after oxidation, which is compared with those of sintered β -sialon-SiC composites. It can be seen that the surface

of the sintered SiC after oxidation was covered by α - SiO_2 films and these films were cracked during the cooling. In the case of sintered β -sialon-SiC composites after oxidation, the crystalline phase at the surface was α - SiO_2 , as in the case of sintered SiC, but no crack formation was observed.

Table 3. Surface roughness of sintered materials after oxidation.

Material	Surface Roughness	
	$R_{\text{av}} (\mu\text{m})$	$R_{\text{max}} (\mu\text{m})$
Z=1(+4) 50wt% SiC	0.03	0.19
Z=2(+4) 50wt% SiC	0.09	1.05
Z=3(+4) 50wt% SiC	0.59	3.50

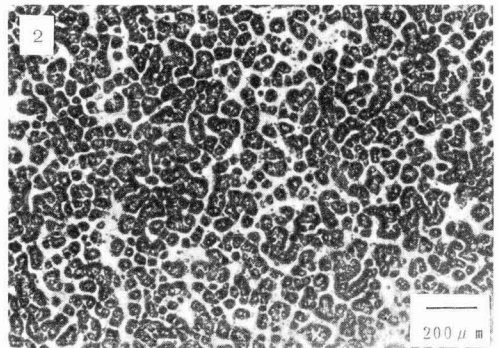
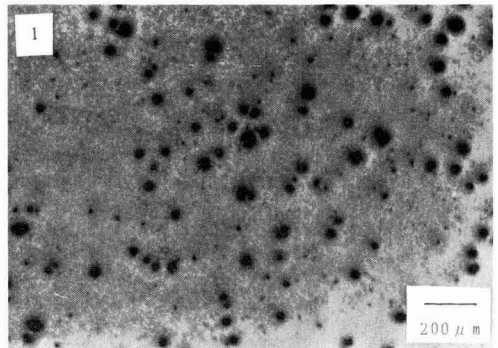


Fig. 3. Optical microscope photograph of sintered materials after oxidation.

- 1) Z=2(+4) + 50wt% SiC
- 2) Z=3(+4) + 50wt% SiC

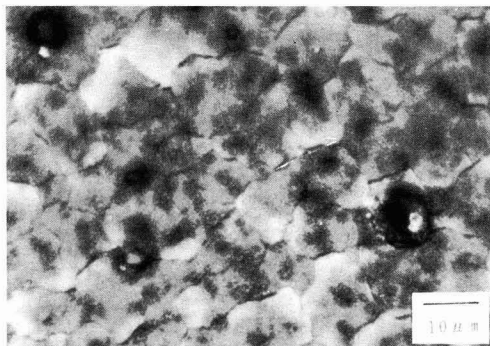
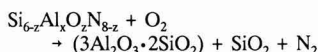


Fig. 4. Optical microscope photograph of sintered SiC (SC-850) after oxidation.

3.5. Relationship between z Number and Oxidation Behavior of Sintered Materials

Table 4 shows weight gain after oxidation of various sintered β -sialon-50wt%SiC composites, with different β -sialon z numbers. It was shown that the weight gain of these sintered composites became a little greater with an increase of z number, and that the crystalline phase at the surface of these sintered composites was always α -SiO₂. In Fig. 3, pitting was not observed on the surface of the sintered β -sialon-SiC composites, with z=2(+4) and z=3(+4), but pitting was not observed when β -sialon had a composition with z=1(+4). Therefore, the surface conditions of sintered β -sialon-SiC composites apparently differed depending upon their z number.

According to Kobayashi et al.⁹⁾ the oxidation of sintered sialon is described by the following equation.



They reported that the crystalline phases formed in oxide films after oxidation of sintered sialon were solid solutions of mullite and cristobalite, or aluminosilicates containing these two compositions, and that a higher z number in sialon, or a higher content of Al and O in sialon in solid solution, formed a greater amount of mullite, and a smaller z number in sialon formed a remarkably high amount of cristobalite. In the case of our experiments, however, we detected no crystalline phase of mullite in the oxide films in either sintered β -sialon or sintered β -sialon-SiC composite.

Hasegawa et al.¹⁾ reported the results of the oxidation test at 1300°C for 720h using sintered sialon with compositions of various z numbers from 1 to 4. According to their results, dense phases filled with silicate glass were formed in the crystal boundaries between cristobalite and mullite in the case of sialon with a small z number, but the contents of cristobalite and glass phases decreased and porous oxide films formed of fine mullite crystals appeared in the case of sialon with

Table 4. Weight gain of sintered materials after oxidation.

Material	Weight Gain (mg/cm ²)
Z=1(+4) 50wt% SiC	0.14
Z=2(+4) 50wt% SiC	0.17
Z=3(+4) 50wt% SiC	0.17

a large z number. They reported also that the smaller the z number, the larger the weight gain due to oxidation observed and the smaller the film thickness formed.

In our experiments using sintered β -sialon-SiC composites, the weight gain of the materials due to oxidation became smaller with the decrease in z number, and α -SiO₂ was the only crystalline phase formed at the surface of the sintered composite after oxidation in any sintered composites, regardless of the z number in β -sialon and SiC content in the composite, and, in contrast to the experimental results of Hasegawa et al. and Kobayashi et al., the formation of mullite was not detected. We have not clarified why our results differed from those of Kobayashi et al. and Hasegawa et al., but we suppose that these differences might have been caused by the short oxidation time of 100h in our test, or by the effect of humidity in the atmosphere during our oxidation test.

4. Conclusions

Powder materials of α -Si₃N₄, α -Al₂O₃ and AlN were mixed to form the composition of β -sialon, and then SiC powder was added to this mixture. This SiC-containing powder mixture was hot-pressed at 1850°C for 1h under a pressure of 300kg/cm² to produce sintered β -sialon-SiC composites. Oxidation tests were carried out at 1300°C for 100h in air obtaining the relationship between SiC content and oxidation behavior of the sintered materials. The results were compared with those obtained by using commercially available sintered SiC. The results were obtained as follows:

- 1) 0.24mg/cm² was the weight gain obtained after oxidation of sintered β -sialon with z=1(+4), but it tended to decrease with an increase of SiC content in the β -sialon-SiC composites until it fell to 0.14mg/cm² when SiC content was increased to 50wt%. Although this value of 0.14mg/cm² is greater than the 0.00mg/cm² weight gain of sintered SiC measured for comparison, we confirmed that the oxidation resistance of β -sialon could be improved by the addition of SiC to β -sialon.
- 2) The bending strength at room temperature of the sintered materials tended to increase slightly after oxidation in comparison to that before oxidation.
- 3) In the case of sintered β -sialon-50wt%SiC composite, the weight gain of this material due to oxidation in-

creased slightly with the increase of z number in the β -sialon which composed the matrix, and pitting was observed on the surface of this sintered composite, in which β -sialon had z numbers of 2(+4) and 3(+4). Therefore, the oxidation resistance of this sintered composite decreased with an increase in z number in the β -sialon.

References:

- 1) Y. Hasegawa, K. Hirota, N. Yamane, M. Mitomo and H. Suzuki, *Yogyo-Kyokai-shi*, 89, 145-55 (1981).
- 2) Y. Hasegawa, M. Mitomo, K. Hirota, H. Tanaka, Y. Fujii and H. Suzuki, *Yogyo-Kyokai-shi*, 89, 533-9 (1981).
- 3) K. Kishi, S. Umeyayashi, E. Tani and K. Kobayashi, Reports of Government Industrial Research Institute, Kyushu, 34, 2207-15 (1985).
- 4) T. Sata and K. Fujii, *Yogyo-Kyokai-shi*, 90, 14-22 (1982).
- 5) J. Dongliang, K. Gao, P. Zhensu, T. Shouhong, M. Jieying and K. Shumin. *High Tech Ceramics*, edited by P. Vincenzini, Elsevier Science Publishers B.V., Amsterdam, 1987.
- 6) K. Kishi, S. Umeyayashi, E. Tani, K. Kobayashi and H. Nakamura, *Yogyo-Kyokai-shi*, 95, 86-8 (1987).
- 7) H. Nakamura, S. Umeyayashi and K. Kishi, *Nippon Seramikkusu Ronbunshi*, 97, 1517-20 (1989).
- 8) K. Kobayashi and S. Kimura, *Bohshoku-Gijutsu*, 32, 331-8 (1983).

This article is a full translation of the article which appeared in *Nippon Seramikkusu Kyokai Gakujutsu Ronbunshi* (Japanese version), Vol.98, No.3, 1990.

Infrared Sensing Properties of a Low-Curie-Point PTC Thermistor

Minoru Inaba*, Masaru Miyayama and Hiroaki Yanagida

Research Center for Advanced Science and Technology, University of Tokyo

4-6-1, Komaba, Meguro-ku, Tokyo 153, Japan

* Tsukuba Research Laboratory, Tokuyama Soda Co., Ltd.

40, Wadai, Tsukuba-shi, Ibaragi 300-42, Japan

Infrared (IR) sensing properties were investigated for a positive temperature coefficient (PTC) thermistor with a composition of $\text{Ba}_{0.621}\text{Sr}_{0.336}\text{Ca}_{0.040}\text{La}_{0.003}\text{TiO}_3 + 2\text{mol}\%\text{SiO}_2 + 0.05\text{mol}\%\text{MnO}$ (the Curie point was 25°C), operated under the self-regulating heating conditions. The results were compared with those of a detector element with the Curie point of 122°C. The sensitivity operated under the self-regulating heating conditions measured at various ambient temperatures in the range from 0° to 30°C was several times larger than that of the detector element with the Curie point of 122°C. Lowering the operating temperature of the detector by using a PTC thermistor with a low Curie point was shown to be effective for improving the sensitivity.

[Received October 24, 1989; Accepted November 22, 1989]

Key-words: PTC thermistor, Barium titanate, Self-regulating heating, Low Curie point

1. Introduction

Positive temperature coefficient (PTC) thermistors are resistors made of semiconducting barium titanate with large positive temperature coefficients. The resistance increases by several orders of magnitude in the vicinity of the Curie point, and the temperature coefficient of resistivity reaches 15 to 100%/K.¹⁾ Infrared (IR) detectors made of PTC thermistors may therefore be much more sensitive than those made of NTC thermistors, which have been used for many years.²⁾ However, because the large temperature coefficient is brought about in a narrow temperature range near the Curie point, the operating temperature of the detector must be regulated carefully.

One promising method is to use the self-regulating heating³⁾ of the PTC thermistor itself. We reported the properties of an IR detector made of a PTC thermistor, the Curie point of which was 122°C, under the self-regulating heating conditions.⁴⁾ It was found that the PTC thermistor responded to IR radiation under the self-regulating heating conditions. The sensitivity decreased with an increase in the temperature difference between the detector element (in the vicinity of the Curie point) and the ambience.

We also discussed theoretical expressions for some IR-sensing properties under the self-regulating heating conditions in the previous study.⁴⁾ As for the sensitivity (the ratio of the resistance change to the resistance before irradiation; $\Delta R/R$), the following

expression was obtained,

$$\begin{aligned} \Delta R/R &= \alpha\eta WA / (G + VI\alpha) \\ &= \alpha\eta WA / G \{ 1 + (T - T_a)\alpha \} \end{aligned} \quad \dots\dots (1)$$

where α is the temperature coefficient of resistance (/K), η is the fraction of incident energy absorbed (the absorption efficiency), W is the IR incident energy (W/cm^2), A is the receiving area of the detector (cm^2), G is the thermal conductance to the surroundings (W/K), V is the applied voltage (V), I is the current before irradiation (A), T is the temperature of the detector element (K), and T_a is the ambient temperature (K). It was considered from Eq. (1) that the increase in $VI\alpha$ or $G(T - T_a)\alpha$, which are required for the self-regulating heating, may cause the ambient temperature dependence of the sensitivity mentioned above. In order to improve the sensitivity, it is therefore desirable to reduce $VI\alpha$ in Eq. (1), that is, to reduce the difference between the operating temperature of the detector element and the ambient one. Such a condition is brought about by lowering the Curie point of the detector.

In the present study, we investigated IR sensing properties of a PTC thermistor with the Curie point of 25°C operated under the self-regulating heating conditions, and compared the properties with those in the previous study.⁴⁾

2. Experimental Procedure

BaCO_3 , SrCO_3 , CaCO_3 (Rare Metallic Co., Ltd., 99.99%), $\text{La}(\text{NO}_3)_3 \cdot 6\text{H}_2\text{O}$ (Kanto Chemical Co., Ltd.), TiO_2 (Fuji Titanium Co., Ltd., rutile, 99.97%), SiO_2 (High Purity Chemicals Co., Ltd., 99.9%), and $\text{Mn}(\text{NO}_3)_3 \cdot 6\text{H}_2\text{O}$ were used as starting materials. A sintered body with a composition of $\text{Ba}_{0.621}\text{Sr}_{0.336}\text{Ca}_{0.040}\text{La}_{0.003}\text{TiO}_3 + 2\text{mol}\%\text{SiO}_2 + 0.05\text{mol}\%\text{MnO}$ was prepared by the usual ceramic processing technique as described in the previous paper.⁴⁾ The sintered body was cut into the detector element ($2\text{mm} \times 5\text{mm} \times 150\mu\text{m}$) as illustrated in Fig. 1. Ohmic silver paste (Dometoron Co., 61900781/347) as electrodes was fired (2mm apart) on one side of the surface at 560°C for 5 min with nickel wires (0.1mm diameter). To measure the temperature of the detector element, a small thermistor (Shibaura Electronics Co., Ltd., PT5-25E5) was attached on the other surface.

A blackbody furnace (Chino Co., Ltd., IR-R24) was used as an IR source. The detector element was

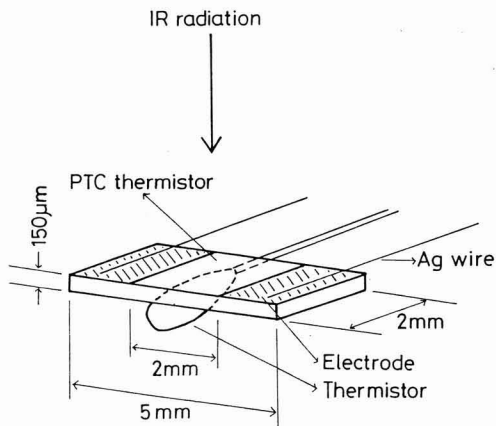


Fig. 1. PTC thermistor IR detector.

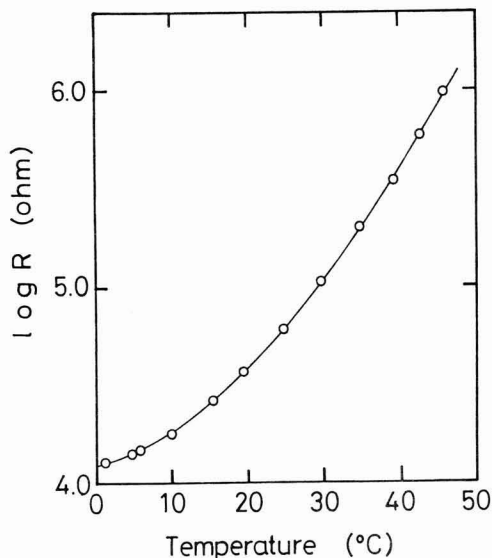


Fig. 2. Resistance-temperature characteristic of the detector element.

mounted in a holder made of polyvinyl chloride with a polyethylene IR-transmitting window (15μm thick), and placed apart from the aperture of the blackbody furnace by 15cm. Ambient temperatures were regulated with a thermostat (Lo Temp Incubator IL-60, Yamato Science Co., Ltd.). Incident IR energy through the polyethylene window was measured by a thermopile IR sensor (Mitsubishi Yuka Co., Ltd., MIR-100s), and was 1.51×10^{-2} W/cm² from a 600K blackbody furnace.

The current change by IR radiation (20 sec) was measured when the steady state was attained. The sensitivity was expressed in the form of the ratio of the resistance change to the resistance before irradiation ($\Delta R/R$).

3. Results and Discussion

Figure 2 shows the resistance-temperature characteristic of the detector element. The temperature coefficient was 13.0%/K at 30°C ($B = -13200K$). The Curie point was determined from the temperature at which the element showed a maximum capacitance in the present study. It was 25°C, and is somewhat higher than that expected from the composition (15°C).¹⁵⁾ Figure 3 shows the surface temperature of the element as a function of applied voltage at various ambient temperatures. Applying sufficiently high voltage can regulate the detector temperature in the region ($>20^\circ C$) where α is large. The thermal conductance G estimated from the relation between the temperature of the element and the power consumption was 1.41×10^{-3} W/K.

Figure 4 shows the temperature change of the element by applying the constant voltage of 40V at the ambient temperature of 20°C. Immediately after the voltage was applied, the element temperature reached 30°C, and was kept constant. If the detector element is heated by other heater elements, it is difficult to regulate the element temperature near room temperature.

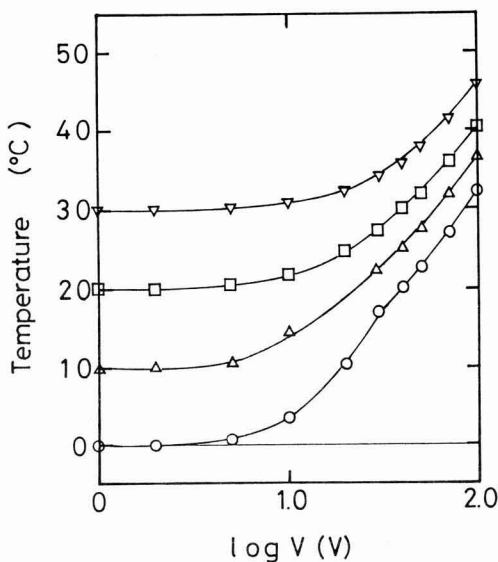


Fig. 3. Surface temperature of the detector element as a function of applied voltage measured at (○) 0°C, (Δ) 10°C, (□) 20°C, and (▽) 30°C.

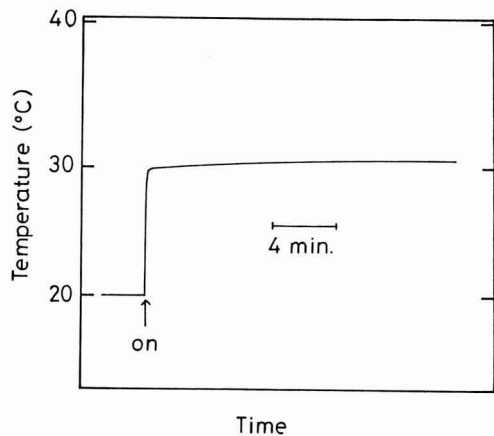


Fig. 4. Temperature change of the element by applying 40V at the ambient temperature of 20°C.

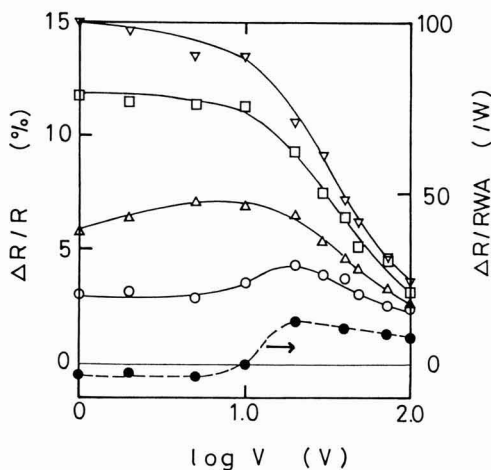


Fig. 5. Sensitivity to 600K blackbody radiation measured at (o) 0°C, (Δ) 10°C, (\square) 20°C, and (∇) 30°C in the present study, --(o)--: the sensitivities of the detector with the Curie point of 122°C measured at 15°C, in the previous study.⁴⁾

The self-regulating heating was found to be an excellent method to regulate the element temperature, in particular, near room temperature.

Figure 5 shows the sensitivity to 600K blackbody radiation at various ambient temperatures in the range 0°C to 30°C. When the ambient temperature lay in the range where the element had large α (20°C and 30°C), the sensitivity was large even at low applied voltage. When the ambient temperature lay in the range where

the element had small α (0°C and 10°C), the sensitivity was small at low applied voltage. The sensitivity increased at voltage enough to raise the element temperature to the large α region. In each case, the sensitivity at higher voltage decreased because of the increase in VIa.

The calculated sensitivity with the approximate equation of the observed resistance-temperature characteristic and Eq. (1) was in good agreement with the observed one (Fig. 6).

To estimate the effect of lowering the operating temperature, that is, the effect of lowering the Curie point, the sensitivity was compared with that in the previous study.⁴⁾ The sensitivity of a PTC thermistor with the Curie point of 122°C to 600K blackbody radiation measured at 15°C⁴⁾ ($\alpha = 18\%/K$) is shown in Fig. 5. The comparison was conducted on the sensitivity per unit energy of incident IR radiation ($\Delta R/RWA$) because the energies were different between the two studies. As shown in Fig. 5, despite having smaller α , the detector in the present study has several times larger sensitivity than that in the previous study.⁴⁾ Lowering the operating temperature by using a PTC thermistor with a low Curie point was therefore shown to be effective for improving the sensitivity.

4. Conclusion

An IR detector was made of a PTC thermistor with a composition of $Ba_{0.621}Sr_{0.336}Ca_{0.040}La_{0.003}TiO_3 + 2mol\%SiO_2 + 0.05mol\%MnO$, having the Curie point of 25°C. The sensitivity under the self-regulating heating conditions measured at various ambient temperatures in

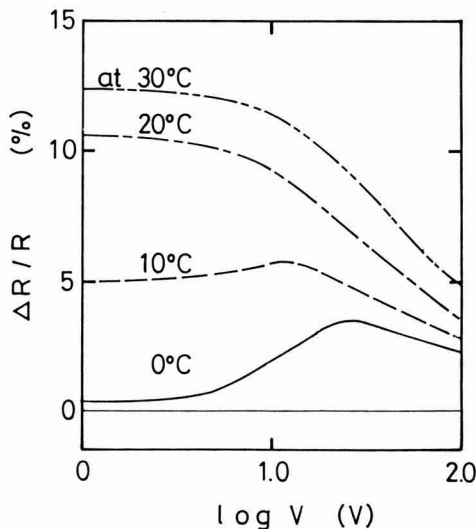


Fig. 6. Calculated sensitivity to 600K blackbody radiation using Eq. (1).

the range 0°C to 30°C was several times larger than that of the detector with the Curie point of 122°C. Lowering the operating temperature by using a PTC thermistor with a low Curie point was shown to be effective for improving the sensitivity.

References:

- 1) O. Suburi, *J. Phys. Soc. Jpn.*, **14**, 1159-1174 (1951).
- 2) H. Yanagida, "Handbook of Detection Systems," Gijyutu-Shiryō Center, Tokyo (1982) pp. 117-122.
- 3) E. Andrich, *Philips Tech. Rev.*, **30**, 170-177 (1969).
- 4) M. Inaba, M. Miyayama, and H. Yanagida, *Seramikkusu Ronbunshi*, **97**, 1250-55 (1989).
- 5) O. Suburi, *J. Phys. Soc. Jpn.*, **44**, 54-63 (1961).

This article appeared in English in *Nippon Seramikkusu Kyokai Gakujutsu Ronbunshi* (Japanese version), Vol. 98, No.3, 1990.

Formation of Spherically Aggregated ZrO₂ Particles by Thermal Hydrolysis of ZrOCl₂ Concentrated Solution

Keiji Daimon, Junji Yamada and Etsuro Kato*

Nagoya Institute of Technology

Gokiso-cho, Showa-ku, Nagoya 466, Japan

*Aichi Institute of Technology

1247, Yachigusa, Yagusa-cho, Toyota 470-03, Japan

Spherically aggregated ZrO₂ particles of about 1 μ m with narrow size distribution were obtained by hydrothermal treatment of highly concentrated ZrOCl₂ solutions at 200°C following the heat-treatment at 300°C in air to dry. The aggregates are joined to each other and are easily collapsed and dispersed to ultrafine particles of smaller than 10nm by adding water before drying. The powder composed of the aggregates maintaining the shape as well as formed at the stage of the hydrothermal treatment was obtained when the 'double structured vessel' was employed for the hydrothermal treatment.

[Received September 12, 1989; Accepted November 22, 1989]

Key-words: Spherical aggregates, ZrO₂ particles, Hydrolysis, Hydrothermal treatment, Concentrated ZrOCl₂ solution

1. Introduction

It is desirable that the powders used to manufacture ceramics by the conventional processes of press-forming and normal sintering consist of aggregated ultra-fine particles of suitable sizes and become densely packed when pressed.¹⁾ Therefore, it is important to study methods of controlling the particle size of the raw materials to the desired conditions. There have been several reports published on the particle size control of zirconia. Aggregates of particles in sizes of less than 100nm, oriented like a twin crystal pattern with extremely fine zirconia crystals (several nm), were obtained by heating a dilute aqueous solution (0.1 to 0.3 mol/l) of zirconyl chloride (ZrOCl₂) at low temperature (<100°C) for a long time,^{2,3)} and the size of aggregated particles could be controlled by coexisting ions.⁴⁾ Other reports discuss the formation of spherical aggregates of particles of zirconia, composed of amorphous fine particles with narrow size distribution produced by the hydrolysis of alkoxide.^{5,6)}

The authors previously reported⁷⁾ that a highly dispersed sol consisting of ultrafine zirconia particles (5 \times 10nm) was formed by thermal hydrolysis of a highly concentrated aqueous solution of zirconyl chloride. However, the products were obtained as a white slurry, and changed to the highly dispersed sol when the slurry was diluted with water. This phenomenon suggests that the ultrafine zirconia particles are in some aggregated state at a moment after formation by thermal hydrolysis. In the present study, we succeeded in forming

spherically aggregated zirconia particles, which were considered to be in a solidified state of the aggregates composed of ultrafine zirconia particles.

2. Experimental Procedure

The starting material was guaranteed reagent zirconium oxychloride (ZrOCl₂·8H₂O, zirconyl chloride). This was placed in a hard-teflon container (internal volume 25ml) with or without a small amount of water, and the teflon container placed in a pressure vessel made of stainless steel. The starting material was hydrothermally treated at temperatures controlled in the range of 150° and 200°C. This hydrothermal treatment was carried out by placing the pressure vessel in a drying oven heating by air circulation. After the hydrothermal reaction, the vessel was cooled down to room temperature using an air-blower, and the sample removed from the vessel after confirming that the temperature inside the vessel was lower than the boiling point of the starting material. The zirconia was stabilized after formation by direct dehydration and drying of the thermal hydrolysis products in the pressure vessel at the temperature used for the thermal hydrolysis. The apparatus for this experiment is shown in Fig.1(b). A soft-teflon container with an internal volume of 7ml was placed in the hard-teflon container, and the space outside this inner container in the hard-teflon container was filled with γ -alumina grains. The intention of these arrangements was to absorb moisture in the γ -alumina instead of in the inner container when the vessel was cooled after the thermal hydrolysis. This vessel shown in Fig.1(b) is called the double-structured vessel, and the vessel shown in Fig.1(a) the ordinary vessel.

The zirconia formation ratio was determined by the following procedure. After thermal hydrolysis, the sample was removed from the vessel, and dropped into water to dilute the reaction products and the unreacted components with water, and then hydrochloric acid added to precipitate zirconia particles, which were then separated by subsequent filtration. An aqueous solution of ammonia was added to this filtrate to precipitate the unreacted components precipitated as zirconium hydroxide, which was separated by subsequent filtration. By applying the ashing method to these two precipitates, the amounts of zirconia formed and zirconium remaining unreacted were obtained. The zirconia formation ratio against total zirconium involved was calculated from these. The morphology of the zirconia particles formed was observed using a SEM.

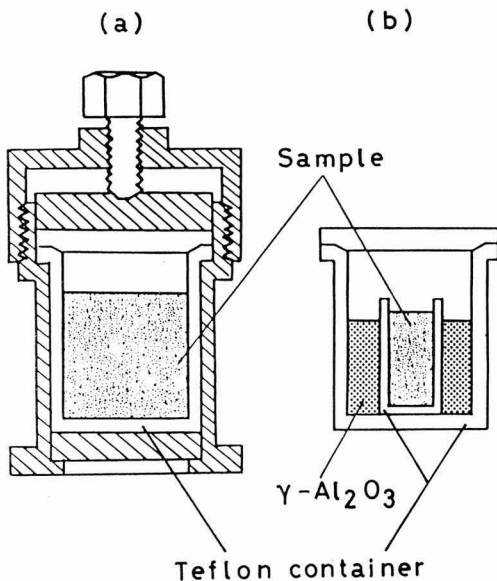


Fig. 1. Sealed decomposition vessels used for the hydrothermal treatment.
 (a) A set of ordinary vessel composed of a stainless cover and a teflon container.
 (b) A set of teflon containers used in a double structured vessel, which is put in a stainless cover, the same as (a).

3. Results and Discussion

When the zirconyl chloride hydrate (actahydrate) was hydrothermally treated without additional water in the ordinary vessel, the crystals of zirconyl chloride were dissolved in the water of crystallization, and the products of thermal hydrolysis at temperatures higher than 170°C were a white-colored slurry. These reaction products appeared to be solid when taken out of the vessel, but easily changed to a liquid state of good fluidity when agitated, for instance, by manipulation with a spoon, since they contained a high water content. When these slurry products were heated and dried, they became solids. These solids were easily crushed into powder particles by even light grinding with a mortar and a pestle. X-ray diffraction analysis carried out on these powders showed that the crystalline phase formed was extremely fine monoclinic zirconia.

The thermal hydrolysis of zirconyl chloride was carried out at various temperatures for a fixed time of 24h to compare the zirconia formation ratios, the results of which are shown in Fig.2. The zirconia formation reaction took place when the thermal hydrolysis temperature was higher than 160°C. When the ordinary vessel was used for thermal hydrolysis, the zirconia formation ratio increased with an increase in thermal

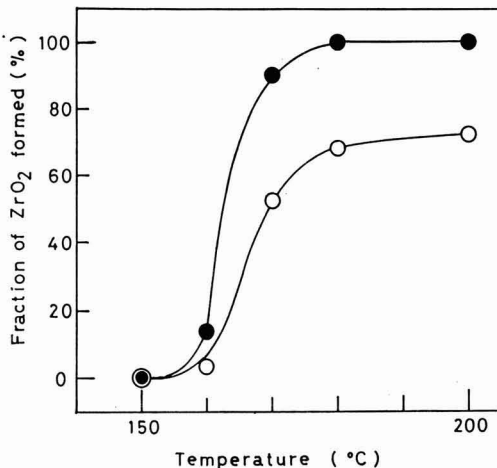


Fig. 2. Changes of the ratio of ZrO₂ formed by the hydrothermal treatment for 24h with the treatment temperature.
 o: ordinary vessels were used.
 ●: double structured vessels were used.

hydrolysis temperature, but the increase rate was lowered in the temperature range over 180°C, showing a tendency to come closer to a saturated ratio (≈75%) of zirconia formation. When the hydrolysis temperature was increased to 200°C, lengthening of the treatment time from 24h to 72h only resulted in a small increase in the zirconia formation ratio from 73% to 76%. Presumably the zirconia is formed by the following reaction,



but the small increase in zirconia formation as mentioned above may be resulted from the suppression of this reaction due to the HCl being produced in high concentration.

The X-ray diffraction pattern for the sample dried at 150°C after the thermal hydrolysis at 200°C for 72h is shown in Fig.3(a). From these diffraction patterns, the diameters of the crystallites were calculated by the Debye-Scherrer method, obtaining $D_{111} = 4\text{nm}$ and $D_{111} = 7\text{nm}$.⁸⁾ These crystallite diameters decrease with decreasing the thermal hydrolysis temperature. When the reaction products from the thermal hydrolysis of $\text{ZrOCl}_2 \cdot 8\text{H}_2\text{O}$ were put into distilled water before complete drying, a zirconia sol with a bluish color and transparency was obtained. As shown in Fig.3(b), this sol consists of ultrafine particles (<10nm in diameter), which are very well dispersed and so isolated from each other, and the particle diameter almost agrees with the apparent crystallite diameter calculated from the powder X-ray diffraction pattern.⁷⁾

After thermal hydrolysis at various temperatures ranging from 160° to 200°C for 24h using the ordinary vessel, the same conditions as used above, the vessel

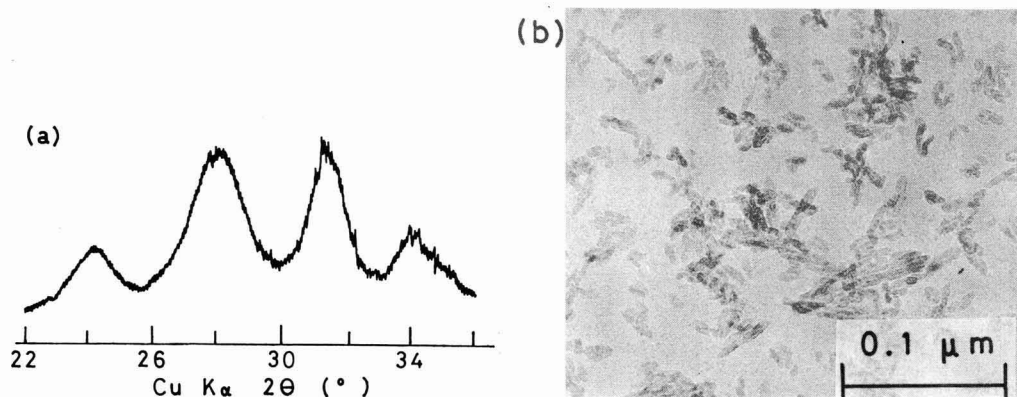


Fig. 3. Monoclinic ZrO_2 produced by heating zirconyl chloride hydrate ($ZrOCl_2 \cdot 8H_2O$) without any other H_2O at $200^\circ C$ for 3 days.
 (a) A powder X-ray diffraction pattern of the product dried at $150^\circ C$ for 24h after the hydrolysis.
 (b) TEM photograph of the product dispersed into distilled water before drying.

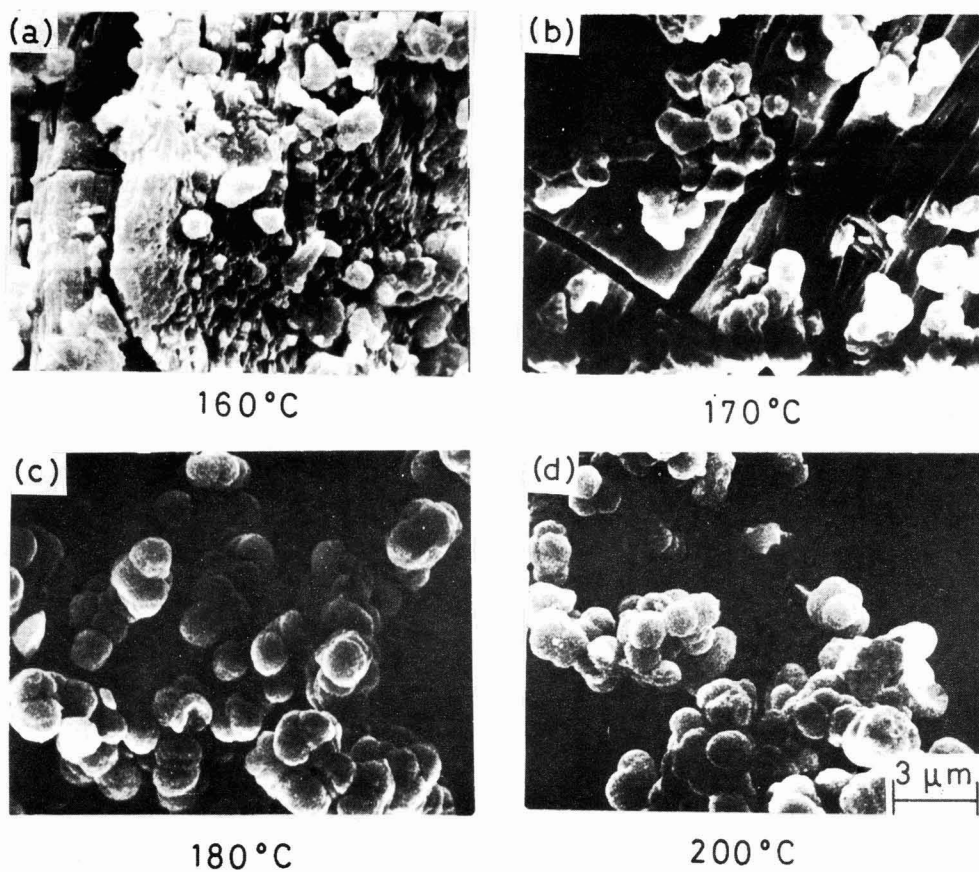


Fig. 4. SEM photographs of the products heated at $300^\circ C$ for 24h after the hydrolysis with ordinary vessels at the temperatures ranging from 160° to $200^\circ C$.

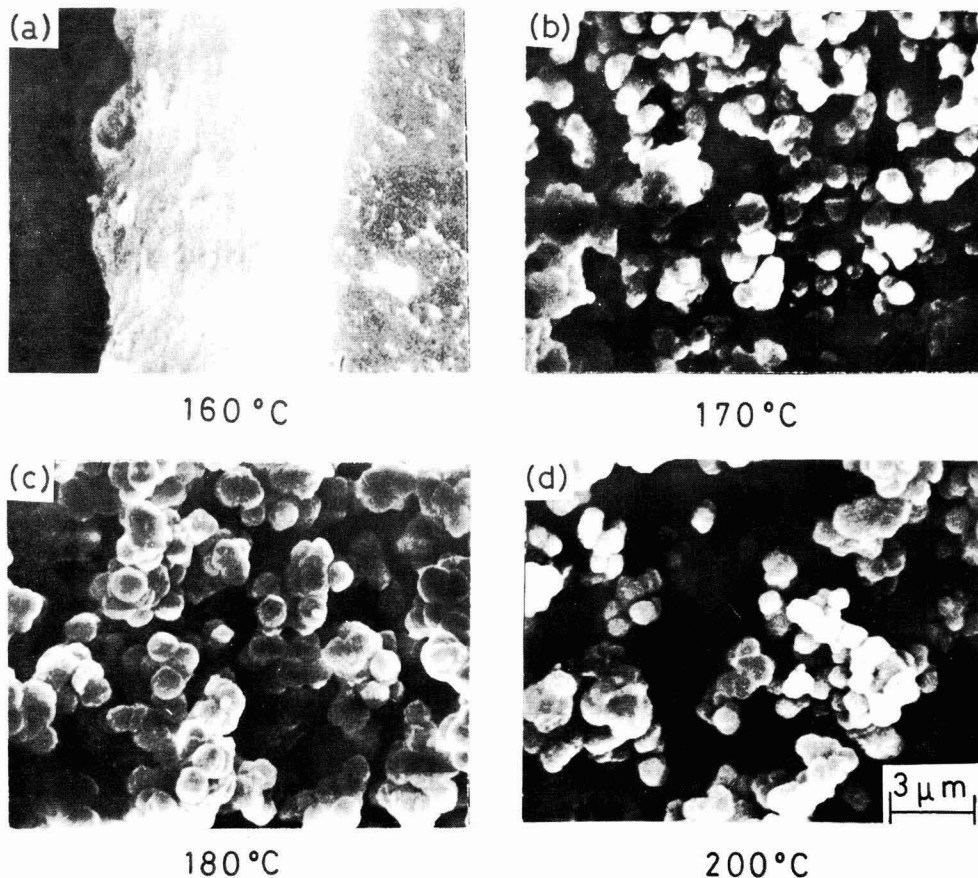


Fig. 5. Morphologies of the products treated at the same conditions as Fig.2 except using double structured vessels.

was cooled at room temperature for 25min, and then the sample removed from the vessel, completely dried at 300°C in open air and crushed into powder. Figure 4 shows the SEM photographs of these powders prepared at different hydrolysis temperatures. Spherically aggregated particles were observed when the samples were prepared at hydrolysis temperatures of 170°C and higher. When this temperature was 200°C, spherically aggregated particles were mostly in contact with each other, or coherent with each other, but the particle sizes were distributed in a relatively narrow range, with an average size of 1.3μm. When the hydrolysis reaction products before complete drying were dropped into water, the white color easily disappeared and a transparent sol was produced. Therefore, we assume the spherically aggregated white particles prior to complete drying had a very weak aggregate structure, in which the liquid phase was included among ultrafine particles. When the hydrolysis products were completely dried and crushed into powder, aggregate particles were produced in various deformed and collapsed shapes, which indicated that the maintenance of spherical particle shapes varied widely with a slight difference in the cooling and

drying conditions, or by a difference in the sampling position in the product. This trend of deformation or collapse of spherically aggregated particles was particularly remarkable when water was added as well as when a long cooling time (over 50min) after thermal hydrolysis was allowed. The latter phenomenon presumably suggests that the aggregates of the ultrafine zirconia particles (<<10nm) produced absorb moisture and are softened at room temperature after cooling, and easily disintegrate, deform or collapse during drying.

Since it was intended to stabilize the aggregates of ultrafine zirconia particles as closely as possible to those formed, the double structured vessel was used for formation of zirconia by the thermal hydrolysis process in the following experiments. When the vessel was cooled after the end of the thermal hydrolysis, the outside teflon vessel was cooled more quickly than the inside one, so water was condensed on the outside vessel because of the temperature difference between the outside and the inside vessels. Consequently, the effect of water removal from the zirconia particles produced in the inside vessel was more accelerated with a higher temperature thermal hydrolysis and with a

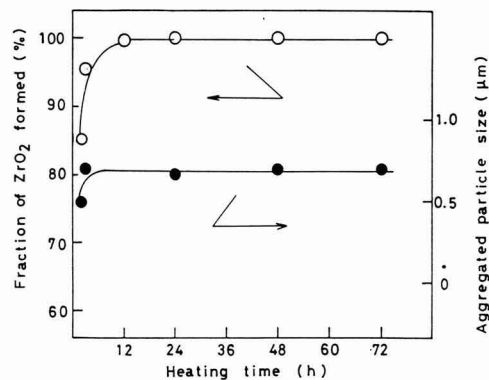


Fig. 6. Time dependence of ZrO₂ formation and aggregated particle size by thermal hydrolysis of 4 M ZrOCl₂ solution at 200°C.

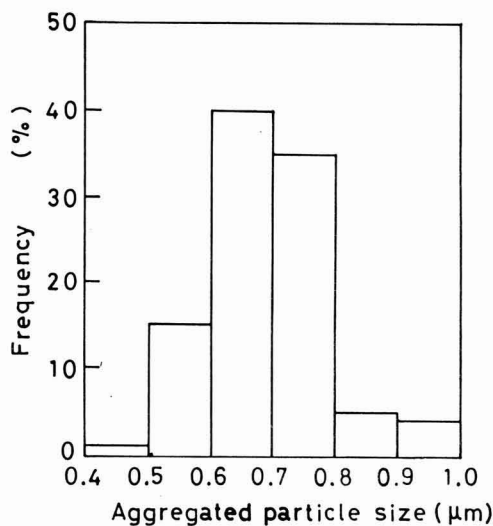


Fig. 7. Size distribution of aggregated m-ZrO₂ particles produced by heating 4M ZrOCl₂ solution at 200°C for 4h.

faster cooling rate after the treatment.

Figure 5 shows SEM photographs of zirconia particles obtained by complete drying and crushing of the reaction products of thermal hydrolysis using the double structured vessel. In this case, the zirconia formation reaction progressed faster than when using the ordinary vessel, so the zirconia formation ratio reached almost 100% even when the thermal hydrolysis temperature was as low as 180°C (Fig.2). We assume this increased zirconia formation ratio was caused by the adsorption of the HCl produced in the hydrolysis reaction by active alumina, which would promote the completion of the hydrolysis reaction. When the thermal hydrolysis temperature was increased to 200°C, the samples taken out of the vessel after cooling showed that the water and HCl in the reaction products were almost all adsorbed by the active alumina. The samples of zirconia particles obtained in the solid state were dry and easy to crack, and did not smell of HCl. When this reaction product was put in water, no transparent sol was produced, but a suspension which consisted of aggregates of 0.1 to 0.2 μm. This is assumed to have been caused by the stronger bonding among the primary particles inside the spherical aggregates in the reaction products, as a result of water removal and drying by active alumina during cooling of the vessel. When these zirconia samples produced by thermal hydrolysis were further dried by heating at 300°C in air, the spherical aggregates became stronger so that they were not disintegrated even when washed with water. This experimental result was highly reproducible, and differences due to sampling position were very small. The aggregated zirconia particles produced by thermal hydrolysis at 200°C for 72h using a double structured vessel were mostly in contact with each other or coherent with each other, similar to the case of using a normal vessel, but the particle size of about 1.0 μm was a little smaller than that obtained by using a normal vessel (Fig.5(d)).

When an amount of water was added to the zirconyl chloride crystals in thermal hydrolysis, if the concentra-

tion of zirconyl chloride aqueous solution was maintained higher than around 3mol/l, spherically aggregated zirconia particles could be obtained by heating the reaction products at 300°C in air. In this case, the aggregated particle size decreased with a decrease in the concentration of the zirconyl chloride solution. In the case of a concentration of zirconyl chloride aqueous solution of 4mol/l, the dependence on treatment time of zirconia formation ratio and aggregated particle size are shown in Fig.6, and the size distribution of aggregated zirconia particles is shown in Fig.7. Except in the early period when the zirconia formation reaction was rapid, the aggregated particle size obtained changed little, and the particle size distribution was very sharp with a standard deviation of $\sigma = 0.098$ ($\sigma^2 = \sum(r_i - \bar{r})^2 / n^2$; r = grain size, \bar{r} = mean grain size, $n = 1000$). As mentioned before, the size of the spherical aggregates of zirconia particles changes with the water content in the reaction system, but when water content was further increased, contact area between the spherical aggregates gradually increased with an increase in water content, and the shape of the particles themselves became vague, so the reproducibility of experimental results became poor.

It has been reported⁵⁾ that zirconia particles with high sphericity and high dispersibility are produced by hydrolysis of organic zirconium metal compounds. They are aggregates of ultrafine amorphous particles constructed as if the ultrafine particles were stacked. In contrast, the zirconia particles obtained in our experiments are spherical aggregates of particles which consist of extremely fine but crystalline particles which are mostly bonded to each other. In addition, the spherical aggregates of zirconia particles obtained have rough surfaces. We assume that these aggregates were formed

through a process of aggregates of ultrafine particles which were not well dispersed due to a low water content in the course of zirconia formation being solidified without a change in shape when heated and dried at 300°C. Spherical aggregates of ultrafine crystalline particles as above discussed is a new phenomenon which we recognized in this study on the thermal hydrolysis of concentrated zirconyl chloride aqueous solution, and has not been reported previously. We are continuing to investigate the mechanism of this aggregation as well as the grain size control of aggregates and the change in aggregates by heating.

References:

- 1) H. Saito, edited, "Fine Ceramics-no-Katsuyo" Vol.1, pp.12-23, published by Ohkawa Shuppan Co. (1986).
- 2) Y. Murase and E. Kato, *Nippon Kagaku Kaishi*, 1976, 425-30, (1976).
- 3) Y. Murase, E. Kato and M. Hirano, *Yogyo-Kyokai-Shi*, 92, 64-70 (1984).
- 4) E. Kato, M. Ezoe, M. Kondo, Y. Murase and K. Matoba, *Yogyo-Kyokai-Shi*, 95, 984-90 (1987).
- 5) T. Ikemoto, N. Mizutani, M. Kato and Y. Mitarai, *Yogyo-Kyokai-Shi*, 93, 585-6 (1985).
- 6) B. Fegley, P. White and H.K. Bowen, *Am. Ceram. Soc. Bull.* 64 [8] 115-20 (1985).
- 7) M. Ezoe, Y. Murase, K. Daimon and E. Kato, *Yogyo-Kyokai-Shi*, 94, 923-6 (1986).
- 8) H.P. Klug and L.E. Alexander, "X-ray Diffraction Procedures," John Wiley & Sons, Inc., New York (1954).

This article is a full translation of the article which appeared in *Nippon Seramikkusu Kyokai Gakujutsu Ronbunshi* (Japanese version), Vol.98, No.3, 1990.

Thermal Diffusivity Measurements of Boron Oxide Melts by Laser Flash Method

Gaku Ogura, In-Kook Suh, Hiromichi Ohta* and Yoshio Waseda

Research Institute of Mineral Dressing and Metallurgy, Tohoku University
2-1-1, Katahira, Sendai 980, Japan

* Department of Metallurgical Engineering, Faculty of Engineering, Ibaraki University
4-12-1, Nakanarusawa, Hitachi 316, Japan

Thermal diffusivities of molten boron oxide, which is one of the favorable liquid capsule materials for producing GaAs or GaP single crystals, have been measured systematically in the temperature range between 1000K and 1500K using a three layered laser flash method. The thermal diffusivity of molten boron oxide was found to decrease with increasing content of P_2O_5 or In_2O_3 additives.

[Received October 2, 1989; Accepted December 11, 1989]

Key-words: Thermal diffusivity, Boron oxide, Oxide melt, Laser flash method, Heat transfer, Compound semiconductor

1. Introduction

In producing single crystals supplied for semiconductor devices of compounds in groups III through V such as GaAs and GaP, for example by Czochralski method, as, P etc., which have high vapor pressures are likely to diffuse from the master melts, causing the original compositions to change. To reduce such trouble, boron oxide melts have recently been widely used as liquid capsules to encase molten semiconductors. To obtain high quality single-crystal semiconductors with a low dislocation density, it is necessary to minimize the temperature gradient in the melt by accurate temperature control. For this purpose, the thermal diffusivity of a liquid capsule material is one of the important properties. Within the best knowledge of the present authors, however, no report has been available on the thermal diffusivity of molten boron oxide. Using a laser flash method, we measured the thermal diffusivities of molten boron oxide, containing a small amount of phosphorus or indium oxide, which was studied as a liquid capsule material for practical use, as well as molten boron oxide without such additives. This paper describes our new results.

2. Experimental Procedures and Data Analysis

The laser flash apparatus for measuring the thermal diffusivity has been described previously.¹⁻³⁾ The new three layered cell system employed in the present study is schematically illustrated in Fig. 1. The first layer irradiated by the ruby laser as a heating pulse source, output 6J and beam dia. 10mm, consists of a platinum

crucible of 0.20mm thickness, 10mm height and 12mm inner dia. glued to a quartz tube 11.4mm o.d. and 1mm thickness, which can be moved vertically by a micrometer. The liquid sample is the second layer and is contained in a platinum crucible (the third layer) of 0.20mm thickness, 14.5mm height and 14mm inner dia. which is placed on alumina pins to thermally insulate the rear side. With the container charged with a liquid sample, the top crucible was allowed to drop until it came into contact with the top surface of the bottom crucible and then the top crucible was raised by the micrometer to produce the liquid layer. To determine the thickness of the liquid layer accurately, the top and bottom platinum cells were held horizontally with the help of levels. On the basis of the results of preliminary measurements, we determined the thickness of a liquid sample to be 1.40mm. The three layered cell system was placed in a high-temperature furnace with platinum coils for heating up to 1700K and held within $\pm 2K$ of the required temperature controlled by a thermocouple installed near the sample. The experiment was carried out in air and the temperature response was measured by sensing the infrared rays emitted from the back surface of the third layer platinum crucible with an InSb semiconductor detector. Several times during measurement, the top platinum crucible was raised to check visually that there were no bubbles in the sample. To analyze the measured temperature response curves, the following method was employed. Because the initial time region of the temperature response curves were unlikely to be affected by heat losses by conduction from the sample to the holder and radiation, James

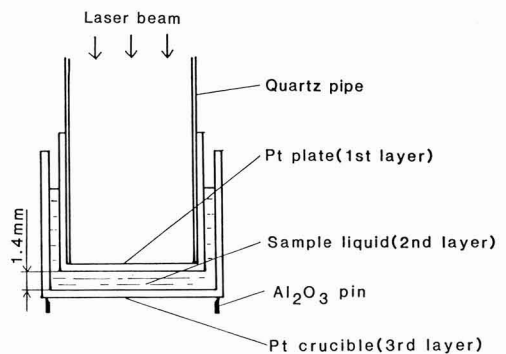


Fig. 1. Schematic diagram of the sample cell assembly.

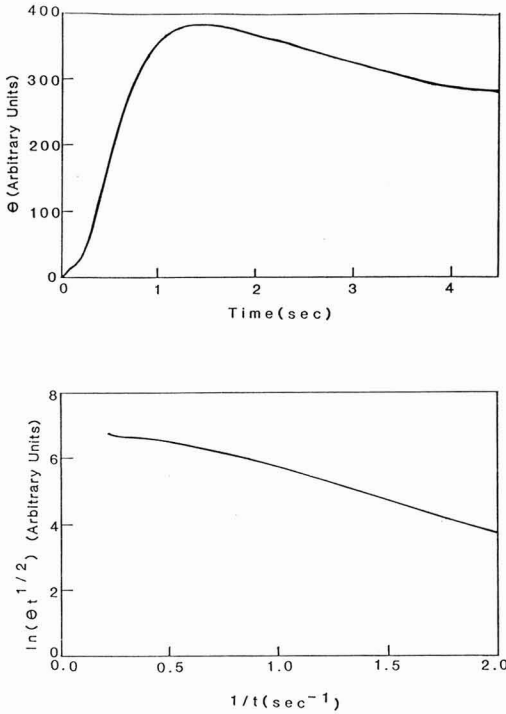


Fig. 2. Temperature response curve of the back surface of the sample cell for molten boron oxide containing 120ppm water at 1083K. (a) observed temperature response. (b) converted temperature response with respect to $\ln(\theta t^{1/2})$ and $1/t$.

developed the method for determining the thermal diffusivity value of a sample using only the initial time region of the temperature response curves and also showed that a similar analysis is possible for two layered cell system.⁴⁾ Recently we showed that this data processing can be effectively extended to three layered cell system consisting of a liquid layer between two metal plates.⁵⁾ It was thus employed in the present study. For the initial time region of the temperature response curves for three layered cell system, the following equation can be obtained:

$$\frac{(\eta_1 + \eta_2 + \eta_3)^2}{4} = -\tan^{-1} \frac{\ln(\theta t^{1/2})}{1/t} \dots\dots(1)$$

$$\eta_i = \kappa_i / \sqrt{\kappa_i} \quad ; \quad i = 1, 2, 3 \quad \dots\dots(2)$$

where θ : temperature rise, κ : thermal diffusivity, t : time after irradiating a pulse laser beam, l_i : thickness of each layer and subscripts 1, 2 and 3: layers. In the present measurements, the thermal diffusivity of the first and the third platinum layers ($\kappa_1 = \kappa_3 = 0.245\text{cm}^2/\text{s}$), their thicknesses ($l_1 = l_3 = 0.02\text{cm}$) and the

thickness of the melt (second layer) (l_2) are known. Thus, the thermal diffusivity κ_2 of the melt can be obtained by obtaining the temperature rise θ of the back surface of the platinum crucible (third layer) after flashing a pulse laser beam onto the surface of the first-layer platinum, plotting $\ln(\theta t^{1/2})$ against $1/t$, and using Eq. (1) with the slope of the straight line obtained. From the results of measurement using the three layered cell filled with distilled water and methanol, it was found that the experimental uncertainties were within $\pm 6\%$ of the literature values. Also, from the results of systematic measurement with samples having different diameters larger than that of the laser beam, it was proved that the shape of the three layered cell employed in the present study reduces heat losses to the sample container and the radial heat flow was confirmed to be insignificant.

3. Results and Discussion

Considering the regulation of the opaque quartz pipe used as a component of the three layered cell, we carried out measurements at intervals 50 to 100K over the temperature range of 1000 to 1500K, although the high-temperature furnace could be heated up to 1700K. Figure 2 shows the temperature response curve using the results of molten boron oxide with a water content of 120ppm at 1083K, as an example and the relationship between $1/t$ and $\ln(\theta t^{1/2})$. Although analysis with $t \rightarrow 0$ s is theoretically ideal, in short time region such as $t < 0.5$ s, the temperature rise is so small that signal is very weak, causing the SN ratio to decrease, generally resulting in wide scattering of data. Thus, on the basis of measured temperature response, we plotted $1/t$ versus $\ln(\theta t^{1/2})$, finding the good linear relationship in the range $0.5\text{s} < t < 1.0\text{s}$ as shown in Fig. 2. Therefore, the data in this region was used in our study. In addition, we excluded data in the region above 1.0s because such longer time region involved difficulties such as heat losses and was beyond the scope of the James equation. With different water contents, Figs. 3 and 4 show the results of measurements of the thermal diffusivity of molten boron oxide containing 0.08mol% In_2O_3 and molten boron oxide containing a small amount of P_2O_5 respectively. In all cases, the thermal diffusivity of molten boron oxide increases as the temperature rises. Variations in thermal diffusivity, which are not prominent, systematically decrease as the contents of In_2O_3 and P_2O_5 increase. Qualitatively it can be understood that these results are due to an increase of the anharmonicity of the boron oxide melt resulting from the addition of other oxide, which causes the mean free path of phonons to decrease as compared with the values for pure boron oxide melts,⁶⁾ although some further studies are required to obtain the definite comments. The results of the present study can rather be seen as useful information about the essential properties for basic studies to obtain GaAs and GaP semiconductor single crystals with low dislocation density quality by using molten boron oxide as a liquid capsule material. It may be noted that unless a forced dehydrating treatment such as bubbling is employed, the water content of the boron oxide melts does not change

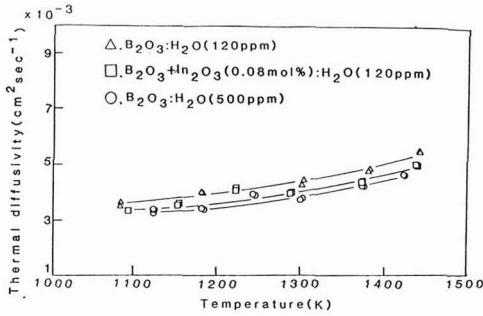


Fig. 3. Thermal diffusivities of molten boron oxide containing H₂O and In₂O₃ as a function of temperature.

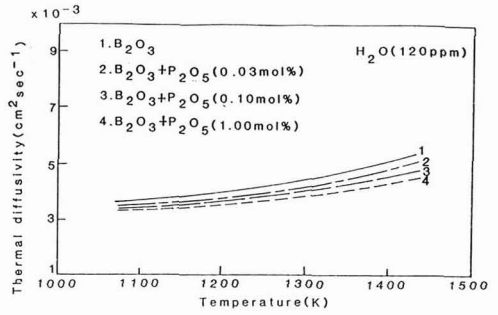


Fig. 4. Effect of the P₂O₅ content on thermal diffusivity of molten boron oxide (containing 120ppm water) as a function of temperature.

even if samples are heated up to the temperature range of 1000 to 1500K.

Acknowledgments

The liquid capsule materials, boron oxide, used in the present measurements were supplied by Rasa Industries. Prof. M. Suzuki and Dr. Z. Yamashita, Department of Biochemical Engineering, Faculty of Engineering, Tohoku University offered us useful suggestions about James' method. We express our thanks to them.

References:

1) H. Ohta and Y. Waseda, *High Temp. Mater. Processes*, 7, 179-

84 (1986).
 2) M. Ohta and Y. Waseda, *Journal of the Ceramics Society* 94, 295-9 (1986).
 3) H. Ohta and Y. Waseda, *Proceedings of the Joint International Symposium on Molten Salts*, Oct. 18-23 (1987), Hawaii, The Electrochem. Soc., USA, pp. 353-62 (1987).
 4) H.M. James, *J. Appl. Phys.*, 51, 4666-72 (1980).
 5) H. Ohta, G. Ogura, Y. Waseda, M. Suzuki and Y. Yamashita, *Rev. Sci. Instrum.*, 60 (1989), to be submitted.
 6) T. Nakamura, *Ceramics and Heat*, Gihodo, 1985, p. 81.

This article is a full translation of the article which appeared in *Nippon Seramikkusu Kyokai Gakujutsu Ronbunshi* (Japanese version), Vol.98, No.3, 1990.

Oxidation of TiB₂-Al₂O₃ Composites in Air

Junichi Matsushita, Shinsuke Hayashi* and Hajime Saito*

Toshiba Ceramics Co., Ltd.

1, Minamifuji, Ogakie-cho, Kariya-shi 448, Japan

*Department of Mechanical Systems Engineering, Toyota Technological Institute

2-12-1, Hisakata, Tempaku-ku, Nagoya-shi 468, Japan

The oxidation of TiB₂-Al₂O₃ composites prepared by pressureless sintering at 1900°C was investigated. TiB₂-Al₂O₃ composites were oxidized at 1000°C for 36h in air, and weight changes were measured to estimate the oxidation resistance of the composites. The composites showed good oxidation resistance with increasing amount of Al₂O₃. The weight gain at 1000°C for 36h in air of the TiB₂ specimen was about 20mg/cm², that of the composite containing 50wt% Al₂O₃ was about 3mg/cm². TiB₂-90wt%Al₂O₃ composite had excellent oxidation resistance.

[Received October 6, 1989; Accepted December 11, 1989]

Key-words: Oxidation, TiB₂, Al₂O₃, Pressureless sintering, Densification, Oxide layer, Weight gain

1. Introduction

Sintered TiB₂ has such a high melting point, hardness, electric conductivity, etc., that it is expected to be applicable as a heat and wear resistant or electrode material.^{1,2)} However, it is difficult to sinter because of its high level of covalent bonding. To obtain densely sintered TiB₂, much research has been directed to discover effective sintering promoters or produce composites.³⁻⁸⁾

Previously, to obtain a high-density, high-strength sintered TiB₂ composite, the authors selected a system composed of TiB₂ and Al₂O₃ additive and sintered it under normal pressure, discovering that a dense and strong sintered composite could be obtained from TiB₂ plus 50wt% Al₂O₃.⁹⁾ However, TiB₂ has the drawback of being so readily oxidized that its application is limited.¹⁰⁾ Some measures must be taken to increase its resistance to oxidation.

To eliminate this drawback, we investigated the oxidation resistance of sintered TiB₂-Al₂O₃ composites. This paper reports the results.

2. Experimental

Sintered TiB₂-Al₂O₃ composites were formed as reported previously. TiB₂ (Cerac) was wet-mixed with α-Al₂O₃ (Sumitomo Chemical Industries) at ratios of Al₂O₃ 10, 25, 50, 75 and 90wt% in ethyl alcohol for 24h. The mixtures were molded under 30MPa and CIP-treated at 300MPa. The compacts were then sintered at 1900°C for 1h in an Argon atmosphere. Blocks 3×4×20mm were cut out of them and the surfaces were polished with a diamond disk to make the samples. The densities were

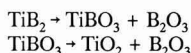
obtained by the Archimedeian method. Table 1 shows their properties.

The samples were placed in a holder made of high-purity alumina and heated at 1000°C in air and the weight increases due to oxidation were measured after certain intervals. Also, the surfaces were observed under a scanning electron microscope (SEM) and the oxide layers were identified by using the powder X-ray diffraction method.

3. Results and Discussion

Figure 1 shows the relation between the Al₂O₃ contents of sintered TiB₂-Al₂O₃ and weight increases due to oxidation for 36h. Evidently, the weight gain decreases as the Al₂O₃ content increases.

When oxidized, TiB₂ is assumed to form oxides as follows:



When oxidized, sintered TiB₂ composites form TiO₂ and B₂O₃ on their surfaces. Even if B₂O₃ vaporizes at high temperatures, the weight of the samples are assumed to increase during oxidation. While sintered TiB₂ without additives gained weight by about 20mg/cm² after 36h oxidation, sintered TiB₂ with 50wt% Al₂O₃ gained only about 3mg/cm², showing a higher resistance to oxidation. TiB₂ without additives has a low density and contains mostly open pores, which are assumed to be directly related to the weight increases

Table 1. Properties of TiB₂-Al₂O₃ composites.

specimen	1	2	3	4	5	6
Al ₂ O ₃ content (wt%)	0	10	25	50	75	90
relative density (%)	78	86	91	94	95	96
bending strength (MPa)	180	240	310	450	310	220
Vickers hardness (GPa)	6	8	13	14	15	15
electrical resistivity (ohm-cm)	10 ⁻⁵	10 ⁻⁵	10 ⁻⁵	10 ⁻⁴	10 ⁻³	10 ⁻⁵

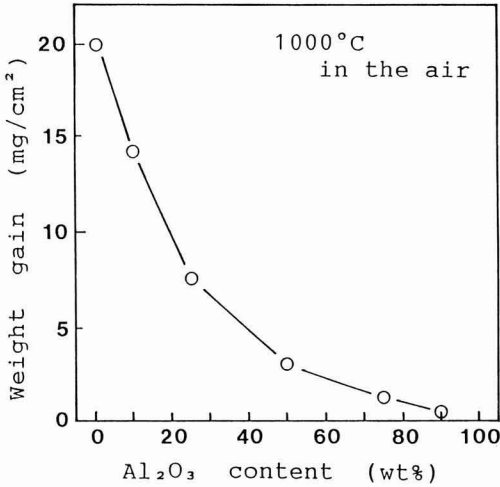


Fig. 1. Al₂O₃ contents vs. weight gains after oxidation at 1000°C for 36h in air. Specimens were fabricated by pressureless sintering at 1900°C for 1h in Argon gas.

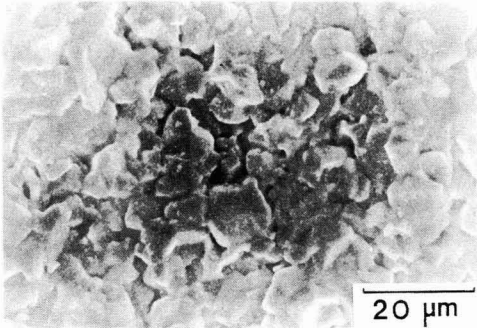


Fig. 3. SEM micrograph of the oxidized surface on the TiB₂-50wt% Al₂O₃ composite. The oxidation time is 36h.

due to oxidation. After the oxidation test, the surfaces of the sintered composites with low Al₂O₃ contents were covered with white oxide layers.

Figure 2 shows the results of the powder X-ray diffraction analysis of these oxides. The layers formed here are evidently a TiO₂(rutile) phase. No TiB₂ or B₂O₃ phases were detected. The samples with Al₂O₃ contents below 50wt% showed no α-Al₂O₃ peaks, only diffraction peaks for TiO₂ (rutile). Figure 3 is the SEM photograph of the surface of the sintered sample with 50wt% Al₂O₃ after 36h of oxidation. Figure 4 is the optical micrograph of the surface of the same sample

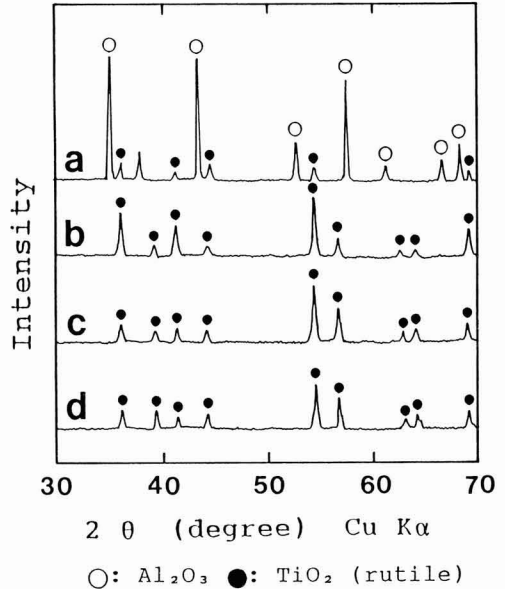


Fig. 2. X-ray diffraction patterns of oxidized surfaces on (a) TiB₂-90wt% Al₂O₃, (b) TiB₂-50wt% Al₂O₃, (c) TiB₂-10wt% Al₂O₃ and (d) TiB₂ specimens. The oxidation time is 36h.

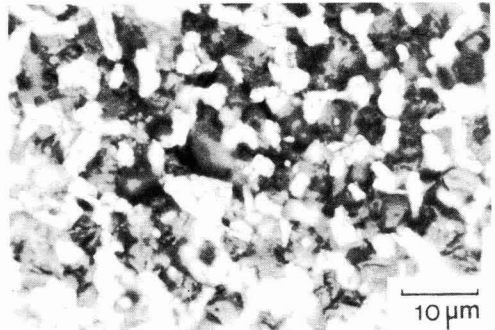


Fig. 4. Photomicrograph of the polished surface of the TiB₂-50wt% Al₂O₃ composite.

before oxidation. The surfaces of numerous TiB₂ grains (white portions in Fig.4) around Al₂O₃ grains were probably oxidized, producing TiO₂ layers, which covered the Al₂O₃ grains while becoming denser, consequently allowing only TiO₂ peaks to be observed. In the sample with 90wt% Al₂O₃, on the other hand, no white oxides were produced but a layer assumed to be a vitreous substance covered the surface. X-ray diffraction analysis detected only TiO₂(rutile) and α-Al₂O₃ peaks.

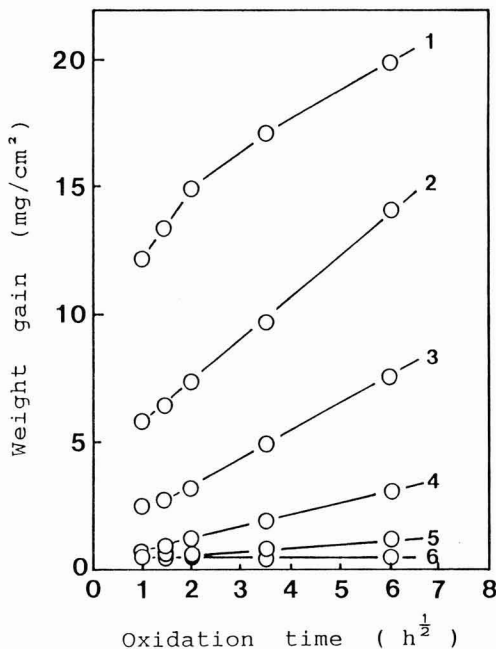


Fig. 5. Change of weight gains with oxidation time. 1): TiB₂, 2): TiB₂-10wt% Al₂O₃, 3): TiB₂-25wt% Al₂O₃, 4): TiB₂-50wt% Al₂O₃, 5): TiB₂-75wt% Al₂O₃ and 6): TiB₂-90wt% Al₂O₃.

Figure 5 shows the weight gains due to oxidation at 1000°C of sintered TiB₂-Al₂O₃. For samples with Al₂O₃ contents above 50wt%, oxidation including initial phases follows the parabolic rule. This trend implies that the TiO₂ layer produced by oxidation serves as a protective layer against oxygen, causing the oxidation rates to be determined by the diffusion of oxygen through the TiO₂ layer.^{11,12} The sintered TiB₂ sample with 90wt% Al₂O₃ had a weight gain of 0.15mg/cm² in the first hour of oxidation but no further weight gains in subsequent oxidation.

The samples with Al₂O₃ contents of 25wt% or less, on the other hand, greatly increased in weight in the first hour of oxidation, which is inconsistent with the parabolic rule. This may be because these samples had numerous open pores, allowing oxidation to proceed rapidly inward from the surface. After the initial period of oxidation, weight gains proceeded nearly in proportion to the square root of oxidation time and the oxidation rates were probably determined by the diffusion of oxygen through the TiO₂ layer.

Figure 6 is the optical micrograph of the surface of the sample with 90wt% Al₂O₃ before oxidation. TiB₂ grains (part A in Fig.6) are individually surrounded by Al₂O₃ grains, with hardly any two grains in contact with each other. This can also be assumed from the results of the measurement of the resistivity of the

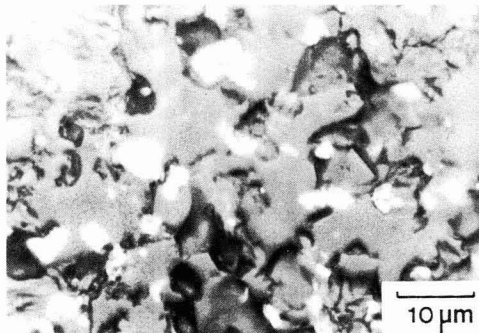


Fig. 6. Photomicrograph of the polished surface of the TiB₂-90wt% Al₂O₃ composite.

sintered TiB₂-Al₂O₃ samples. With Al₂O₃ from 75 to 90wt%, the probability of contact between TiB₂ grains rapidly decreases, while the resistivity rises from 10³ to 10⁵Ω·cm. This agrees well with the trend mentioned above.⁹⁾ For TiB₂ in the samples with 75 or 90wt% Al₂O₃ to be oxidized, oxygen must diffuse through Al₂O₃ grains. This may be why TiB₂ surrounded by Al₂O₃ grains is little oxidized.

4. Conclusions

To increase the oxidation resistance of TiB₂, we investigated the oxidation resistance of sintered TiB₂-Al₂O₃ composites, discovering the following.

- 1) The oxidation resistance of sintered TiB₂-Al₂O₃ composites increased as the Al₂O₃ content increased.
- 2) While sintered TiB₂ without additives increased in weight by about 20mg/cm² in 36h of oxidation at 1000°C, sintered TiB₂ with 50wt% Al₂O₃ increased by only about 3mg/cm², showing that it had a much higher resistance to oxidation.
- 3) The TiB₂-90wt% Al₂O₃ sample showed hardly any weight gains due to oxidation after the initial period of oxidation.

Reference:

- 1) Г. В. САМСОНОВ и И. М. ВИННИЦКИИ, Handbook on High-Melting-Point Compounds, Nisso Tsushinsha (1977).
- 2) A.D. McLeod, J.S. Haggerty and D.R. Sadoway, J. Am. Ceram. Soc., 67, 705-08 (1984).
- 3) D.R. Pendse and P.L. Pratt, Special Ceramics 5, 134-46, The British Ceramics Research (1972).
- 4) V.J. Tennery, C.B. Finch, C.S. Yust and G.W. Clark, Science of Hard Materials, 891-909 (1981).
- 5) T. Watanabe and S. Kouno, Am. Ceram. Soc. Bull., 61, 970-73 (1982).

- 6) T. Watanabe and K. Shobu, *J. Am. Ceram. Soc.*, 68, C34-C36 (1985).
- 7) W.A. Zdaniewski, *J. Am. Ceram. Soc. Bull.*, 65, 1408-14 (1986).
- 8) S. Torizuka and H. Nishio, *Powders and Powder Metallurgy*, 36, 100-04 (1989).
- 9) J. Matsushita, S. Hayashi and H. Saito, *Nippon Seramikkusu Kyokai Gakujutsu Ronbunshi* 97, 1206-10 (1989).
- 10) K. Shobu and T. Watanabe, *Yogyo-Kyuokai-Shi* 95, 991-98 (1987).
- 11) M. Kinoshita, S. Kose and Y. Hamano, *Yogyo-Kyokai-Shi* 78, 64-73 (1970).
- 12) Y. Maeda, K. Nakamura and N. Azuma, *Nippon Seramikkusu Kyokai Gakujutsu Ronbunshi* 96, 795-98 (1988).

This article is a full translation of the article which appeared in *Nippon Seramikkusu Kyokai Gakujutsu Ronbunshi* (Japanese version), Vol.98, No.3, 1990.

Information & communications

News

Highest Critical Current Density With Thin Film Without Heat-treatment

Sumitomo Electric Industries Ltd. and the Tokyo Electric Power Co., Ltd. have announced that they have made an yttrium family superconducting oxide film with the critical temperature of 91.5K. This oxide has the world's highest critical current density of 800A/cm² at zero magnetic field, and 170A/cm² at 1T. The results were realized with a 0.48 micrometer polycrystalline film deposited on a magnesia substrate by laser deposition technology without using any heat-treatment. So far the best critical current density was 600/cm² achieved by Belrove, an American company. This result is considered to have enlarged the possibility of choice of substrates, and they consider it a step to the goal of realization of superconducting oxide wire.

Secondary Battery Current Source for Superconducting Magnet

A joint research team of the Osaka Electro-Communication University, Osaka University and Fuji Electro-chemical Co., Ltd. has reported the world's first successful test of energizing a superconducting magnet using a secondary battery. The idea that for energization of a superconducting magnet a cell could be used was not new, but difficulty in controlling current through a variable resistor to a superconducting magnet hindered realization of this method. The group controlled current by changing the size of electrode areas which were dipped into electrolyte, and realized 5T magnetic field with current of 100A. The battery method would reduce the size of the current source to about 1/5, and the weight to under 30kg. Larger current source could be easily obtained by series connection of batteries. Fuji Electro-chemical Co., Ltd. plans to put the moving electrode-type current sources on the market, with a price below 100 million yen.

Y-family Superconductor Wire

Kobe Steel Ltd. announced the first success of wire drawing of an yttrium

family superconductor. The superconducting material used was the 1-2-4 type superconductor of which Kobe Steel has already reported the establishment of mass-production technology. The well known 1-2-3 superconductor was difficult to draw into wire and had a serious heat-treatment temperature limit at 400°C. The wire has stable characteristics and critical current density of 5,000A/cm² at zero magnetic field and liquid helium temperature. For actual use for a coil the critical current density should be increased to the order of several tens of thousands of amperes per cm². Kobe Steel consider that the yttrium family superconducting wires could realistically be used in place of the Nb₃Sn wires now widely used.

Hi-Tc Superconductor Thin Film on Metal

Ishikawajima-Harima Heavy Industries Co., Ltd. have announced the success of the test formation of an yttrium family high temperature superconductor thin film on metal of which the critical temperature stayed as low as 30K. It said this was the first success by ship-building and heavy industry companies in this field. The metal substrate used was a 20mm square nickel based alloy on which the yttrium family material was deposited by sputtering technology with the help of a magnesia intermediate layer, by which the undesired effects of metal atoms on superconductivity was restrained. The company considered that superconducting wires could be manufactured when the thin film was formed on the surface of metal wire, a superconducting coil could be obtained when it was formed on the surface of a coil-shaped metal piece and an electromagnetic wave shielding sheet could be formed when the thin film was formed on a metal shield. So far Furukawa Electric Co., Ltd. and other companies reported the successful formation of 82K super-conducting thin film on metal with help of intermediate oxide layers.

The Front Line of HiTc Superconductor Device Processing

Superconducting electronics are highlighted with the debut of high temperature

superconductors. What sort of possibility lies in superconducting electronics, and what can we expect with superconducting devices? Professor Takeshi Kobayashi of the Faculty of Engineering Science of Osaka University gave an answer to these questions in the recent Nikkan Kogyo Shinbun. Here is a summary of his report:

The Information Revolution wants higher quality in data and signal transfer and transformation. As a response to these requirement efforts in which the response time is reduced are continued. So far the finest processing plays a major role for this, but extension along this line however cannot be thought of as hopeful. Physics contains more than is in today's silicon LSI technology. Superconducting devices are expected to overcome limitations on the state of the art. There are two prominent aspects with superconductors. The first is the zero electric resistivity, and the second is the long range quantum effect.

We well remember the sudden rise of the critical temperature of superconductivity up to 125K with the discovery of the new class of superconducting oxides. In USA organized R & D efforts for applied superconductivity have started. AT&T Bell Research Laboratory has been successful in development of a high quality signal transfer line of high temperature superconductor in order to pick up pico-second order electric pulsed signals at 5cm distance.

Superconductive quantum effect devices are the only devices which can show ideal responses independent of the device size. Superconducting oxides consisting of from four to six elements seemed at first to be difficult to process to form thin film, but outstanding progress has been established in which only 2nm thick ultra-thin film shows very good superconducting characteristics. The almost complete transparency of this superconducting thin film is also interesting for actual use of this material.

The world's first Josephson device produced by Matsushita Electric Industrial Co., Ltd. with bismuth-family superconducting oxides showed high sensitive response capability to micro-wave frequencies. Successful formation of a SQUID (superconductive quantum interference device) was obtained by IBM Research Lab, USA using thallium family superconducting oxides. The SQUID will be used as a fun-

damental device of high speed digital circuits which use the flux-quantum as an information signal unit. Fujitsu Research Lab. have developed a device which attained the world's highest switch action time of 1 pico-second order, with which a device of 3 or 4 orders higher integration level can be expected.

Along the Josephson line flux-quantum run at nearly light velocity. This corresponds to the signal transfer mechanism in the human neuro-system. The R & D for using this as a circuit element of a neuro-computer has begun. It may be that the shortest way to the realization of a man-like computer is to introduce quantum effect devices.

Pastes and Substrates for Hi-T_c Superconductor Films

Dowa Mining Co., Ltd. has put on sale pastes for thick films of yttrium-system and bismuth-lead-system superconductors, and ceramic-polycrystalline and metal substrate materials for thick films. Superconducting oxide thick films can be easily formed by printing/spreading and bake methods with these pastes. The pastes and substrates will be used for making Josephson elements and devices, magnetic shielding surfaces and superconducting wiring on ceramic substrates. There are three kinds of yttrium system pastes for thick films and also three kinds of bismuth-lead-system pastes, and their costs will be between 15,000 to 20,000 yen per 20grs. Large size substrates of polycrystalline magnesia and yttrium/zirconium ceramics and copper and silver metals will cost between 500 to 13,000 yen a sheet.

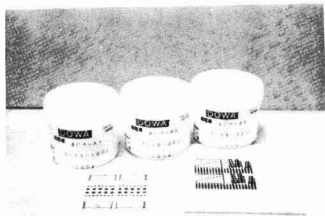
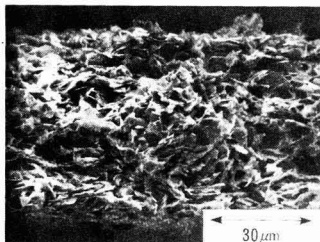


Photo 1. Dowa Mining's pastes and substrates

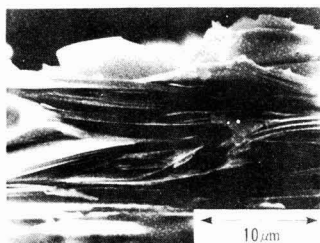
High Magnetic Field Hi-T_c Superconductor Film With 16,700A/cm² at 23T

The National Research Institute of Metals and Asahi Glass Co., Ltd. have reported the successful test fabrication of

a tape of bismuth family superconductor which had the critical current density of 16,700A/cm² under the magnetic field of 23T at 4.2K. The critical current density in zero magnetic field was 50,000A/cm². This tape was developed for in-liquid-helium use, which would show the excellent performance at 4.2K. Here the newly developed doctor blade base technology and heat-treatment control technology were used to make long 10 to 20 micron thick tapes. The total length of the test-fabricated tape was 10cm.



(a) 5 hour heat treatment at 870°C



(b) 5 hour heat treatment at 880°C

Photo 1. Cross sectional view of the newly developed tape by NRIM and Asahi Glass

Coating a Biocompatible Material on Ceramics

The Nagoya Government Industrial Research Institute of the Agency of Industrial Science and Technology has succeeded in coating biocompatible β -calcium phosphate (TCP) on partially stabilized zirconia (Y-PSZ) using magnesium metaphosphate (MP) as an intermediate material. This is the first example of coating a calcium phosphate-group compound on ceramics and it is raising expectations of a new cementless junction technology. Coating was conducted using the reactive fusion method, a method for thermal processing of materials in an electric furnace. Y-PSZ and β -TCP chemically react with the intermediate material.

The close adhesion by thermal processing at about 1200°C prevents alkaline calcium oxide, which results from cracked calcium phosphate and which adversely affects the human body, from being produced. This method can provide a film thickness of 100 μ . With this film thickness, ceramics can be a place for osteoblasts to form bone growth. Calcium phosphate-group compounds, such as β -TCP and apatite hydroxide, have superior biocompatibility, and have attracted attention as candidate materials for artificial bones and teeth.

Production of Porous Ceramics by Casting

H. Ichinose, researcher at the Fine Ceramics Division of the Saga Prefectural Ceramics Experimental Station, has developed a coarse-grain casting technology for manufacturing porous ceramics using bentonite as a molding sintering assistant. Ichinose used eight types of alumina materials of particle size between 0.2 and 150 μ m, with a molding sintering assistant of sodium-substituted bentonite and an organic dispersion binder, to produce the ceramics. Bentonite, superior in swelling character, controls the sedimentation in the slurry during casting and penetrates grains of the alumina to expand voids among them, thereby functioning as a plasticizer for compacts.

Experiment shows there is a nearly constant linear relationship between the material size and the pore diameter. Material size of 0.2 μ m gives average pore diameter of 0.06 μ m, 0.4 μ m gives 0.13 μ m, 16 μ m gives 5.9 μ m, 48 μ m gives 17.7 μ m and 150 μ m gives 53 μ m pores. The porosity ranges between 47 and 54%, and does not depend much upon the material size. Expected applications include bioreactor carriers.

Mass Production of Brake Rings for Use in BN Horizontal Continuous Casting Machines

Koransha Co., Ltd. has established a mass production facility for brake rings for use in boron nitride (BN) horizontal continuous casting machines using the slip cast method and atmospheric sintering. The brake ring in a horizontal continuous casting machine is mounted on the smelting takeoff port in the tundish and plays the role of a packing material for the connection with a water-cooled copper mold. Therefore, it must withstand the difference in temperature between about 1500°C of the smelting side and several tens of degrees Celsius at the mold. The brake ring presently marketed by Koransha

provides a bending strength of 5kg/mm^2 at over 1200°C in a nitrogen atmosphere, two times that of one produced by the hot press method. BN has a sublimation temperature as high as 3400°C and has been considered unsinterable in air. The company developed the atmospheric sintering method for BN two years ago jointly with Prof. K. Morinaga, Kyushu University. The method involves adding a small quantity of additive to BN, molding it by the original slip cast method, and then sintering it by a new sintering method in air. The company has recently started full-scale sales targeting domestic steel manufacturers and intends to ship 50 pieces to US steel manufacturers on a test basis.

Artificial Ivory

Sakai Physical and Chemical Research Institute has successfully developed artificial ivory with egg shells as the main material. The artificial ivory is manufactured by adding milk as an adhesive to eggs crushed together with their shells and mixing this with lipase, a fat-splitting enzyme, and with titanium oxide for weight adjustment. With the use of natural materials, the product is substantially the same in composition as natural ivory, featuring high hygroscopicity compared to synthetic resin counterparts. The company intends to make future improvements so as to provide it with ivory's distinctive stripe patterns and sense of massiveness. The company also plans to promote a study of how to make it feel natural when held in the hand by increasing the coefficient of friction to make it as close to natural as possible. Expectations of the practical applications of artificial ivory are high in industries such as music instrument manufacturers who use ivory for piano keyboards and manufacturers of Japanese seals. The company will launch its practical applications under contract to Fukuvi Chemical Industry Co., Ltd.

Success in Synthesizing Asbolite

The Government Industrial Research Institute, Nagoya, has determined that the main component mineral of natural asbolite is thin plate-shaped lithiophilite containing cobalt, and has also succeeded in producing a new type of synthetic asbolite by hydrothermal synthesis. Natural asbolite is mainly produced at Seto, Aichi Prefecture, but the price is high since no one prospects for it and only ceramic artists use it. For general use, spinel solid-solution synthetic asbolite is used. However, it has problems such as inferior workability under the painter's brush, diffusion on the base during painting, and the difficulty of sintering in light indigo. The new syn-

thetic asbolite has been produced by hydrothermal processing at about 240°C for three days from a starting material containing lithium hydroxide, aluminum hydroxide, manganese dioxide and cobalt hydroxide. The particle size of synthetic asbolite is 0.1 to $1\mu\text{m}$. The fine plate-shaped particles make handling of a painting brush easy and the solubility in water makes the diffusion of paint on the base excellent. The unique coloring of asbolite is likely to be applied to industrial products of new design.

High Toughness Realized for Silicon Nitride Ceramic

NKK (Nippon Kokan K.K.) has developed a silicon nitride ceramic with a fracture toughness of 12, which is double the value of conventional ceramic. The company tried to improve toughness by minute structure control aiming at improving the reliability of the normally brittle ceramic material. They achieved this aim making the needle crystals in the structure larger, and by preventing the cracks from running linearly. Needle crystals are much larger than whiskers, and toughness increases as the grain size increases. Generally speaking the bending strength decreases as the fracture toughness increases, but the bending strength of this silicon nitride ceramic is more than 0.10g/mm^2 , which is the same level as the conventional material. The Weibull coefficient (derived from the correlational relation between three points of bending strength and accumulated fracture probability) is 26.1, which exceeds 20, the final target value of the national project. As this ceramic does not contain extraneous material like whiskers, complicated shapes can easily be cast by injection molding. Since the brittleness, which has been the biggest demerit of this ceramic, has been greatly improved, applications in the field of automobiles and machine parts are anticipated.

Manufacturing Technology for Sintered Titanium Boride

The Research Development Corp. of Japan (JRDC) has selected a manufacturing technology for sintered titanium boride as an item which can be developed for commercialization. The technology is a result of research made by Prof. H. Saito of the Toyota Institute of Technology, and Toshiba Ceramics Co., Ltd. will conduct the commercialization development. Titanium boride has low specific gravity and high hardness, corrosion resistance and electro-conductivity and it can easily be separated from molten metal. It also commands attention as an industrial material because it is chemically stable. Sinterability is greatly improved by mixing with a small volume of sintering aids such as chromium powder or nickel powder and carbon powder. Dense sintered titanium boride is manufactured by sintering under atmospheric pressure in an inert gas atmosphere. In this way it is possible to manufacture titanium boride which has a large and complicated shape with excellent hardness, corrosion resistance and electro-conductivity. The development period is two and a half years and the entrusted development expenditure will be about 350 million yen.

Electroheating Lighter Using Ceramic Fiber

The Free Energy Research Institute has developed a high temperature resistant electroheating lighter with a ceramic fiber used as an exothermic heating wire. Previously lighters of this type used platinum or nichrome wire. The ceramic fiber used this time is much superior in heat-resistance and heat-response performance to the conventional metal wires. The lighter is instantly white-heated when switched on, using two dry batteries of 3V. As there is no flame as in a gas or oil lighter, it is very safe and can be used in strong wind with no problem. The

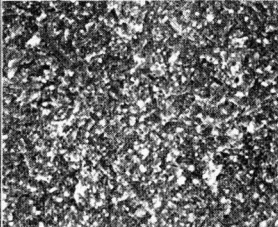
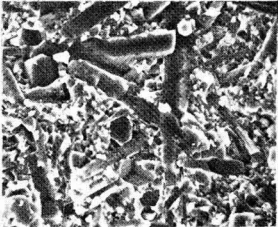
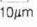
Microstructure		
		
$\sigma_{3B}(\text{Kgr/mm}^2)$	117	79
$K_{IC}(\text{MPa} \cdot \text{m}^{1/2})$	5.7	11.3

Photo 1. Microstructure of silicon nitride ceramic, by existing process (left) and by new process

company is aiming at the commercialization of the product with such variations in the design as switch type and method of applying a shutter to the heater surface.

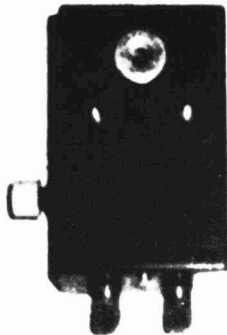


Photo 1. Electroheating lighter

Metal Baking Ceramic Material for Dental Use

Noritake Co., Ltd. has been promoting the research and development of high-tech materials utilizing the ceramic technology developed through its manufacture of high grade ceramic tablewares. One of the areas of development is dental-use materials, and ceramic material for metal baking is a representative product. The product was developed in joint research with Ms. Kiyoko Saka, who was instruction chief at Tokai School for Dental Treatment at that time. The product has three superior characteristics. (1) There is no change in thermal expansion at any baking condition, and so there will be no cracks for a wide range of metals. (2) As there is no need to worry about yellowing, semi-precious materials including silver can be used without anxiety. (3) The material has an ideal fluorescent color which shows no difference from the color of natural teeth. The company sells, at the present time, dental materials such as ceramics, alloy metals, calcined gypsum, anhydride, embedding materials, fire-resistant model

making materials, etc., and presently occupies about 20% of the domestic market. Although domestic and imported products are competing on equal terms and the competition is very tough, the company is aiming at obtaining a 30% market share.



Photo 1. Ceramic material for metal baking

Abstracts of Articles on Ceramics from the Selected Journals of the Learned Societies

Kagaku Kagaku Ronbunshu
Vol. 15, No. 6 (1989)
1179-1186

Periodic Dynamic Filtration by Use of Ceramic Filter with Rotating Cylinder

Toshiro Murase, Eiji Iritani, P. Chidphong
and Katsuhiro Kano

Dept. of Chem. Eng., Nagoya Univ., Nagoya 464-01

Key Words : Solid Liquid Separation, Filtration, Dynamic Filtration, Periodic Operation, Yeast, Rotating Cylinder, Ceramic Membrane

A coaxially rotating cylinder type of dynamic filter with a ceramic membrane was used for microseparation of a "difficult-to-filter" suspension containing very fine particles. In this study a high filtration rate of suspended yeast was investigated, using a periodic dynamic filtration by rotating the cylindrical membrane intermittently.

Periodic dynamic filtration comprises two operational modes: 1) the filtering of a dilute suspension with a static membrane at a constant pressure, and 2) the sweeping of filter cake from the membrane by closing the filtrate drainage channel and rotating the membrane at a high speed. A much higher filtrate flux can be achieved by this newly developed technique than that produced by conventional dynamic filtration with a continuously rotated medium. Based on the fact that medium resistance can be empirically evaluated in terms of the repeated number of filtration cycles, Ruth's filtration equation is used here to predict the time change of filtrate volume. It is shown that the optimum filtration time, $\theta_{f,opt}$, gradually increases with the increase of total operational time, θ_t .

Kagaku Kagaku Ronbunshu
Vol. 15, No. 6 (1989)
1197-1200

Experimental Investigation of the Decrease of Grinding Rate in Planetary Ball Milling

Qian-Qiu Zhao and Genji Jimbo

Dept. of Chem. Eng., Nagoya Univ., Nagoya 464

Key Words : Grinding, Grinding Rate, Coating, Planetary Ball Mill, Two-Phase Model

Dry grinding experiments were carried out with a planetary ball mill. Layer particles adhering to the mill wall and freely movable particles in the mill were separated from each other and changes in their weight fractions, size distributions and specific surface areas with grinding time were measured for various balls, feed sizes and powder fillings. Certain correlation between the decrease of grinding rate and the increase of coating particles was confirmed and a new empirical equation for expressing the change of specific surface area of product in batch grinding were derived.

Japanese Journal of Applied Physics
Vol. 28, No. 12, December, 1989
pp. L2182-L2184

Growth of the High- T_c Phase in the Bi-Pb-Sr-Ca-Cu-O Superconducting Oxide System

Yasushi HAYASHI, Hideo KOGURE and Yasuo GONDŌ

Faculty of Engineering, Yokohama National University, Yokohama 240

We studied the effects of the sintering temperature and the cooling rate on the depth profiles of the fraction of the high- T_c phase in the Bi-Pb-Sr-Ca-Cu-O superconductors. We used X-ray diffraction patterns to estimate the fraction of the high- T_c phase. We found that the larger fraction of the high- T_c phase grew inside the samples. Such depth profiles can possibly be explained by the desorption of oxygen in heating and the absorption of oxygen in cooling.

KEYWORDS: Bi-Pb-Sr-Ca-Cu-O superconductor, high- T_c phase, X-ray diffraction patterns, depth profile, cooling rate, sintering temperature

Vol. 28, No. 11, November, 1989
pp. L1912-L1914

Nonresonant Microwave Absorption of Single Crystals in the Bi-Sr-Ca-Cu-O System

Kimihito TAGAYA, Nobuo FUKUOKA and Shigemitsu NAKANISHI

Department of Materials Science, University of Osaka Prefecture, Sakai, Osaka 591

A nonresonant microwave absorption was observed for single crystals in the low- T_c phase of the Bi-Sr-Ca-Cu-O system, and a critical field in the resonance was investigated. This field may be the lower critical field. The anisotropy of critical field was uniaxial along the c -axis, and its principal values were determined to be 26 and 36 Oe at 77 K for the c -axis and the c -plane, respectively. Further, the lower critical field at 0 K was roughly estimated.

KEYWORDS: high- T_c superconductor, nonresonant microwave absorption, Bi-Sr-Ca-Cu-O, low- T_c phase, lower critical field, anisotropic property

Japanese Journal of Applied Physics
Vol. 28, No. 11, November, 1989
pp. L1915-L1917

Mass Reduction Mechanism in High T_c Superconductivity —Estimate of T_c —

Satoshi ISHIZAKA and Takeo IZUYAMA

*Institute of Physics, College of Arts and Sciences,
University of Tokyo, Komaba 3-8-1, Meguro-ku, Tokyo 153*

A two-dimensional electron lattice with alternating spin alignment is considered. When a certain number of holes or excess electrons are injected into this lattice, they will fall into the bound state with the lower energy, leading to novel superconductivity. The bound state is formed by a pair of holes (or excess electrons) through the mass reduction mechanism. The transition temperature for superconductivity is given by the gap equation, which is solved exactly.

KEYWORDS: origin of high T_c superconductivity, mass reduction mechanism, T_c

Japanese Journal of Applied Physics
Vol. 28, No. 11, November, 1989
pp. L1918-L1921

Reaction Mechanism of High- T_c Phase ($T_c=110$ K) Formation in the Bi-Sr-Ca-Cu-O Superconductive System

Jun TSUCHIYA, Hozumi ENDO, Naoto KUJIMA,
Akihiko SUMIYAMA, Masaaki MIZUNO and Yasuo OGURI

*Research Center, Mitsubishi Kasei Corporation,
1000 Kamoshida-cho, Midori-ku, Yokohama 227*

The reaction mechanism to produce the high- T_c phase was investigated using X-ray powder diffractometry and thermogravimetry and differential thermal analysis (TG-DTA). The high- T_c phase was produced through the low- T_c phase (Bi₂Sr_{1-x}Ca_xCu₂O_z, $1 < x < 2$) which was formed as an intermediate reaction product and also as a precursor of the high- T_c phase. In order to produce the high- T_c phase, it is necessary that the melting point of the low- T_c phase be lower than that of the high- T_c phase. Increase of Ca content in the low- T_c phase or decrease of ambient partial oxygen pressure during calcination are quite efficient to decrease the melting point of the low- T_c phase, and hence to enhance the formation of the high- T_c phase.

KEYWORDS: superconductor, Bi-Sr-Ca-Cu-O system, solid-state reaction, reaction mechanism, X-ray diffraction, TG-DTA

Japanese Journal of Applied Physics
Vol. 28, No. 11, November, 1989
pp. L1922-L1925

Effect of Low-Temperature Annealing on the Coupling at Grain Boundaries in Sb-Doped (Bi, Pb)₂Sr₂Ca₂Cu₃O_y Superconductors

Ryuji SATO, Takayuki KOMATSU, Kazumasa MATUSHITA
and Tsutomu YAMASHITA¹

*Department of Chemistry, Nagaoka University of Technology, Nagaoka 940-21
¹Department of Electronics, Nagaoka University of Technology, Nagaoka 940-21*

We examined the effect of further annealing at low temperatures in the range of 300°C to 700°C on the coupling at grain boundaries of the high- T_c phases in superconducting Sb-doped (Bi, Pb)₂Sr₂Ca₂Cu₃O_y ceramics prepared by the melt-quenching method. It was found that the weak coupling at grain boundaries of the high- T_c phases was remarkably improved by annealing at 500°C under the presence of oxygen. The improved coupling at grain boundaries was again weakened by annealing at 600°C or 700°C due to the occurrence of a new reaction.

KEYWORDS: Bi-Pb-Sr-Ca-Cu-O system, Sb-doped, weak coupling, grain boundary, melt-quenching method

Nippon Kinzokugaku Kaishi
Vol. 53, No. 11 (1989)
1153-1160

Characterization of Nitride Ceramic-Metal Joints Brazed with Ti Containing Alloys

Masako Nakahashi*, Makoto Shirokane* and Hiromitsu Takeda*

Joining nitride ceramics to metals was tried using various brazing alloys containing titanium. Ti-Ag-Cu and Ti-Cu brazing alloys showed good bondability to both silicon nitride and aluminum nitride. The microstructural and compositional change in the joints were investigated by X-ray diffraction, scanning electron microscopy, auger electron microscopy and other analytical methods.

Japanese Journal of Applied Physics
Vol. 28, No. 11, November, 1989
pp. L1926-L1928

Crystal Structure and Characterization of the New $\text{Ti}(\text{La},\text{Sr})_2\text{CuO}_5$ -Type Superconductor

Takashi MOCHIKU, Toshio NAGASHIMA[†], Masaya WATAHIKI[†],
Yuh FUKAI[†] and Hajime ASANO

Institute of Materials Science, University of Tsukuba, Tsukuba, Ibaraki 305
†Faculty of Science and Engineering, Chuo University, Bunkyo-ku, Tokyo 112

We have discovered a new superconductor $\text{Ti}(\text{La},\text{Sr})_2\text{CuO}_5$ with transition temperature of about 40 K. The crystal structure of this material was determined by Rietveld analysis of powder X-ray diffraction data. The result indicates Cu-substitution for the Ti site and/or deficiency in the Ti site, and location of La and Sr on the Sr site in the Ti-O monolayer $\text{TiSr}_2\text{CuO}_5$ compound: the compounds have general formulas $\text{Ti}_{1-x}\text{La}_x\text{Sr}_{2-x}\text{Cu}_{1-y}\text{O}_5$ and $\text{Ti}_{1-x}\text{La}_x\text{Sr}_2\text{CuO}_5$. In both systems, superconducting properties were improved by Cu-substitution for the Ti site and deficiency of the Ti site.

KEYWORDS: superconductivity, $\text{TiSr}_2\text{Ca}_{x-1}\text{Cu}_y\text{O}_{3+2n}$, $(\text{Ti},\text{Cu})(\text{La},\text{Sr})_2\text{CuO}_5$, powder X-ray diffraction, electrical resistivity, magnetic susceptibility, electron probe microanalysis, Rietveld analysis

Japanese Journal of Applied Physics
Vol. 28, No. 11, November, 1989
pp. L1929-L1931

On the Formation of High- T_c Phase in Mo-Doped (Bi, Pb) $_2\text{Sr}_2\text{Ca}_2\text{Cu}_3\text{O}_y$ Superconductors

Ryuji SATO, Takayuki KOMATSU, Nozomu TAMOTO,
Kazuhiko SAWADA[†], Kazumasa MATSUTA and Tsutomu YAMASHITA^{††}

Department of Chemistry, Nagaoka University of Technology, Nagaoka 940-21
†Central Research Laboratory, Mitsubishi Cable Industries, LTD., Amagasaki 660
††Department of Electronics, Nagaoka University of Technology,
Nagaoka 940-21

We prepared superconducting $\text{Bi}_{1-x}\text{Pb}_x\text{Mo}_y\text{Sr}_2\text{Ca}_2\text{Cu}_3\text{O}_y$ ($x=0.05$ and 0.1) and $\text{Bi}_{1-x}\text{Pb}_x\text{Mo}_y\text{Sr}_2\text{Ca}_2\text{Cu}_3\text{O}_y$ ($x=0.1, 0.2, 0.3$ and 0.4) ceramics by the melt-quenching method and examined the effect of Mo addition on the superconducting properties. It was found that the formation of the high- T_c phase was largely enhanced by the coexistence of Pb and Mo elements. It was concluded that the lowering of the partial melting temperature at around 870°C caused by the addition of Mo element was very important for the formation of the high- T_c phase.

KEYWORDS: high- T_c superconductor, Bi-Pb-Sr-Ca-Cu-O system, high- T_c phase, Mo-dope, melt-quenching method

Japanese Journal of Applied Physics
Vol. 28, No. 11, November, 1989
pp. L1932-L1935

Superconducting Glass-Ceramic Fine Rods in $\text{Bi}_1\text{Ca}_1\text{Sr}_1\text{Cu}_2\text{Al}_0.5\text{O}_x$ Prepared under a Temperature Gradient — T_c and the Texture of Specimen—

Yoshihiro ABE, Hisashi ARAKAWA, Masahiro HOSOE,
Yasuo HIKICHI, Jiro IWASE, Hideo HOSONO
and Yukio KUBO*

Department of Materials Science and Engineering,
Nagoya Institute of Technology, Gokiso-cho, Showa-ku, Nagoya 466

Fine glass rods (dia. 1–2 mm) in $\text{Bi}_1\text{Ca}_1\text{Sr}_1\text{Cu}_2\text{Al}_0.5\text{O}_x$ prepared by pumping up the melt at 1150°C into SiO_2 glass tubes were reheated to 845°C according to a given procedure under a temperature gradient ($\approx 30^\circ\text{C}/\text{mm}$) or under no temperature gradient. The incorporated Al enhanced the glassification. In the former specimen crystals grew well to become much larger, and impurity Al was excluded from the superconducting phases on crystallization under a temperature gradient to form aluminous fibers; the $T_c(\text{zero})$ is ≈ 80 K and a shoulder appears around 110 K.

KEYWORDS: superconducting glass-ceramics, crystallization, temperature gradient, bismuth-oxide-based superconductor, glass-ceramics, superconducting rods

Japanese Journal of Applied Physics
Vol. 28, No. 12, December, 1989
pp. L2178-L2181

Properties of a Fluorine-Doped Y-Ba-Cu-Oxide Superconductor Prepared by Hot-Pressing

Tsuneyuki KANAI, Tomoichi KAMO and Shin-pei MATSUDA

Hitachi Research Laboratory, Hitachi Ltd., Hitachi, Ibaraki 317

Fluorine doped Y-Ba-Cu-oxide samples prepared by hot-pressing showed superconductivity without a subsequent heat treatment in oxygen, in contrast to the semiconducting behavior of undoped samples. CuF_2 powder was used as the fluorine source. Powders with the nominal composition $\text{YBa}_2\text{Cu}_3\text{O}_7\text{F}_x$ were hot-pressed in oxygen atmosphere at 900–950°C; a density of 5.72–5.83 g/cm³ was obtained. The Meissner effect was observed at 93 K and 75 K in the samples hot-pressed at 900°C and 950°C, respectively. The differing superconductivity between the undoped and F-doped samples may be due to changes in the average copper valence in the Y-Ba-Cu-O system.

KEYWORDS: high- T_c superconductor, Y-Ba-Cu-O-F system, hot-pressing

Japanese Journal of Applied Physics
Vol. 28, No. 11, November, 1989
pp. L1939-L1941

Effect of 120 MeV ^{16}O Ion Irradiation at Liquid Nitrogen Temperature on Superconducting Properties of Bi-Pb-Sr-Ca-Cu-O

Akihiro IWASE, Mitsuo WATANABE, Tadao IWATA
and Takeshi NIHIRA[†]

Department of Physics, Japan Atomic Energy Research Institute,
Tokai-mura, Naka-gun, Ibaraki 319-11

[†]Faculty of Engineering, Ibaraki University, Hitachi, Ibaraki 316

Bi-Pb-Sr-Ca-Cu-O superconductor is irradiated at liquid nitrogen temperature with 120 MeV ^{16}O ions up to the fluence of $3.5 \times 10^{16}/\text{cm}^2$. Transition temperature T_c and critical current I_c at 77.3 K decrease with increasing ion fluence. Annealing of the specimen up to 300 K after irradiation causes a slight recovery of T_c and I_c . However, recovery of the electrical resistance above 100 K is not observed.

KEYWORDS: Bi-Pb-Sr-Ca-Cu-O, electrical resistance, 120 MeV ^{16}O ion irradiation, recovery of T_c and I_c

Japanese Journal of Applied Physics
Vol. 28, No. 11, November, 1989
pp. L1942-L1944

High-Resolution Transmission Electron Microscopy of Defects in $\text{YBa}_2\text{Cu}_3\text{O}_8$

Koji YAMAGUCHI, Takayuki MIYATAKE, Tsutomu TAKATA,
Satoshi GOTOH, Naoki KOSHIZUKA and Shoji TANAKA

Superconductivity Research Laboratory,
International Superconductivity Technology Center,
Shinonome 1-10-13, Koto-ku, Tokyo 135

Microscopic structures of the high- T_c superconductor $\text{YBa}_2\text{Cu}_3\text{O}_8$ ($T_c = 80$ K) are examined by high-resolution transmission electron microscopy. Planar defects are observed as white spot lines in the micrograph of the single-phase $\text{YBa}_2\text{Cu}_3\text{O}_8$ and they have a structure with an absence of one Cu-O chain in the double Cu-O chain of $\text{YBa}_2\text{Cu}_3\text{O}_8$. $\text{YBa}_2\text{Cu}_3\text{O}_8$ and $\text{Y}_2\text{Ba}_4\text{Cu}_5\text{O}_{13}$ -like local structures exist around the planar defects.

KEYWORDS: high temperature superconductor, $\text{YBa}_2\text{Cu}_3\text{O}_8$, transmission electron microscopy, planar defects

Japanese Journal of Applied Physics
Vol. 28, No. 11, November, 1989
pp. L1945-L1947

Absorption and Desorption of Oxygen in $\text{Y}_1\text{Ba}_2\text{Cu}_3\text{O}_{7-\delta}$

Toshio UMEMURA, Kunihiko EGAWA, Mitsunobu WAKATA
and Kiyoshi YOSHIZAKI

Materials & Electronic Devices Laboratory, Mitsubishi Electric Corporation,
1-1-57 Miyashimo, Sagamihara, Kanagawa 229

The absorption and desorption velocities of oxygen in a $\text{Y}_1\text{Ba}_2\text{Cu}_3\text{O}_{7-\delta}$ sintered sample were measured by a thermogravimetric analysis when the atmospheric gas of nitrogen was exchanged for oxygen and oxygen for nitrogen. The weight change of the sample could be expressed by an exponential function of time in each process. In the absorption process of oxygen, the time constant was a complex function of the temperature, while in the desorption process, it was the monotonous temperature dependence. The diffusion constant and the activation energy were estimated at the temperature range of the tetragonal phase.

KEYWORDS: high- T_c superconductor, $\text{Y}_1\text{Ba}_2\text{Cu}_3\text{O}_{7-\delta}$, diffusion coefficient, diffusivity, activation energy, polycrystal

Japanese Journal of Applied Physics
Vol. 28, No. 11, November, 1989
pp. L1948-L1951

High Pressure Oxygen Treatment and the Substitution of Sr for Ba on $(\text{Nd}_{1/3}\text{Ba}_{2/3})_2(\text{Ce}_{1/3}\text{Nd}_{2/3})_2\text{Cu}_3\text{O}_y$ Superconductor

Hitoshi NOBUMASA, Kazuharu SHIMIZU, Yukishige KITANO[†],
Masataka TANAKA[†] and Tomoji KAWAI^{††}

Composite Material Lab., Toray Ind. Inc., 2-1, Sonoyama 3-chome, Otsu, Shiga 520

[†]Toray Research Center Inc., 1-1, Sonoyama 1-chome, Otsu, Shiga 520

^{††}The Institute of Scientific and Industrial Research,
Osaka University, Ibaraki, Osaka 567

Substitution of Sr for Ba in the $(\text{Nd}_{1/3}\text{Ba}_{2/3})_2(\text{Ce}_{1/3}\text{Nd}_{2/3})_2\text{Cu}_3\text{O}_y$ superconductor has been performed together with high pressure oxygen treatment, and the relationship among Sr content, lattice parameter, hole concentration and superconducting properties has been clarified. It has been found that there is a strong relationship between superconducting transition temperature (T_c) and c-axis length. The highest $T_{c,max}$ and $T_{c,min}$ of the $(\text{Nd}_{1/3}(\text{Ba}_{3/4}\text{Sr}_{1/4})_{2/3})_2(\text{Ce}_{1/3}\text{Nd}_{2/3})_2\text{Cu}_3\text{O}_y$ treated under 1300 atm oxygen pressure at 600°C for 24 hours are 59.3 K and 41.4 K, respectively. These transition temperatures are about 10 K higher than those of unsubstituted one.

KEYWORDS: $(\text{Nd}_{1/3}(\text{Ba}_{1-x}\text{Sr}_x)_{2/3})_2(\text{Ce}_{1/3}\text{Nd}_{2/3})_2\text{Cu}_3\text{O}_y$ superconductor, high pressure oxygen treatment, substitution effect, hole concentration, lattice parameter, the Cu valence state

Japanese Journal of Applied Physics X-Ray Photoemission Spectroscopy of $\text{Nd}_{2-x}\text{Ce}_x\text{CuO}_{4-y}$ and $\text{La}_{2-x}\text{Sr}_x\text{CuO}_4$
 Vol. 28, No. 11, November, 1989
 pp. L1952-L1954

Hiroyoshi ISHII, Takehito KOSHIZAWA, Hiromichi KATAURA,
 Takaaki HANYU, Hiroyuki TAKAI, Kenji MIZOGUCHI,
 Kiyoshi KUME, Ikuyo SHIOZAKI and Shigeo YAMAGUCHI

*Department of Physics, Faculty of Science, Tokyo Metropolitan University,
 Fukazawa, Setagaya-ku, Tokyo 158*

We have measured the Cu 2p and O 1s X-ray photoemission spectra of the high- T_c superconductors $\text{Nd}_{2-x}\text{Ce}_x\text{CuO}_{4-y}$ and $\text{La}_{2-x}\text{Sr}_x\text{CuO}_4$, and the copper oxides CuO and Cu_2O . The Cu 2p spectra of superconductors show features similar to those of CuO with divalent Cu ions. For $\text{Nd}_{2-x}\text{Ce}_x\text{CuO}_{4-y}$, the intensity ratio of the satellite to the main peaks decreases with increasing Ce content. The O 1s spectra exhibit a single-peaked structure and are insensitive to whether either electron or hole is doped.

KEYWORDS: XPS, $\text{Nd}_{2-x}\text{Ce}_x\text{CuO}_{4-y}$, $\text{La}_{2-x}\text{Sr}_x\text{CuO}_4$, carrier, valence

Japanese Journal of Applied Physics
 Vol. 28, No. 11, November, 1989
 pp. L1955-L1958

**Contact Resistance and $V-I$ Characteristics
 in a Ag-Doped Bi-Sr-Ca-Cu-O Superconductor**

Noriyuki SHIMIZU*, Kazuo MICHISHITA, Yutaka HIGASHIDA,
 Hisanori YOKOYAMA**, Yumi HAYAMI, Yukio KUBO,
 Eikichi INUKAI, Akira SAJI[†], Noboru KURODA[†]
 and Hiroshi YOSHIDA[†]

Japan Fine Ceramics Center, 2-4-1 Mutsumo, Atsuta, Nagoya 456
[†]*Electric Power Research and Development Center, Chubu Electric Power Co., Inc.,
 20-1 Kitasekiyama, Odaka, Midori, Nagoya 459*

Contact resistance and $V-I$ characteristics were investigated in Ag-doped and undoped Bi-Sr-Ca-Cu-O bulk samples prepared by the floating-zone method. In undoped samples, with increasing current pulse width, rapidity of voltage rise in $V-I$ characteristics increases and J_c decreases. The contact resistance is nonohmic and temperature dependence is semiconductorlike. In a Ag-doped sample, rapidity of voltage rise and J_c are not influenced by pulse width, and deviation of J_c among samples is small. The ohmic contact resistance has metallike temperature dependence, and its value is less than 1/500 of that in an undoped sample.

KEYWORDS: Bi-Sr-Ca-Cu-O system, Ag-doping, floating zone method, $V-I$ characteristics, contact resistance, critical current density, pulse width, n value

Japanese Journal of Applied Physics
 Vol. 28, No. 11, November, 1989
 pp. L1959-L1962

Relation between Cu L X-Ray and Cu 2p Photoelectron in $\text{YBa}_2\text{Cu}_3\text{O}_x$

Masanori FUJINAMI, Hiroki HAMADA, Yoshihiro HASHIGUCHI
 and Takashi OHTSUBO

*Materials Characterization Research Laboratory, Nippon Steel Corporation,
 1618 Ida, Nakahara-ku, Kawasaki 211*

X-ray emission spectroscopy (XES) is applied to the study of the electronic structure of Cu in $\text{YBa}_2\text{Cu}_3\text{O}_x$ superconductors. It is shown that the $\text{Cu } L_{\beta_1}/L_{\alpha}$ intensity ratio of the orthorhombic sample is about 4% higher than that of the tetragonal sample. The origin of this difference can be discussed consistently using Cu 2p X-ray photoelectron spectroscopy (XPS) spectra, indicating that the effect of charge transfer from O 2p to the Cu 3d hole is comparatively small for the orthorhombic sample in generation of Cu 2p hole. It is confirmed that the probability of $12p3d^9L_1$ and $12p3d^{10}L_2$ in the intermediate state for the tetragonal becomes higher in L line X-ray emission than that for the orthorhombic. As the result, the population of M_4 for the orthorhombic becomes low and only the intensity of L_{α} line is decreased.

KEYWORDS: high- T_c superconductor, $\text{YBa}_2\text{Cu}_3\text{O}_x$, X-ray emission spectroscopy, X-ray photoelectron spectroscopy, Cu L X-ray intensity, charge transfer

Japanese Journal of Applied Physics
 Vol. 28, No. 11, November, 1989
 pp. L1963-L1966

The Oxygen Potentials in the $\text{Y}_2\text{O}_3\text{-BaO-CuO}_x$ System

K. BOROWIEC and K. KOLBRECKA

*Warsaw University of Technology, Institute of Solid State Technology,
 00-664 Warsaw, Noakowskiego 3, Poland*

The oxygen potential for some chosen four and three-phase combinations has been measured at 750-1000°C using solid $\text{ZrO}_2 + \text{CaO}$ electrolyte. On the basis of $\log P_{\text{O}_2}$ values, the Gibbs energies of reactions for many possible reactions in the system were obtained. The reactions with the Y_2BaO_4 on the left sides exhibit negative entropy due to decomposition of Y_2BaO_4 below about 850°C. The positive entropy for several reactions clearly indicates that ternary cuprates such as Y_2BaCuO_5 , $\text{YBa}_2\text{Cu}_3\text{O}_x$, $\text{YBa}_4\text{Cu}_7\text{O}_{13}$ and $\text{Y}_3\text{Ba}_5\text{Cu}_8\text{O}_{19}$ are entropy-stabilized compounds. These cuprates become increasingly less stable with decreasing temperature and on cooling there are temperature limits below which these cuprates are metastable.

KEYWORDS: superconductivity, Y-Ba-Cu-O system, oxygen potential, stability of cuprates, EMF measurements, the Gibbs energies of reactions

Japanese Journal of Applied Physics
Vol. 28, No. 11, November, 1989
pp. L1936-L1938

Preparation of a Ag-Doped Bi-Sr-Ca-Cu-O Bulk Sample by the Floating-Zone Method

Yukio KUBO, Kazuo MICHISHITA, Noriyuki SHIMIZU*,
Yutaka HIGASHIDA, Hisanori YOKOYAMA**, Yumi HAYAMI,
Eikichi INUKAI, Akira SAJI†, Noboru KURODA†
and Hiroshi YOSHIDA†

Japan Fine Ceramics Center, 2-4-1 Mutsuno, Atsuta-ku, Nagoya 456

*Electric Power Research and Development Center,
Chubu Electric Power Co., Inc., 20-1 Kitasekiyama, Odaka-cho, Midori-ku, Nagoya 459

Bulk samples with nominal composition of $\text{Bi}_2\text{Sr}_2\text{CaCu}_2\text{O}_x$ doped with 0, 10 and 20 weight % Ag were prepared by the floating-zone method at growth rates of 2 mm/h and 5 mm/h. Ag-doping seems to slightly enhance J_c , while annealing is very effective for J_c enhancement. From preliminary ac susceptibility measurements, the J_c enhancement by annealing is considered to be due to improvement of the weak link between superconducting grains.

The 10% Ag-doped sample grown at 2 mm/h possessed J_c of 5360 A/cm² at 77 K under zero magnetic field after annealing.

KEYWORDS: Bi-Sr-Ca-Cu-O system, Ag-doping, critical current density, floating-zone method, annealing

Japanese Journal of Applied Physics
Vol. 28, No. 11, November, 1989
pp. L1970-L1972

Improvement of Surface Flatness on BiSrCaCuO Film

Yasuhiro NAGAI and Koji TSURU

NTT Applied Electronics Laboratories, Tokai, Ibaraki 319-11

This paper reports on the improvement of the surface flatness on BiSrCaCuO films. By keeping the film surface in contact with a MgO(100) plane during annealing, it is possible to greatly improve the surface flatness at each annealing temperature. The smooth surface is mainly made up of several- μm platelike crystals approximately 60 nm thick. The average surface roughness is determined by the annealing temperature, regardless of film thickness, in the range of 0.1-1.5 μm . As the critical temperature and surface morphology change due to the contacted MgO crystal plane, the improvement of surface flatness is considered to result from the crystal growth restriction on the film surface in contact with a MgO(100) plane.

KEYWORDS: surface flatness, BiSrCaCuO film, MgO-contact annealing, crystal growth restriction

Nippon Kagaku Kaishi
1989 (12)
p. 2018-2021

Firing Process of Calcium Phytate and Synthesis of Hydroxyapatite†

Fumiaki YAMADA, Yasuhari KANEKO and Hiromichi IWASAKI*

Department of Chemistry, Faculty of Science and Engineering, Ritsumeikan University:
Toji-in Kitamachi, Kita-ku, Kyoto-shi 603 Japan

A hydroxyapatite (HAp) has been synthesized using as a P-source phytin contained in rice bran. Phytin was extracted from the oilless rice bran by HCl solution. The mixtures of CaCO_3 (0.7 g) and $\text{Ca}(\text{OH})_2$ (0.3 g) were added to the extract of 200 ml containing phytin to obtain the precipitate of calcium phytate including CaCO_3 . Finally the precipitate fired at 1000°C for 3 h to yield HAp powders.

In this paper, the formation process of calcium phytate were observed with TEM and the composition of the fired HAp powders were examined by using X-ray diffraction, IR measurement etc.

The density of HAp powder obtained was 3.12 g/cm³. While shape of HAp powder was spherical particle of about 0.2 μm in diameter. It was also confirmed that the spherical HAp maintained a stable HAp structure even in the heat treatment at 1300 C, but decomposed into CaO , α -TCP, α - $\text{Ca}_2\text{P}_2\text{O}_7$, β - $\text{Ca}_2\text{P}_2\text{O}_7$ at 1400 C.

† Synthesis of Hydroxyapatite Powder from Rice Bran as Starting Materials. III.

Chem. Pharm. Bull
37 (11) 3079-3073 (1989)

Effect of Particle Shape on the Compaction and Flow Properties of Powders

Kazumi DANJO,* Kazutoshi KINOSHITA, Kazutaka KITAGAWA, Kotaro IIDA, Hisakazu SUNADA and Akinobu OTSUKA
Faculty of Pharmacy, Meijo University, Yagoto-Urayama, Tempaku-cho, Tempaku-ku, Nagoya 468, Japan. Received March 3, 1989

In order to clarify the effect of particle shape on the mechanical properties of powders, such as compaction and flow, the centrifugal compaction test, the tensile test, the direct shear test and Carr's flowability test were carried out on several kinds of fine powders having various particle shapes. Introducing the concept of "apparent adhesion," the effect of particle shape on the porosity, was examined. It was found that the porosity of a powder bed diminished as the sphericity of the particles increased. The flow properties were also affected by particle shape. With increasing shape factor, the flowability increased.

Keywords: particle shape, compaction, porosity, tensile strength, apparent adhesion, repose angle, flowability

Shigen Sozaigaku Kaishi
105 (1989) No. 13
981-986

Applicability of Displacement Discontinuity Method to Crack Problems

by Takumi SHIBA¹, Katsuhiko KANEKO², Yuzo OBARA² and Katsuhiko SUGAWARA³

Displacement Discontinuity Method (DDM) is one of useful means for analyzing the stress state and the deformation of the discontinuous body. However, it is well known that the accuracy of DDM analysis using the conventional scheme is not satisfactory for solving the crack problem.

In this paper, the improvement of the accuracy of DDM analysis on the crack problem and the applicability of DDM to the stress analysis of the jointed rock are discussed. Firstly, the analytical error of the DDM on the crack problem is discussed and a new scheme for numerical modeling of the crack is presented. Secondly, some numerical results of crack problems are shown and it is confirmed that the stress and the displacement fields can be analyzed sufficiently and accurately by DDM based on the proposed scheme. Finally, the mechanical behavior of elastic body which contains many cracks is analyzed and it is made clear that the deformability of the elastic body is strongly affected by not only the density and orientations of cracks but also geometrical distribution of them.

It is concluded that the DDM based on the proposed scheme make a promise to analyze the stress state and deformation of the discontinuous material like jointed rock.

Shigen Sozaigaku Kaishi
105 (1989) No. 13
995-999

Influence of Particle Shape on Grindability

— Relationship between probability of fracture and shape index —

by Yoshiteru KANDA¹, Yoshio MAKUTA² and Toshihiko IMAMURA²

In order to study the influence of particle shape on grindability, a crushing test was performed using a simple drop weight method. The samples used were quartz and limestone. The number of specimens prepared were 10,000 pieces of 5 ~ 6 mesh quartz and 5,000 pieces of 4 ~ 6 mesh limestone. The shape index defined by (diameter of a circumscribed circle/thickness) was measured by slide caliper and classified by value of shape index into five groups respectively. Assuming that the potential energy of a ball was the energy input to a specimen, the relationships between probability of fracture and dropping height of a ball or specific energy input to specimens were obtained experimentally. As a result, it was found that the probability of fracture increased with increase in shape index.

Chem. Pharm. Bull
37(11) 2897-2901 (1989)

Interactions of Aspartic Acid, Alanine and Lysine with Hydroxyapatite

Hideji TANAKA,^{*+11} Koichiro MIYAJIMA,^o Masayuki NAKAGAKI,^{o,21} and Saburo SHIMABAYASHI^h

Faculty of Pharmaceutical Sciences, Kyoto University, Yoshida-Shimoadachi-cho, Sakyo-ku, Kyoto 606, Japan*
The University of Tokushima,^h Shomachi 1-78-1, Tokushima 770, Japan. Received May 19, 1989

Hideji TANAKA,^{*+11} Koichiro MIYAJIMA,^o Masayuki NAKAGAKI,^{o,21} and Saburo SHIMABAYASHI^h

Faculty of Pharmaceutical Sciences, Kyoto University, Yoshida-Shimoadachi-cho, Sakyo-ku, Kyoto 606, Japan and Faculty of Pharmaceutical Science, The University of Tokushima,^h Shomachi 1-78-1, Tokushima 770, Japan. Received May 19, 1989*

Adsorption of amino acids (aspartic acid, alanine and lysine) on synthetic hydroxyapatite (HAP; $\text{Ca}_{10}(\text{PO}_4)_6(\text{OH})_2$) was investigated. The surface ion (calcium or phosphate ion) with the same sign of the electric charge as that of the terminal group of the adsorbed amino acid was released from HAP. Aspartic acid and lysine showed high affinity to HAP in weak acidic solution and in weak alkaline solution, respectively, owing to the opposite charges of HAP and these amino acids. On the other hand, the affinity of alanine was low and almost independent of the solution pH. It was concluded that the dominant factor for the adsorption is the electrostatic interaction between the amino acid and the HAP surface. This interaction was shielded by the addition of an indifferent salt for HAP: KCl. However, when calcium or phosphate ion was added to the solution, the adsorbed amount of aspartic acid or lysine increased, respectively, due to the increase in the opposite surface charges to that of the adsorbed amino acid.

Keywords hydroxyapatite; adsorption; amino acid; electrostatic interaction; release; incongruent dissolution; aspartic acid; alanine; lysine

Japanese Journal of Applied Physics Superconductivity in Ti-Bi-Ca-Sr-Cu-O and Ti-Bi-Pb-Ca-Sr-Cu-O Systems
Vol. 28, No. 12, December, 1989
pp. L2192-L2195

Yasuko TORII, Hiromi TAKEI and Kouji TADA

*Basic High-Technology Laboratories, Sumitomo Electric Industries, Ltd.,
 1-1-3 Shimaya, Konohana-Ku, Osaka 554*

The influence of the substitution of Bi for Ti on the formation of the superconducting phases in Ti-Bi-Ca-Sr-Cu-O and Ti-Bi-Pb-Ca-Sr-Cu-O systems was investigated. The superconducting (Ti, Bi)Ca₂Sr₂Cu₂O₈ phase with critical temperature of 113 K showing both zero resistivity and diamagnetism is prepared in a Ti-Bi-Ca-Sr-Cu-O system. The crystal structure of this phase is tetragonally symmetric with lattice constants of $a = 3.813(3)$ Å and $c = 15.266(5)$ Å. The superconducting tetragonal phase of (Ti, Bi, Pb)Ca₂Sr₂Cu₂O₈ is also formed in a Ti-Bi-Pb-Ca-Sr-Cu-O system.

KEYWORDS: superconductivity, Ti-Bi-Ca-Sr-Cu-O system, Ti-Bi-Pb-Ca-Sr-Cu-O system, Bi substitution, Pb substitution, critical temperature, DC magnetic susceptibility

Zairyo
Vol. 39, No. 435, Dec. 1989
1415-1421

Evaluation of Thermal Shock Resistance in Ceramic Materials

Shiro AKIYAMA*, Yuji KIMURA** and Michio SEKIYA**

Evaluations of thermal shock resistance, including the onset of crack propagation and progressive crack growth, and examinations to the deterioration property for tetragonal zirconia polycrystalline (TZP), silicon nitride and silicon carbide were conducted under various repeated thermal shock conditions. Vickers indented specimens with various surface flaws sizes were employed for these experiments.

The results obtained were summarized as follows:

(1) The minimum thermal shock condition required for the onset of crack propagation was proportional to the inverse square root of surface crack length under repeated thermal shock conditions.

(2) The actual stress intensity factor K_I of crack near the specimen surface was obtained by using a fracture mechanics formula for semielliptical flaws and making some corrections to the thermal stress value by taking the Biot modulus difference into considerations. As a result, K_I values of TZP, silicon nitride and silicon carbide were found to be about 17~33%, 17% and 6.9% compared with those calculated without corrections from the surface half crack length by employing usual fracture mechanics formula.

(3) TZP, which has the largest K_{Ic} value and bending strength, showed superior character, when the resistance of material under repeated thermal shock conditions was evaluated by the amount of crack growth per each cycle. Silicon carbide had the smallest resistance under the repeated thermal shock condition.

Key words: Thermal shock resistance, Tetragonal zirconia polycrystalline, Silicon nitride, Silicon carbide, Vickers indentation

J. Sci. Hiroshima Univ., Ser. A
Vol. 53, No. 3 pp. 25-48,
December 1989

Lifetime Broadening Picture in Oxide High-Temperature Superconductors

Jun TAKADA

Central Research Laboratories, Kanegafuchi Chemical Industry Co., Ltd.
Kobe 652

Anomalous behavior of the London penetration depth λ_L of Cu based oxide superconductors is studied and the effect of finite states in the energy gap on λ_L is discussed. Experiments of electron tunneling in single-crystal thin film of $YBa_2Cu_3O_{7-x}$ has been carried out and details of the quasiparticle density of state which can be understood in the framework of the Bardeen-Cooper-Schrieffer theory are presented. As the temperature approaches the transition point, the energy gap edge is lifetime broadened. The recombination lifetime of quasiparticles at 60K is estimated to be 10^{-13} s. A gap parameter Δ (4.6K) of 9.0 ± 1.8 meV in the perpendicular direction to the Cu-O planes and a coupling constant of $2.4 \pm 0.5(2\Delta / (0)/kT_c < 3.5 \pm 0.7$ were obtained.

Gypsum & Lime
No. 224 (1990) 15-20

Lattice-Ion Reaction Characteristics of Hydroxyapatite for Fe^{2+} , Fe^{3+} and Pb^{2+} Ions in Acidic Aqueous Solutions

Takashi SUZUKI and Toshiaki HATSUSHIKA

(Department of Chemistry and Biology, Faculty of Engineering, Yamanashi University;
Takeda, Kofu-shi 400)

Lattice ion reaction characteristics between Ca^{2+} ions of synthetic hydroxyapatite (HAP) samples and Fe^{2+} , Fe^{3+} ions in acidic aqueous solutions (pH: 2.0~5.0) have been investigated in detail by a normal batch method at 25°C. It was found that Fe^{2+} ions are slightly exchanged with Ca^{2+} ions of the HAP samples over pH of 4.0 but under pH of 4.0, dissolved reactions of HAP with H^+ ions become dominant instead of the exchange reaction. Removal behavior of Fe^{3+} ions, however, was found to be quite different from that of Fe^{2+} ions, i.e., Fe^{3+} ions are easily removed, assisted by the loosening effect of H^+ ions on the skeletal structure of the HAP samples, and the HAP samples are transformed into stable amorphous products ($FePO_4 \cdot mH_2O$) even in acidic solutions with low pH of 3.0 or below. Moreover, coexisting systems of Fe^{3+} and Pb^{2+} ions, with which HAP samples have been found to be easily converted into crystalline stable lead apatite in acidic solution, have been investigated under the conditions of low pH values (pH: 2.3~5.2). An interesting effect was found that the two ions suppress each other the reactions of the ions with HAP samples. These results are important in discussion concerned with reaction characteristics between human bones and teeth, whose main constituent is HAP, and invaded Fe^{2+} , Fe^{3+} and Pb^{2+} ions into human bodies.

Key words: Hydroxyapatite, Lattice-ion reaction, Fe^{2+} , Fe^{3+} , Pb^{2+} ions, Acidic solution

Zairyo
Vol. 38, No. 435, Dec. 1989
1428-1433

A Study on Strength Distribution and Size Effect of Ceramics by Computer-simulated Experiments

Yoshifumi TANIGUCHI*, Junichi KITAZUMI* and Toshiro YAMADA**

In order to investigate the change of strength of ceramics due to the size effect, the strength distribution was simulated by the Monte-Carlo method. The tensile strength, 3- and 4-point bending strength of four kinds of specimens of different sizes were calculated, by using the model of specimens with a number of penny-shaped inner cracks of which diameters followed the prescribed distribution. The strength obtained was plotted on the Weibull probability papers and represented by the 2-parameter Weibull distribution. As some experimental data had indicated, the Weibull modulus had a tendency to increase as the effective size decreased. It became clear that this tendency was caused by the existence of the upper limit of crack strength. The strength distribution function for this model was also expressed and compared with the simulation results. Although the Weibull plot of that function was slightly concave, it showed good agreement with the simulation results.

Furthermore, the relation between the mean strength and the effective volume was discussed, using the Weibull statistics. As a result, it was indicated that the Weibull statistics could not explain the change of strength due to the size effect satisfactorily.

Key words: Ceramics, Monte-Carlo simulation, Weibull modulus, Strength, Inner crack, Size effect

Journal of the Physical Society
of Japan

Vol. 58, No. 12, December, 1989
pp. 4280-4283

Electronic States in High- T_c Copper-Oxide Superconductors

Hisao JICHU, Tamifusa MATSUURA¹ and Yoshihiro KURODA²

¹Aichi College of Technology, Gamagori, Aichi 443

²Department of Physics, Nagoya University,
Chikusa-ku, Nagoya 464-01

The electronic states in the CuO_2 -layer have been studied by using the p - d model with the help of the bosonic technique for treating the local electronic correlation properly. What have been found are: at sufficiently low temperature the electronic states form coherent bands but there is a significant difference between the effects of electron doping and those of hole doping. In particular, the hole doping brings about a new band around the Fermi level inside the energy gap and intensity of the band increases as the number of holes increases. These band schemes may well explain the experiments.

Japanese Journal of Applied Physics
Vol. 28, No. 12, December, 1989,
pp. 2463-2467

The Contact Resistance of the $\text{YBa}_2\text{Cu}_3\text{O}_{7-\delta}$ -Metal Film System

Yoshihiko SUZUKI, Tadaoki KUSAKA, Akira AOKI,
Takahiro AOYAMA¹, Tsutomu YOTSUYA and Soichi OGAWA

¹Osaka Prefectural Industrial Technology Research Institute, 2-1-53 Enokojima, Nishiku, Osaka 550
²Daihen Co. Tagawa, Yodogawaku, Osaka 532

The electrical properties and X-ray photoelectron spectroscopy (XPS) of $\text{YBa}_2\text{Cu}_3\text{O}_{7-\delta}$ (YBCO) contacts formed by Ag, Au, Sn, Zn, In and Al metal films have been studied. The Cu, In, Zn and Sn film contacts show high resistivities with semiconductive temperature dependence. The Au, Ag, and Pt film contacts have low resistivities with metallic temperature dependence. The XPS analyses show that Sn and Al react with the oxygen on the YBCO surface. However, little change in copper and oxygen states can be observed in Ag/YBCO and Au/YBCO systems. It is assumed that the oxygen-deficient layer at the interfaces of Sn/YBCO and Al/YBCO systems makes the contact resistance high, while the semiconductive layer is insignificant at the Ag/YBCO and Au/YBCO interfaces, and their resistance is low. Analyses indicate that Ag/YBCO and Au/YBCO systems provide very effective ohmic contacts.

KEYWORDS: high- T_c superconductors, ohmic contact, XPS analysis

Japanese Journal of Applied Physics
Vol. 28, No. 12, December, 1989
pp. 2479-2484

Superconductive Wire Bonding with High Reliability at 4.2 K

Toshinori OGASHIWA, AKIhisa INOUE¹ and Tsuyoshi MASUMOTO²

¹Tanaka Denshi Kogyo, Ltd., 8-5-1 Shimorenjaku, Mitaka, Tokyo 181
²Institute for Materials Research, Tohoku University, Sendai 980

A superconductive bonding technique for superconducting electronic devices such as the DC-SQUID was developed by using a rapidly solidified $\text{Pb}_{78}\text{In}_{20}\text{Au}_2$ (at%) wire. The wire was bonded on the Nb pad coated with 30 nm-thick Au film to form the superconducting connection operating at 4.2 K. Mechanical stability of the wire bond parts remains unchanged by 15 thermal cycles in the temperature range 4.2 to 273 K. No appreciable degradation of the superconducting connection is observed even after the thermal cycling. These results lead us to expect that the present bonding technique will be useful in practical applications.

KEYWORDS: superconductive wire bonding, SQUID, Nb/Au pad, $\text{Pb}_{78}\text{In}_{20}\text{Au}_2$, rapidly solidified wire, wedge-wedge bonding, proximity effect, thermal cycling

Japanese Journal of Applied Physics
Vol. 28, No. 11, November, 1989
pp. 2211-2218

Crystallization Induced by Laser Irradiation
in Ba-Y-Cu-O Superconducting Films
Prepared by Laser Ablation

Shigeru OTSUBO*, Toshiharu MINAMIKAWA†, Yasuto YONEZAWA†,
Toshihiro MAEDA, Akiharu MORIMOTO and Tatsuo SHIMIZU

Department of Electronics, Faculty of Technology Kanazawa University,
Kanazawa, Ishikawa 920

†Industrial Research Institute of Ishikawa, Kanazawa, Ishikawa 920.02

Ba₂YCu₃O₇ superconducting films were prepared by laser ablation with some newly developed laser processing techniques. First, we revealed that a rapid postannealing by laser irradiation converts an amorphous film to a crystallized superconducting one. Second, we tried the *in situ* preparation without a high-temperature postannealing. To reduce the substrate temperatures T_s for the film preparation, we examined the effect of the laser irradiation on the growing film surface. We found that *in situ* excimer laser irradiation of the growing film surface improves the superconducting properties and the surface morphology of the films prepared at a relatively low T_s . This improvement is brought about mainly by the enhancement of the film crystallization, rather than by providing additional oxygen atoms to the film.

KEYWORDS: Ba-Y-Cu-O superconducting films, crystallization, excimer laser ablation, excimer laser irradiation, laser processing, crystalline silicon substrate, no buffer layer

Japanese Journal of Applied Physics
Vol. 28, No. 11, November, 1989
pp. L1902-L1905

Normal-State Resistivity of the (Bi/Pb)-Ca-Sr-Cu-Oxide System

Sang-Geun LEE*, Kyung-Soo Yi, Chong-Yun PARK*
and Min-Su JANG

Department of Physics, Pusan National University, Pusan 609-735, Korea

We measured the electrical resistivity $\rho(T)$ of the Bi_{1-x}Pb_xCa₂Sr₂Cu₃O₇ ($x=0.2, 0.4, 0.6$) system with $T_c \cong 108$ K in air and in the temperature range of 20 K < T < 800 K. The $\rho(T)$ shows linear temperature dependence in the range $T_c < T < T_2$ and upturn for $T > T_2$ where T_2 is in the range 610-680 K, depending upon the sample composition. The resistivity saturation was not observed over the temperature range we measured. From the linear behaviour of $\rho(T)$, we estimated the order to magnitude of the electron-phonon coupling constant λ and the electron mean free path l of high- T_c superconducting Bi-compounds in the high-temperature region.

KEYWORDS: Bi-system oxide superconductors, high- T_c phase, normal-state resistivity, electron-phonon coupling, electron mean free path

Japanese Journal of Applied Physics
Vol. 28, No. 11, November, 1989
pp. L1906-L1908

Temperature Dependence of Flux Creep in High- T_c Superconductors

Takanori FUJIYOSHI, Kiyoshi TOKO, Teruo MATSUSHITA
and Kaoru YAMAFUJI

Department of Electronics, Faculty of Engineering, Kyushu University,
6-10-1 Hakozaki, Higashi-ku, Fukuoka 812

The normalized decay rate R of magnetization due to thermally activated flux creep is typically given by $R = k_B T / U_c$, where k_B is the Boltzmann constant, T is the absolute temperature and U_c is the effective pinning potential. Some observed data for high- T_c superconductors show that R increases with increasing T_c , while in other studies, R takes a peak at a certain temperature T_m below the critical temperature T_c , where T_m decreases with increasing external magnetic field. These temperature dependences of R are explained systematically on the basis of a recent theory of flux creep developed by the authors.

KEYWORDS: high- T_c superconductor, flux creep, temperature dependence, effective pinning potential, correlation length, flux bundle, critical current density

Japanese Journal of Applied Physics
Vol. 28, No. 11, November, 1989
pp. L1909-L1911

Complex Susceptibility of YBa₂(Cu_{1-x}Fe_x)₃O₇

Hiromasa MAZAKI, Shigeru KATSUYAMA†, Hiroshi YASUOKA,
Yutaka UEDA†* and Koji KOSUGE†

Department of Mathematics and Physics, The National Defense Academy, Yokosuka 239
†Department of Chemistry, Faculty of Science, Kyoto University, Kyoto 606

The superconducting transitions of YBa₂(Cu_{1-x}Fe_x)₃O₇ ($0 \leq x \leq 0.20$) compounds were measured in terms of complex susceptibility, $\chi = \chi' - i\chi''$. Two groups of samples were prepared. Group I was prepared by slow cooling from 850°C in flowing O₂ gas. Group II was prepared by heating in flowing N₂ gas at 800°C for 20 h, followed by slow cooling to room temperature in the same atmosphere and then by annealing in flowing O₂ gas below 400°C for more than 20 h. Comparisons of the results suggest that the clustering of substituted Fe ions takes place in the Cu₁-O planes of the samples in group II, and that the flux motion is restrained.

KEYWORDS: oxide superconductor, complex susceptibility, superconducting transition, YBa₂(Cu_{1-x}Fe_x)₃O₇

*Present address: The Institute for Solid State Physics, Tokyo University, Tokyo 106.

DAILY RECORD

- * The Government Industrial Research Institute, Osaka, has developed novel ceramics of high strength and high heat resistance with a lubricating effect. They are composite ceramics of particulate dispersion type, in which numerous fine graphite particles are dispersed in carbide ceramics, and the lubricating effect is provided by these graphite particles.
- * The National Research Institute for Metals has developed a new forming method for BN thin films, which are films of low gas-adsorbing type, in conditions of ultra-high vacuum. Using a high-frequency magnetron sputtering electrode, BN films are formed on a substrate of stainless steel at the low temperature of 300°C, which is about half the temperature conventionally required, and so these films can be formed on a substrate of ordinary stainless steel.
- * Sumitomo Electric Industry Co., in cooperation with Tokyo Electric Power Co., has succeeded in the production of a Y-system superconductive thin film of high-temperature type which exhibits $J_c = 8,000,000 \text{ A/cm}^2$ at 77K, and has a T_c of 91.5K. The production process was a laser vapor deposition method, and the substrate used was MgO.
- * The Noritake Company Limited has developed and commercialized a precision filtration apparatus for the fine particles which are generated during the grinding of ceramics.
- * The Government Industrial Research Institute, Nagoya has developed a semiconductor of Nb-added TiO_2 film, with low electrical resistance, by applying a sol-gel method. TiO_2 was used as the substrate, and it was first deposited with SiO_2 films. This semiconductor film is expected to be used as an oxygen sensor, a humidity sensor, and so on.
- * Murata Manufacturing Co. has developed a supersonic type of bubble sensor in which a piezoelectric ceramic of PZT was used. It will be marketed as a sensor for air bubble examination in medical instillation solution or for air bubble detection in brake oil.
- * Noritake Company Limited has developed and commercialized a drying system for paint on wooden furniture which uses a heater with far-infrared-radiation ceramics coated onto the surface of steel pipes, heated with steam.
- * The National Institute for Research in Inorganic Materials has developed a mass production process of rBN which is expected to be the raw material for the production of cBN. The starting materials used in this process are $\text{Na}(\text{BH}_4)$ and NH_4Cl . They are added to KCN during heating, and after cooling they are heated again to complete the process.
- * The Electric Power Resources Development Corp., in cooperation with Asahi Glass Co. and the Gadelius Co., has developed a ceramic filter of the inside-tube-surface type made of low-expansion cordierite. This filter can be used for the filtration of high-temperature gas up to 1,000°C, with a dust separation efficiency of 99.99%, and it can be back-washed with a high efficiency.
- * The Electric Chemical Industry Co. has succeeded in the development of a sintered Si_3N_4 body with exceptionally high toughness by sintering Si_3N_4 particles mixed with ultra-fine particles of TiN or of mixed Si_3N_4 and TiN in the matrix. The fracture toughness is 8.7MPa, which is about twice as high as that of a sintered body of simple Si_3N_4 .
- * The Mechanical Engineering Laboratory has confirmed that PZT dispersed with Al_2O_3 exhibits extremely high abrasion resistance in water.
- * The National Institute for Research in Inorganic Materials, in cooperation with Kamishima Chemical Industry Co., has succeeded in the production of transparent YAG ceramics. The process used was a modified wet precipitation method, which features the addition of sulfuric acid ions as reagent into an aqueous solution of HY and Al chlorides.
- * Hitachi Tool Manufacturing Co. has developed and commercialized an end mill head capable of cutting high-hardness materials. It has a hexagonal cross section and has a TiN coating on its surface.
- * Asahi Glass Co. had developed a novel technique for improving the toughness of composite ceramics from 1.5 to 1.8 times by using unidirectional fusion and solidification to sintered composite ceramics in an infrared suspension fusion furnace shaped in the form of two ellipses.
- * The National Chemical Laboratory has developed a new ceramic material of the LaCrO_3 system which can be sintered by a wet process after replacing part of its composition with Ca. This development result will make it possible to produce a more economic separator for a fuel cell, thus bringing closer the commercialization of fuel cells.
- * Hiroaki Katsuki, Special Researcher of Saga Prefectural Experiment Station, has developed a surface modification technique for ceramics such that needle-type mullite crystals can be densely grown on the surface of Al_2O_3 at a desired position and with desired thickness. The process utilized the coincidence between the sintering temperature of Al_2O_3 ceramics and the growing temperature of needle-type mullite.
- * Nobuhiro Sata, Senior Researcher, and his colleagues of the Geothermal Development Section of the Machine and Metals Department of the Government Industrial Research Institute, Tohoku, has developed a gradient-functional material of the TiB_2 -Cu system by using a self-exothermic-reaction method. This material can endure a maximum temperature of about 1,500°C, and a temperature difference of about 800°C between its two surfaces.
- * The Research Laboratory of the Fujitsu Co. has succeeded in the experimental manufacture of a highly efficient HBT using SiC by inhibiting the generation of crystal defects on hetero boundaries by the addition of fluorine.
- * Fujikoshi Co. has developed and commercialized an apparatus for coating cutting tools with TiN films, which, in addition to increased resistance to abrasion and sticking, have 1.5 to 2 times higher adhesion strength than TiN film coated by the conventional method.

Journal of the CERAMIC SOCIETY of Japan, *International Edition*

Vol.97 Oct. 1989

- High-Temperature Electrical Conduction in $\text{Bi}_2\text{-(Sr,Ca,Y)}_3\text{Cu}_2\text{O}_7$ Solid Solutions
- Structure Modulation and Superconducting Properties in $\text{Bi}_{2-x}\text{Pb}_x\text{Sr}_2\text{CaCu}_2\text{O}_{8+d}$ and $\text{Bi}_{2-x}\text{Pb}_y\text{Sr}_2\text{YCu}_2\text{O}_{8+d}$
- Effect of Fluorine Doping on the Synthesis of High- T_c Bi-Based Superconductors
- Influences of Additives on Superconducting Properties and Crystallization Process of Bi-Sr-Ca-Cu-O Glass-Ceramics
- Crystallization Process of Bi-Contained Superconductors Prepared from Rapidly Quenched Amorphous Materials and Effects of CdO Addition on the Process
- Single Crystal Growth of $\text{Bi}_2\text{Sr}_2\text{Ca}_{n-1}\text{Cu}_n\text{O}_y$ Superconductors by the Floating Zone Method
- Preparation of Superconducting Bi-Sr-Ca-Cu-O Films on Metal Substrates Using ZrO_2 as a Buffer Layer by Pyrolysis of Organic Acid Salts
- Effects of Microstructure on the Critical Current Density of Superconducting $\text{YBa}_2\text{Cu}_3\text{O}_x$
- Effects of Synthesis Conditions on Microstructure of a $\text{YBa}_2\text{Cu}_3\text{O}_x$ Superconductor by Partial Melting Process
- Orthorhombic-Tetragonal Transition of High T_c Superconductor $\text{YBa}_2\text{Cu}_3\text{O}_{7-x}$ and Its Behavior in the Release and Absorption of Oxygen during Heat Treatment
- Effect of Ba Salts on the Preparations of $\text{Ba}_2\text{YCu}_3\text{O}_{7-x}$ Superconductors
- Superconducting Properties of $\text{YBa}_2\text{Cu}_3\text{O}_x$ Ceramics Containing Ag_2O and Degradation in Moisture
- C-Axis Oriented Y-Ba-Cu-O Oxide Superconductor
- Fabrication of Screen-Printed Superconducting $\text{Ba}_2\text{YCu}_3\text{O}_{7-y}$ -Ag Metal Composite Thick Films
- New Techniques for Device Fabrications of High- T_c Superconducting Thin-films
- Syntheses and Characterization of $\text{LnBa}_2\text{Cu}_2\text{MO}_y$ ($\text{Ln}=\text{La, Pr}$ and $\text{M}=\text{Ta, Nb}$)
- Ionic Conductivity of Y_2O_3 Stabilized $\text{ZrO}_2\text{-ZrSiO}_4$ Ceramics
- Preparation of $\text{ZrO}_2\text{-MgO}$ Thin Films by OMCVD
- Preparation of Beta-Alumina Fibers by Sol-Gel Method
- Influences of Yttrium-Substitution on the Protonic Conduction of Apatite Ceramics
- Effects of Thermal Treatments on the Microstructure and the Conductivity of Superior-Conducting Glass-Ceramics in the System $\text{Na}_2\text{O-R}_2\text{O}_3\text{-P}_2\text{O}_5\text{-SiO}_2$ ($\text{R}=\text{Y, Sm, Gd}$)
- Ionic Conductivity of $\text{Na}_2\text{O-ZrO}_2\text{-P}_2\text{O}_5\text{-SiO}_2$ System Glass Ceramics
- Preparation and Electrical Properties of the Glasses in the Pseudoternary System $\text{CuI-Cu}_2\text{-MoO}_4\text{-Cu}_3\text{PO}_4$
- Electrical Conductivity and Determination of Mobile Ion Species in the Glasses of the System $\text{ZrF}_4\text{-BaF}_2\text{-LiF}$
- Hydrothermal Synthesis of Semiconductive PZT Solid Solutions and Electromechanical Properties of Sintered Bodies
- Dependence of Composition on Electrical Properties of La_2CuO_4 Ceramics
- Hot Pressing of Perovskite LaNiO_3
- Phase Transition and Electrical Properties of VO_2 (A)
- Preparation and Electrical Properties of Conductive Vanadium Bronze Ceramics
- Electrical Conduction and Structure of $\text{Fe}_2\text{O}_3\text{-V}_2\text{O}_5\text{-TeO}_2$ Glasses (Part 1) -Dc Conductivity -
- Electrical Conduction and Structure of $\text{Fe}_2\text{O}_3\text{-V}_2\text{O}_5\text{-TeO}_2$ Glasses (Part 2) -Discussion on the Structure-
- Preparation of $\text{Li}_{1+x}\text{Ti}_{2-x}\text{O}_4$ Thin Films by Sol-Gel Method and Electrical Properties
- Low Temperature Synthesis of Highly Conductive Transparent Films of F-doped Zinc Oxide
- Observation of SrTiO_3 -Ceramic Surface by Tunneling Spectroscopy
- Effects of Sintering Additives on the Thermoelectric Properties of SiC Ceramics
- Effect of Sintering Time on Electrical Conductivity of Sintered SiC
- Preparation and Electrical Conductivities of Layer Structured Crystals ZrNX ($\text{X}=\text{Br, I}$)
- Fabrication of Zirconium Nitride Sintered Bodies and the Application for Electrode Materials
- Properties of Hot-Pressed SiC Matrix Composites with Internally-Synthesized TiB_2
- Electrical Conductive Ceramics and Metal Bonding Using the Electrical Discharge Machining Technique
- Pressureless Sintering of $\text{TiB}_2\text{-Al}_2\text{O}_3$
- Characterization of Interface States in ZnO Varistors by DLTS Method
- Detection and Characterization of Trap Centers in ZnO Varistor by ICTS
- Relationship between Degradation Phenomenon and Trap Centers in ZnO Varistor
- Capacitance-Voltage Characteristics of ZnO Varistors and the Role of Dopants
- Effect of Additives on the Electrical Properties and Microstructure of Ceramic Varistors in ZnO-SrO System
- Influence of the Addition of BN and Bi_2O_3 on the Microstructure and the PTCR Effect in High-Curie-Point Barium-Lead Titanate Ceramics
- PTC Effect and Elementary Distribution near the Grain Boundary in a BaTiO_3 Semiconductor
- Infrared Sensing Properties of BaTiO_3 PTC Thermistor
- Ambient Temperature Solid-State Oxygen Sensor Using Fast Ion Conductors
- Humidity Sensitive Characteristics of β -Alumina Type $\text{M}^+\text{-}\beta$ -Ferrites ($\text{M}^+:\text{K}^+, \text{Rb}^+, \text{Cs}^+, (\text{Na}^+, \text{K}^+)$ and

Special Issue: Progress of Electrically Conductive Materials and Their Material Science

Vol.97 Oct. 1989

- NH₄⁺)
- Hydrogen Gas Sensing Properties in Polycrystalline Tin Oxide Films of Submicron Thickness
- Synthesis and Gas Adsorption Property of Conductive SnO₂ Porous Gels
- Electrical Characteristics of Na-Doped Alumina Humidity Sensor
- Synthesis of Bi₂(Ca, Sr, Ba)₃Fe₂O_x
- Effect of Extrusion on Critical Current of YBa₂Cu₃O₇₋₈ Superconducting Wires
- Humidity Sensor Characteristics of Porous Zeolite
- Ceramics at Elevated Temperatures
- Oxygen Sensor Using Proton-Conductor Thick-Film Operative at Room Temperature
- Infrared Detection by SiC-Fiber Thermistor
- Ionic Conductivity of Mg²⁺-Doped NH₄⁺-β-Gallate
- Effects of Mo₂B₅ Addition to MoSi₂ Ceramics
- Electrical Conductivity of Sintered SiC Containing Ni
- Simulation of ac Conduction in Ceramic Semiconductors
- Preparation of Spherical Si₃N₄ Particles from Polysilazane by Ultrasonic Spray Pyrolysis Technique

ORDER FORM

To: Circulation Div., the Journal of the Ceramic
of Japan, Society International Edition
c/o Fuji Technology Press, Ltd.
Daini Bunsei Bldg., 1-11-17 Toranomon
Minato-ku, Tokyo 105, Japan

Date: _____

Please enter my subscription to **special issue, progress of Electrically Conductive Materials and their Material Science (Vol.97 Oct. issue) of Journal of the Ceramic Society of Japan, International Edition** (for _____ copy/ies)

Name: _____

Position: _____

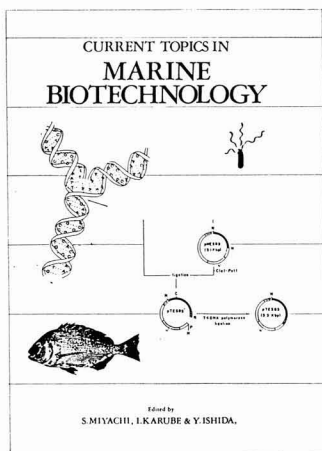
Address: _____

Signature: _____

Payment enclosed
(Payment enclosed is preferred)

Bill me
Airmail ¥30,000

CURRENT TOPICS IN MARINE BIOTECHNOLOGY



This is a collection of papers presented at the First International Conference on Marine Biotechnology held in Tokyo from September 3 through 6, 1989. About 400 scientists from 23 different countries conferred about developments in marine biology, meeting in six sections: microorganisms, microalgae, macroalgae, fish, shellfish and other marine animals, and supporting technology and interfacial subjects. There were many very lively discussions and reports of exciting new findings in every area.

Many participants agreed that marine biology can develop only through multidisciplinary and international cooperation, and a committee meeting was held during the Conference to plan for future International Conferences. Considering the rapid progress in this field, it was unanimously decided that one should be held every two years. By vote, Washington, D.C., U.S.A. was chosen as the place for the second conference, as proposed by Dr. O.R. Zaborsky of National Research Council, National Academy of Sciences, U.S.A. The third meeting will be held in Norway, and the fourth in France. The organizers are happy that meeting sites have been fixed so long in advance, since we observe that marine biotechnology is growing so rapidly in many parts of the world.

This Conference was made possible by the advice, help and cooperation of many people, both in scientific and governmental organizations and in private companies. I would like to express our special thanks for the cooperation of government agencies including the Ministry of Agriculture, Forestry and Fisheries, the Ministry of Education, Science and Culture, the Ministry of Health and Welfare, the Ministry of International Trade and Industry, the Science and Technology Agency and the Ministry of Foreign Affairs. There was financial support from the Commemorative Association for the World Exposition (1970) and ninety private companies listed in the proceedings. Special thanks should be extended to the staff of Marine Biotechnology Institute Co., Ltd., for their devoted help in the organization of this Conference.

ORDER FORM

To: Circulation Div., Current Topics in
Marine Biotechnology,
c/o Fuji Technology Press Ltd.
Daini Bunsei Bldg., 1-11-17 Toranomon
Minato-ku, Tokyo 105, Japan

Date: _____

Please enter my subscription to **Current Topics in Marine Biotechnology** (for _____
copy/ies)

Name: _____

Position: _____

Address: _____

Signature: _____

Payment enclosed
(Payment enclosed is preferred)

Bill me
Airmail US\$250.00

